INTERPRETING GRAVITATIONAL WAVES AND DEVELOPING RELATIVISTIC MULTIPHYSICS SOLVERS FOR CORE-COLLAPSE SUPERNOVA SIMULATIONS

By

Michael Anton Pajkos

A DISSERTATION

Submitted to
Michigan State University
in partial fulfillment of the requirements
for the degree of

Astrophysics and Astronomy & Computational Mathematics, Science, and Engineering – Doctor of Philosophy

2022

ABSTRACT

INTERPRETING GRAVITATIONAL WAVES AND DEVELOPING RELATIVISTIC MULTIPHYSICS SOLVERS FOR CORE-COLLAPSE SUPERNOVA SIMULATIONS

By

Michael Anton Pajkos

Core-collapse supernovae (CCSNe) mark the endpoint for millions of years of massive stellar evolution. After a successful explosion, supernovae increase the metallicity of the interstellar medium, generate intense electromagnetic radiation ionizing their surroundings, generate compact objects such as black holes or neutron stars, and create ripples in spacetime—gravitational waves (GWs). Advances in supernova theory over the past few decades have furthered our understanding of CCSNe. However, constraints on the physics enshrouded in the supernova center would further illuminate their explosion mechanisms. Advances in high performance computing (HPC) resources and the ever-increasing sensitivities of GW observatories have positioned the field of astrophysics between two recent technological advances. The work presented here leverages HPC to perform CCSN simulations, allowing astronomers to translate between GW signals and internal physics. Using this insight, astronomers are better positioned to constrain the physics driving these explosive events that have such a widespread influence throughout astronomy.

Investigating the evolution of 12-, 20-, 40-, and 60 $M_{\odot}$ progenitors, I perform axisymmetric neutrino radiation-hydrodynamic CCSN simulations, to relate the convective activity behind the supernova shock to the expected GW strength. I quantify how the rotational content of the supernova lowers GW frequencies. I present a novel method that combines two features of a single GW event to constrain the mass distribution within the stellar progenitor. By only requiring the two most detectable parts of the GW signal, astronomers can also potentially predict the explosion properties ~days before shock breakout. I present work with my undergraduate research assistant, that considers the impact of viewing angle on detecting GWs from CCSNe. Presented is a novel analysis method to identify the distribution of GW emission over all angles, accompanied with results showing that the preferred direction of GW emission for CCSNe migrates over time.

Lastly, I present new numerical solvers targeted at exascale computing platforms that account for magnetized fluid evolution with velocities near the speed of light and in extreme spacetimes. These solvers are accompanied with stringent baseline tests, paired with 1D and 2D supernova simulations making use of these features.

To Mom, Dad, Sarah, Jeff, and Gracie Mae. Na Zdrowie.

ACKNOWLEDGEMENTS

I am indebted to everyone who encouraged me to pursue my dreams. To my grandparents, aunts, uncles, cousins, and family, your love has propelled me to new heights. To my friends, thank you for taking this journey with me and pushing me to become a better person.

To Sean, thank you. From the south side of Chicago to Jena, Germany, you have always encouraged me to take challenges head on paired with the faith I would complete them; those are some of the most empowering traits an advisor, and a friend, can have.

I am grateful to Kyle Smuda, Kole Sedlack, Jordan Hochstetler, and Josh Excell for taking this wild graduate school ride with me, while making big moves of your own.

Thank you to my current and past group mates Carl Fields, Steve Fromm, Brandon Barker, Zac Johnston, Kuo-Chuan Pan, Chelsea Harris, and Jenn Ranta.

I am grateful to my committee Brian O'Shea, Jay Strader, Tyce DeYoung, Wolfgang Kerzendorf, and Luke Roberts for your time, patience, and advice. Thank you to Devin Silvia for teaching me how to better connect with students and teach others about astronomy in an accessible way. Thank you to Kim Crosslan for being one of the unsung heroes of the department. I am thankful to the Argonne team—Anshu Dubey, Jared O'Neal, Klaus Weide, and Carlo Graziani—whose patience and expertise helped me become a better computer scientist.

Thank you to my astronomy cohort: Adam Kawash, Justin Grace, and Claire Kopenhafer, as well as the younger and older astronomy graduate students. I am grateful for the friends I made at MSU: Cameron Kilgore, Anna Bosgraaf, Swapna Mishra, Steve Hemmerle, Nathan Frantz, Nick Valverde, Zoe Hansen, Macy Pell, Kurt Walcheske, and Meeshon Rogers. I am thankful for my collaborators for your insight and advice: Michele, Claudia, and Laura.

I am grateful to my professors at Butler: Dr. Dan Kosik, Dr. Gonzalo Ordonez, Dr. Brian Murphy, and Dr. Xianming Han for cultivating my interest in physics. Thank you to Dr. Ricardo Salinas for giving me my first professional research experience, and ensuring a piece of me will always be an observer.

Thank you to Mary Ann Wentzlaff, Linda Gilmore, and Dr. Prem Sharma, for teaching me the value of asking the right questions and initially setting me on this path.

This work was supported under a Michigan State University Distinguished Fellowship. Likewise, many of the simulations were completed with the help of the Institute for Cyber-Enabled Research, High Performance Computing Center.

TABLE OF CONTENTS

LIST OF TABLES

LIST OF FIGURES

CHAPTER 1

INTRODUCTION

1.1 Summary

The evolution of massive stars and their explosive endings—core-collapse supernovae (CCSNe)—are vital to understanding multiple astronomy subdisciplines, from acting as catalysts for the chemical enrichment of the universe, to creating compact objects like black holes or neutron stars. CCSNe are rich sources of observables: electromagnetic (EM) waves, neutrinos, and gravitational waves (GWs). These observables make CCSNe valuable laboratories to explore matter in extreme environments, with conditions currently unattainable from Earth-based experiments. With such potential astrophysical insights enshrouded in the center of the explosion, paired with the relative rarity of CCSNe in the Galaxy, astronomers have employed numerical models to connect physical observables to internal explosion physics. However, with the recent introduction of GW detectors, drawing these connections, while respecting detector sensitivities, is still a relatively new field. Likewise, with supercomputing technology constantly evolving, new numerical tools that actualize the potential of next generation computing platforms is requisite to ensure the longevity of CCSN science.

This Dissertation addresses the need to interpret GWs in unique ways and utilize so called next generation 'exascale' supercomputers. I present insights regarding the previously poorly understood effect of rotation on CCSN evolution and GW generation. I then introduce observationally motivated methods to determine the structure of the progenitor star from multiple components of a single GW event. I present work that considers the impact of viewing angle on the observability for CCSNe. Lastly, I present novel numeric solvers that incorporate general relativistic effects into a future-focused, multiphysics code. In short, this work has added to the field of gravitational astrophysics, resting at the juncture between numerical implementations, observational considerations, and theoretical advances to unveil information encoded in the brilliant endings of massive stars.

1.2 Physical Insights from Core-collapse Supernovae

Stars with zero age main sequence (ZAMS) masses $\gtrsim 8 M_{\odot}$ have sufficient overlying material to synthesize elements more massive than carbon after core hydrogen and helium fusion ceases. As these stars become supergiants, and eventually ascend the asymptotic giant branch, they continuously synthesize heavier elements in their cores, with concentric overlying elemental layers. With an inert iron core, the overlying silicon shell burning remains in a quasi-equilibrium (QSE) with α particle neighbors such as Ar and Ca: a network of reactions of these elements with protons, neutrons, α particles, and photons gradually deposits Fe group elements onto the core (Hix & Thielemann, 1996). As the Fe core is primarily supported by electron (e^-) degeneracy pressure, the additional mass causes the core to contract, and the central temperature rises. Once core temperatures reach $\sim$ 5 GK, gamma rays have sufficient energy to photodissociate the Fe nuclei, in a net endothermic process; the core collapses. With increasing central temperatures gamma rays continue to photodissociate Fe nuclei. Simultaneously, electron captures onto nuclei and free protons create copious amounts of electron type neutrinos: $p + e^- \Longleftrightarrow n + \nu_e$.

The once stellar core contracts from a radius $\sim$ 1000s of km, down to a radius $\sim$ 10s of km. The core reaches nuclear densities $\gtrsim 2 \times 10^{14}$ g cm^{-3}, and the strong nuclear force between baryons in the neutron-rich core becomes repulsive, rapidly halting the material infall in a process known as core bounce. The neutron rich central object is referred to as a protoneutron star (PNS). A shock then propagates outward, but is robbed of energy as it moves out of the supernova gravitational potential well, photodissociates overlying material, and cools via neutrino production—eventually stalling. An additional source of energy is required to revive the shock and cause a successful explosion.

After the shock is launched, the neutrinos created during the collapse decouple from the overlying stellar material 10s of km above the PNS surface (i.e., 'the neutrinosphere') and stream towards the outer parts of the stellar envelope. While the neutrino interactions occur relatively sparsely with the stellar plasma, because roughly 10^{53} ergs of energy is released through the

creation of these particles, some energy is deposited in the shocked material and strengthens turbulence behind the shock. According to the neutrino driven paradigm, this delayed neutrino heating is sufficient to launch a successful explosion (Bethe & Wilson, 1985) and is considered one of the most promising explosion mechanisms.

According to the magnetorotational mechanism of explosion, during collapse magnetic field lines are compressed and, in sufficiently rotating models, can be wound and amplify due to the magnetorotational instability (MRI) (e.g., Akiyama et al., 2003; Burrows et al., 2007). A columnated magnetic jet drives bipolar outflows with sufficient energy to drive a successful explosion as well (Bisnovatyi-Kogan, 1970; LeBlanc & Wilson, 1970). Although theory is still attempting to explain the exact formation channel for rapidly rotating, highly magnetized massive stars, this explosion mechanism is a promising candidate to explain the high luminosities in superluminous supernovae, luminosities the neutrino heating mechanism alone cannot explain (Greiner et al., 2015). Furthermore, investigating the connections between energetic CCSNe and gamma ray bursts (GRBs) has been a growing field, with one of the first clear observational connections from GRB030329 (Greiner et al., 2003) with associated supernova SN2003dh (Matheson, 2004; Woosley & Bloom, 2006).

For the case of successful explosions, there are two possibilities for the ultimate fate of the PNS. For a sufficiently energetic explosion, mass accretion onto the central compact object halts and the PNS cools to form a neutron star (NS). By contrast, if adequate material falls back onto the PNS, even if a shock breaks out of the stellar envelope, it will collapse to form a black hole (BH). It is estimated roughly a quarter of all CCSNe fail to explode, yielding material that falls back onto the PNS, forming a BH; these events are known as 'failed supernovae' (Kochanek et al., 2008).

1.2.1 The Influence of CCSNe on Astronomy

CCSNe impact a variety of areas of study within astrophysics. Although massive stars are rarer than low mass stars, the relatively short lifespans of massive stars allows multiple generations of CCSNe to leave a distinct imprint on the chemical evolution of the universe. Principally, CCSNe

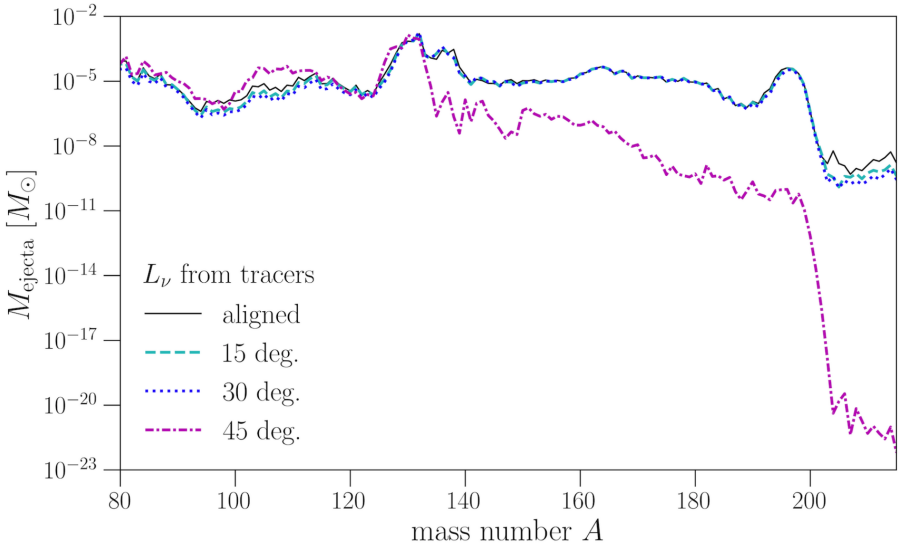

Figure 1.1: Elemental abundances produced for the magnetized CCSN models from Halevi & Mosta (2018) with varying levels of alignment between the rotation and magnetic field axes. For nearly aligned cases, magnetically driven CCSN produce elements with atomic numbers beyond 200.

are responsible for distributing the vast majority of the oxygen created. CCSNe also deposit heavier elements up to iron that are made during massive stellar evolution. Elements beyond Fe can be created due to proton and neutron captures onto these massive nuclei during the explosion phase. In particular, CCSNe are thought to be potential sites of the weak rapid neutron capture process (r-process) for neutrino driven explosions, creating elements with atomic numbers A < 130 (Arcones & Montes, 2011). For magnetically driven explosions, numeric models show creation of heavier r-process elements, with $A > 200$ (Winteler et al., 2012; Halevi & Mosta, 2018). Figure 1.1 quantifies the yields of different elements from magnetized CCSN models. With each successive generation of massive stars, explosion outflows chemically enrich the interstellar medium, protoplanetary disks, and future generations of stars.

Serving as furnaces that forge compact objects, CCSNe provide the initial conditions for the formation of NSs and BHs that can leave an imprint on their observables. Isolated objects such as pulsars (Antoniadis et al., 2013), rare magnetic NSs like magnetars (Olausen & Kaspi, 2014), binary interactions causing X-ray bursts (Steiner et al., 2010), or merging compact objects (Abbott

et al., 2016b) represent major events explored by various subfields within astronomy. The masses, spins, and magnetic fields of these compact objects are set by the conditions within the respective supernovae. By further constraining the formation channel by which these objects form, theorists can more precisely predict the range of physical conditions observers can expect to detect.

With densities $10^{14} - 10^{15}$ g cm^{-3} and temperatures on the order of 10^9 K, CCSNe act as sites well-described by the hot nuclear equation of state (EOS). The hot nuclear EOS is an active area of research in the nuclear astrophysics community, as supported by the creation of international collaborative efforts, such as the *Facility for Rare Isotope Beams* (Gade & Sherrill, 2016) and the National Science Foundation-supported *Nuclear Physics from Multi-Messenger Mergers* (NP3M)[1] collaboration. The hot nuclear EOS is a pivotal input to simulations of CCSNe and NS mergers, impacting the dynamics of the systems, resulting multimessenger signals, and composition of resulting ejecta—factors vital in identifying sites for the origin of the elements and quantifying their abundances (Winteler et al., 2012; Kasen et al., 2017).

1.2.2 Conventional Observations of Supernovae

This subsection reviews what can be learned from EM and neutrino observations of CCSNe, as they relate to predictions provided by numerical models. Likewise, it outlines the strengths and limitations of each method to extract new physics from supernovae.

1.2.2.1 Insights from Electromagnetic Observations

Using stellar spectra observed from supernovae dates back to original classification of CCSNe with Rudolph Minkowski classifying supernovae based on the presence of hydrogen (Minkowski, 1941). Further sub-classifications have emerged based on spectral features such as the presence of helium or silicon, and the width of spectral lines. Beyond classifications, spectra from supernova—elements like Ni, Ti, and Co—serve as valuable probes to the internal structure of the explosion.

[1] https://np3m.org/

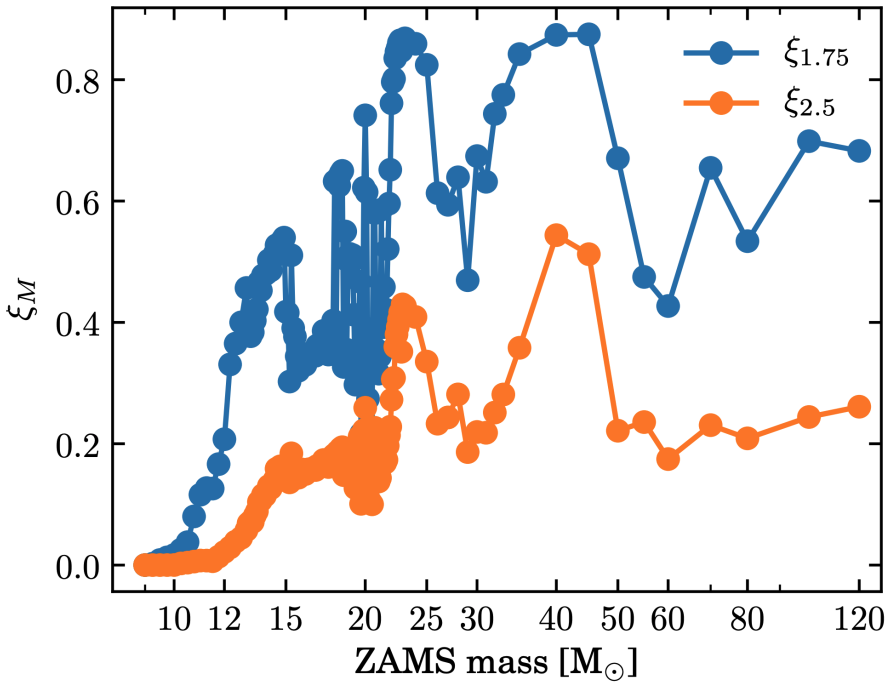

Figure 1.2: Measure of compactness ξ versus ZAMS mass at different mass cuts from the Sukhbold et al. (2016b) progenitor series. This figure displays the non-monotonicity of mass distribution within massive stars just before collapse, due to the nonlinearities present throughout stellar evolution. Figure taken from (Couch et al., 2020a).

To explain the connection between spectral signatures and core structure, consider the quantity referred to as compactness ξ (O'Connor & Ott, 2010). Compactness is a measure of how much mass is contained within a given radius of the supernova core at collapse. Physically, the more compact a core, the more gravitationally bound. Stars with high compactness have shallow density gradients near their core and will accrete more material during the supernova evolution. With more material closer to the highly energetic supernova core, greater quantities of material with higher atomic numbers—Ti, Fe, Ni, Co—will be synthesized and launched in the supernova ejecta (Sukhbold et al., 2016b). Observationally, as these unstable isotopes radioactively decay, they produce EM radiation that will leave spectral signatures of these elements. It is important to emphasize there is a non-monotonic relationship between ZAMS mass and stellar core compactness at collapse, due to the inherent nonlinearities involved in stellar evolution (Sukhbold et al., 2016b), as displayed in Figure 1.2.

As stars with higher core compactness also produce higher mass accretion rates, more thermal energy will be deposited on their cores. Due to pair production of neutrinos and anti neutrinos, this thermal energy will be liberated with higher neutrino luminosities (Müller, 2019). In turn, increased neutrino heating drives more active convection in the post shock region and, in the case of successful explosions, will drive a more energetic explosion. This dense wall of material will ionize more hydrogen in the stellar atmosphere as the shock breaks out. As the photons emitted from recombination of electrons with ionized H are the principal driver for the 'plateau luminosity' for Type IIP supernovae, there is a connection between higher plateau luminosity and increased core compactness (Barker et al., 2021).

Another observable of value is the velocity of the photosphere after shock breakout. As established, for successful explosions, progenitors with higher core compactness will produce more energetic explosions. These more violent shock breakouts will in turn launch the ejecta with higher velocity away from the core of the star. The velocity of this outgoing material can be observed via Doppler shifts of spectral lines. In practice, FeII lines have been used and typical photospheric velocities are of the order of 1000s of km s^{-1} (Gutiérrez et al., 2017).

The advantage of measuring supernova spectra, plateau luminosities, and photospheric velocities is the plethora of telescopes available that collect EM radiation. From smaller survey telescopes such as ASAS-SN (Kochanek et al., 2017), to 4 meter class telescopes such as the Southern Astrophysical Research (SOAR) telescope, to 10 meter class telescopes such as the KECK Observatory, networks of telescopes in all time zones allow for virtually continuous observation of the night sky (e.g., Las Cumbres (Brown et al., 2013)). Likewise, the high efficiency of optical mirrors, has allowed astronomers to view supernovae at distances over 9 billion light years (Ly) (Strolger & Riess, 2006). Nevertheless, photons are prone to extinction due to interstellar dust, making observing sources from the densest regions of the Milky Way—the Galactic disk and Galactic center—difficult. Furthermore, due to stellar opacities, the photons emitted from CCSNe are limited to those from the outermost layers of an explosion. While previously mentioned work (Barker et al., 2021) attempts to circumvent this issue with important correlations with core compactness,

observers must wait ~months for sufficiently small optical depths, before receiving any *direct* photons from the supernova core.

1.2.2.2 Insights from Neutrino Observations

The first detection of supernova neutrinos came from the Super-Kamiokande, or Super-K, detector from supernova 1987A (Hirata et al., 1987). As research in CCSNe evolved, neutrino observations developed from simply making detections of CCSNe to constraining the properties of the explosion based on neutrino properties, such as the the energies of different flavors and total number of neutrino counts.

The first significant source of neutrinos arises from the burst of electron type neutrinos that escape from the supernova neutrinosphere with energies $\sim$ 10 MeV (Müller & Janka, 2014). The characteristic rise in neutrino counts can be useful for timing the occurrence of the core bounce, a quantity of particular use for improving detectability of GWs. As the supernova ensues, the increased production of electron, muon, and tau type (anti)neutrinos encodes information about the mass accretion history of the PNS. As the mass accretion rate is related to the compactness of the progenitor, the number of counts and energies of the neutrinos—in both failed and successful explosions—has been show to correlate with ξ (Warren et al., 2020).

During the accretion phase, as the PNS approaches a critical mass, it may collapse to a BH. During the final collapse of a PNS to a BH, neutrino energies are expected to moderately rise, as the core increases in temperature before BH formation (Müller, 2019). Following the creation of a BH, the neutrino signal would abruptly cease, providing astronomers with an estimation of BH formation time (t_{BH}). This observable feature is valuable for calibrating stellar evolution calculations and supernova models, as stellar structure is intimately related to t_{BH} (O'Connor & Ott, 2010).

For CCSNe that retain NSs in their core, following the accretion phase, the NS enters the Kelvin-Helmholtz cooling phase. During this phase, the diffusion of neutrinos out of the NS gradually cools the compact object. While the duration of the cooling phase is expected to depend on the

nuclear EOS, there exists no simple mapping between cooling phase duration and EOS properties. Rather, bulk properties of the PNS like the mass and binding energy are simpler to extract (Lattimer & Prakash, 2001).

The benefit of neutrino observations for extracting supernova characteristics lies in the ability of the neutrinos to pass through lower density matter unobstructed. This feature allows neutrino observatories to detect *direct* signals emitted from the supernova core mere seconds after core bounce. Furthermore, for supernovae that may occur in the Galactic disk, they will not suffer from extinction like EM waves. Examples of observatories that can (will) detect supernova neutrinos are Super-K (Hyper-K) (Abe et al., 2021) which are water Cherenkov detectors sensitive to $\bar{\nu}_e$. Although Ice-cube (Köpke & IceCube Collaboration, 2011) is designed for neutrinos with energies > 100 GeV, the large detector volume will be able to identify signatures of MeV neutrinos via increases in its dark current. Likewise, with 2 ms timing resolution, Ice-Cube would provide fine resolution timing information. The Deep Underground Neutrino Detector (DUNE) (Abi et al., 2021) is a liquid argon detector that would provide finely sampled ν_e light curves. The Jiangmen Underground Neutrino Observatory (JUNO) is a liquid scintillator detector sensitive to $\bar{\nu}_e$, and offers fine energy resolution to help determine the energy spectrum of incoming neutrino events (An et al., 2016).

The difficulty posed by neutrino observations is the lack of understanding regarding neutrino oscillations between different flavors: in particular, interpreting neutrino observations and connecting them to supernova physics (Mirizzi et al., 2016). In supernova modeling, accounting for neutrino interactions in vacuum, in matter, and between other neutrinos is prohibitive due to computational cost. Thus, interpreting observables can be less reliable until the effect of neutrino oscillations can be properly accounted for. Additionally, the imprint of stellar rotation on neutrino signals, although briefly explored (Ott et al., 2012), is still not fully understood.

Given the limitations of observations of EM waves and neutrinos, there is motivation to rely on other observables that can constrain stellar rotation, provide direct information from the supernova core, and can readily connect signal features to source physics. To meet this scientific demand

and make use of timely instrumentation—the Laser Interferometer Gravitational-wave Observatory (LIGO) (LIGO Scientific Collaboration et al., 2015), Virgo (Acernese et al., 2015), and KAGRA (Kagra Collaboration et al., 2019)—GWs offer a natural remedy to expand the CCSN scientific horizon.

1.3 Characteristics of Gravitational Waves

Einstein's theory of general relativity (GR) quantifies the distance between events based on a spacetime metric commonly denoted $g_{\mu\nu}$. This metric is a symmetric tensor, acting as a linear function that accepts vectors which represent events—one time component and three spatial components—as inputs and returns the distance between the events. Fundamentally, $g_{\mu\nu}$ represents a general curved spacetime, that depends on the mass and energy distribution surrounding a region of interest:

$$G_{\mu\nu} = 8\pi T_{\mu\nu}, \tag{1.1}$$

where $G_{\mu\nu}$ is the Einstein tensor and $T_{\mu\nu}$ is the stress energy tensor. In this work Newton's constant G, the speed of light c, and solar masses $M_\odot$ are set to unity, unless otherwise noted. This condensed form represents Einstein's field equations of GR. Here $G_{\mu\nu}$ depends on derivatives of the spacetime metric $g_{\mu\nu}$, and in general, quantifies the curvature of spacetime. $T_{\mu\nu}$ describes distributions of stress-energy for various sources: fluids, EM radiation, particles, general scalar fields. Equations (1.1) yield powerful insight that matter curves spacetime and spacetime determines how matter moves. With this connection, one realizes dynamic matter distributions must create dynamic spacetimes. Far away from matter sources, spacetime is considered flat and described by the Minkowski metric which can be described in Cartesian coordinates as

$$\eta_{\mu\nu} = \begin{pmatrix} -1 & 0 & 0 & 0 \\ 0 & 1 & 0 & 0 \\ 0 & 0 & 1 & 0 \\ 0 & 0 & 0 & 1 \end{pmatrix}. \tag{1.2}$$

As a note, this work follows Einstein's summation convention; that is whenever indices are repeated, a sum over all possible values is performed. Greek letters can be 0, 1, 2, or 3 and Latin letters can be 1, 2, 3. When observing slowly moving matter or extreme sources (e.g., coalescing compact objects or CCSNe) from a large distance, $g_{\mu\nu}$ can be described by perturbations to the Minkowski metric:

$$g_{\mu\nu} = \eta_{\mu\nu} + h_{\mu\nu}, \tag{1.3}$$

where elements of $h_{\mu\nu}$ are taken to be much less than one. Substituting Equation (1.3) into Equation (1.1) and retaining first order terms in $h_{\mu\nu}$ yields

$$(-\partial_t^2 + \partial_i\partial^i)\bar{h}_{\mu\nu} = -16\pi T_{\mu\nu} \tag{1.4}$$

where $\bar{h} = h_{\mu\nu} - \eta_{\mu\nu}h^{\mu}_{\mu}/2$ and ∂_μ represent partial derivatives with respect to μ. Regarding notation, $\partial_i = \partial/\partial x^i$. Thus, the implied summation of partial derivatives recovers the familiar Laplacian operator $\partial_i\partial^i = \partial^2/\partial x^2 + \partial^2/\partial y^2 + \partial^2/\partial z^2$. Equation (1.4) represents a set of wave equations for these perturbations to the spacetime metric. The solutions to these equations are given by the Green function for the wave operator yielding

$$h_{ij}^{TT} \sim \frac{2}{D}\ddot{I}_{ij}^{TT}(t - D), \tag{1.5}$$

where TT indicates a tensor whose trace is 0 and transverse components are 0—also known as transverse-traceless (Baumgarte & Shapiro, 2021), $\ddot{I}_{ij}$ is the acceleration of the reduced mass quadrupole moment of a matter distribution, and D is the distance to the source. This definition describes that, for slow moving weak field sources, perturbations to the spacetime metric, or GWs, depend on $\ddot{I}_{ij}^{TT}$ to leading order.

GWs are transverse waves, with the valuable characteristic that they pass through matter unobstructed. Thus, GWs act as valuable signals that can be emitted *directly* from sources previously unobservable via EM radiation. Thus far GWs have been detected from binary BH (Abbott et al., 2016c), binary NS (Abbott et al., 2017), and BH-NS systems (Abbott et al., 2021). However, as

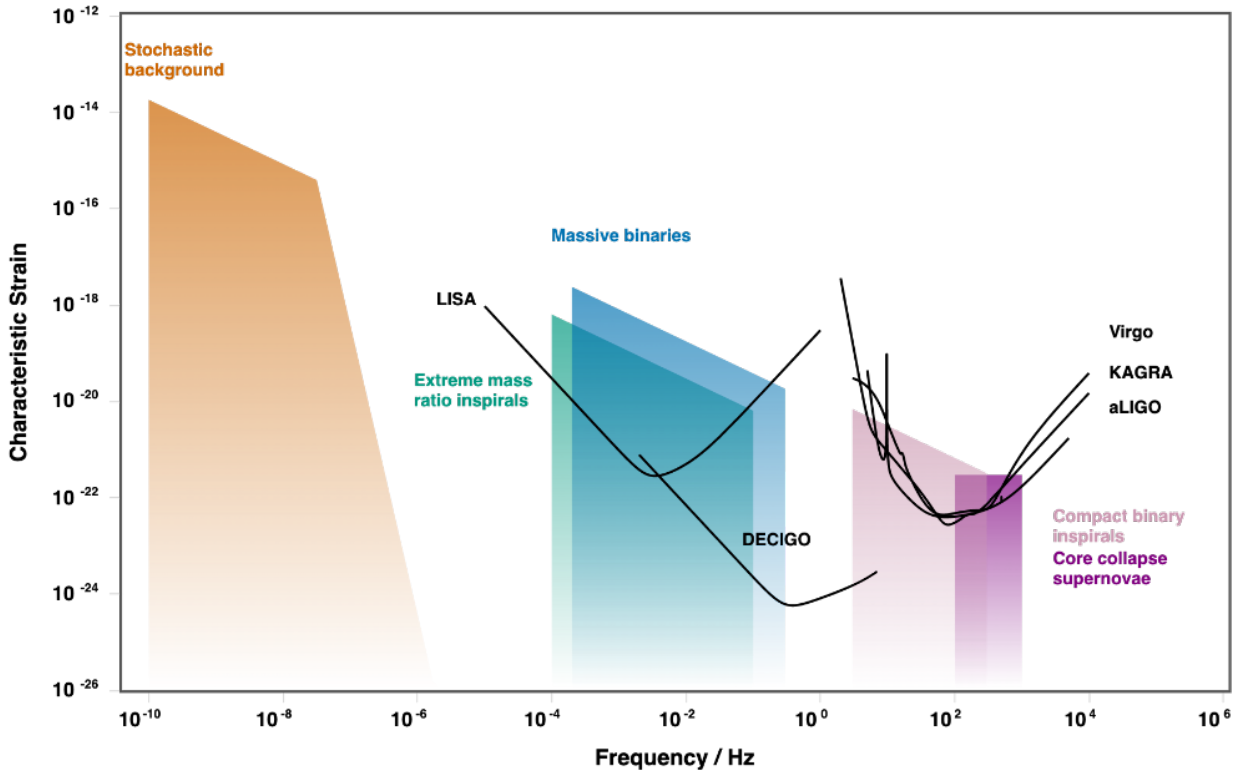

Figure 1.3: Sensitivity curves selected current—LIGO, Virgo, and KAGRA—and future—LISA and DECIGO—GW observatories. While CCSN processes produce GWs across many frequencies, current observatories are sensitive to Galactic events with GW frequencies 10s - 100s of Hz. Figure taken from Moore et al. (2014).

long as Equation (1.5) is satisfied, ripples in spacetime will be generated. Thus, other proposed sources of detectable GWs involve accreting pulsars (Abbott et al., 2020), phase transitions from the early universe (Ellis et al., 2019), and CCSNe (Kotake, 2013).

1.3.1 Connecting GW Signals to CCSN Physics

The generation of GWs from CCSNe has been expected for decades (Wheeler, 1966; Finn & Evans, 1990). As modern computing resources allow for wider explorations of parameter space, the need for templates of possible waveforms is slowly being met [2]. Although modern GW observatories would require a Galactic CCSN for adequate signal strength, the potential physics insight from these signals could provide one of the most valuable measurements of hot nuclear matter to date.

[2] https://stellarcollapse.org/gwcatalog.html

With larger collections of GW templates, and instrument sensitivities improving, *there is a current need by the observational community to connect observable GW features to source physics*.

During collapse, centrifugal support within rotating supernovae will cause the PNS to deform, becoming oblate. During core bounce, due to ram pressure imparted by the infalling collapsing material, the PNS will rapidly become more spherical. This deformation of material at nuclear densities produces a signal that scales roughly with the angular momentum of the PNS squared and produces broadband emission. This signal is well templated in the time domain, leaving it as one of the more promising candidates for observation, by using its well defined structure to improve detectability from LIGO background noise (Edwards et al., 2014).

During the accretion phase, as accreted matter overshoots the surface of the PNS, vibrational modes of the compact object can cause oscillations, producing another robust source of GWs. Multiple modes may simultaneously emit gravitational radiation from 100s of Hz to the order of kHz, as the PNS contracts and its dynamical frequency increases (Torres-Forné et al., 2019b). For vibrational modes that are restored by gravity (g-modes), they produce GW amplitudes of comparable order to the previously mentioned bounce signal, with frequencies near the upper end of the LIGO sensitivity curve at a few hundred Hz. Figure 1.3 displays the sensitivity curves for multiple GW observatories, with current ground-based GW observatories detecting the upper end of the frequency spectrum. These oscillatory modes encode information about the mass and radii of the PNS just after bounce and can be used to track the cooling rate of the compact object (Torres-Forné et al., 2019a).

Although of smaller amplitude, direct mass motions behind the supernova shock can also directly generate GWs. Convective overturn (Pajkos et al., 2019), hydrodynamic instabilities like the Standing Accretion Shock Instability (SASI) (Andresen et al., 2017), or the low T/W instability (Takiwaki et al., 2021) have been shown to create GWs $\sim$ 200 Hz. However, while the GWs directly produced from turbulence may be of lower amplitude, instabilities such as the SASI or low T/W may produce bulk asymmetries in the motion of the PNS, which can in turn create stronger GWs (Andresen et al., 2019). Near the end of a successful explosion, asymmetric neutrino production

(Mukhopadhyay et al., 2021) or direct ejection of the compact object (Burrows & Hayes, 1996) due to bipolar outflows can produce unique GWs. The bulk asymmetries in the CCSN system would yield modest amplitudes 10 - 100 times weaker than the GWs generated from PNS oscillations, with frequencies of the order 1 Hz, and can produce direct offset signals that permanently distort spacetime, also know as 'GW memory' (Vartanyan & Burrows, 2020). These low frequencies are outside of current detector sensitivity ranges and would need to be observed by future space based observatories like the Laser Interferometer Space Antenna (LISA) (Amaro-Seoane et al., 2017) or Deci-hertz Interferometer Gravitational Wave Observatory (DECIGO) (Kawamura et al., 2021).

While these connections between GW features and specific physical properties are insightful, it is important to take these predictions in the context of observation. As meaningful detections of GWs have only been occurring for less than a decade, the subfield of connecting GWs *detectable by current instruments* to CCSN features is still in its infancy. As supernova modeling becomes increasingly sophisticated and GW observatories increase sensitivity, framing theoretical predictions beyond detector sensitivity curves will help align CCSN models with experimental efforts by considering factors in unique data extraction pipelines [e.g., coherent WaveBurst (Klimenko et al., 2021) or BayesWave (Gill et al., 2018)]. Furthermore, the potential to motivate and inform the construction of future GW observatories exists to make use of more unique features of GW signals, such as polarization and viewing angle dependence (Hayama et al., 2016).

Having discussed the connection between GW observables and internal supernova processes, I now consider the relevant physics influencing the supernova evolution that must be numerically implemented to perform proper numerical models of these stellar explosions.

1.4 The Multiphysics Nature of CCSNe

While supernova modeling is an evolving field due to technological advances in computing and detectors, there are core principles that motivate ongoing research: exploring various initial conditions that respect massive star observations, solving systems of coupled partial differential equations (PDEs) that robustly model the underlying physics with reasonable simulation times, and interpreting simulation output to provide meaningful predictions that can be validated with

observations. Numerical models of CCSNe are one of the most challenging computational problems to solve because of the multitude of physics treatments incorporated for a given set of coupled PDEs.

As 99% of the energy released from CCSNe is in the form of neutrinos, accounting for radiation transport is paramount to properly capturing supernova evolution. Evolving neutrinos in numerical models requires solving the relativistic collisional Boltzmann transport equation (Lindquist, 1966)

$$p^{\alpha}\left[\frac{\partial f_{\nu_i}}{\partial x^{\alpha}} - \Gamma^{\beta}_{\alpha\gamma} p^{\gamma} \frac{\partial f_{\nu}}{\partial p^{\beta}}\right] = \left[\frac{df_{\nu}}{\partial \tau}\right]_{\text{collision}}, \tag{1.6}$$

where f_{ν_i} is the neutrino distribution function, x^{α} is the position vector, p^{α} is the momentum vector, $\Gamma^{\beta}_{\alpha\gamma}$ are Christoffel symbols (describing spacetime curvature), and neutrino interactions (e.g., scattering, absorption, with surround matter and other neutrinos) are captured in the collision term $[df_{\nu}/\partial\tau]_{\text{collision}}$.

Fully solving for the 7-dimensional neutrino distribution function—three spatial degrees of freedom, three momentum degrees of freedom, and time evolution—incurs an immense computational cost. Various approximations exist to mitigate this expense. The first approximation relevant to this work are so called 'leakage schemes'. Leakage schemes do not formally evolve the neutrino distribution function, rather, interpolate between free emission rates and emission rates resulting from the diffusion approximation (O'Connor, 2015). While computationally inexpensive, leakage schemes have difficulty reproducing neutrino heating in problems that deviate from spherical symmetry. The so called 'M1 scheme' is considered to be state of the art for CCSN simulations.

M1 reduces the angular dependence of the Boltzmann transport equation by taking moments of the neutrino distribution function $f = f(x^{\mu}, \epsilon_{\text{neut}}, \Omega)$ and providing an analytic closure (Cardall et al., 2013). When using units of $\hbar = c = 1$, the first three moments of the distribution function, in the frame comoving with the fluid, retain physical meanings as

$$\mathcal{J} = \epsilon_{\text{neut}} \int f d\Omega, \tag{1.7}$$

representing the energy density,

$$\mathcal{H}^{\mu} = \epsilon_{\text{neut}} \int \ell^{\mu} f \, d\Omega, \tag{1.8}$$

representing the energy flux, and

$$\mathcal{K}^{\mu\nu} = \epsilon_{\text{neut}} \int \ell^{\mu} \ell^{\nu} f \, d\Omega, \tag{1.9}$$

representing the radiation stress. Here $d\Omega = \sin\theta d\theta d\phi$ represents a differential element of solid angle of the unit sphere, for a polar angle θ and azimuthal angle ϕ, ϵ_{neut} the neutrino energy, and $(\ell^0,\ \ell^1,\ \ell^2,\ \ell^3) = (0,\ \cos\theta,\ \sin\theta\cos\phi,\ \sin\theta\sin\phi)$. These moments are related to the evolution equations

$$\frac{\partial D_{T,n}}{\partial t} + \frac{\partial F^{i}_{T,n}}{\partial x^{i}} + \frac{1}{\epsilon^{2}_{\text{neut}}} \frac{\partial}{\partial \epsilon_{\text{neut}}} [\epsilon^{2}_{\text{neut}} (R_{T,n} + O_{T,n})] = G_{T,n} + C_{T,n}, \tag{1.10}$$

for the conserved energy density $D_{T,n}$ and flux of conserved energy $F^{i}_{T,n}$ and

$$\frac{\partial (D_{T,\gamma})_{j}}{\partial t} + \frac{\partial (F_{T,\gamma})^{i}_{j}}{\partial x^{i}} + \frac{1}{\epsilon^{2}_{\text{neut}}} \frac{\partial}{\partial \epsilon_{\text{neut}}} [\epsilon^{2}_{\text{neut}} ((R_{T,\gamma})_{j} + (O_{T,\gamma})_{j})] = (G_{T,\gamma})_{j} + (C_{T,\gamma})_{j}, \tag{1.11}$$

for the conserved momentum densities $(D_{T,\gamma})_{j}$ and flux of conserved momenta $(F_{T,\gamma})^{i}_{j}$. Here $R_{T,(n,\gamma)}$ and $O_{T,(n,\gamma)}$ represent gravitational shifts and observer corrections, respectively. $G_{T,(n,\gamma)}$ and $C_{T,(n,\gamma)}$ represent gravitational source terms and collision source terms, respectively. Terms with n subscripts correspond quantities evolving the neutrino energy density and terms with γ subscripts influence the evolution of the neutrino momentum density. Lastly, this system of moments is closed by choosing an appropriate closure condition

$$\mathcal{K}^{\mu\nu} = \frac{1}{3} \mathcal{J} h_{P}^{\mu\nu} + a(\mathcal{J}, \mathcal{H}) \left(\mathcal{H}^{\mu} \mathcal{H}^{\nu} - \frac{1}{3} \mathcal{H}_{\mu} \mathcal{H}^{\mu} h_{P}^{\mu\nu} \right), \tag{1.12}$$

where $h_{P}^{\mu\nu}$ is the orthogonal projector relative to the comoving frame (Cardall et al., 2013),

$$a(\mathcal{J}, \mathcal{H}) = \frac{\mathcal{J}}{\mathcal{H}^{\mu} \mathcal{H}_{\mu}} \frac{(3\chi - 1)}{2}, \tag{1.13}$$

and $\chi = \chi(\mathcal{J}, \mathcal{H})$ is a constant chosen according to the Minerbo closure (Minerbo, 1978; Pons et al., 2000). While more expensive than leakage schemes, M1 provides results much closer to full Boltzmann transport calculations. In Chapter 2 and Chapter 3, the software architecture `FLASH` (Dubey et al., 2009; Fryxell et al., 2010) uses the M1 neutrino treatment. The CCSN models in Chapter 5 use a leakage scheme.

Another vital component impacting a successful explosion is turbulence of the stellar plasma behind the shock. Modeling magnetized fluid flow involves incorporating magnetohydrodynamics (MHD). In general, MHD requires conservation of mass, momentum, energy, species number, and maintain that the divergence of the magnetic field remains zero. In a condensed form, these equations can be described as a coupled system of hyperbolic PDEs

$$\frac{\partial \mathbf{U}}{\partial t} + \frac{\partial \mathbf{F}_i}{\partial x^i} = \mathbf{S}, \tag{1.14}$$

where $\mathbf{U}$ is a vector of conserved quantities, $\mathbf{F}_i$ are spatial fluxes in the i^{th} direction, and $\mathbf{S}$ accounts for sources and sinks (Toro, 2009). While Equation 1.14 is a condensed form describing the evolution of a general hyperbolic system, the specific MHD components developed in this work—in terms of quantities like density, velocity, and magnetic field—are described in detail in Chapter 5. Unless otherwise noted, the simulations used throughout this Dissertation make use of `Spark`: a directionally unsplit ideal MHD solver, with a strong stability preserving (SSP) second order Runge-Kutta time integrator (Couch et al., 2021). Likewise, they make use of fifth order weighted essentially non-oscillatory (WENO5) spatial reconstruction and the HLLC approximate Riemann solver (Toro et al., 1994). The MHD scheme accounts for fundamental characteristics of the fluid, also called primitive variables, which other solvers depend on, such as density, pressure, internal energy, and velocity. Furthermore, the source terms in Equation (1.14) account for the influence of radiation transport, gravity, and nuclear reactions as well—emphasizing the coupled nature of these systems of equations.

The gravitational treatment contributes to the success or failure of an explosion, the features of multimessenger signals, and the final compact object remnant. Fully solving the set of Einstein's

field equations using standard methods—the Baumgarte-Shapiro-Shibata-Nakamura (BSSN) formulation (Shibata & Nakamura, 1995; Baumgarte & Shapiro, 1998)—involves solving a system of 40 coupled hyperbolic PDEs. When used with previous advanced physics treatments, such as neutrino transport, calculations become increasingly expensive, especially for 3D simulations. In `FLASH`, a commonly used, less expensive approximation is known as the GR 'effective potential', or GREP (Marek et al., 2006). The GREP involves contributions such as the pressure and internal energy of the matter to the gravitational potential, as opposed to merely integrating over a density distribution. Thus, in one dimension, the equation for this Tolman-Oppenheimer-Volkhoff (TOV) mass, which contributes to the gravitational potential, is described by

$$\frac{dm_{\mathrm{TOV}}}{dr} = 4\pi r^2 \left(\rho + \rho\epsilon + E_\nu + \frac{v_i F_\nu^i}{\Gamma} \right) \Gamma \tag{1.15}$$

where ρ is the rest mass density, ϵ is the specific internal energy, E_ν is the energy density of the neutrinos, F_ν^i is the neutrino momentum density, v_i is the average radial velocity, and Γ as a function of distance r represents an empirical factor that more closely resembles full GR calculations

$$\Gamma = \left(1 + v^2 - \frac{2m_{\mathrm{TOV}}}{r} \right)^{1/2}. \tag{1.16}$$

Equation 1.15 and Equation 1.16 contribute to the GR 'effective potential' ϕ_{eff} by

$$\frac{\partial \phi_{\mathrm{eff}}}{\partial r} = \frac{m_{\mathrm{TOV}}(r) + 4\pi r^3 (P + P_\nu)}{r^2 \Gamma^2} \left(1 + \epsilon + \frac{P}{\rho} \right), \tag{1.17}$$

where P_ν is the pressure exerted by neutrinos.

While computationally efficient, in practice, the GREP tends to overestimate GW frequencies produced by the PNS in numerical simulations (Müller et al., 2013). This discrepancy motivates the work outlined in Chapter 5, to implement a more robust treatment of gravity within `FLASH`, without the computational burden of a BSSN-like scheme.

The EOS enforces that thermodynamic variables—for example, ρ, ϵ, pressure, and temperature—follow a consistent relationship. One of the most common is the ideal gas EOS, which relates

pressure to other thermodynamic quantities with an adiabatic index γ: $P = (\gamma - 1)\rho\epsilon$, which has been used to describe CCSN material not in nuclear statistical equilibrium (Steiner et al., 2013a). The advantage of the ideal gas EOS is that it follows a simple analytic relationship. However, it poorly describes material near the center of the supernova engine, compared to more sophisticated methods. The Helmholtz EOS describes the stellar material in terms of photons, an ideal gas of ions, and a fully ionized electron-positron gas (Timmes & Swesty, 2000). It provides a more proper description of low density stellar material, by accounting for different species of ions, however does not completely describe the dense nuclear material at the supernova core. State of the art EOS treatments include tabulated nuclear EOSs often used in CCSN and NS merger simulations. Some notable examples include SFH(o/x) (Steiner et al., 2013a,b), LS220 (Lattimer & Swesty, 1991), and FSUGold (Todd-Rutel & Piekarewicz, 2005). Likewise, 'customized' EOSs perform a Taylor series expansion about the nuclear saturation density to characterize empirical parameters of the nuclear material, such as the effective mass of the nucleon or nuclear symmetry energy (Schneider et al., 2019). Such tabulated nuclear EOSs use a relativistic mean theory model to attempt matching nuclear experimental data, as well as mass/radius NS measurements; these EOSs provide a sophisticated treatment of the matter allowing for contributions from protons, anti-protons, neutrons, anti-neutrons, electrons, positrons, photons, and nuclei (Hempel et al., 2012). While more properly describing the hot, dense nuclear matter, in practice they require a more expensive iterative interpolation procedure, compared to analytic EOS counterparts. The CCSN models in this work use the SFH(o/x) and LS220 EOSs and are specified in the respective chapters.

Accounting for nuclear reactions requires evolving reaction networks of related nuclear species. Updating these networks modifies the nuclear species as well as the thermodynamic properties of the surrounding environment, through source terms $\mathbf{S}$. In principle, each species Y_i evolves according to a total reaction rate $\dot{R}_i$

$$\frac{dY_i}{dt} + \nabla \cdot (Y_i \mathbf{V}_i) = \dot{R}_i \tag{1.18}$$

where $\mathbf{V}_i$ represents the mass diffusion velocity for a given species. Calculating $\dot{R}_i$ involves solving

for individual forward and reverse nuclear reaction rates, which couple species together; mathematically this process reduces to solving sparse linear systems and then solving the ordinary differential equations (ODEs) represented by Equation (1.18). `FLASH` includes a 7 isotope alpha chain, 13 isotope alpha chain and heavy ion network, a 19 isotope reaction network that additionally contains proton-proton chain, Carbon-Nitrogen-Oxygen cycle and ^{54}Fe photodisintegration contributions (Weaver et al., 1978), and a 21 isotope network that also accounts for ^{56}Fe and ^{56}Cr (Paxton et al., 2010). Other networks used in CCSN models include Xnet[3] (Hix & Thielemann, 1999) and SkyNet (Lippuner & Roberts, 2017). The CCSN models in this work do not include nuclear reactions because of the relatively short simulation times (< 0.5 sec). Within this time span, the supernova material is in nuclear statistical equilibrium (NSE), leaving the use of an extended network unecessary. The additional cost of evolving nuclear species is typically completed in works that continue later in the supernova evolution to infer spectral characteristics of the optical light curves (Utrobin et al., 2017) or explicitly quantify r-process abundances (Mösta et al., 2018). While interesting applications for future projects, they remain beyond the scope of this work.

1.4.1 The Influence of Relativity

To save computational cost, Newtonian treatments (or post Newtonian approximations) of the aforementioned physics are involved, as many calculations reduce to a simple analytic form. However, for systems that involve high densities, extreme pressures, and velocities of a significant fraction of c, general relativistic effects must be taken into account in order to capture proper behavior. CCSNe are one such setting because of the rapid matter motions near the core and highly curved spacetimes present as compact objects form. It is important to emphasize relativistic effects impact multiple aspects of CCSN physics, beyond gravity. For clarity, consider an intuitive explanation.

Equation (1.1) relates the curvature of spacetime $G_{\mu\nu}$ to a matter distribution $T_{\mu\nu}$. For simplicity,

[3] https://github.com/starkiller-astro/XNet

consider the stress energy tensor for an ideal fluid

$$T_{\mu\nu} = \rho(1 + \epsilon + P/\rho)u_\mu u_\nu \tag{1.19}$$

where $u_\mu = W(1/\alpha, v_i)$ is the four-velocity one-form described by the Lorentz factor W, lapse function α (proxy for time dilation), and the velocity v_i. As $G_{\mu\nu}$ is related to $T_{\mu\nu}$, ρ, ϵ, and fluid velocities all contribute to spacetime curvature. Consider, by contrast, the Newtonian case, where Poisson's equation describes the gravitational potential ϕ as

$$\nabla^2\phi = 4\pi G\rho. \tag{1.20}$$

This equivalence only depends on ρ. Because the GR case accounts for additional contributions beyond rest mass density, GR systems tend to be more gravitational bound than Newtonian systems. For turbulence in a deeper gravitational well, the fluid has less kinetic energy for a given energy budget. This difference produces less pronounced convective overturn that occurs on longer timescales. For the GWs generated directly from matter motions in the post shock region of the supernova, this will decrease the GW frequencies emitted (Müller et al., 2013).

With the strong field effects of GR, the PNS will also become more massive and form at a smaller radius. With a compact object that is more gravitationally bound, the neutrinosphere will exist at a smaller radius, compared to a Newtonian case. As the region where neutrinos decouple from the matter is closer to the center of the supernova, neutrinos will free stream in a region at higher temperatures. The increased temperature in this region will create a harder neutrino spectrum, which will contribute to increased neutrino heating (Kotake et al., 2012). Additionally, as the PNS will be more compact—consequently a higher dynamical frequency—the GW frequency emitted from the oscillating PNS will increase for models that include general relativistic magnetohydrodynamics (GRMHD).

1.5 The Need for High Performance Computing

It is important to address the computational resources available for numerical simulations of CCSNe, as well as the impact of CCSN algorithm development on the HPC ecosystem. In practice, relating the systems of PDEs and ODEs from Section 1.4 results in a system with a high degree of nonlinearity. To meet the resulting computational demand, CCSN simulations have consistently driven hardware advances that have had broader societal benefits. Some examples include improved aerospace design for commercial flights, increased energy efficiency in urban settings, advances in material science through the construction of new alloys, and machine learning-driven pharmaceutical development [4].

However, as leadership class computing platforms become increasingly advanced, only the *potential* to complete computationally challenging problems increases. The responsibility of code developers increases as well; 'codes should not just be fast'. HPC moves beyond a need for advanced machines, to a need for balanced algorithms. The first of four considerations for a balanced algorithm is maintanability. 'Maintainability' is the ease with which a code sustain consistent updates. A maintainable code includes sufficient documentation, insightful comment lines, clear variable names, and effective use of white space that makes working with a code base streamlined for developers. 'Extensibility' is closely tied to modularity and refers to the ability of a code to apply to more general use cases, without having to change the core functionality. Modular code has independent elements that can be easily interchanged, for example, a different time integrator, EOS, or data reduction pipeline. 'Portability' is the proficiency with which a code can translate to different machines. From local laptops to supercomputing clusters, every computing platform has a unique architecture. Moreover, every computing architecture may contain unique compilers that translate developer-written software to machine executables. Differing amounts of memory, the interconnectedness of different elements, the presence of accelerators (e.g., a graphics processing unit (GPU)), and the pipeline through which data is written all impact how software will

[4] Other HPC projects through the Innovative and Novel Computational Impact on Theory and Experiment (INCITE) program: https://www.doeleadershipcomputing.org/awardees/

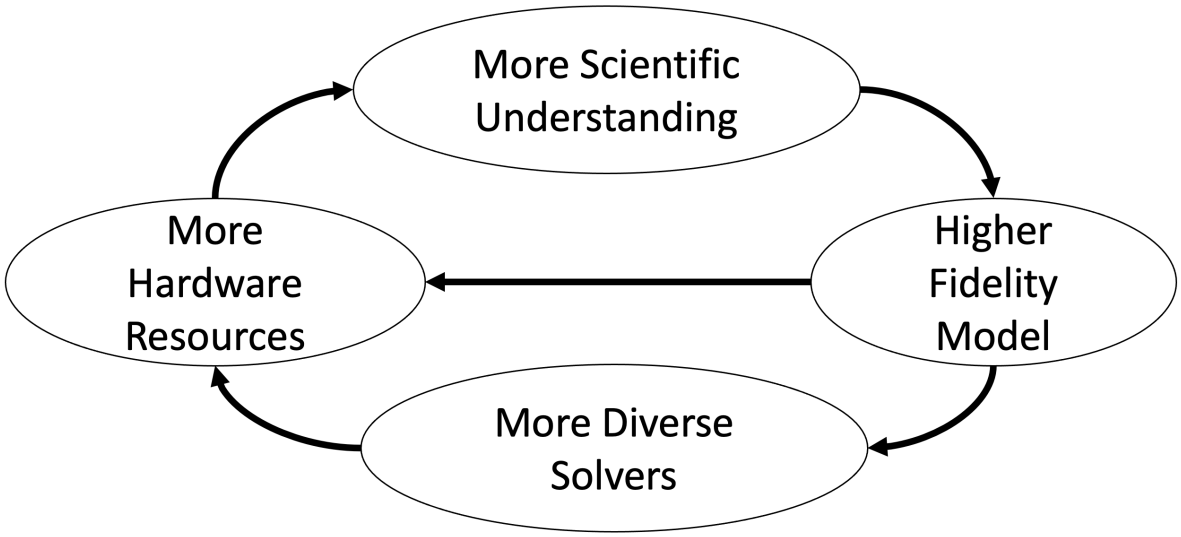

Figure 1.4: Cycle of scientific output for computational research projects. Adapting code to evolving computational platforms is a vital component to ensuring the longevity of computational research projects, without which limits the scale of the scientific questions that can be answered. Figure adapted from Anshu Dubey, Argonne National Lab.

perform. Portable code aims to use more abstract elements that can 'adapt' to specific hardware specifications. Lastly, 'performance' quantifies how much a code actualizes the potential of a machine. One metric of performance may refer to wall clock time, or how long it takes a simulation to complete. Another refers to scalability. For example, if there is a proportional reduction in runtime when using more computing resources for a fixed problem size (strong scaling), or how much the amount of computational work per computing resource remains constant if both problem size and computing resources increase (weak scaling).

Developing balanced algorithms is not a stylistic choice, but actively eliminates bottlenecks to scientific discovery in computational science. When using computation in the scientific process, software is used to test a hypothesis. A certain algorithm, or set of instructions, is applied in the code base. The algorithm is then executed on the computer and a result is produced. This result provides some data to be interpreted by the domain expert that supports or refutes the hypothesis. In the event researchers do not actively maintain their software to anticipate changes in hardware, their code base could eventually become obsolete. If software and hardware fail to advance at a similar rate,

results from numerical experiments are limited, or in extreme cases are unable to be completed. By contrast, balanced code, designed to advance with supercomputing technology, accelerates scientific productivity by matching performance gains from hardware advances with increases in research output. This interrelatedness between scientific output and software development is illustrated in Figure 1.4. In practice, scientific research and algorithm development must be balanced, in order to address immediate scientific needs, while ensuring the longevity, and therefore value, of a scientific project.

In pursuit of increasingly challenging scientific problems to bolster scientific research and produce broader societal benefits, international interest has grown to advance HPC—both its infrastructure and numerical algorithms. Such examples of leading supercomputing platforms are Aurora (*Argonne National Laboratory*), Frontier (*Oak Ridge National Laboratory*), Frontera (*Texas Advanced Computing Center*), Fugaku (*RIKEN Centre for Computational Science*), and Summit (*Oak Ridge National Laboratory*). Furthermore the Department of Energy is actively supporting the Exascale Computing Project (ECP) which aims to develop a set of balanced algorithms to utilize exascale computing platforms—supercomputers capable of completing 10^{18} floating point operations per second (FLOPs). The work presented in Chapter 5 represents my contributions to the Exastar [5] arm of the ECP, whose goal is to determine the origin of elements, ultra-dense matter behavior, and different sources of GWs. Having explored the value for hardware construction and responsible algorithm development, the next section explores the history of CCSN modeling, to place this work in the context of the field.

1.5.1 Leveraging High Performance Computing for Supernova Research

In the mid 1900s, state of the art CCSN models involved 1D, or spherically symmetric, calculations with simplified treatments of physics, such as the EOS and gravity (Burbidge et al., 1957; Colgate & White, 1966). In the late 1900s, 2D, or axisymmetric, calculations emerged to investigate multidimensional hydrodynamic effects and the impact of rotation (Mueller, 1982; Herant et al.,

[5] https://www.exascaleproject.org/research-project/exastar/

1992). In the new millennium, suites of early time 2D simulations became possible (Dimmelmeier et al., 2008; Abdikamalov et al., 2014). In the past decade, on the order of a few 3D simulations per year has become possible with access to millions of node hours on modern CPU architectures (Müller et al., 2017; Summa et al., 2018; O'Connor & Couch, 2018a). Beyond `FLASH`, other multiphysics codes used to perform intensive multiphysics calculations involve `Fornax` (Skinner et al., 2019), `Chimera` (Bruenn et al., 2020), `GRHydro` (Mösta et al., 2014), `Prometheus-Vertex` (Müller et al., 2010), `Phoebus`[6], `SpECTRE` (Deppe et al., 2022), `WhiskyTHC` (Radice et al., 2014) , and the code introduced in Kuroda et al. (2016).

There are three popular techniques for supernova modeling in modern computing, depending on the amount of compute resources available. The first involves large ensembles of 1D simulations evolved for $\sim$ 1 sec after core bounce. Works of this type attempt to cover a wide breadth of parameter space and build up statistics regarding explosion behavior (Warren et al., 2020). A single robust 1D CCSN simulation can requires hundreds of core hours to complete. While some approximations exist to capture multidimensional turbulent behavior (Couch et al., 2020a), in general, spherically symmetric calculations fail to self consistently capture multidimensional physical and observational effects. Evolving 10s-100s of axisymmetric simulations 10s of ms $\sim$ 1 sec after core bounce has emerged for constructing templates of GW signals (Richers et al., 2017; Pajkos et al., 2021). An axisymmetric CCSN simulation for $\sim$ 1 sec of evolution can requires tens of thousands of core hours. Such works are less expensive than 3D cases and are able to capture certain rotational elements. However, they lack azimuthal instabilities that may arise (e.g., SASI or low T/W) that can contribute to a successful explosion. Lastly, evolving of order a few 3D simulations, with comprehensive physics—GR gravity, M1 neutrino transport, and GRMHD—beyond core bounce for $\sim$ 1 sec allows for all spatial degrees of freedom to be explored. These studies allow for investigation of viewing angle effects, distributions of elemental abundances, and the morphology of the shock evolution (Mösta et al., 2018). Nevertheless, 3D simulations require extensive computational resources: with a robust physics treatment and $\sim$ 0.5 sec of evolution

[6] https://github.com/lanl/phoebus

needing upwards of tens of millions of core hours.

It is important to emphasize, these areas should not be in competition, but work in conjunction. As computing time allocations required to complete fully 3D models are increasingly competitive, lower dimension simulations should act as exploratory laboratories to inform which areas of parameter space to conduct 3D simulations. The majority of this Thesis work involves 2D CCSN simulations because they make efficient use the Michigan State University, Institute for Cyber-Enabled Research; likewise, as further outlined in Chapter 2 and Chapter 3, the assumption of axisymmetry does not compromise the fidelity of the results.

1.6 Outline

To address the need to better interpret GW observables, and fulfill the topical breadth for this PhD, Chapter 2, Chapter 3, and Chapter 4 detail three astrophysics investigations. Chapter 2 investigates the role of rotation on supernova evolution and resulting GW emission. Chapter 3 presents novel methods to quantify the influence of rotation on the GW signal and an original framework that connects GW observables to potential explosion properties. Chapter 4 discusses work by my undergraduate research assistant and I to identify the influence of viewing angle on the observability of GWs. Chapter 5 addresses the computational-focused requirement for this work. It outlines GR updates to the `FLASH` code, verifies code behavior with baseline tests, presents results from 1D and 2D CCSN simulations, and discusses advances in preparing this code for the next generation of HPC platforms.

CHAPTER 2

FEATURES OF ACCRETION-PHASE GRAVITATIONAL-WAVE EMISSION FROM TWO-DIMENSIONAL ROTATING CORE-COLLAPSE SUPERNOVAE

This section reviews published work: M.A. Pajkos, S. Couch, K.C. Pan, E. O'Connor, 2019, *ApJ*, 878, 13.

2.1 Abstract

We explore the influence of progenitor mass and rotation on the gravitational-wave (GW) emission from core-collapse supernovae, during the postbounce, preexplosion, accretion-phase. We present the results from 15 two-dimensional (2D) neutrino radiation-hydrodynamic simulations from initial stellar collapse to ~300 ms after core bounce. We examine the features of the GW signals for four zero-age main sequence (ZAMS) progenitor masses ranging from 12 $M_\odot$ to 60 $M_\odot$ and four core rotation rates from 0 to 3 rad s^{-1}. We find that GW strain immediately around core bounce is fairly independent of ZAMS mass and—consistent with previous findings—that it is more heavily dependent on the core angular momentum. At later times, all nonrotating progenitors exhibit loud GW emission, which we attribute to vibrational g-modes of the protoneutron (PNS) star excited by convection in the postshock layer and the standing accretion shock instability (SASI). We find that increasing rotation rates results in muting of the accretion-phase GW signal due to centrifugal effects that inhibit convection in the postshock region, quench the SASI, and slow the rate at which the PNS peak vibrational frequency increases. Additionally, we verify the efficacy of our approximate general relativistic (GR) effective potential treatment of gravity by comparing our core bounce GW strains with the recent 2D GR results of other groups.

2.2 Introduction

Core-collapse supernovae (CCSNe) became the first extra-solar multimessenger objects when SN 1987A was detected by the Kamiokande II experiment and Irvine-Michigan-Brookhaven water Cerenkov detector in 1987 (Bionta et al., 1987; Hirata et al., 1987) along with concurrent elec-

tromagnetic (EM) observations (see Arnett et al., 1989). With the recent detection of a neutron star merger–GW170817–in both photons and gravitational waves (GWs) by the LIGO and Virgo collaborations (Abbott et al., 2016b), we have entered the era of GW multimessenger astronomy. So far, only the mergers of black hole binaries and a neutron star binary have been detected in GWs, but CCSNe are also predicted to be prodigious GW sources, although not quite as "loud" as compact object binary mergers. Accurate predictions of the expected GW signal from CCSNe is key to increasing the likelihood of detection by GW observatories such as Advanced LIGO (aLIGO) and Advanced Virgo (AdV) and will be crucial in our ability to extract physical meaning from a future CCSN GW detection (Abdikamalov et al., 2014; Gossan et al., 2016).

CCSNe are routinely observed in the EM window, and the data-collecting power of synoptic surveys such as the Large Synoptic Survey Telescope and Zwicky Transient Facility may increase the volume of such data for CCSNe by orders of magnitude (Ivezić et al., 2019; Bellm et al., 2019). Still, until the late nebular phase, which is often too dim to be easily observed for distant CCSNe, the EM emission arises from the very outermost layers of the progenitor star and the central core regions, where the explosion is driven, are obscured. This makes it challenging to connect EM emission from CCSNe directly to the mechanism that powers them. Due to their relatively small interaction probabilities with matter, both neutrinos and GWs offer windows through which to peer directly into the heart of a CCSN explosion. Moreover, these observations have broader astrophysical applications: restricting nuclear equations of state, verifying angular momentum transport in plasmas, and better understanding stellar rotation.

An observation of either GWs or neutrino emission from a nearby CCSN combined with multiband observations would allow us to place unique constraints on the physics of the explosion mechanism and key nuclear physics, such as the nuclear equation of state (EOS). There has yet to be a single astrophysical object detected via all three of these messengers. Albeit a rare event, a Galactic CCSN offers the perfect opportunity to observe such a multimessenger "trifecta." In order to increase our chances of "hearing" such an event in GWs, and in order to be able to extract the greatest scientific meaning from them, we need accurate predictions for CCSN GW signals from

the wide range of initial conditions that give rise to these stellar explosions.

Modeling GWs from CCSNe incurs all of the challenges of simulating the CCSN mechanism itself, along with a heightened emphasis on the importance of the general relativistic (GR) treatment of gravity. The increased expense of including a fully dynamical spacetime evolution coupled to GR dynamics (see Ott, 2009; Ott et al., 2012) can further reduce the size of the parameter space that it is feasible to explore. Approximations that maintain sufficient numerical accuracy become necessary in order to reduce computational cost. A common approach for CCSNe, particularly in 2D, is the conformal flatness condition (CFC) approximation wherein the spatial three-metric is obtained approximately from the flat spacetime three-metric. CFC has been shown to accurately reproduce prebounce and early postbounce signals from CCSNe to within a few percent when compared with direct solutions to Einstein's field equations (Ott et al., 2007). Likewise, while some differences appear, Shibata & Sekiguchi (2004) find good qualitative agreement between the effective GR potential and CFC. This conformal flatness approach has also been extended to an "augmented CFC" scheme as introduced by Saijo (2004), refined by Cordero-Carrión et al. (2009), and utilized by Müller (2019). A further approximation, also common in simulations of the CCSN mechanism, is to couple an effective GR gravitational potential to otherwise Newtonian dynamics (Rampp & Janka, 2002; Marek et al., 2006; Bruenn et al., 2016; Morozova et al., 2018; O'Connor & Couch, 2018b). This relativistic effective potential empirically satisfies the solution to hydrostatic equilibrium according to a modified Tolman-Oppenheimer-Volkoff equation (Rampp & Janka, 2002; Marek et al., 2006). This approach further reduces the computational expense of CCSN simulations relative to the CFC approach and reproduces fairly accurately gross features of CCSN simulations (Marek et al., 2006; Müller et al., 2012; O'Connor & Couch, 2018b).

After the infalling matter from collapse reaches nuclear densities, the core nuclei dissolve into nucleons and, eventually, the strong force becomes repulsive, halting the material infall. On the time scale of tens of microseconds, the subsonic inner core encounters the supersonic outer core, forming a shock front. As this shock front photodissociates overlying material and releases an enormous neutrino flux, it leaves behind a negative entropy gradient (Mazurek, 1982; Bruenn, 1985,

1989). This scenario is unstable according to the Ledoux criterion, causing prompt convection in the postshock region (Burrows & Fryxell, 1992), therefore creating an associated emission of gravitational radiation (Marek et al., 2009; Ott, 2009). This prompt convection is an important feature that occurs in simulations that incorporate either GR or Newtonian treatments of gravity during the early postbounce phase (Müller, 2017; Richers et al., 2017; Nagakura et al., 2018).

Early research into GW emission from CCSNe focused on the bounce and early postbounce phase of the explosion in rotating progenitors. These investigations found that increasing the angular momentum of the core leads to a larger strain peak at bounce (Mueller, 1982; Moenchmeyer et al., 1991; Yamada & Sato, 1995; Zwerger & Mueller, 1997; Dimmelmeier et al., 2002; Kotake et al., 2003b; Shibata & Sekiguchi, 2004). More recent investigations of rotating core collapse examine the role of the angular momentum distribution within the supernova progenitor and find it is only important in the rapid rotation regime, where the ratio of kinetic to gravitational potential energy ($T/|W|$) $\gtrsim$ 8% at bounce (Abdikamalov et al., 2014). In order to examine GW emission at later times, different groups have considered other factors for nonrotating cases—for example, convection in the postshock region (Burrows & Hayes, 1996; Mueller & Janka, 1997; Müller et al., 2004; Marek et al., 2009; Murphy et al., 2009), the standing accretion shock instability (SASI) (Blondin et al., 2003; Blondin & Mezzacappa, 2006; Ohnishi et al., 2006; Foglizzo et al., 2007; Scheck et al., 2008; Iwakami et al., 2009; Fernández, 2010), and protoneutron star (PNS) vibrational modes (Cerdá-Durán et al., 2013; Torres-Forné et al., 2018, 2019a). Morozova et al. (2018) investigate GW emission for moderate rotational speeds ($\Omega_{\rm core}$ = 0.2 rad s^{-1}) for a single progenitor mass ($13 M_\odot$) over 1 second postbounce. Pan et al. (2018), Kuroda et al. (2018), Cerdá-Durán et al. (2013), and Ott et al. (2011) investigate the relationship between black hole formation and GW emission, for a nonrotating 40 $M_\odot$, a nonrotating 70 $M_\odot$, a rotating 35 $M_\odot$, and a rotating 75 $M_\odot$ progenitor, respectively. These studies also find stronger GW emission at bounce with increased progenitor angular momentum and loud GW emission at later times for nonrotating CCSNe.

In this work, we present 15 axisymmetric (2D) neutrino radiation-hydrodynamic CCSN simulations. Our parameter space spans four progenitor masses ranging from 12 $M_\odot$ to 60 $M_\odot$ (Sukhbold

et al., 2016a) and four peak core rotation speeds: $0 - 3$ rad s^{-1}. We examine the variation in key features of the GW emission from CCSNe at these different masses and rotation rates. Rapid rotation rates up to 2 and 3 rad s^{-1} are likely rare in typical massive stars at solar metallicity due to efficient transport and loss of angular momentum (Heger et al., 2005). While Woosley & Heger (2006) observe that only 1% of massive stars may reach the rapid rotation regime, there are high uncertainties in the stellar mass loss and magnetic braking calculations (Smith, 2014). Moreover, albeit a small percentage, de Mink et al. (2013) show the distinct possibility of rapidly rotating stars formed from binary interactions. Thus, there is some likelihood of rapidly rotating supernova progenitors in the mass range we explore.

In addition to the breadth of parameter space we cover, we also explore the role of rotation up to 300 ms postbounce. We find that rotation restricts the growth of SASI by centrifugally flattening the shock, leaving it slightly oblate. Likewise, the positive angular momentum gradient created by the rotation stabilizes the postshock convection according to the Solberg-Høiland stability criterion (Endal & Sofia, 1978; Fryer & Heger, 2000). Not only are the SASI and postshock convection contributions to the gravitational radiation diminished, but the PNS vibrational signals are damped because of less turbulent downflows of matter onto the PNS surface. This results in a "muting" of the GW signal with increasing rotation speeds. While the origins of this muting are physical, such behavior may not be seen in full 3D simulations of CCSNe due to the appearance of spiral modes of the SASI and magnetorotational instabilities (MRI) (Cerdá-Durán et al., 2007; Andresen et al., 2019) .

Compared with previous works, the strength of this project is its ability analyze GWs from multiple progenitors hundreds of milliseconds postbounce while accurately accounting for rotation and neutrinos. The wide breadth of parameter space we examine allows us to reveal certain rotational effects on the GW signal in the context of a controlled study.

In the present simulations we use an approximate, effective GR potential (Marek et al., 2006; O'Connor & Couch, 2018b). In order to validate this approximate approach for studying GWs from CCSNe, we compare our results to those of Richers et al. (2017), who use a CFC GR approach.

We find that our simulations produce nearly identical GW bounce signals to those of Richers et al. (2017).

This paper is organized as follows: in Section 5.4 we present our methods and treatment of microphysics within our FLASH simulations. We present a new method for applying initial rotation to the progenitor. Because each progenitor evolves at a different rate and we terminate our simulations at 300 ms postbounce, we refrain from asserting which explode. Rather, in Section 3.4, we begin by addressing the shock front evolution for each of the progenitor masses and initial rotation velocities. We then verify our gravitational treatment by comparing our bounce signal to GR simulations. We explore the effect of rotation on GWs emitted hundreds of milliseconds after core bounce and discuss implications on their detectability. In Section 5.7.2 we conclude and summarize the influence of rotation on GWs from initial collapse to 300 ms postbounce.

2.3 Methods and Simulation Setup

We utilize the FLASH (version 4) multiscale, multiphysics adaptive mesh refinement simulation framework for our simulations (Fryxell et al., 2000; Dubey et al., 2009).[7] We employ a modified, GR, effective potential (Marek et al., 2006; O'Connor & Couch, 2018b) incorporated into the multipole Poisson solver of Couch et al. (2013), where we retain spherical harmonic orders up through 16. We utilize the SFHo EOS in all of our 15 simulations (Steiner et al., 2013a). Our grid setup is a 2D cylindrical geometry with the PARAMESH (v.4-dev) library for adaptive mesh refinement (MacNeice et al., 2000). The outer boundary is 10^4 km in all directions, with nine levels of refinement, yielding a finest grid spacing of about 0.65 km. The maximum allowed level of refinement is decreased as a function of spherical radius, r, in order to maintain a resolution aspect ratio, $\Delta x_i/r$, of about 0.01, corresponding approximately to an "angular" resolution of 0.5°.

Neutrinos play a vital role in CCSNe. Directly after collapse, they provide an avenue through which the PNS can cool. As the shock propagates outward, they also provide heating in the gain region that is crucial in reviving the explosion, according to the neutrino heating mechanism. The opacity of the material to these outflowing neutrinos must be carefully accounted for in an energy-

[7] https://flash.rochester.edu/site/

dependent way. We incorporate a multidimensional, multispecies, energy-dependent, two-moment scheme with an analytic closure, or the so-called M1 scheme. Our implementation is based on O'Connor (2015), Shibata et al. (2011), and Cardall et al. (2013). A detailed outline of the M1 implementation in FLASH is in O'Connor & Couch (2018b). This combination of rotation and the M1 neutrino treatment is similar to the work of Obergaulinger & Aloy (2017) and Obergaulinger et al. (2018). In order to reduce computational costs to explore the wide parameter space for our study, we neglect velocity-dependent neutrino transport and do not account for inelastic neutrino-electron scattering. We use 12 energy bins spaced logarithmically up to 250 MeV, and the full set of rates and opacities we use is described in O'Connor et al. (2017). Specifically, we use the effective, many-body, corrected rates for neutrino-nucleon, neutral current scattering of Horowitz et al. (2017).

We use the 12, 20, 40, and 60 $M_\odot$ nonrotating, solar-metallicity progenitors models from Sukhbold et al. (2016a) for the present work.

2.3.1 Treatment of Rotation

The progenitor models we use are evolved without rotation. At the start of core collapse, when we map the 1D models into our 2D grid, we apply an artificial rotation profile

$$\Omega(r) = \Omega_0 \left[1 + \left(\frac{r}{A} \right)^2 \right]^{-1}, \tag{2.1}$$

where $r = \sqrt{R^2 + z^2}$ is the spherical radius for a given cylindrical radius R and altitude z, Ω_0 is the central angular speed of the star, and A is the differential rotation parameter (Eriguchi & Mueller, 1985). For large values of A, the stellar rotation is nearly solid body, whereas small values of A lead to a more differential profile. The linear rotational velocity is then calculated by multiplying the angular speed with the distance from the rotation axis, $v_\phi(R, z) = R\Omega(r)$.

The precise rotation rates and profiles of massive stellar cores at collapse are uncertain. Previous work (e.g., Abdikamalov et al., 2014) treated the differential rotation parameter A as a free parameter and explored the impact of its variation. Examining the stellar evolution models of Heger et al.

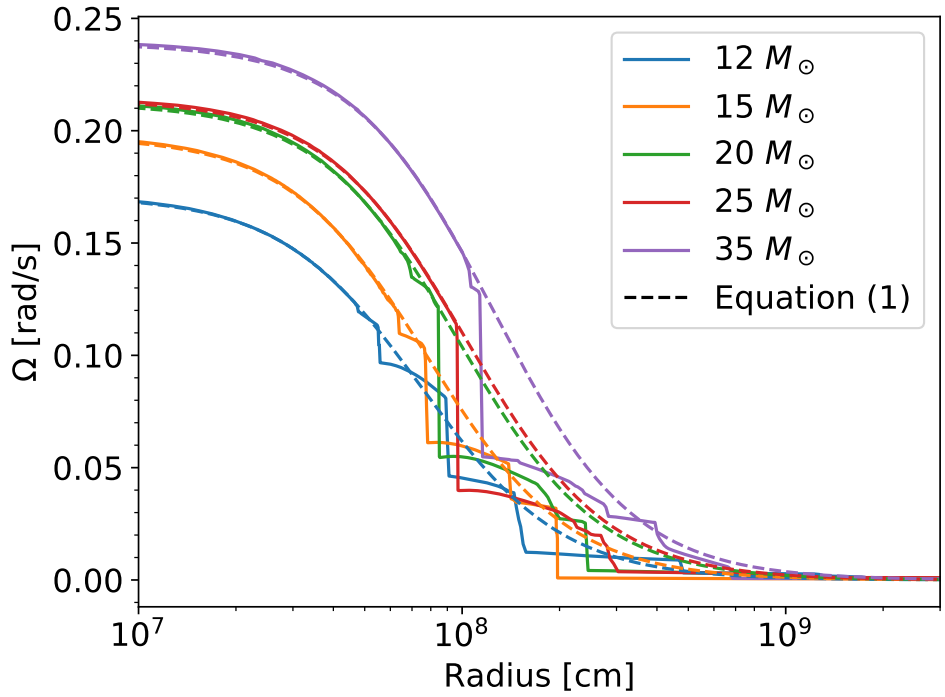

Figure 2.1: The rotation profiles for five of the Heger et al. (2005) progenitors. Each solid line represents Heger et al.'s (2005) model, and the dashed lines are Equation (3.1) applied to the respective progenitor, with the appropriate differential rotation parameter.

(2005), which include angular momentum transport due to the Tayler-Spruit dynamo (Spruit, 2002), we find that A is strongly determined by the compactness (O'Connor & Ott, 2011) of the stellar core. In order to demonstrate this, we fit the rotation profiles of the 20 progenitor models from Heger et al. (2005) to Equation (3.1) in order to determine the best-fit A. The models of Heger et al. (2005) include stars of zero-age main sequence (ZAMS) masses 12, 15, 20, 25, and 35 $M_\odot$, with various angular momentum transport parameters and initial ZAMS rotation rates. Using the `curve_fit` function (in the `scipy.optimize` library) available in `Python`, we obtain A values that correspond to the most accurate fits of Equation (3.1) to the rotation profiles of these models. Figure 2.1 displays the radial, rotation profile for five of the aforementioned progenitors, compared with our implementation of Equation (3.1), with the best-fit A value.

The core compactness as introduced by O'Connor & Ott (2011) is defined as

$$\xi_M = \left.\frac{M/M_\odot}{R(M_{\rm bary} = M)/1000{\rm km}}\right|_{\rm collapse}, \tag{2.2}$$

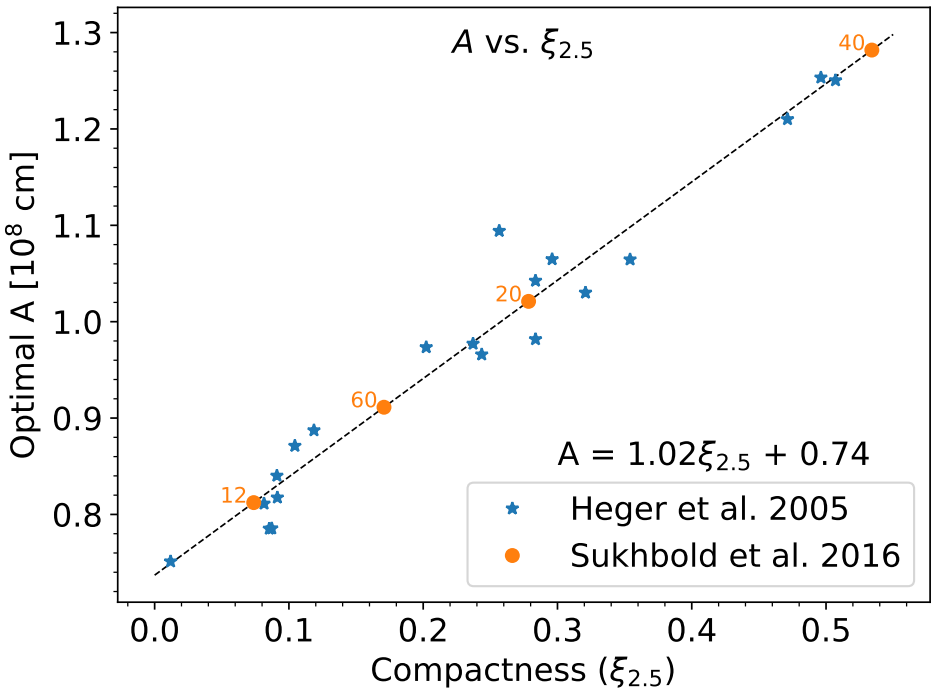

Figure 2.2: Linear relation between differential rotation parameter, A, and compactness parameter of the inner 2.5 $M_\odot$, $\xi_{2.5}$. The linear trend is constructed from the Heger et al. (2005) rotation profiles. We then apply the relation to the compactness values from Sukhbold et al. (2016a) to yield the differential rotation parameters. The progenitor ZAMS masses are labeled in units of $M_\odot$ for each respective point.

Progenitor Mass ($M_\odot$)	Compactness	A(1000 km)
12	0.0738	0.8123
20	0.2785	1.021
40	0.5341	1.282
60	0.1708	0.9112

Table 2.1: Listed values for ZAMS Mass, Compactness Calculated from Sukhbold et al. (2016a), and Differential Rotation Parameter A.

where we choose $M = 2.5M_\odot$, and $R(M_{\rm bary} = M)$ as the radius at which the internal baryonic mass is $2.5M_\odot$, at collapse. Figure 2.2 shows the compactness parameters from the Heger et al. (2005) models (blue stars) plotted against their best-fit A values. A clear linear relation exists between A and $\xi_{2.5}$.

Using this relationship, we calculate optimal A values for the four Sukhbold et al. (2016a) progenitors we use in this work (orange circles in Figure 2.2). The full list of progenitor masses,

compactness values, and A values we use is given in Table 2.1.

As a note, we choose to omit the 40 $M_\odot$ progenitor at $\Omega_0 = 3$ rad s^{-1} from our following analysis with a numerically motivated rationale. The $\xi_{2.5}$ value of this progenitor is nearly double that of the 20 $M_\odot$ progenitor (the next closest compactness value). This fact displays that the 40 $M_\odot$ has a much larger differential rotation parameter compared with the other progenitors, resulting in a nearly solid-body rotation of the core. This endows the core in the 40 $M_\odot$ model with drastically more angular momentum than the other models. The vast amount of angular momentum ultimately led to numerical instabilities in our calculations; thus, we omit the 40 $M_\odot$, with $\Omega_0 = 3$ rad s^{-1} from our analysis.

2.4 Results

To extract the GW signal from our simulations, we adopt the dominant, quadrupole moment formula for the gravitational strain, through the slow motion, weak-field formalism (eg. Blanchet et al., 1990; Finn & Evans, 1990)

$$h_+ \approx \frac{2G}{Dc^4}\frac{d^2 I_{zz}}{dt^2}, \tag{2.3}$$

where I_{zz} is the reduced-mass quadrupole moment, G is the gravitational constant, c is the speed of light, and D is the distance to the source (our fiducial value is $D = 10$ kpc) and we assume optimal source orientation—GWs emitted from the equator of the CCSN.

When plotting the amplitude spectral density (ASD) of the GW signal we compute the discrete Fourier transform consistent with Anderson et al. (2004) and LIGO's implementation

$$\widetilde{h}_{+k} = \sum_{j=0}^{N-1} h_{+j} e^{-i2\pi jk/N} \tag{2.4}$$

where $i = \sqrt{-1}$.

To quantify the strength of convection within our simulations, we characterize the anisotropic

velocity of the fluid motion within the postshock region according to Takiwaki et al. (2012):

$$v_{\rm aniso} = \sqrt{\left\langle \rho \left((v_r - \langle v_r \rangle)^2 + v_\theta^2 + v_\phi^2 \right) \right\rangle / \langle \rho \rangle} \tag{2.5}$$

where $\langle\rangle$ represents an angle average, v_r is the radial velocity, v_θ is the velocity component in the polar direction, v_ϕ is the velocity component in the azimuthal direction, and ρ is the density.

With the introduction of rotation, a positive angular momentum gradient can be established, leading to inhibited convection, according to the Solberg-Høiland stability criterion. To quantify this criterion we calculate the condition at the equator for stability in the vertical direction, $R_{\rm SH}$, consistent with Heger et al. (2000):

$$R_{\rm SH} := \frac{g}{\rho} \left[\left(\frac{d\rho}{dr} \right)_{\rm ad} - \frac{d\rho}{dr} \right] + \frac{1}{r^3} \frac{d}{dr} (r^2 \omega)^2 \geq 0 \tag{2.6}$$

where g is the local gravitational acceleration, ρ is the density, $(d\rho/dr)_{\rm ad}$ is the radial density gradient at constant entropy and composition, r is the distance from the axis of rotation, and ω is the rotational velocity.

To examine the shape of the shock front, $R_S(\theta, \phi)$, we represent it as a linear combination of spherical harmonics, $Y_l^m(\theta, \phi)$:

$$R_S(\theta, \phi) = \sum_{l=0}^{\infty} \sum_{m=-l}^{l} a_l^m Y_l^m(\theta, \phi) \tag{2.7}$$

$$Y_l^m = \sqrt{\frac{2l+1}{4\pi} \frac{(l-m)!}{(l+m)!}} P_l^m(\cos(\theta)) e^{im\phi} \tag{2.8}$$

where P_l^m are the associated Legendre polynomials (Burrows et al., 2012; Takiwaki et al., 2012). However, because of the 2D nature of our simulations $\phi = 0$ and all $m = 0$ as well; thus the coefficients a_l^0 are

$$a_l^0 = \int_0^\pi d\theta \sin(\theta) R_S(\theta) Y_l^0(\theta). \tag{2.9}$$

It follows that a_0^0 corresponds to the average shock radius.

2.4.1 Rotation's Influence on Shock Front Evolution

While our focus in the present work is on the GW signals up to 300 ms postbounce, we briefly discuss the impact of rotation on the evolution of the shock front as it propagates outward. In certain cases, independent of the mechanism, the shock front may require over 300 ms to revive and complete a successful explosion. Because our simulations are only run until 300 ms postbounce, we refrain from asserting which progenitors successfully explode. Rather, we remark on how the average shock radii develop with time.

Of our 15 simulations, only the nonrotating 20 $M_\odot$ and 60 $M_\odot$ progenitors show substantial shock expansion. The effect rotation has on reviving the shock is not a simple one. In one respect, one expects greater centrifugal support to lead to a larger shock front. However, there are two factors that inhibit the shock from propagating outward. The first is the inhibited convection due to the positive angular momentum gradient within the progenitor. Weaker convection results in less efficient neutrino heating (Dolence et al., 2013; Murphy et al., 2013) and less positive support from turbulence in the gain region (Couch & Ott, 2015; Mabanta & Murphy, 2018). The second rotational element that inhibits explosions is the lack of neutrino production. Rotation centrifugally supports matter that is infalling during the initial collapse of a star. As such, the collapsing material does not settle as deeply into the gravitational potential of the stellar core, thereby releasing less gravitational binding energy. This process results in a lower neutrino luminosity and slower contraction of the PNS (Summa et al., 2018). These two dominant effects, weaker convection and reduced neutrino luminosity, can create an unfavorable scenario for a supernova explosion that is revived by neutrino heating.

Despite rotation inhibiting certain aspects of a successful explosion, some of our rotating models (Ω_0 = 3 rad s^{-1}, 20 $M_\odot$, and 60 $M_\odot$) have advancing shock radii. With longer simulation times, these could lead to explosion. In these cases, it seems that rotation could be sufficiently rapid to overcome the deleterious effects on convection and reduced neutrino luminosity. Similar nonmonotonic behavior is reported by Summa et al. (2018) in their 2D simulations. Hence, the introduction of rotation involves competing forces that can enhance or diminish the shock. Figure

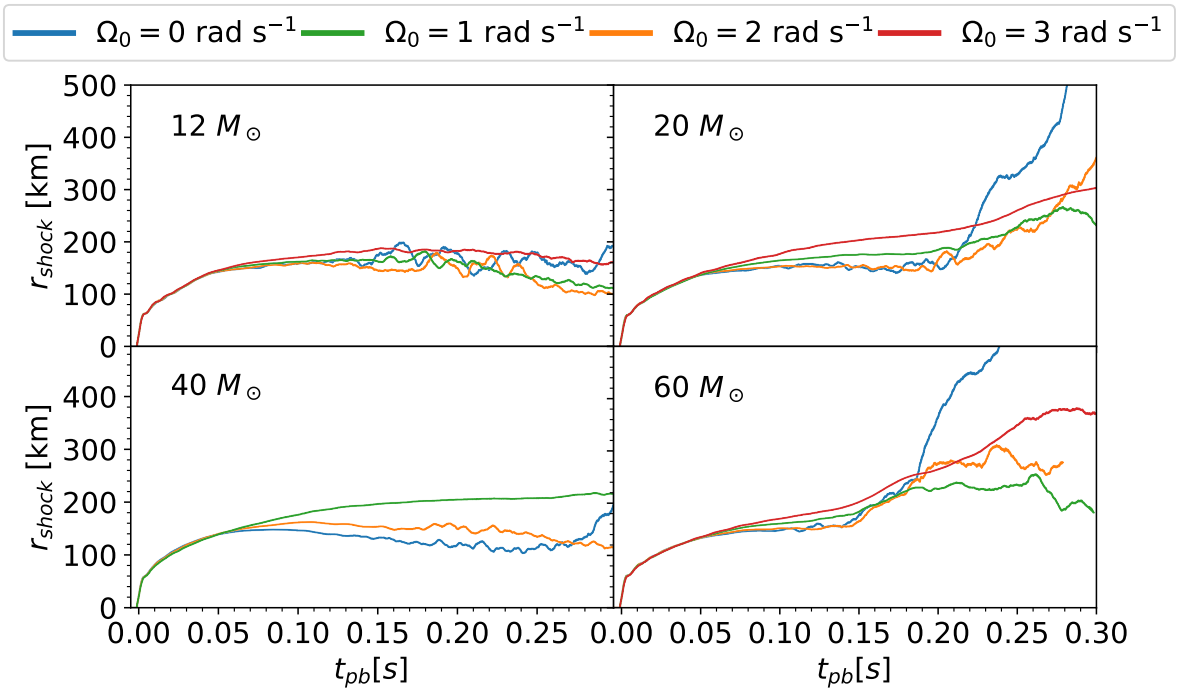

Figure 2.3: Shock radius evolution of the four progenitor models versus time (postbounce). As different progenitors evolve at different rates, they may not have enough time to revive their shock front within the 300 ms interim. As such, only the nonrotating 20 $M_\odot$ and 60 $M_\odot$ progenitors show substantial shock expansion.

3.1 shows the average shock radius evolution versus time (postbounce) over our entire parameter space.

2.4.2 Comparison with CFC GR

In multidimensional simulations of CCSNe, the treatment of gravity must offer a balance between numerical accuracy and computational cost. The CFC offers a nearly identical GW signal, compared with full GR, while reducing simulation time (Ott et al., 2007). Figure 2.4 offers a qualitative check of our effective GR potential compared with CFC (Richers et al., 2017). We incorporate an identical deleptonization profile (Liebendörfer, 2005) and SFHo EOS (Steiner et al., 2013a) for a 12 $M_\odot$ progenitor (Woosley & Heger, 2007). Moreover, we match the differential rotation parameter and rotation profile by selecting an $A = 634$ km and $\Omega_0 = 3$ rad s^{-1}. For this comparison, we match the neutrino physics of Richers et al. (2017)'s simulation by using a ray-by-ray, three-species, neutrino leakage scheme (O'Connor & Ott, 2010; Couch & O'Connor, 2014). We capture a nearly identical

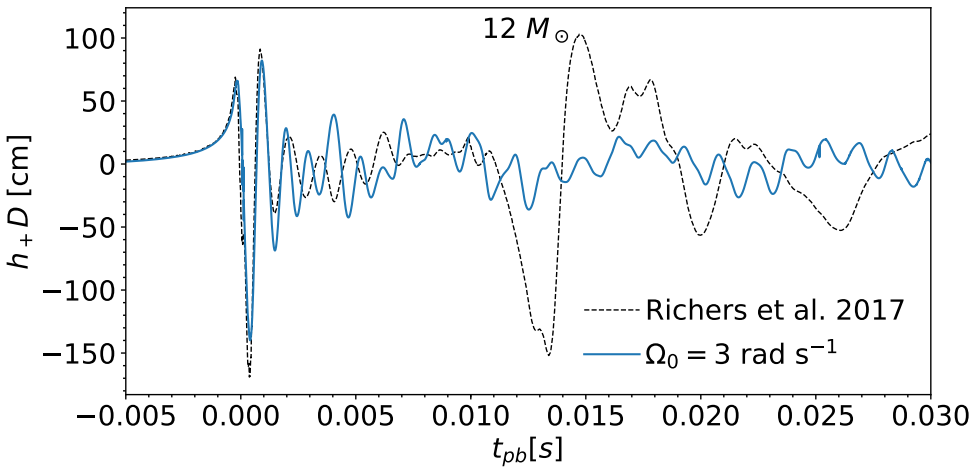

Figure 2.4: GW strain vs. time (postbounce) for a 12 $M_\odot$ progenitor (Woosley & Heger, 2007) with $\Omega_0 = 3$ rad s^{-1}. Plotted in the dashed line is the GW strain from Richers et al. (2017) using the CFC `CoCoNuT` code, and the solid line is our result using the effective relativistic potential coupled with Newtonian dynamics. While the different grids and treatment of hydrodynamics lead to differences in the strain in the early postbounce phase, we qualitatively verify our gravitational treatment by obtaining a nearly exact bounce signal.

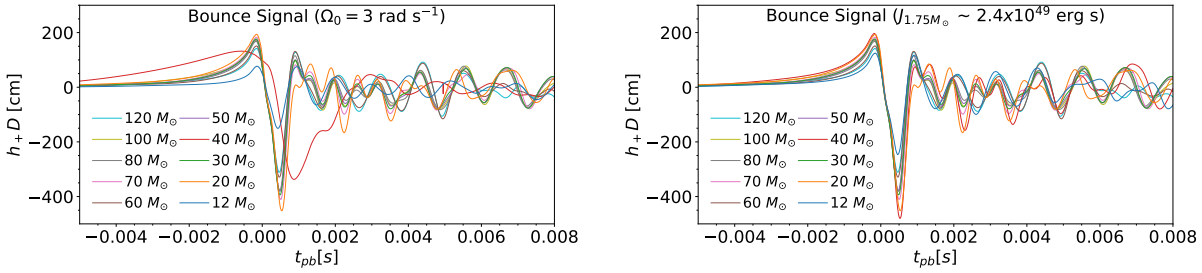

Figure 2.5: (Left) GW bounce signal from all 10 progenitor masses with $\Omega_0 = 3$ rad s^{-1}. By applying Equation (3.1), we assign a radially dependent, angular velocity to our progenitors. Because the central density profiles of each progenitor are different—namely, a less compact 12 $M_\odot$ and more compact 40 $M_\odot$—the progenitor cores are endowed with different amounts of angular momenta. (Right) Modified bounce signals after adjusting rotation rates to yield similar angular momenta ($\sim 2.4\times10^{49}$erg s) of the inner 1.75 $M_\odot$ of matter. As predicted by Dimmelmeier et al. (2008) and Abdikamalov et al. (2010, 2014), the GW bounce signals depend on the inner core angular momentum at bounce, not the original ZAMS mass.

bounce signal and similar strain up to 5 ms postbounce.

However, after the initial bounce signal ring-down, it is clear that the different computational treatments of hydrodynamics and grid geometry result in differences in the GW strains. Although not exact, the efficiency of the effective GR potential offers a reasonable method to accurately

model the GW signal from CCSNe to within 10% and allows for larger sweeps of parameter space (Müller et al., 2013).

2.4.3 ZAMS Influence on Gravitational Bounce Signal

While different progenitors $\gtrsim 8\,M_\odot$ will experience widely varied evolution, once their iron cores reach the effective Chandrasekhar mass (Baron & Cooperstein, 1990) and collapse commences, the physics of the collapse becomes somewhat universal. In particular, the mass of the homologously collapsing inner core is fixed more by microphysics than by the macrophysics of varied stellar evolution. This nearly identical inner core mass across the ZAMS parameter space yields similar core angular momenta, for identical rotation rates. Hence, the core bounce signal is nearly indistinguishable between progenitor masses. For further verification of our gravitational treatment, we perform 12 additional simulations using neutrino leakage—from collapse—until 8 ms after core bounce, in order to replicate this bounce signal degeneracy, using the Sukhbold et al. (2016a) progenitors. Outlined by Ott et al. (2012), neutrino leakage has a small effect on the GW bounce and early postbounce signal. Moreover, our results are consistent with 3D, fully GR predictions given by Ott et al. (2012) that similar core angular momenta yield similar GW bounce signals.

Figure 2.5 displays the bounce signals for all 10 progenitor masses, ranging from 12 $M_\odot$ to 120 $M_\odot$. The left panel is for uniform rotational velocity prescriptions at $\Omega_0 = 3$ rad s^{-1}. As previously highlighted, the angular momentum of the inner core is the main contributor to the gravitational bounce signal. While many of the waveforms have similar amplitudes, there are two clear outliers: the 12 $M_\odot$ and 40 $M_\odot$ progenitors. The 12 $M_\odot$ and 40 $M_\odot$ progenitors, respectively, have lower and higher compactness values at collapse, by nearly a factor of 2. Because we endow each progenitor with angular velocity, and not specific angular momentum, the more compact 40 $M_\odot$ progenitor will receive more angular momentum, compared with the remaining progenitors, thereby affecting the resulting GW bounce signal. As outlined by Dimmelmeier et al. (2008), once a star is sufficiently rotating, the centrifugal support slows the bounce, diminishing the GW bounce amplitude and widening out the bounce peak of the waveform.

The inverse is true for the $12\,M_{\odot}$ case. Because it has a less compact inner core at collapse, using Equation (3.1) leads to less initial angular momentum, thereby producing a lower amplitude bounce signal. After modifying the initial rotation rates of both progenitors, to match the progenitor core angular momenta (right panel of Figure 2.5), the change produces nearly identical GW bounce signals.

Hence, our results from exploring the bounce signal over a wide range of progenitor masses support the results of previous studies of the angular momentum dependence of the GW signal (Dimmelmeier et al., 2008; Abdikamalov et al., 2010, 2014) but also serve as a cautionary note for future groups who perform rotating CCSN simulations with a wide variety of progenitor models. It is worth noting that other rotational treatments exist beyond the simple angular velocity law, such as specifying a radial, specific angular momentum profile (eg., O'Connor & Ott, 2011) or using the rotational profile from the rotating stellar evolution models directly (Summa et al., 2018). The profiles used by O'Connor & Ott (2011) lead to a roughly uniform rotation rate within a mass coordinate of 1 $M_{\odot}$ and $\Omega(r)$ decreasing with r^2 outside this mass coordinate. Summa et al. (2018) utilize two different rotation schemes: one that matches the Heger et al. (2005) models seen in Figure 2.1 and one that is solid body out to $\sim$ 1500 km and then falls as $r^{-3/2}$.

2.4.4 Rotational Influence on Accretion-phase GW Emission

Our results in the previous section support the efficacy of our effective GR potential for accurately modeling the GW signals from CCSNe. While the effective GR potential has been shown to overestimate peak frequency from GWs compared with GR, it produces similar GW amplitudes and accurately captures PNS compactness during the accretion-phase (Müller et al., 2013). Thus we now turn to exploring the rotational effects on the GW signal during the accretion-phase, up to 300 ms after bounce.

While the consistency of the inner core mass for a collapsing iron core creates a setting where envelope mass has little effect on the bounce signal, the postbounce dynamics of the explosion largely depend on the mass surrounding the PNS. For nonrotating CCSNe, the shock front prop-

agates outward and loses energy due to dissociation of iron nuclei and neutrino cooling. In the case of rotation, the initial progenitor and resulting shock front become more oblate. Rotation can affect the GW emission in three respects: the postshock convection is damped, the SASI becomes restricted, and it slows the rate at which the PNS peak vibrational frequency increases.

As the Ω_0 value increases in our models, a positive angular momentum gradient is established within the postshock region, partially stabilizing it to convection via the Solberg-Høiland instability criterion (Endal & Sofia, 1978; Fryer & Heger, 2000). We quantify the reduced convection in Figure 2.6. Brighter colors correspond to higher values of the anisotropic velocity as outlined in Equation (2.5). As expected, the convection in the gain region is reduced with increasing rotational velocity. To tie this inhibited convection to the Solberg-Høiland instability criterion, we follow the prescription of Section 2.3.2 of Heger et al. (2000). We quantify this instability criterion as outlined in Equation (2.6) by taking slices along the equator and tracking its evolution. Figure 2.7 displays the $R_{\rm SH}$ value along the equator of the 12 $M_\odot$ progenitor for all four rotational velocities. As the Ω_0 increases, the propensity for convection (colored red) within the postshock region clearly decreases. This inhibited convection results in weakened turbulent mass motion within the gain region, thereby reducing the GW amplitude at later times.

Furthermore, we recast our analysis by focusing on regions within the CCSN that emit GWs. The lower panel of Figure 2.8 displays the inhibited convective signal with increasing rotation, as the GW signal in the gain region becomes increasingly muted. The typical convective signals in the early postbounce regime are then quickly washed out by the postbounce ring-down of the PNS, as rotation increases.

Under nonrotating conditions, the shock can grow unstable due to nonradial deformations exciting a vortical-acoustic cycle that leads to the growth of large-scale shock asymmetries, that is, the SASI (Blondin et al., 2003; Blondin & Mezzacappa, 2006; Scheck et al., 2008; Marek & Janka, 2009). In 2D simulations, the SASI excites large, oscillatory flows along both poles that drive changes in entropy capable of causing postshock convection. It is worth noting in 3D simulations that the SASI can excite 'spiral' modes that correspond to nonzero m values (Blondin

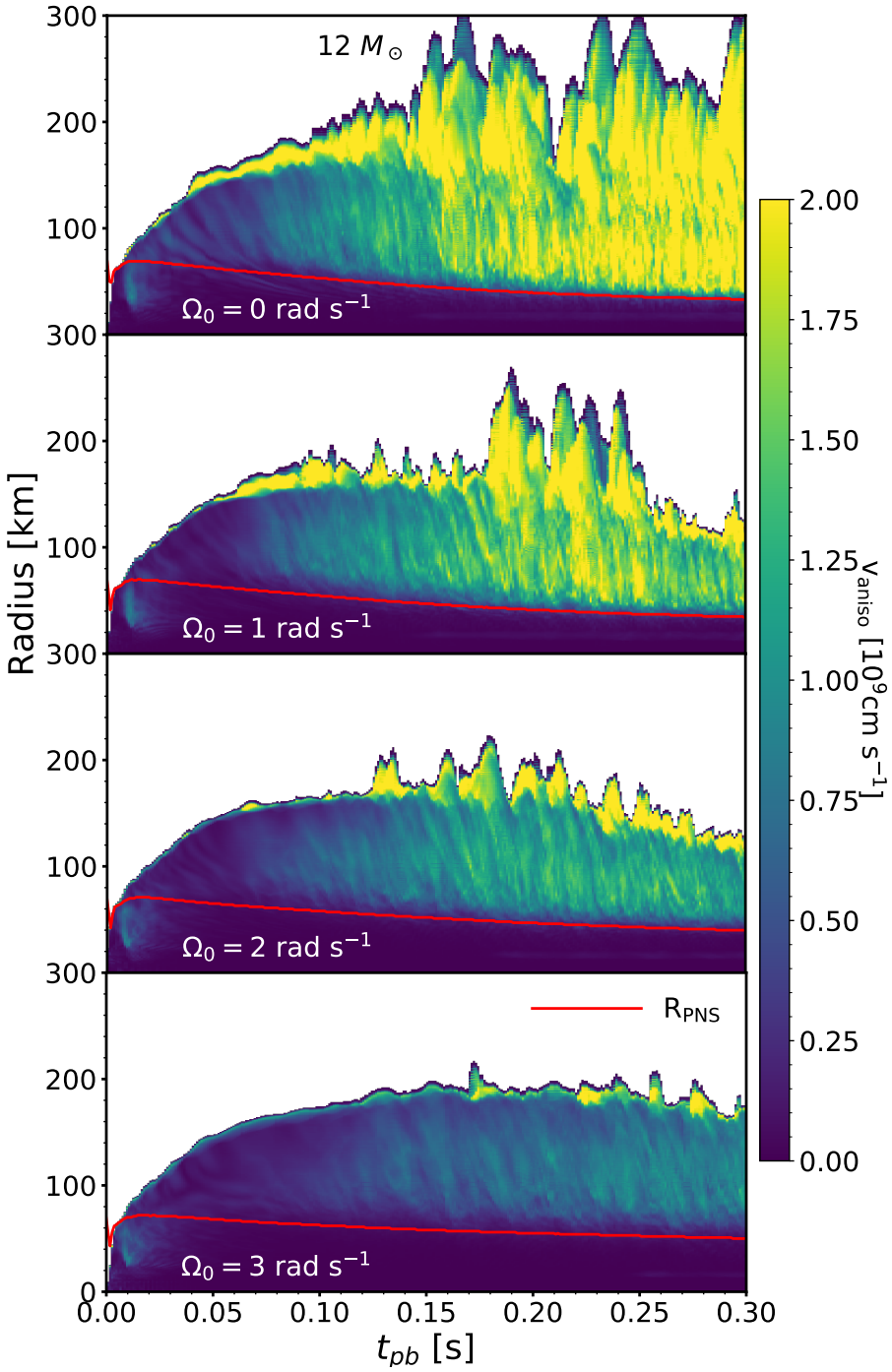

Figure 2.6: Spherically averaged anisotropic velocity of the postshock region for the 12 $M_\odot$ progenitor. Brighter colors correspond to increased convection in the postshock region according to Equation (2.5). As rotational velocity increases, convective activity is inhibited. Traced in red is the radius of the PNS.

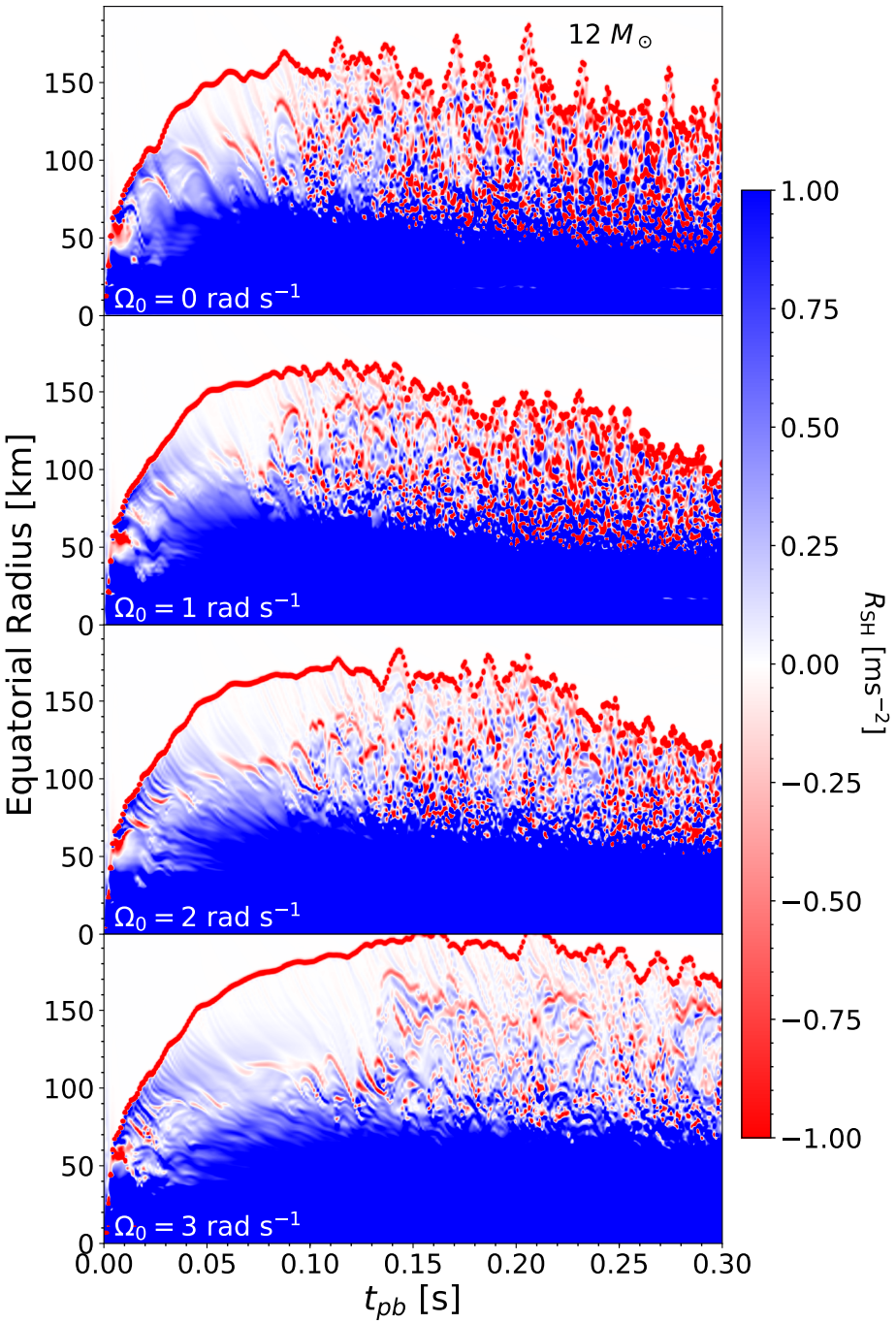

Figure 2.7: Slices along the equator of the 12 $M_\odot$ progenitor at each rotational velocity. Colors correspond to the Solberg-Høiland stability criterion, $R_{\rm SH}$, from Equation (2.6). As rotational velocity increases, not only does the convectively stable band in the core grow (seen in blue), but the amount of convection within the postshock region (seen in red) decreases as well. The differences in shock radius evolution between Figure 2.6 and this figure arise because Figure 2.6 uses an angular average over the domain, whereas this figure uses equatorial slices.

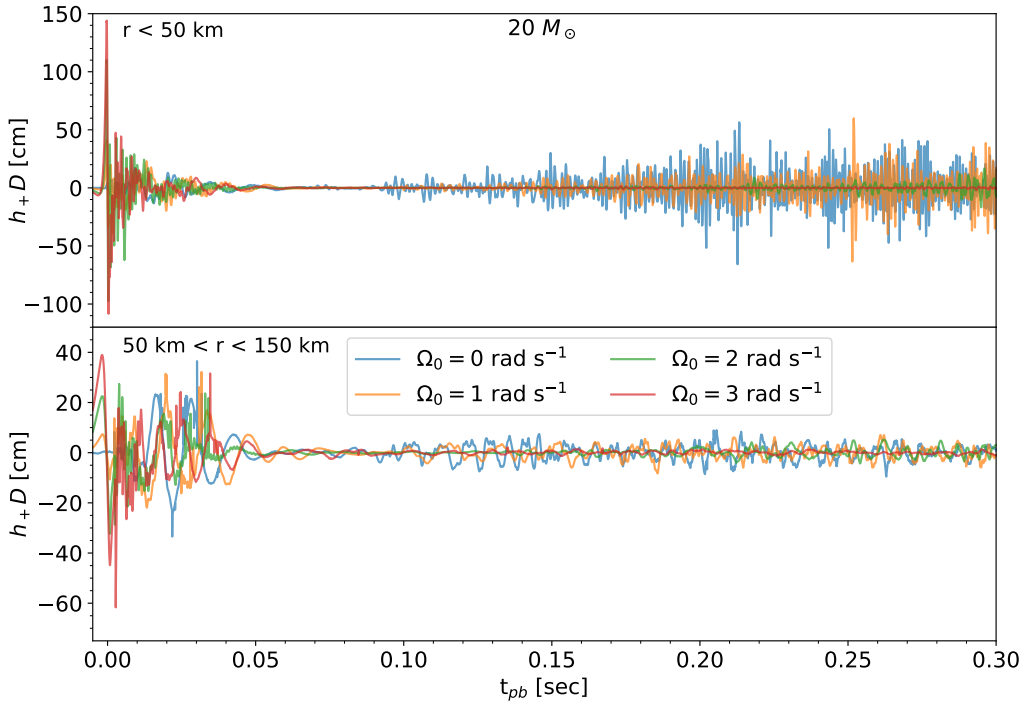

Figure 2.8: Time domain waveforms for the 20 $M_\odot$ progenitor. Each panel corresponds to the region from which the GWs are emitted. The large contribution in the top panel indicates the main source of GWs during the accretion-phase is from the vibrating PNS. The lower panel displays the inhibited convective signal ~ 50–100 ms postbounce that is characteristic of this quiescent phase.

& Shaw, 2007; Kuroda et al., 2016). The high degree of nonlinearity among the hydrodynamic flows, neutrino interactions, and gravitational effects can yield matter flow that is quadrupolar, thereby resulting in GW emission. However, when the shock becomes restricted in the polar direction, due to centrifugal effects, SASI development is inhibited. To quantify the role of SASI, we decompose the shock front into coefficients based on the spherical harmonics, Y_l^m, according to Equation (2.9). Figure 2.9 illustrates the evolution of the a_1^0 and a_2^0 coefficients over time. Both coefficients quantify the deviation of the shock from spherical symmetry. Specifically, the a_1^0 term describes the overall dipole nature of the shock, and the a_2^0 term describes its quadrupole nature. Both coefficients are normalized by the mean shock radius, a_0^0. Clearly, both approach zero with increasing rotational velocity. Physically, this effect corresponds to a shock that is becoming less

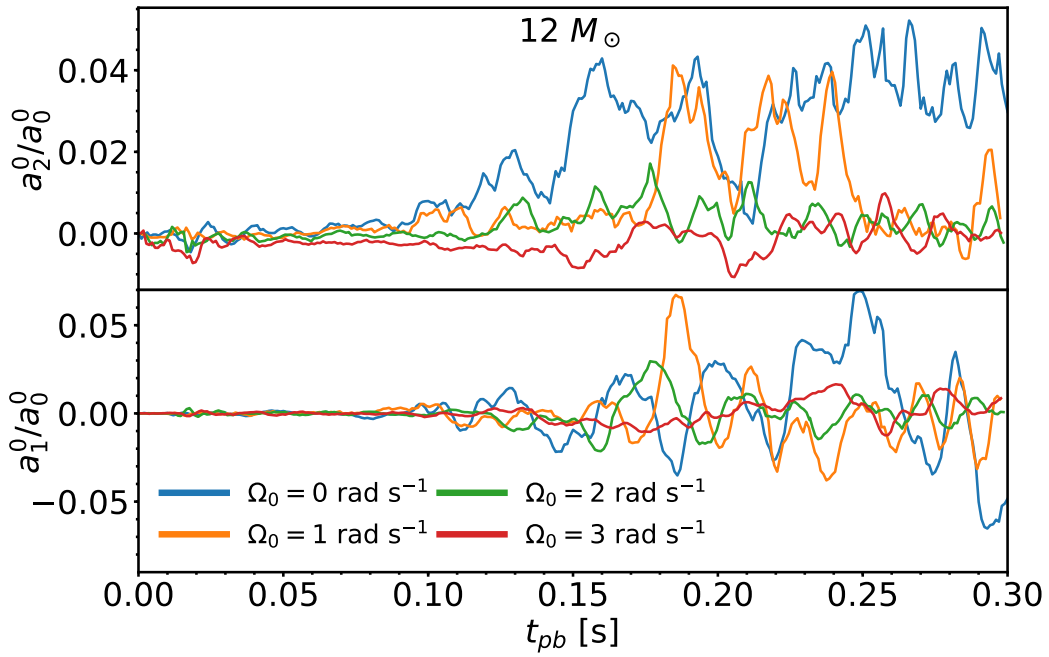

Figure 2.9: Coefficients from spherical harmonic decomposition of the shock front, outlined in Equation (2.9). The a_1^0/a_0^0 and a_2^0/a_0^0 terms describe the overall dipole and quadrupole nature of the shock front, respectively. As the SASI is one of the main contributors to the creation of asymmetries in the shock front, the lower a values correspond to a less prolate shock, or one with diminished SASI.

prolate. To further illustrate this transition, we direct the reader to Figures 2.6 and 2.7. Figure 2.6 takes an angular average to calculate v_{aniso}, whereas Figure 2.7, by contrast, uses equatorial slices to calculate the Solberg-Høiland stability criterion. The boundary between the white and colored region in both panels then acts as a proxy for average shock radius and equatorial shock radius, respectively. Thus, as rotational velocity increases, average shock radius decreases, while increasing the equatorial shock radius. Put more simply, the rotation in our 2D simulations acts to create less prolate shock fronts. Hence, because SASI plays a significant role in creating a shock that is extended along the axis of rotation, we conclude that the effect of SASI is reduced as rotational velocity increases in our 2D simulations. While we expect the SASI activity to contribute uniquely to the GW spectrum, depending on progenitor mass, the rotational muting of the GWs is universal across ZAMS mass parameter space, as illustrated in Figure 2.10. Both Burrows et al.

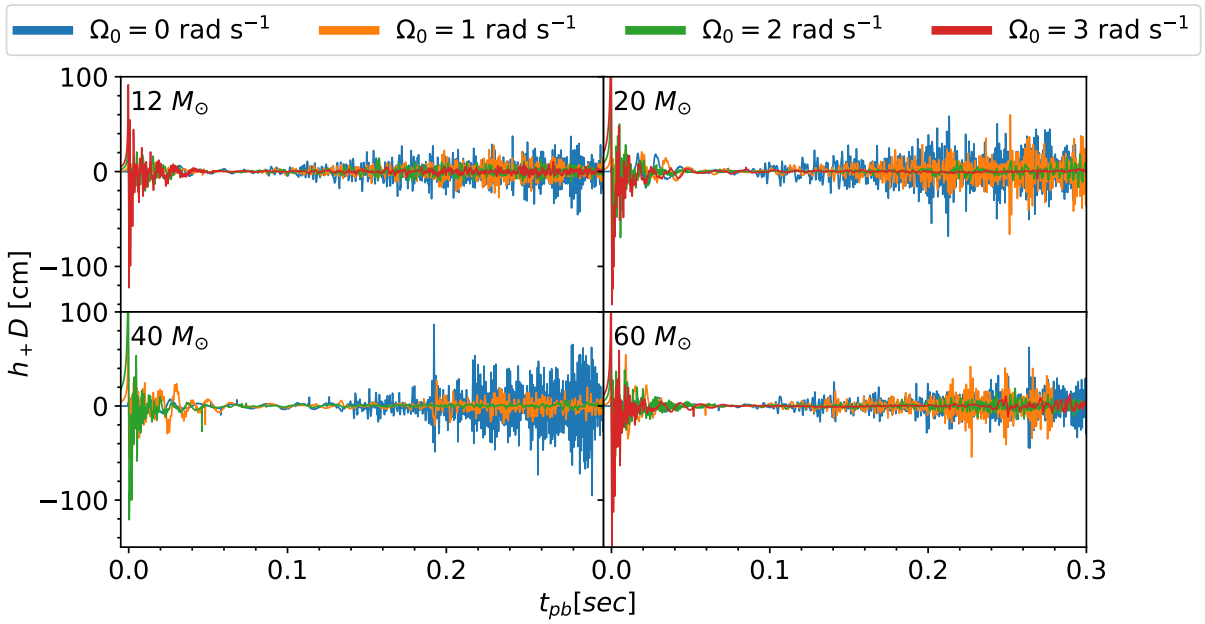

Figure 2.10: Time domain waveforms over our entire parameter space. For all four progenitor masses, the rotational muting of the accretion-phase GW signal is clear. While there is some weak dependence in the character of the accretion-phase GW signals with progenitor ZAMS mass, the rotational muting occurs for all progenitors.

(2007) and Morozova et al. (2018) point out the partial suppression of SASI, but the former does not focus on the gravitational radiation emitted and the latter only examines a single, slow rotating, progenitor. Our work provides strong support for the rotational muting of accretion-phase GWs, over such a wide region of parameter space of 2D CCSN simulations.

With respect to PNSs, a variety of oscillatory modes exist that could be of interest to current and future GW astronomers: fundamental f-modes, pressure based p-modes, and gravity g-modes—due to chemical composition and temperature gradients (Unno et al., 1989). The typical frequency of the PNS f-mode is around 1 kHz, and p-modes have frequencies greater than f-modes, which are of little use to GW astronomers, with the current detector capabilities (Ho, 2018). The frequencies of g-modes, however, are on the order of hundreds of hertz, falling squarely within the detectability range of current GW detectors (Martynov et al., 2016). The top panel of Figure 2.8 displays the contribution of the vibrating PNS to the majority of the GW signal during the accretion-phase, with h_+D normalized strain amplitudes around 50 cm. These g-modes are thought to be excited by downflows from postshock convection or internal PNS convection (Marek et al., 2009; Murphy

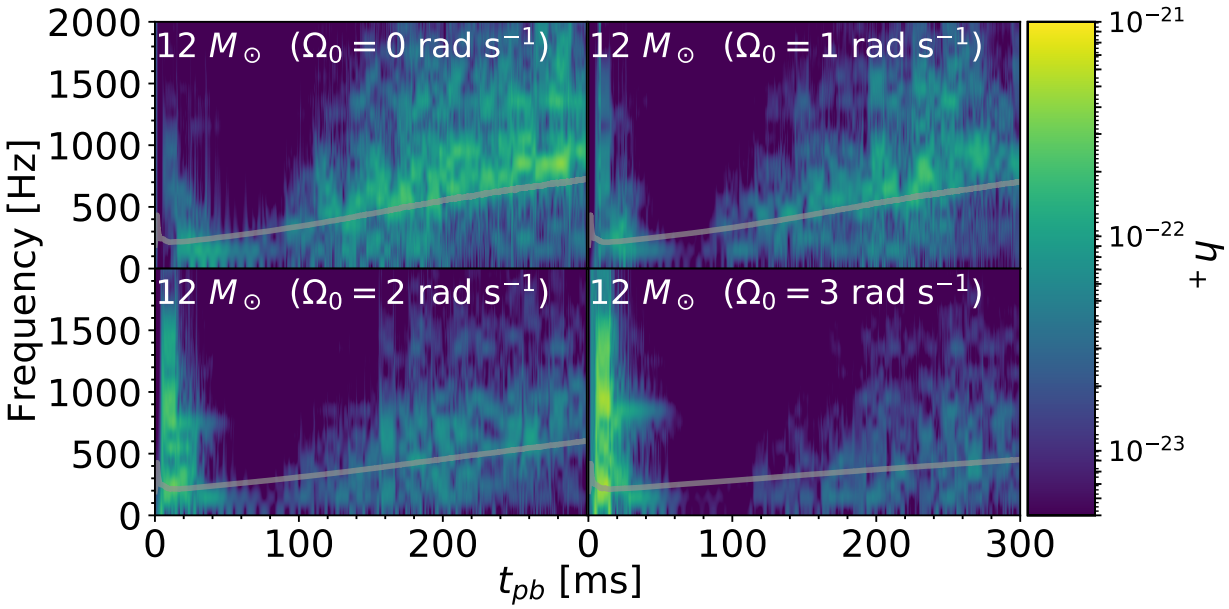

Figure 2.11: Spectrograms for the $12M_\odot$ progenitor over all four rotational velocities. The key aspects revealed by the spectrogram are the rotational muting of GWs and the flattening of the signal from the surface g-mode of the PNS. This flattening is a product of the enlarged radius of the PNS due to centrifugal effects and can be characterized by the dynamical frequency ($f_{dyn} = \sqrt{G\overline{\rho}}$), overlaid in gray.

et al., 2009; Müller et al., 2013). Figure 2.11 shows a spectrogram for the 12 $M_\odot$ progenitor over all rotational speeds, where lighter colors represent greater strain amplitudes, h_+. The dominant yellow band that extends from 100 to 1000 Hz represents this contribution. Overlaid in gray is the dynamical frequency that is characterized by the average density of the PNS, $\overline{\rho}$, and gravitational constant, G, $f_{\rm dyn} = \sqrt{G\overline{\rho}}$, that evolves synchronously with the g-mode contribution. The synchronized evolution of $f_{\rm dyn}$ and the frequency at which the PNS emits gravitational radiation are no coincidence. As both are fundamentally related to the mass and radius of the PNS, we expect that both are affected similarly when introducing rotation. The initial progenitor rotation will centrifugally support the PNS, thereby leaving it with a larger average radius. Similar to two tuning forks of different lengths, the PNS with a larger radius will emit at a lower frequency, compared with a smaller PNS. This "flattening" of the emitted frequency is displayed in Figure 2.11. Furthermore, Figure 2.11 provides a different lens through which the rotational muting is displayed, via the progressively darker panels

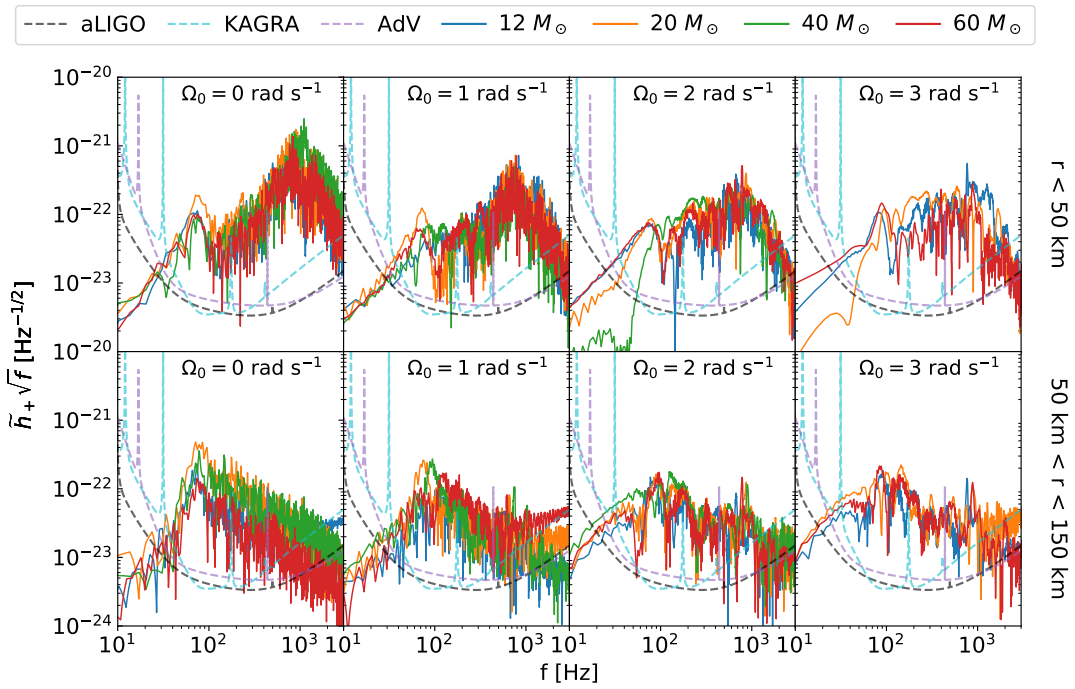

Figure 2.12: ASD plot of all progenitors for all rotation rates from $t_{be} + 6$ ms $\rightarrow$ $t_{be} + 300$ ms, with an assumed distance of 10 kpc. The rotational muting of the fundamental PNS g-mode is displayed as the peak frequency ($\sim$ 800 Hz) becomes less prevalent, with increasing rotation rate. Likewise, the low-frequency signals ($\sim$ 40 Hz) from the gain region become more audible, with increasing rotational velocity. The damping of the vibrational modes of the PNS allows the slower postshock convection to contribute more to the overall GW signal. Plotted in the black dashed line is the design sensitivity curve for aLIGO in the zero-detuning, high-sensitivity configuration (Barsotti et al., 2018). The cyan dashed line is the predicted KAGRA detuned, sensitivity curve (Komori et al., 2017). The purple dashed line is the design sensitivity curve for AdV (Abbott et al., 2018).

with increasing rotational velocity. We note that more robust peak GW frequency calculations exist (e.g., Müller et al., 2013; Morozova et al., 2018), but we find that the simple $f_{\rm dyn}$ relation gives a good estimate of the PNS peak frequency.

We also Fourier transform the accretion-phase GW signal, as displayed in Figure 2.12 and scale the magnitude of the Fourier coefficients by $\sqrt{f}$ in order to produce ASD plots. These plots commonly display the sensitivity curves of current and next-generation GW detectors. We define $t_{\rm be}$ similar to Richers et al. (2017) as the third zero crossing of the gravitational strain. We focus on the signal later than $t_{\rm be} + 6$ ms in order to remove the bounce signal and early postbounce oscillation contribution to the signal. The dominant contributions are the prompt convection, SASI,

and surface g-modes of the PNS—as displayed by a peak frequency ranging from 700 to 1000 Hz. Universally, the prevalence of the peak frequency decreases with increasing rotational velocity. It is worth noting this peak could shift to higher frequencies with longer simulation times.

When incorporating magnetic fields into CCSN simulations, other instabilities may arise that can compromise stability in the postshock region and possibly affect the behavior of the PNS. The α–Ω dynamo and MRI are two such mechanisms that can reexcite postshock convection; however, work from Bonanno et al. (2005) suggests that the α–Ω dynamo is unimportant on dynamical timescales. MRI has the potential to drive convection in the postshock region, yet as the strength and geometry of magnetic fields in 3D simulations are largely still unknown, we exclude them from our simulations (Cerdá-Durán et al., 2007).

2.4.5 Observability of the Accretion-phase Signal

Overlaid on our ASD plots is the expected sensitivity of future GW observatories. In the black, cyan, and purple dashed lines we have plotted the sensitivity curves of design sensitivity for aLIGO in the zero-detuning, high-sensitivity configuration, the predicted KAGRA detuned sensitivity curve, and design sensitivity for AdV, respectively (Komori et al., 2017; Abbott et al., 2018; Barsotti et al., 2018). These curves represent the incoherent sum of the principal noise sources to the best understanding of the respective collaborations. While these curves do not guarantee the performance of the detectors, they act as good guides for their anticipated sensitivities nonetheless.

Beyond the decreased prevalence of the peak frequency, an interesting trend emerges in Figure 2.12 as rotation increases. We separate the GW signals by region within the star. The top row of Figure 2.12 corresponds to GWs originating from the inner 50 km of the supernova, and the GW signal in the bottom row originates from radial distances between 50 and 150 km from the supernova center. In the top row, we note the first peak of emission, around 80 Hz, is independent of rotation. We point to the bright, higher v_{aniso} region in Figure 2.6 within the first 25 ms postbounce that is present for all rotational velocities. Focusing on the bottom row, we highlight a noticeable difference in the amplitude of the low-frequency contributions, particularly around 40 Hz. The

nonrotating progenitors have undetectable low-frequency signals for all three detectors, whereas rotating progenitors create measurable signals at low frequencies. This enhanced low-frequency signal may provide an observable feature that can help determine progenitor angular momentum information.

The amplitude of low-frequency GWs in the 50–150 km region of the supernova increases with rotational velocity, but this trend does not occur within the inner 50 km. As such, we restrict the low-frequency GW contribution to the gain region. We note the two main physical mechanisms in this region correspond to postshock convection and the SASI. While both mechanisms are reduced in strength due to rotational effects, they do not completely cease. This fact is displayed in Figure 2.6, as the region between 50 and 150 km is nonzero. For the nonrotating case, the high convective velocities (bright yellow) create higher frequency GWs within the 100 km region of interest. As rotation velocity increases, convective velocities decrease enough to cease exciting the vibrational modes of the PNS. These slower convective flows thereby reduce the total amount of power produced by the GWs and push the peak GW frequency—from the gain region—to lower frequencies. Performing an order-of-magnitude estimate on the source of the low-frequency signal, from Figure 2.6, we find $v_{\rm aniso} \sim 1 \times 10^9$ cm s^{-1} for $\Omega_0 = 0$ rad s^{-1} and $v_{\rm aniso} \sim 5 \times 10^8$ cm s^{-1} for $\Omega_0 = 3$ rad s^{-1}. As the region of interest is $\sim 10^7$ cm, we yield an estimated frequency of emission $f_{\rm low}$ around ~ 100 Hz and ~ 50 Hz, respectively. These quantitative frequency estimates are reflected in the ASD as the contribution from peak frequency (~ 100 Hz) from the gain region decreases, while the contribution ~ 40 Hz increases.

2.5 Summary and Conclusion

The strength of this project is its ability analyze GWs hundreds of milliseconds postbounce from multiple progenitors while accurately accounting for rotation and neutrinos. The wide breadth of parameter space we examine allows us to reveal certain rotational effects on the GW signal in the context of a controlled study. We have explored the influence of rotation on the GW emission from CCSNe for four different progenitors and four different core rotational speeds. We point out that there exists a roughly linear relation between compactness, ξ, and the differential rotation

parameter, A, as defined in Equation (3.1). Using this relation, we calculate appropriate A values for each progenitor mass, based on their individual compactness parameters of the Sukhbold et al. (2016a) progenitors. Of our 15 simulations, only two nonrotating progenitors have average shock radii that show substantial shock expansion, while the remaining rotating progenitors do not because of rotationally inhibited convection in the gain region and less neutrino production. In agreement with other recent work (e.g., Summa et al., 2018), we find a complex interplay between centrifugal support and neutrino heating as successful explosions do not display a monotonic relationship with rotation.

While there are more accurate treatments of gravity, we utilize the effective GR potential in order to streamline calculations, granting us the ability to explore larger sections of parameter space. We find that our results utilizing this approximation match very closely the CCSN bounce signal of CFC gravity with GR hydrodynamics (Richers et al., 2017).

The main contributors to the GW signal (10–300 ms postbounce) are postbounce convection, the SASI, and the surface g-modes of the PNS (Morozova et al., 2018). By establishing a positive angular momentum gradient, the convection is suppressed according to the Solberg-Høiland stability criterion (Endal & Sofia, 1978; Fryer & Heger, 2000). The more oblate shock front inhibits the bipolar sloshing of the SASI. Since the SASI and convection are the principal drivers exciting the g-modes of the PNS, vibrational emission from the PNS is also inhibited by rotation. We, therefore, find that rotation in 2D CCSN simulations results in the muting of GW emission. This result is consistent across progenitors with different ZAMS masses.

Before the PNS g-mode signal is completely muted, as rotation gradually increases, this signal is pushed to lower peak frequencies and can be characterized by its dynamical frequency. This observation is no coincidence as both fundamentally depend on the radius and mass of the PNS. With more centrifugal support, the PNS has a larger radius. This larger radius causes the surface of the PNS to emit at lower frequencies, thereby producing a "flatter," lower frequency signal.

We reveal a novel rotational effect on the GW signal during the accretion-phase. We notice that the nonrotating progenitors all produce low-frequency signals ($\sim$ 40 Hz) that are below the

plausible detection threshold of the aLIGO and KAGRA detectors, whereas the progenitors with larger angular velocities produce measurable GW signals in this frequency range. We attribute this increase of low-frequency emission to the SASI and postshock convection. For nonrotating progenitors, the convective velocity within the postshock region is high, emitting GWs $\sim$ 100 Hz. As rotational velocity increases, the PNS GW contribution is reduced. Likewise, as the convection slows, the mass within the gain region emits at lower GW frequencies. The slower convective flows reduce the total amount of GW power and push the peak GW frequency from the gain region to lower values. Whereas previous rotating core-collapse GW studies have focused on the bounce signal as a means to determine rotational features, or have focused on late time signals without rotation, our study unifies both facets and opens the door to measuring GW signals beyond the bounce phase that encode progenitor, angular momentum information. We postpone asserting quantitative relations between low-frequency emission and progenitor angular momentum until we incorporate more detailed microphysics.

While our approximations have allowed us to make large sweeps of parameter space, they leave room for us to include more robust microphysics. In an ideal situation, we would compute 3D simulations, including full GR, magnetohydrodynamics, and GR Boltzmann neutrino transport that incorporates velocity dependence and inelastic scattering on electrons and nucleons. These additions would allow for more accurate gravitational waveforms and allow other phenomena to occur, for example the $m \neq 0$ (spiral) modes of the SASI. Andresen et al. (2019) recently highlighted the rotational effects on GWs in 3D. Inherent to its 3D nature, their study finds the strongest GW amplitudes at high rotation velocities due to these spiral modes. The 2D geometry of our study, however, allows us to observe the relative strength of the convective signal, without interference from $m \neq 0$ modes, as we extend beyond the case of a single rotational velocity. While the physical origin of this muting that damps the convection and the SASI is not constrained only to 2D, in 3D, as Andresen et al. (2019) point out, other nonaxisymmetric instabilities can contribute to significant GW emission at late times, negating this rotational muting effect. Thus, once again, we are reminded of the key role of 3D simulations in the study of the CCSN mechanism.

We would like to thank Jess McIver for pointing us to the aLIGO and AdV sensitivity curves. M.A.P. was supported by a Michigan State University Distinguished Fellowship. S.M.C. is supported by the U.S. Department of Energy, Office of Science, Office of Nuclear Physics, under award Nos. DE-SC0015904 and DE-SC0017955 and the *Chandra X-ray Observatory* under grant No. TM7-18005X. This research was supported by the Exascale Computing Project (17-SC-20-SC), a collaborative effort of two U.S. Department of Energy organizations (Office of Science and the National Nuclear Security Administration) that are responsible for the planning and preparation of a capable exascale ecosystem, including software, applications, hardware, advanced system engineering, and early testbed platforms, in support of the nation's exascale computing imperative. The software used in this work was in part developed by the DOE NNSA-ASC OASCR Flash Center at the University of Chicago.

Software used in this work: FLASH (see footnote 7) (Fryxell et al., 2000, 2010), Matplotlib[8] (Hunter, 2007), NuLib[9] (O'Connor, 2015), NumPy[10] (van der Walt et al., 2011), SciPy[11] (Jones et al., 2001–)

[8] https://matplotlib.org/
[9] http://www.nulib.org
[10] http://www.numpy.org/
[11] https://www.scipy.org/

CHAPTER 3

DETERMINING MASSIVE STELLAR PROGENITORS FROM SUPERNOVA GRAVITATIONAL WAVES

This section reviews published work: M.A. Pajkos, M. Warren, S. Couch, E. O'Connor, K.C. Pan, 2021, *ApJ*, 914, 80.

3.1 Abstract

The gravitational wave (GW) signal resulting from stellar core collapse encodes a wealth of information about the physical parameters of the progenitor star and the resulting core-collapse supernova (CCSN). We present a novel approach to constrain CCSN progenitor properties at collapse using two of the most detectable parts of the GW signal: the core-bounce signal and evolution of the dominant frequency mode from the protoneutron star. We focus on the period after core bounce but before explosion and investigate the predictive power of GWs from rotating CCSNe to constrain properties of the progenitor star. We analyze 34 2D and four 3D neutrino-radiation-hydrodynamic simulations of stellar core collapse in progenitors of varied initial mass and rotation rate. Extending previous work, we verify the compactness of the progenitor at collapse to correlate with the early ramp-up slope, and in rotating cases, also with the core angular momentum. Combining this information with the bounce signal, we present a new analysis method to constrain the pre-collapse core compactness of the progenitor. Because these GW features occur less than a second after core bounce, this analysis could allow astronomers to predict electromagnetic properties of a resulting CCSN even before shock breakout.

3.2 Introduction

Gravitational waves (GWs) provide astronomers with an entirely new spectrum of signals to detect, coming from a variety of astrophysical processes. As current GW observatories—Advanced Laser Interferometer Gravitational-wave Observatory (aLIGO), Advanced Virgo, and Kamioka Gravitational Wave Detector (KAGRA)—continue observing runs and with future GW obser-

vatories on the horizon—Deci-hertz Interferometer Gravitational Wave Observatory (DECIGO), Einstein Telescope, LIGO-India, and the Laser Interferometer Space Antenna (LISA)—the number of GW detections will only increase (Gossan et al., 2016). One site of particular interest for some of these observatories is the explosive endings of massive stars: core-collapse supernovae (CCSNe). CCSNe are important in a broader astrophysical context because they contain matter with densities over many orders of magnitude. Acting as unique laboratories, better understanding these stellar explosions has a broad impact on many areas of astronomy: predicting compact object birth, restricting the nuclear equation of state (EOS), and constraining stellar rotation, to name a few.

After being produced in the center of a CCSN, GWs pass through the outer stellar envelope unobstructed. For decades, astronomers have attempted to leverage this unique characteristic to prepare for the next CCSN event by connecting the features of a GW signal with the internal physics of the supernova or protoneutron star (PNS) inside. Currently, the detection range for GWs from CCSNe is Galactic in scale, leaving the expected rate to be $\sim$ 2 events per century (Diehl et al., 2006). Given the rarity of potential observations, GW predictions from numerical models have been important to prepare GW astronomers for the next CCSN event.

While the CCSN problem involves a variety of physics, a proper treatment of gravity is one of the most important aspects when predicting GWs. While a numerical scheme that simulates a dynamically evolving space-time (e.g. Shibata & Nakamura, 1995; Baumgarte & Shapiro, 1999) may be ideal for accuracy, the immense computational cost can prevent incorporating other robust physics features, such as magnetic fields or neutrinos. Approximations have been made to capture some of the general relativistic (GR) features for a given mass distribution within a supernova. Previous works have paired Newtonian hydrodynamics with an effective GR gravitational potential (GREP) (Rampp & Janka, 2002; Marek et al., 2006; Bruenn et al., 2016; Morozova et al., 2018; O'Connor & Couch, 2018b). Consistent with a modified Tolman-Oppenheimer-Volkhoff equation, GREP empirically satisfies the solution to hydrostatic equilibrium and has been shown to fairly accurately reproduce overall features of CCSN numerical models (Rampp & Janka, 2002; Marek

et al., 2006; Müller et al., 2012; O'Connor & Couch, 2018b; da Silva Schneider et al., 2020). Another, more advanced, approximation is the so-called conformal flatness condition (CFC), in which the spatial three metric is approximated by the flat space-time three metric. This scheme qualitatively agrees with CCSN results using GREP (Shibata & Sekiguchi, 2004) and reproduces early CCSN GW signals within a few percent of similar simulations that directly solve Einstein's field equations (Ott et al., 2007). As a variant, CFC has also been reformulated as an *augmented CFC* scheme to address uniqueness issues of the elliptic constraints present in CFC (Saijo, 2004; Cordero-Carrión et al., 2009; Müller, 2019).

Once the core temperature for a massive star ($\gtrsim 8\,M_\odot$) becomes sufficiently high ($T \sim 5$ GK), iron nuclei begin to photodissociate and undergo electron capture. These processes result in a net loss of pressure, triggering the core to collapse inward. At sufficiently high densities ($\sim 2\times10^{14}\,\mathrm{g\,cm^{-3}}$), the nuclear force halts the matter infall on the timescale of microseconds and, in the case of rotating CCSNe, a burst of GWs is produced: the GW *bounce signal*. The bounce signal has been studied extensively and it is found that—except in extreme scenarios—more angular momentum in the supernova center will produce a bounce signal with higher amplitude (Mueller, 1982; Moenchmeyer et al., 1991; Yamada & Sato, 1995; Zwerger & Mueller, 1997; Dimmelmeier et al., 2002; Kotake et al., 2003b; Shibata & Sekiguchi, 2004; Abdikamalov et al., 2014).

As the subsonic inner core meets the supersonic outer core, a shock front ensues, photodissociating material at larger radii as it propagates outward. This process forms a negative lepton gradient via neutrino production, causing prompt convection in the post-shock region (Mazurek, 1982; Bruenn, 1985, 1989; Burrows & Fryxell, 1992). This prompt convection is an important feature in CCSN evolution and has been shown to directly contribute to the GW signal (Marek et al., 2009; Müller, 2017; Richers et al., 2017; Nagakura et al., 2018).

As the shock front continues to propagate outward, the matter motion behind the shock is subject to a variety of instabilities that can emit GW signals: post-shock convection (Burrows & Hayes, 1996; Mueller & Janka, 1997; Müller et al., 2004; Murphy et al., 2009; Müller et al., 2013), the standing accretion shock instability (SASI) (Blondin et al., 2003; Blondin & Mezzacappa, 2006;

Ohnishi et al., 2006; Foglizzo et al., 2007; Scheck et al., 2008; Iwakami et al., 2009; Fernández, 2010; Kuroda et al., 2016; Andresen et al., 2017), and the PNS vibrational modes (Mueller & Janka, 1997; Cerdá-Durán et al., 2013; Torres-Forné et al., 2018, 2019a).

Perturbation theory has been used historically to provide analytic estimates of PNS properties by identifying the resonant frequencies (GW astroseismology), or vibrational modes—for example, g-, f-, p-, r-, and w-modes (Unno et al., 1989). As outlined by Gautschy & Saio (1995), the restoring force for p-modes comes from the pressure of the gas. The restoring force for g-modes is the buoyancy force. Andersson (1998) and Kokkotas & Stergioulas (1999) describe r-modes arising in rotating stars and grow unstable due to the emission of GWs from the stellar interior. Kokkotas & Schutz (1992) identify the presence of so-called w-modes that are closely related to the oscillations in the space-time metric. Andersson & Kokkotas (1996) built on this work by suggesting the f-mode evolves with the average density of the star and the damping rate of the w-mode depends linearly on compactness.

More recently, Sotani & Takiwaki (2016) used multiple 1D simulations to show that PNS oscillation frequencies are almost independent of PNS electron fraction (Y_e) and entropy per baryon profiles. Sotani et al. (2017) use 3D models to relate the w_1-mode to the PNS mass and radius. Sotani & Sumiyoshi (2019) use 1D simulations to examine PNS structure during the accretion phase, en route to black hole (BH) formation; moreover, various groups have even used GWs to probe BH formation itself for a variety of progenitor masses (Ott et al., 2011; Cerdá-Durán et al., 2013; Kuroda et al., 2018; Pan et al., 2018). Other works investigate the influence of rotation and magnetic fields in the core-collapse scenario (Obergaulinger & Aloy, 2017; Obergaulinger et al., 2018). Warren et al. (2020) recently explored the GW signal a few seconds after bounce, displaying correlations between initial progenitor compactness and the slope of the GW frequency emitted from the dominant PNS mode, in frequency versus time space (hereafter referred to as "ramp-up slope"). Sotani & Takiwaki (2020b) explore the dimensional dependence of GW generation from the PNS. They point out correlations between the relative strengths of different modes compared to PNS characteristics: average density and compactness. Likewise, research continues into how

these different modes interact via *avoided crossing* (Sotani & Takiwaki, 2020a). Morozova et al. (2018) examine GW emission for a moderately rotating CCSN ($\Omega_{\rm central} \sim 0.2$ rad s^{-1}). Radice et al. (2019) and O'Connor & Couch (2018a) use a suite of 3D simulations to show how turbulent kinetic energy accreted by the PNS relates to the GW energy radiated. Mezzacappa et al. (2020) recently explored the GW production, by region, from a 15 $M_\odot$ star. Vartanyan et al. (2019) relate multimessenger signals from CCSNe to physical properties at the center of the supernova. Like previous works, Vartanyan & Burrows (2020) investigate GW production from neutrino emission asymmetries in CCSNe (Mueller & Janka, 1997; Kotake et al., 2009). Pan et al. (2020) and Shibagaki et al. (2021) study GW emission from rotating 3D progenitors. And in even more exotic scenarios, Zha et al. (2020) identify the GW signals expected from a quantum chromodynamic phase transition of a protocompact star, originating from a CCSN.

As discussed, many studies that use multidimensional simulations have either explored only the bounce signal, in the case of rotation, or the accretion phase signal from nonrotating supernovae. As all stars rotate to some degree, an opportunity arises to investigate the effect of rotation on GWs emitted from CCSNe during the accretion phase. Furthermore, there exists a growing need in the supernova community to not only predict gravitational waveforms but extract information from them in new ways, in order to constrain physical properties of the progenitor star. In this work, we show the GW signal from the dominant PNS mode encodes angular momentum information of the CCSN at bounce in a quantifiable way. We also present a novel analysis that combines multiple features of the GW signal from a single rotating CCSN to help constrain the properties of the progenitor star.

The strength of this technique stems from its observational considerations. Previous works depend on tracking multiple, relatively weaker modes of a PNS to constrain mass and radius. This work only depends on the loudest components of the GW signal and are thus most likely to be reconstructed by current GW detectors (McIver, 2015). Furthermore, this analysis is valuable because it uses multimessenger signals that are emitted less than a second after core bounce to constrain core compactness. Applying previous works that draw correlations between core

compactness and electromagnetic (EM) observables days after a supernova explosion (Sukhbold et al., 2016b), our work provides a predictive framework that would allow astronomers to anticipate EM properties of the supernova, even before shock breakout occurs.

This paper is organized as follows: in Section 5.4 we present our methods and treatment of microphysics within our FLASH simulations. Section 3.4 contains our analysis and outlines observational considerations. Finally, in Section 5.7.2 we discuss and conclude.

Label	M($M_\odot$)	Ω_0(rad s^{-1})	A(10^3 km)	EOS	2D/3D	ν Treatment	e^- rates	$M^{\rm B}_{\rm core}(M_\odot)$	$Y^{\rm c}_e$	$\beta^{\rm B}_{\rm core}$	$t^{\rm pb}_{\rm end}$ (s)
s12o0	12	0	0.8123	SFHo	2D	M1	SNA	0.578	0.278	0.000	0.3
s12o0.5	12	0.5	0.8123	SFHo	2D	M1	SNA	0.580	0.279	0.001	0.3
s12o1	12	1	0.8123	SFHo	2D	M1	SNA	0.581	0.279	0.006	0.3
s12o2	12	2	0.8123	SFHo	2D	M1	SNA	0.584	0.279	0.021	0.3
s12o3	12	3	0.8123	SFHo	2D	M1	SNA	0.576	0.280	0.042	0.3
s20o0	20	0	1.021	SFHo	2D	M1	SNA	0.564	0.273	0.000	0.3
s20o.5	20	0.5	1.021	SFHo	2D	M1	SNA	0.567	0.273	0.006	0.3
s20o1	20	1	1.021	SFHo	2D	M1	SNA	0.572	0.274	0.021	0.3
s20o2	20	2	1.021	SFHo	2D	M1	SNA	0.568	0.274	0.066	0.3
s20o3	20	3	1.021	SFHo	2D	M1	SNA	0.534	0.274	0.106	0.3
s40o0	40	0	1.282	SFHo	2D	M1	SNA	0.556	0.267	0.000	0.3
s40o0.5	40	0.5	1.282	SFHo	2D	M1	SNA	0.560	0.268	0.011	0.3
s40o1	40	1	1.282	SFHo	2D	M1	SNA	0.562	0.268	0.037	0.3
s40o2	40	2	1.282	SFHo	2D	M1	SNA	0.554	0.268	0.101	0.3
s60o0	60	0	0.9112	SFHo	2D	M1	SNA	0.571	0.276	0.000	0.3
s60o0.5	60	0.5	0.9112	SFHo	2D	M1	SNA	0.574	0.276	0.003	0.3
s60o1	60	1	0.9112	SFHo	2D	M1	SNA	0.576	0.277	0.013	0.3
s60o2	60	2	0.9112	SFHo	2D	M1	SNA	0.571	0.277	0.043	0.3

s60o3	60	3	0.9112	SFHo	2D	M1	SNA	0.557	0.278	0.076	0.3
s12o0x‡	12	0	0.8123	SFHx	2D	M1	SNA	0.563	0.273	0.000	0.3
s12o0.5x	12	0.5	0.8123	SFHx	2D	M1	SNA	0.564	0.273	0.001	0.005
s12o2x‡	12	2	0.8123	SFHx	2D	M1	SNA	0.580	0.273	0.022	0.3
s12o3x‡	12	3	0.8123	SFHx	2D	M1	SNA	0.578	0.272	0.042	0.3
s20o0.5x	20	0.5	1.021	SFHx	2D	M1	SNA	0.550	0.267	0.006	0.005
s20o1x	20	1	1.021	SFHx	2D	M1	SNA	0.568	0.268	0.022	0.005
s20o2x	20	2	1.021	SFHx	2D	M1	SNA	0.570	0.267	0.068	0.005
s20o3x	20	3	1.021	SFHx	2D	M1	SNA	0.507	0.270	0.103	0.005
s40o0.5x	40	0.5	1.282	SFHx	2D	M1	SNA	0.562	0.262	0.011	0.005
s60o0.5x	60	0.5	0.9112	SFHx	2D	M1	SNA	0.557	0.271	0.003	0.005
s60o1x	60	1	0.9112	SFHx	2D	M1	SNA	0.558	0.271	0.012	0.005
s60o2x	60	2	0.9112	SFHx	2D	M1	SNA	0.572	0.271	0.044	0.005
s60o3x	60	3	0.9112	SFHx	2D	M1	SNA	0.562	0.271	0.078	0.005
s12o2$^{\nu}$	12	2	0.8123	SFHo	2D	M1	LMP+N50	0.520	0.259	0.020	0.005
s60o2$^{\nu}$	60	2	0.9112	SFHo	2D	M1	LMP+N50	0.535	0.259	0.044	0.005
s27o2^{3D}	27	2	0.7700	LS220	3D	M1*	SNA	N/A	N/A	N/A	0.005
s40o0^{3D}	40	0	1	LS220	3D	Ye(ρ)+IDSA	SNA	0.576	0.272	0.000	0.3
s40o0.5^{3D}	40	0.5	1	LS220	3D	Ye(ρ)+IDSA	SNA	0.509	0.272	0.008	0.3

s40o1^{3D}	40	1	1	LS220	3D	Ye(ρ)+IDSA	SNA	0.562	0.272	0.028	0.3

Table 3.1: Information regarding setup information for all 38 models in this study. Column labels represent the following: M–zero age main sequence mass, Ω_0–central rotation rate at collapse, A differential rotation parameter, EOS, 2D/3D–dimensionality of the simulation, neutrino (ν) treatment, e^- rates–electron capture rates used to construct neutrino opacity tables, $M^B_{\rm core}$–mass of core at bounce, $Y^{\rm c}_e$–central Y_e at bounce, $\beta^{\rm B}_{\rm core}$ is the ratio of rotational kinetic energy to gravitational binding energy at bounce, $t^{\rm pb}_{\rm end}$–simulation end time (post bounce). For e^- rates, SNA represents the single nucleus approximation used by Bruenn (1985). LMP+N50 represents the Laganke-Martinez Pinedo rates (Langanke & Martinez-Pinedo, 2001) supplemented by the calculations of Titus et al. (2018). ‡ denote the three models saved as *test data* for our multidimensional fit in Figure 3.10 and Equation (3.12). For s27o2^{3D} M1* indicates M1 neutrino transport, without inelastic scattering or velocity dependent terms.

3.3 Methods

In this work, we simulate the core collapse of the 12.0, 20.0, 40, and 60 $M_\odot$ nonrotating, solar-metallicity progenitors models from Sukhbold et al. (2016b). We use the `FLASH` (version 4) multiscale, multiphysics adaptive mesh refinement simulation framework (Fryxell et al., 2000; Dubey et al., 2009).[7] Our grid setup is a 2D cylindrical geometry with the PARAMESH (v.4-dev) library for adaptive mesh refinement (MacNeice et al., 2000). The outer boundary is 10^4 km in all directions, with nine levels of refinement—a finest grid spacing of about 0.65 km. The maximum allowed level of refinement is decreased as a function of spherical radius, r, in order to maintain a resolution aspect ratio, $\Delta x_i/r$, of about 0.01, corresponding approximately to an *angular* resolution of 0.5°. We use the GREP for our gravitational treatment (Marek et al., 2006; O'Connor & Couch, 2018b) used alongside the multipole Poisson solver of Couch et al. (2013), where we retain spherical harmonic orders up through 16.

To model the transport of neutrinos, we incorporate an M1 scheme: a multidimensional, multispecies, energy-dependent, two-moment scheme with an analytic closure. Our implementation is based on O'Connor (2015), Shibata et al. (2011), and Cardall et al. (2013). For a detailed outline of the M1 implementation in `FLASH`, we direct the reader to O'Connor & Couch (2018b). We use 12 energy bins spaced logarithmically up to 250 MeV. The full set of rates and opacities we use is described in O'Connor et al. (2017). As outlined by Horowitz et al. (2017), we use the effective, many-body, corrected rates for neutrino-nucleon, neutral current scattering. In this study—unlike our previous work (Pajkos et al., 2019)—we incorporate velocity-dependent neutrino transport and account for inelastic neutrino-electron scattering.

In total, we simulate 34 CCSNe; we use the SFHo EOS for 19 and the SFHx EOS for three of our simulations that run to 300 ms pb (Steiner et al., 2013a,b). We run additional simulations that run through core bounce, 10 of which use the SFHx EOS and two of which use the SFHo EOS with modified electron capture rates (Langanke & Martínez-Pinedo, 2003; Steiner et al., 2013a,b;

[7] https://flash.rochester.edu/site/

Sullivan et al., 2016; Titus et al., 2018). Additionally, we incorporate four 3D simulations into our analysis. We extract the GW bounce signal from the collapse of one rotating 27 $M_\odot$ progenitor (Woosley et al., 2002) that uses the LS220 EOS (Lattimer & Swesty, 1991), M1 neutrino transport, and has a central rotation rate of 2 rad s^{-1}. We examine the bounce signal and accretion phase signal of three simulations that model a 40 $M_\odot$ (Woosley & Heger, 2007) collapse using the LS220 EOS and use the Isotropic Diffusion Source Approximation (IDSA) neutrino treatment (Liebendörfer et al., 2009; Pan et al., 2016, 2018, 2020). The three central rotational velocities are 0, 0.5, and 1 rad s^{-1}. For a detailed outline of all simulation parameters, see Table 3.1.

3.3.1 Rotational Profiles

To begin, the nonrotating 1D progenitor models are mapped onto our 2D Eulerian grid. We then apply an artificial rotation profile

$$\Omega(r) = \Omega_0 \left[1 + \left(\frac{r}{A} \right)^2 \right]^{-1}, \tag{3.1}$$

where $r = \sqrt{R^2 + z^2}$ is the spherical radius for a given cylindrical radius R and altitude z, Ω_0 is the central angular speed of the star, and A is the differential rotation parameter (Eriguchi & Mueller, 1985). Small A values imply a greater degree of differential rotation, while larger A values push the rotation profile closer to solid body. By multiplying the angular speed with the distance from the rotation axis, the linear rotational velocity is calculated: $v_\phi(R, z) = R\Omega(r)$.

The internal rotation rates and profiles of massive stellar cores at collapse are still poorly constrained. Other work (e.g., Abdikamalov et al., 2014) explore varying the differential rotation parameter A and investigate its impact on the GW bounce signal. We assign A values based on compactness (O'Connor & Ott, 2011) of the core at collapse. The core compactness as introduced by O'Connor & Ott (2011) is defined as

$$\xi_M = \left. \frac{M/M_\odot}{R(M_{\rm bary} = M)/1000\,{\rm km}} \right|_{\rm collapse}, \tag{3.2}$$

where M is the baryonic mass, and $R(M)$ is the radius at the corresponding mass coordinate. How A relates to ξ_M is based on an empirical fit determined in our previous work (Pajkos et al.,

2019). In short, this relationship quantifies how the rotational velocity assigned at collapse tracks the progenitor core structure based on the models of Heger et al. (2005).

For our 2D simulations, we select $\Omega_0 = 0, 0.5, 1, 2$, and 3 rad s^{-1} for central rotation rates. Pajkos et al. (2019) showed that the ramp-up slope decreases as the PNS becomes more centrifugally supported for these integer valued rotation rates. In aims to quantify this relationship we select identical rates. Due to magnetic breaking, the presence of rapidly rotating stars—similar to stars with $\Omega_0 \geq 1$ rad s^{-1}—is quite rare (Woosley & Heger, 2006). In an attempt to more finely sample the lower rotation rate parameter space, we extend this previous study by including simulations with $\Omega_0 = 0.5$ rad s^{-1} as well.

To maintain the fidelity of our simulation suite, we choose to omit the 40 $M_\odot$ progenitor at $\Omega_0 = 3$ rad s^{-1} from our following analysis. The $\xi_{2.5}$ value of this progenitor is nearly double that of the 20 $M_\odot$ progenitor (the next closest compactness value), resulting in nearly solid-body core rotation. This rotation profile for the 40 $M_\odot$ results in vast amounts of angular momentum, ultimately leading to likely unphysical rotation dominated dynamics, and in particular, a highly suppressed core-bounce GW signal.

3.3.2 GW Signal Extraction

To extract the GW signal from our simulations, we adopt the dominant, quadrupole moment formula for the gravitational strain, through the slow motion, weak-field formalism (eg., Blanchet et al., 1990; Finn & Evans, 1990)

$$h_+ \approx \frac{3}{2}\frac{G}{Dc^4}\frac{d^2 I_{zz}}{dt^2}\sin^2\theta, \tag{3.3}$$

where I_{zz} is the reduced-mass quadrupole moment, G is the gravitational constant, c is the speed of light, D is the distance to the source (our fiducial value is $D = 10$ kpc), and θ is the latitudinal angle between the supernova axis of rotation and the observer. For extracting the GW signal from our 3D simulations we follow the method outlined in Oohara et al. (1997). For our analysis, we assume optimal source orientation—GWs emitted from the equator of the CCSN ($\theta = \pi/2$). Later, as we outline our method to constrain progenitor ξ_M, we will discuss the impact of source orientation.

When analyzing the frequency structure of the GW signal, the *peak* GW frequency is often a quantity of interest. In this work, for our axisymmetric simulations, we use a similar form of the semianalytic formula proposed by Müller et al. (2013)

$$f_{\rm peak} \sim \frac{1}{2\pi}\frac{GM}{R^2 c}\sqrt{2.1\frac{m_n}{\langle E_{\bar{\nu}_e}\rangle}}\left(1-\frac{GM}{Rc^2}\right)^2, \tag{3.4}$$

where M is the mass of the PNS, R is the PNS radius, $\langle E_{\bar{\nu}_e}\rangle$ is the mean electron antineutrino energy, G is Newton's gravitational constant, c is the speed of light, and m_n is the mass of a neutron. (Note the factor of 2.1, instead of 1.1 in the original work). While this may correspond to a physically higher adiabatic index approximating the pressure of the baryons near the PNS layer, we find this new factor reproduces the peak GW frequencies better for our axisymmetric simulations. For the 3D models s40o[0-0.5]^{3D} we use a similar form (Eqn. (5) of Pan et al. (2018)) that does not have the last quadratic term $(1 - GM/Rc^2)^2$ because the IDSA neutrino treatment does not account for gravitational redshift.

3.3.3 Quality of Fit

As we analyze over 30 multidimensional simulations over a wide range of parameter space, we perform functional fits to our data. To quantify how well our models fit the data we use `curve_fit` in the `scipy.optimize` library to return best-fit parameters as well as the standard deviation errors for each parameter. Furthermore, we calculate the coefficient of determination as

$$r^2_{\rm det} = 1 - \frac{\Sigma_i (y_i - \hat{y}_i)^2}{\Sigma_i (y - \bar{y}_i)^2}, \tag{3.5}$$

where $(y_i - \hat{y}_i)^2$ represents the squared residual between the simulation output data and model fit (Hughes & Grawoig, 1971). The quantity $(y - \bar{y}_i)^2$ represents the variance of the simulation output data. Here, $r^2_{\rm det} = 0$ indicates no correlation with the regression line and $r^2_{\rm det} = 1$ indicates a perfect correlation. We use $r^2_{\rm det}$ to quantify the regression of our fit coefficients seen in the polynomial fits of Figures 3.4, 3.6, 3.8, and 3.10.

3.4 Results

Our analysis synthesizes multiple components of the GW signal to constrain supernova progenitor compactness at collapse. This project builds upon previous works that show the ramp-up slope of a nonrotating CCSN correlates with progenitor compactness (Warren et al., 2020) and that the core-bounce signal encodes core angular momentum information (Abdikamalov et al., 2014). By ramp-up slope, we mean the slope of the peak GW frequency emitted in frequency versus time space. The novel approach we take quantifies the *rotational flattening*—or the decreasing slope of the ramp-up with increasing rotation rate—mentioned in Pajkos et al. (2019). Specifically, we find that the flattening correlates with angular momentum of the inner 1.75 $M_{\odot}$ of the supernova. We then combine these two distinct features of the GW signal—loud bounce signal and dominant ramp-up slope—to constrain the core compactness of the progenitor star at collapse. We first discuss the general evolution of each simulation, outline in detail each step of the analysis, and consider observability as well.

3.4.1 Evolution of Shock Radius

One of the main parameters we vary in this study is the central rotation rate, Ω_0, so it is important to discuss the potential impact it can have on shock radius evolution. On one hand, rotation can stabilize turbulence in the post-shock region, weakening one the main sources that drive a successful supernova explosion (Couch & Ott, 2015; Janka et al., 2016). Likewise, a centrifugally supported PNS that forms at larger radii would result in a softer neutrino spectrum. These less energetic neutrinos could result in reduced heating behind the shock.

On the other hand, rotation can also provide centrifugal support to a collapsing star. This support would allow core bounce to occur at lower central densities, forming a shock at larger radii. This initially, less gravitationally bound shock could be more conducive to a successful explosion. Once again, we are reminded of the strong nonlinearities present when simulating CCSNe and the persistence of Mazurek's law: while changing one piece of physics may increase the likelihood

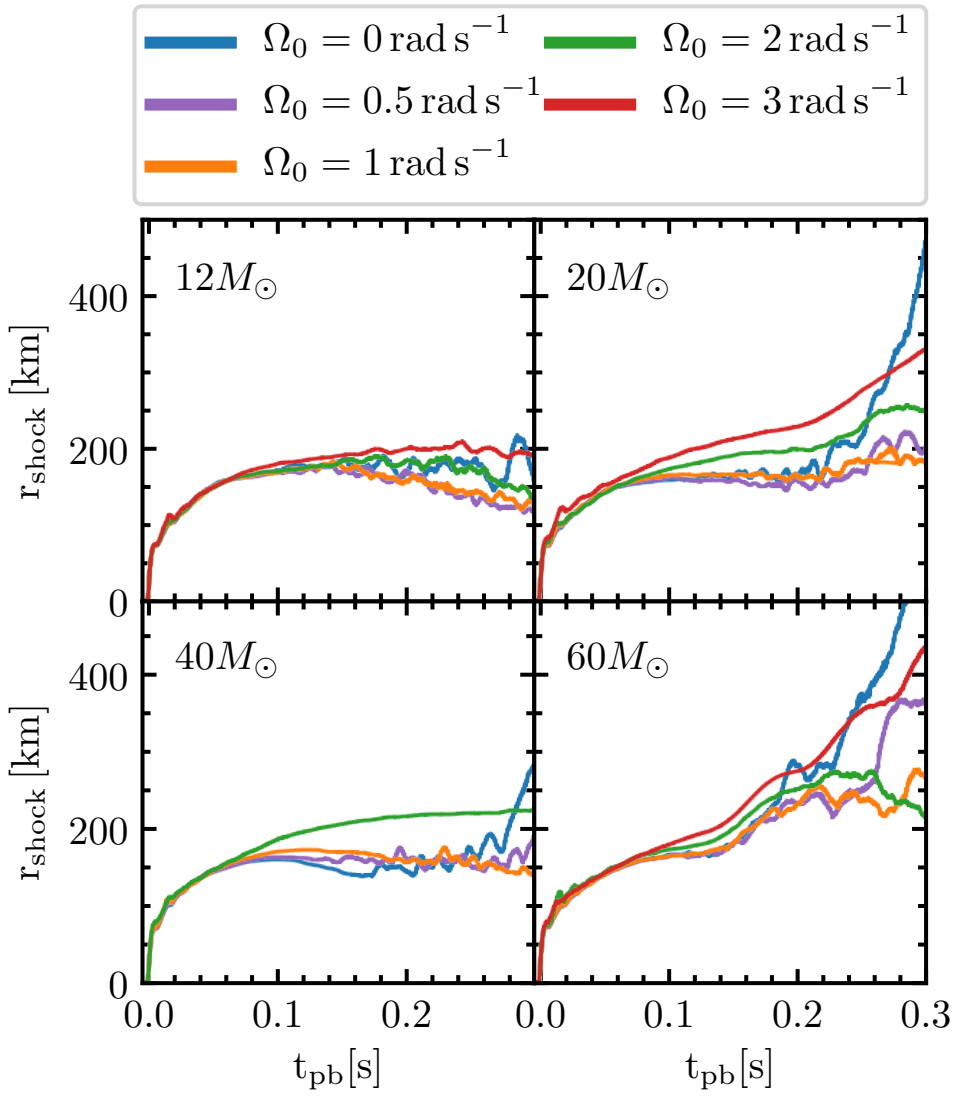

Figure 3.1: Evolution of the average shock radii for 2D all simulations using the SFHo EOS: models s12o[0-3], s20o[0-3], s40o[0-2], and s60o[0-3]. Similar to Pajkos et al. (2019), we notice non-monotonic behavior of the shock expansion when considering progenitor mass and initial rotation rate.

of explosion, another factor is likely to change equally as much to counter that effect (Lattimer & Prakash, 2000).

Here, we report the tendency of our 2D suite of models to explode. Figure 3.1 displays how the average shock radii of the supernovae evolve with time, with each panel dedicated to a specific progenitor mass. The specific models plotted are s12o[0-3], s20o[0-3], s40o[0-2], and s60o[0-3]. Here, we define a simulation to *successfully* explode if its averaged shock radius passes and remains 400 km away from the supernova center. All models that do so also obtain a substantially positive diagnostic explosion energy (Bruenn et al., 2016).

The 12 $M_\odot$ progenitor at all rotational velocities does not undergo any successful explosions within the 300 ms simulation window. It seems neither the supportive nor inhibitive nature of rotation drastically modifies the shock evolution. This is in agreement with previous results using FLASH-M1 for simulations of a nonrotating 12 $M_\odot$ progenitor that also failed to find explosions (O'Connor & Couch, 2018b) and the 2D results using the FORNAX code (Vartanyan et al., 2018). Burrows et al. (2019), however, find a successful explosion for a nonrotating 12 $M_\odot$ progenitor in 3D, as do Summa et al. (2016) in 2D using the PROMETHEUS-VERTEX code.

The 20 $M_\odot$ explodes for the nonrotating case with one of the most aggressively advancing shock radii of the simulation set. For $\Omega_0 = 3$ rad s^{-1}, while it does not reach 400 km within the simulation time, it does display steady growth to larger radii. The simulations with the remaining rotational velocities show no further shock expansion.

The four simulations of the 40 $M_\odot$ progenitor also do not successfully explode. Indeed, it seems the high amounts of angular momentum endowed to this highly compact progenitor have a negative effect on the advancing shock front. While all rotating cases show no significant shock displacement, it is worth noting that by the end of the simulation, the nonrotating case shows significant increase in its *rate* of shock expansion. Perhaps, with longer simulation times, the nonrotating 40 $M_\odot$ could show signs of exploding.

The 60 $M_\odot$ shows the most diverse behavior of the simulation set. While the $\Omega_0 = 1, 2$ rad s^{-1} simulations remain roughly stagnant at 300 ms pb, the remaining simulations advance toward

or beyond 400 km. Interestingly—similar to the 20 $M_\odot$ case—the nonrotating and fastest rotating models have the least bound shock radii. Clearly, for the density profile within the 60 $M_\odot$ progenitor, the nonlinear effects of rotation become apparent.

While analyzing the *explodability* of different models in detail is a key component to CCSN research, it lies beyond the scope of this paper, which focuses on the GW signals emitted. Seconds after the core bounce, when the asymptotic explosion energy approaches a final value, the matter distribution and net neutrino production can be asymmetric. In certain cases, these asymmetries can produce a direct, non-oscillatory, GW signal (sometimes referred to as a memory component) (Vartanyan & Burrows, 2020). While some of our models have significantly expanding shock radii, our simulations do not evolve to late enough times to develop the asymmetries necessary to produce this direct GW offset.

3.4.2 General Features of Rotating GW Signals

Here, we review the general features of the GW signal seen in our rotating and nonrotating 2D simulations using the SFHo EOS. Figure 3.2 shows the bounce signals from all rotation rates, separated by progenitor mass, while Figure 3.3 displays the waveforms over the entire simulation duration. Specifically, the models included in these figures are s12o[0-3], s20o[0-3], s40o[0-2], and s60o[0-3].

The first main feature is the loud bounce signal. As rotation rate increases, the increasing angular momentum of the once-stellar iron core forces it to deviate from spherical symmetry to become an oblate spheroid. At bounce, the nuclear force suddenly halts the infalling matter causing the (once iron core, now) PNS to deform on the time scale of a fraction of a millisecond. More specifically, to leading order, the mass quadrupole moment of the PNS drastically accelerates, resulting in the emission of GWs. In extreme scenarios, for sufficient angular momentum within the inner core, the infalling matter can become centrifugally supported. This slowed infall, in turn, deforms the PNS less at bounce, creating a GW bounce signal with a lower amplitude (Dimmelmeier et al., 2008).

In Figure 3.2, the GW strain the first few milliseconds after bounce corroborates previous

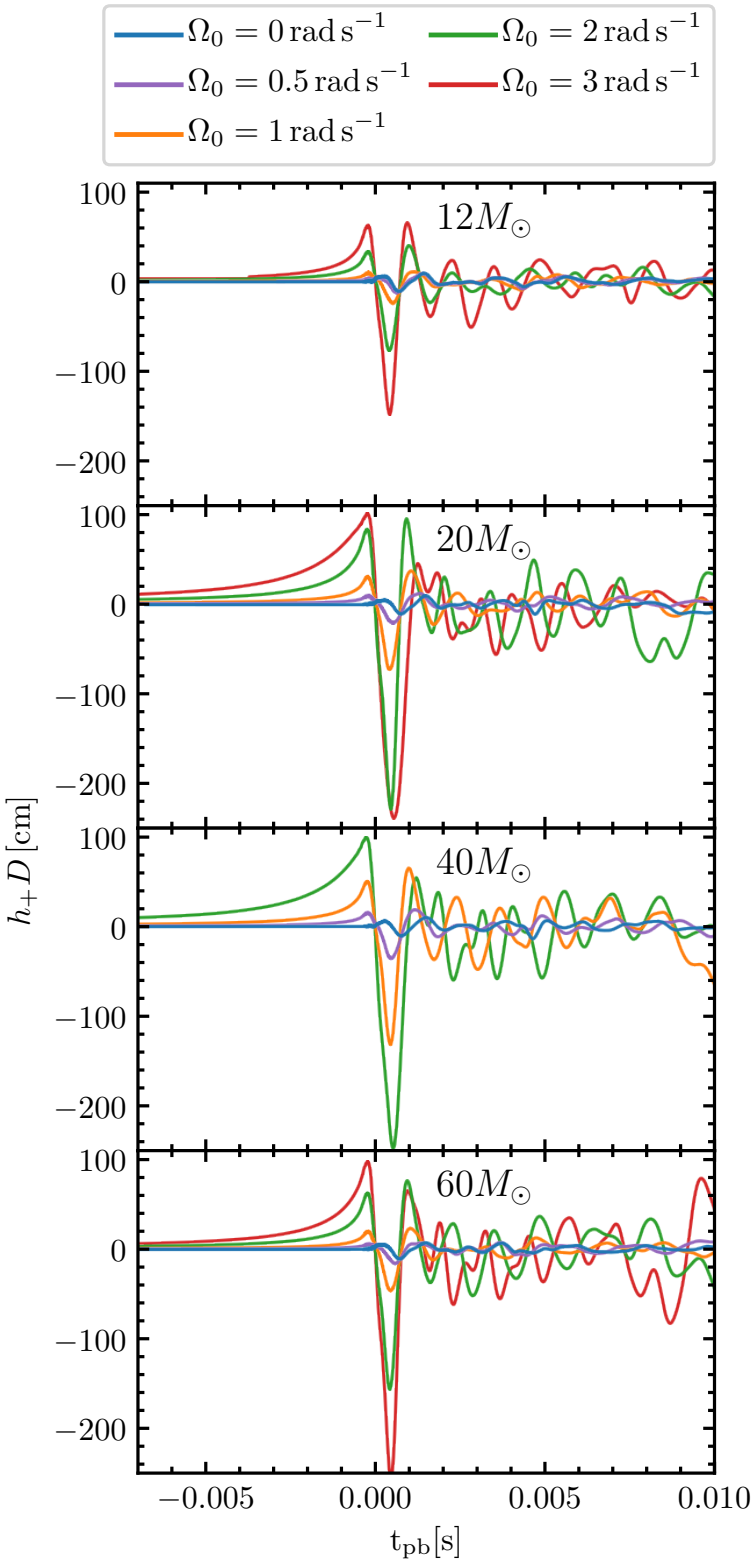

Figure 3.2: Bounce signals for all 2D CCSNe models with the SFHo EOS: models s12o[0-3], s20o[0-3], s40o[0-2], and s60o[0-3]. (Assumed distance of 10 kpc.)

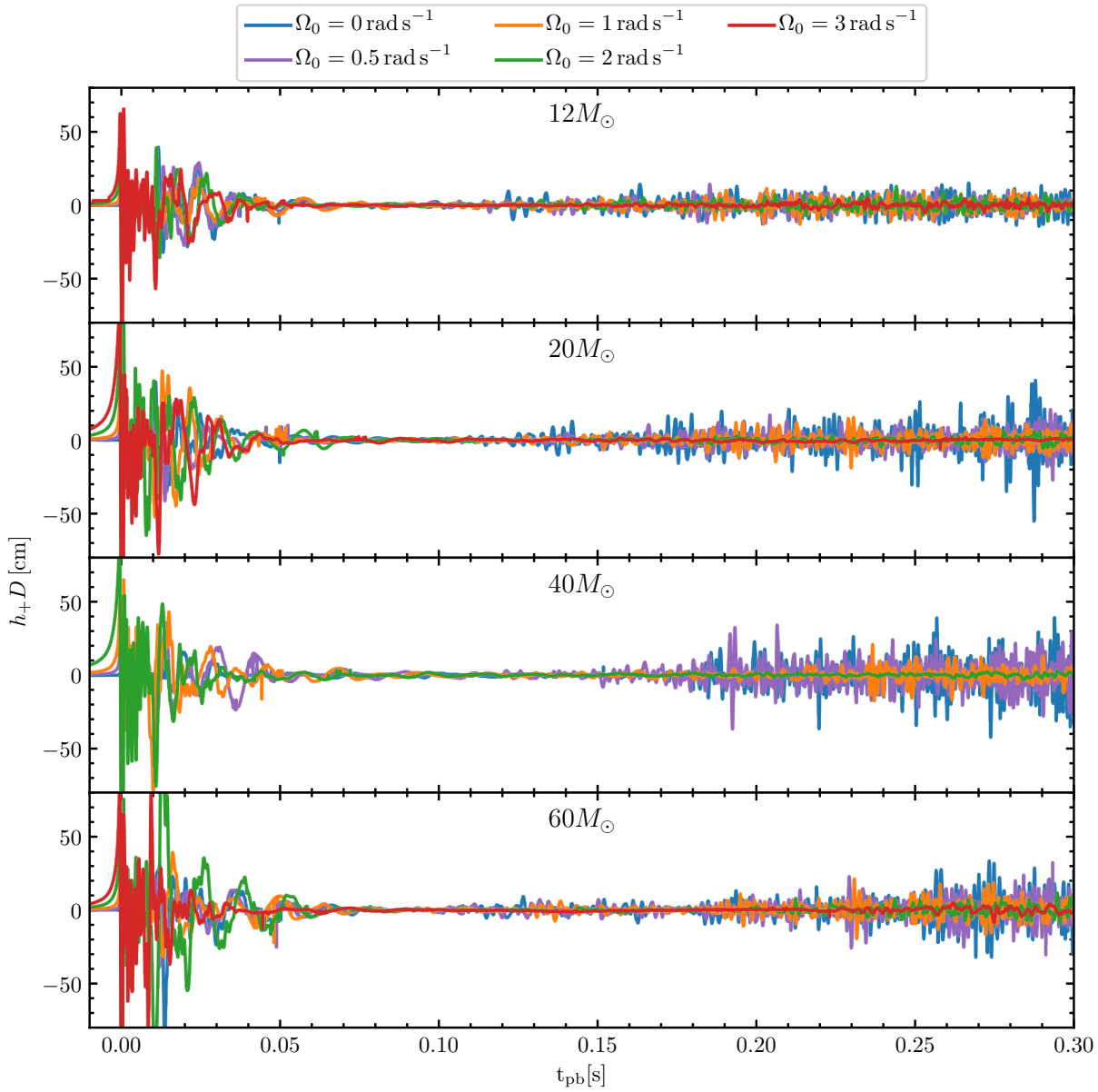

Figure 3.3: Time domain waveforms for all progenitors using the SFHo EOS: models s12o[0-3], s20o[0-3], s40o[0-2], and s60o[0-3]. (Assumed distance of 10 kpc.) Two universal trends seen across our parameter space is that the bounce amplitude increase and the accretion phase GW amplitude decrease, with increasing rotational velocity. In certain rotating cases, the presence of strong prompt convective activity also leads to high amplitude GWs 10s of ms after bounce.

findings that describe, except in these extreme cases, that increasing the angular momentum of the core will yield a larger bounce signal (Dimmelmeier et al., 2008). As this bounce signal is largely governed by the microphysics within the core, the GW bounce signal is predictable and well templated (Scheidegger et al., 2010b), provided a set of assumptions about the microphysics. As the PNS rings down from the energetic bounce, matter motions due to prompt convection contribute to the GW signal 10s of ms after bounce as well.

The accretion phase of the supernova—the hundreds of milliseconds when the PNS is accreting matter—marks the next time during the supernova when significant GWs are produced. During accretion, infalling stellar material and convection in the gain layer can excite oscillatory modes in the PNS. As a result, material at nuclear densities moves on time scales the order of milliseconds and can result in sustained GW emission. For all of our rotating progenitors, we observe this GW signal occurring between $\sim 100 - 300$ ms pb in Figure 3.3. In contrast to the bounce signal, these oscillatory modes are largely stochastic in nature and nearly impossible to template when viewed in the time domain.

Another interesting feature during the accretion phase, across all progenitors, is the decrease in amplitude of the GW signal with increasing rotation rate. As pointed out in previous work, this *rotational muting* is a direct consequence of the Solberg-Hoiland stability criterion, i.e., the stabilizing effect rotation can have in a convective fluid (Endal & Sofia, 1978; Pajkos et al., 2019). Simply put, in these 2D simulations, as rotation rate increases, convective activity slows in the post-shock region of the supernova. This slowed convection will interact less with the PNS—causing less pronounced oscillations—resulting in lower amplitude GWs. Of course, 3D rotational instabilities like the spiral mode of the SASI (Andresen et al., 2019), the low $T/|W|$ instability (Pan et al., 2020; Shibagaki et al., 2021) or magnetorotational instability (MRI) (Akiyama et al., 2003; Cerdá-Durán et al., 2007; Mösta et al., 2015) can create turbulent motion as well, re-exciting the motion of the PNS. Nevertheless, it is promising that rotational muting is still observed in our simulations with an increased fidelity in microphysics—namely, inelastic electron scattering and velocity dependence in the neutrino transport—compared to our previous works.

3.4.3 Connecting Angular Momentum and the Bounce Signal

We now move on to laying out a novel analysis method that will help constrain the rotational information of the supernova at the time of core bounce and mass distribution within the progenitor star at collapse. The first vital piece of information needed is the amplitude of the core-bounce GW signal from observations of a nearby CCSN.

It is well established that the source of the GW bounce signal is the dense supernova core, the region where the previous stellar iron core is forming into a PNS. For rotating CCSNe, the amplitude of this bounce signal is well studied and has been shown to correlate with the ratio of rotational kinetic energy to gravitational potential energy–commonly displayed as $\beta \equiv T/|W|$ (Dimmelmeier et al., 2008). While β can be used to measure the degree of rotation in a supernova, we choose the angular momentum instead, in aims to establish it as another key quantity, when quantifying rotation within a CCSN. Nevertheless, these quantities are related, as they are both metrics that encode information about the supernova rotation profile and mass distribution. For scale, the corresponding upper value in our simulation suite is $J^{\rm bounce}_{1.75M_\odot} \sim 2.8 \times 10^{49}$ erg s. The upper limit for the core of the CCSN is $\beta^{\rm bounce}_{\rm core} \sim 0.10$. Our definition of supernova core is outlined at the end of this subsection.

In Figure 3.4, we relate the amplitude of the bounce signal ($\Delta h_{\rm bounce}$) to the angular momentum of the inner 1.75 $M_\odot$ at bounce, by performing a third order polynomial fit to the 33 simulations using the M1 neutrino treatment and single nucleus approximation (SNA) e^- capture rates (Bruenn, 1985), or all models *except* $s12o2^{\nu}$, $s60o2^{\nu}$, and s40o[0-1]^{3D}. In this work, we define the $\Delta h_{\rm bounce}$ as the difference between the maximum and minimum of the strain within a 3 ms window of the bounce time—the time when the central entropy reaches 3 $k_{\rm B}$ baryon^{-1} and central density exceeds 2×10^{14} g cm^{-3}. Our mass cut of 1.75 $M_\odot$—instead of typical values $\sim 0.6\, M_\odot$ for inner cores—is chosen in anticipation of our analysis that will contain information about the accreted

matter, beyond the canonical PNS. A more detailed justification of this mass cut is discussed in Section 3.4.5.

We now move to outlining the two main features of Figure 3.4: the quadratic J regime and the extreme asymptotic J regime. To explain the quadratic J regime, when $J_{1.75M_\odot} \lesssim 2 \times 10^{49}$ erg s, we appeal to order of magnitude estimates of the bounce signal. As established in (Richers et al., 2017), the bounce signal can be approximated as $\Delta h \sim GMR^2\Omega^2/c^4D$ for a given PNS mass M, radius R, and rotation rate Ω. The angular momentum at the center of the supernova just after core bounce can be approximated as $J \sim MR^2\Omega$. This yields an expression for how Δh depends on J,

$$\Delta h \sim \frac{G}{c^4 DMR^2} J^2. \tag{3.6}$$

Thus, for typical M and R values of the supernova center ($\sim 0.55 M_\odot$ and $\sim$ 15 km in our simulations), one notes the quadratic behavior seen in Figure 3.4 for $J_{1.75M_\odot} \lesssim 2 \times 10^{49}$ erg s. Of course this scaling relation is constructed for the main source of GWs, the PNS, or inner ~ 0.6 $M_\odot$ of matter. Nevertheless, we find this quadratic behavior maps quite well to larger mass cuts, as seen in Figure 3.4.

For $J_{1.75M_\odot} \gtrsim 2 \times 10^{49}$ erg s, the supernova center enters the extreme asymptotic J regime. The supernova center now contains sufficient J to centrifugally support the collapse and causes the bounce signal to occur at lower densities. This effect in turn widens the bounce signal and prevents further growth of $\Delta h_{\rm bounce}$ (Fryer & Warren, 2004; Dimmelmeier et al., 2008).

Another interesting feature of Figure 3.4 is the independence of $\Delta h_{\rm bounce}$ with EOS, which corroborates previous works (Dimmelmeier et al., 2008; Richers et al., 2017). Denoted circles are simulations that use the SFHo EOS: s12o[0-3], s20o[0.5-3], s40o[0.5-2], and s60o[0.5-3]. Inverted triangles use the SFHx EOS: s12o[0.5,2,3]x, s20o[0.5-3]x, s40o0.5x, and s60o[0.5-3]x. Over this parameter space, both EOSs produce similar bounce amplitudes. While we have not exhausted the possible list of available EOSs, the fact that two distinctly different EOSs produce similar bounce signals is promising to apply an analysis of this type to future GW observations and highlights the supernova mass distribution as a contributing factor to determining the bounce amplitude.

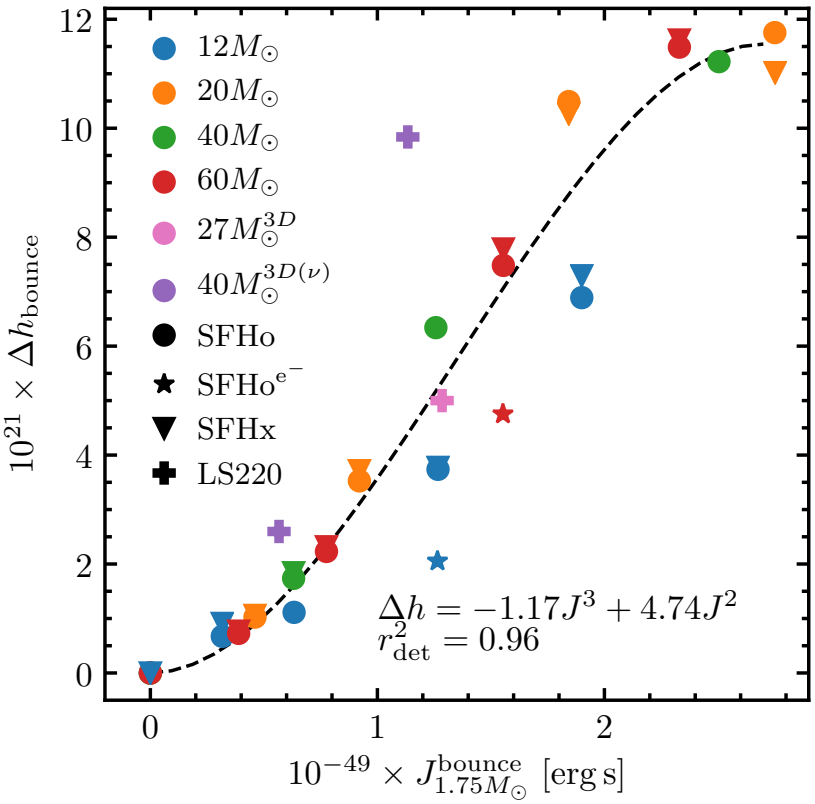

Figure 3.4: Bounce signal amplitude versus angular momentum of inner 1.75 $M_\odot$ for all models in our simulation suite. Overlaid is a third order polynomial fit to the 33 models using the M1 neutrino treatment and the SNA approximation (Bruenn, 1985) when calculating neutrino opacity tables. Colors represent different progenitor masses, whereas the different shapes correspond to the specified EOS listed by each black legend marker. This correlation is nearly EOS independent. Every shape uses the SNA approximation (Bruenn, 1985) when calculating neutrino opacity tables, with the exception of the stars (★). Stars (labeled SFHo$^{e^-}$) use LMP+N50 e^- capture rates which affect the deleptonization of the core during collapse, resulting in a lower amplitude bounce signal (Langanke & Martinez-Pinedo, 2001; Titus et al., 2018). Specifically, the two models that use the LMP+N50 e^- capture rates correspond to s12o2$^\nu$ and s60o2$^\nu$. Likewise, the difference in neutrino treatment used in the $40M_\odot^{3D(\nu)}$ models (s40o0.5^{3D} and s40o1^{3D}) causes deviation from the fit.

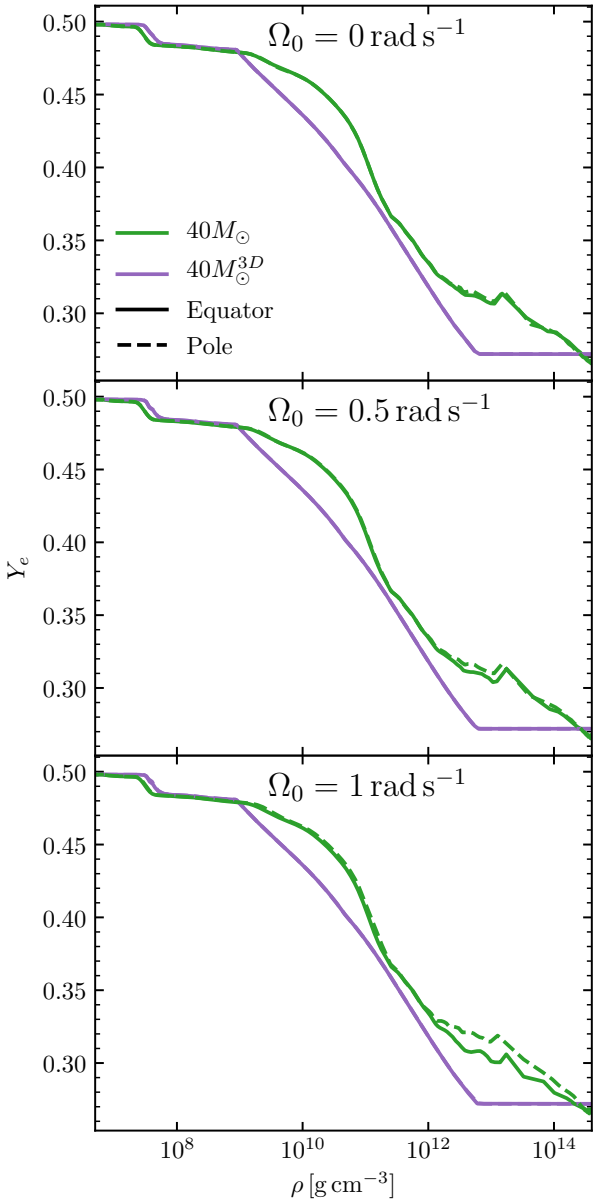

Figure 3.5: Electron fraction vs. density ($Y_e(\rho)$) profiles for model s40o[0-1] and s40o[0-1]^{3D}, which use M1 and parameterized deleptonization (Liebendörfer, 2005) on collapse, respectively. Due to the different treatments of deleptonization on collapse, both cases have extremely similar central Y_e (Y_e^c) values of ~ 0.27 yet produce differences in $\Delta h_{\mathrm{bounce}}$ of up to 4×10^{-21}. Because of this evidence, we caution against using Y_e^c as a predictor for $\Delta h_{\mathrm{bounce}}$. Rather, some metric involving the Y_e over the entire radius of the PNS would be preferred. Examining the s40o[0-1] models (green), we notice an angular dependence of the $Y_e(\rho)$ profiles (solid vs. dashed lines), particularly for $\Omega_0 = 1$ rad s^{-1}. This difference stems from the velocity dependence of the neutrino transport in the M1 scheme, which is affected by changes in the radial velocity field configuration, induced by rapid rotation. Furthermore, it provides evidence against the assumption that deleptonization on collapse is a spherically symmetric process, particularly in rapidly rotating progenitors.

For the 3D simulations, which all use the LS220 EOS, we notice good agreement with the 3D 27 $M_\odot$ case, s27o2^{3D}. However, for the rotating 40 $M_\odot$ simulations (s40o0.5^{3D} and s40o1^{3D}) we notice systematically higher bounce signals that deviate from the polynomial fit in Figure 3.4. This difference can be attributed to the neutrino treatments in each simulation suite. For all 2D and the 27 $M_\odot$ 3D cases, M1 neutrino transport is used beginning at collapse. This treatment gives accurate deleptonization behavior within the supernova center by the time of core bounce. Models s40o0.5^{3D} and s40o1^{3D}, by contrast, use parameterized deleptonization (Liebendörfer, 2005) up until the point of bounce. At densities above 10^9 g cm^{-3} these two schemes yield different electron fraction versus density, or $Y_e(\rho)$, profiles at the time of bounce. As explained in Richers et al. (2017), this effect in turn modifies the amplitude of the bounce signal.

Another piece of physics that impacts the bounce signal significantly are the electron capture rates. We perform two additional simulations with identical initial conditions to the 12 and 60 $M_\odot$ progenitors with $\Omega_0 = 2$ rad s^{-1} (s12o2$^{\nu}$ and s60o2$^{\nu}$), except for different neutrino opacity tables. The control case used for our 2D simulation suite creates the neutrino interaction library for the SFHo EOS using `NuLib` (O'Connor, 2015) and uses the SNA approximation (Bruenn, 1985). To test the effect of modified electron capture rates, we use the weak rate library of Laganke and Martinez-Pinedo (Langanke & Martinez-Pinedo, 2001) supplemented by the calculations of Titus et al. (2018). Between the two cases, we notice bounce signal amplitudes that differ by $\sim 40\%$. Similar to before, this difference in bounce signal is expected. As core collapse commences, electron captures onto nuclei play a significant role in removing pressure support from the iron core. Eventually, at the time of bounce, this will modify the $Y_e(\rho)$ profile, thereby affecting the core mass and resulting GW bounce signal (Richers et al., 2017). Because of this clear dependence of the GW bounce signal on electron capture rates, this work serves as valuable scientific motivation to reduce experimental error on these rates in high density nuclear matter, as they have an impact on our ability to constrain supernova progenitor information from GWs alone.

In many of the primary works that examine GWs from rotating CCSNe, correlations between inner core mass at bounce ($M^B_{\rm core}$) and central electron fraction ($Y^{\rm c}_e$) are treated as diagnostics for

the expected $\beta_{\rm core}^{\rm bounce}$ (and consequently $\Delta h_{\rm bounce}$). (Dimmelmeier et al., 2008; Scheidegger et al., 2010a; Abdikamalov et al., 2014; Richers et al., 2017). One dominant common factor between these works is the inclusion of parameterized deleptonization on collapse (Liebendörfer, 2005). In our work, over the range in values for $0 < \beta_{\rm core}^{\rm bounce} \lesssim 0.10$, we do not see significant changes in values of $M_{\rm core}^{B}$— changes less than a 0.1 $M_{\odot}$. Likewise, the common correlations of increasing $Y_e^{\rm c}$ with increasing $\Delta h_{\rm bounce}$ are not completely upheld with our data. As an example, refer to Figure 3.5. When comparing models s40o1 and s40o1^{3D}, the principle difference during collapse is the neutrino treatment: s40o1 uses velocity-dependent M1 neutrino transport, whereas s40o1^{3D} uses parameterized deleptonization. While both have extremely similar $Y_e^{\rm c}$ values, the $\Delta h_{\rm bounce}$ of s40o1 is only $\sim 60\%$ that of s40o1^{3D}. To explain this difference, we examine the $Y_e(\rho)$ profile at bounce. We observe that at densities greater than 10^{12} g cm^{-3} the difference in profiles can vary by as much as $\Delta Y_e \sim 0.02$ (around 6%), while still maintaining similar $Y_e^{\rm c}$. While we acknowledge the value in the 1D Boltzmann neutrino transport calculations involved in Liebendörfer (2005), we present evidence using our multidimensional velocity-dependent neutrino-radiation hydrodynamic simulations that the inclusion of rotation and multidimensional effects can cause this approximation to break down, and recommend caution for use in future rapidly rotating GW studies.

To define $M_{\rm core}^{B}$ in our work, we look at the magnitude of the velocity along the pole and equator. Where each radial profile has the steepest velocity gradient, we select corresponding points, as this marks the point where sonic contact breaks down. Lastly, we construct an ellipse using these corresponding radial points as the semimajor and semiminor axes. All mass within this ellipse we define as *in sonic contact* with the supernova center.

As a caveat, it is important to note that these bounce signals were calculated with an assumed distance of 10 kpc. In the event of an actual rotating CCSN event, we would rely on other means to constrain the distance. Of course, EM observations remain the gold standard. For a purely multimessenger approach, distance estimates using supernova neutrino measurements still lie on the horizon.

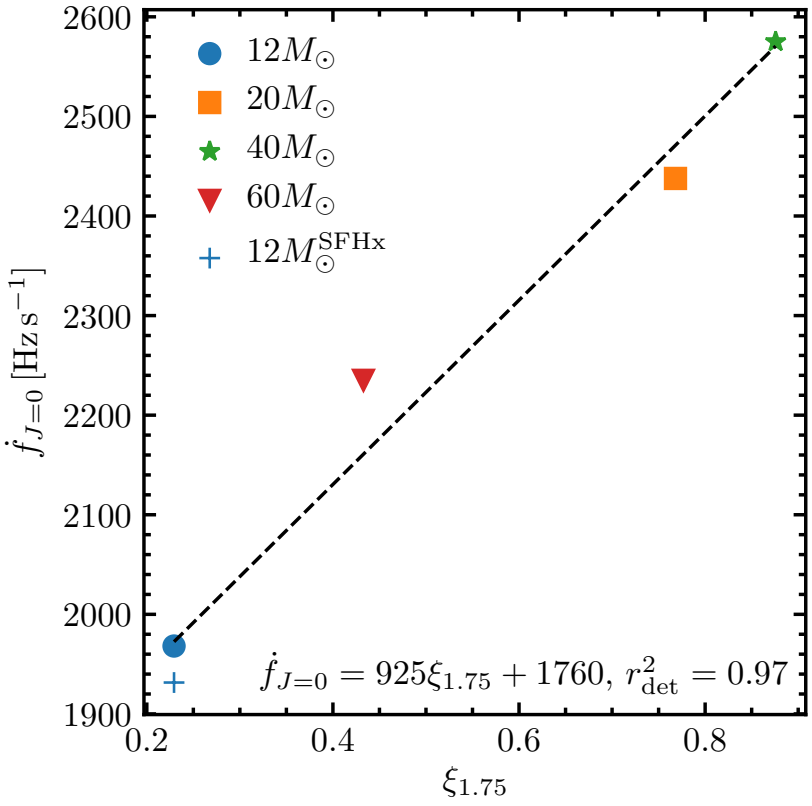

Figure 3.6: Slope of the PNS ramp-up in frequency vs. time space for nonrotating progenitors, as a function of $\xi_{1.75}$ at collapse. These models correspond to s12o0, s20o0, s40o0, s60o0, and s12o0x. More compact progenitor cores will yield higher mass accretion rates, leading to faster contraction of the PNS radius–in turn, steeper ramp-up slopes.

3.4.4 $\dot{f}$ versus Compactness

The next piece of information needed for this analysis requires us to connect a GW observable to the density profile of the supernova. Through a variety of 1D simulations, Warren et al. (2020) recently explored the GW signal a few seconds after bounce, displaying correlations between progenitor compactness at collapse and the slope of the GW frequency ramp-up ($\dot{f}$), in frequency versus time space. To calculate $\dot{f}$, we perform a linear regression to Equation (3.4) between 50 and 300 ms pb. We choose to begin tracking $f_{\rm peak}$ at 50 ms because this approximately marks the end of the post-bounce ring-down GW signal seen in Figure 3.3. Because we are using multidimensional simulations and use a different mass cut for ξ_M at collapse, we do not use the parametric fit

provided in Warren et al. (2020). Instead, we opt to create a unique linear fit for our 2D simulations. Nevertheless, we corroborate a linear relationship between $\dot{f}$ and ξ_M in 2D simulations. Figure 3.6 displays $\dot{f}$ versus $\xi_{1.75}$ at collapse, for the nonrotating simulations in our suite: specifically, models s12o0, s20o0, s40o0, s60o0, and s12o0x. When comparing the EOS dependence of ramp-up slopes for nonrotating progenitors, we note only a difference of $\sim 2\%$ between SFHo and SFHx.

Physically, this $\dot{f}$ and ξ_M relationship should be expected. At the onset of collapse, a higher compactness value corresponds to more mass closer to the stellar core. As the inner part of the resulting supernova will be more gravitationally bound, the mass accretion rate onto the PNS should be higher, compared to a lower ξ_M progenitor. With a higher mass accretion rate, the PNS should contract on shorter time scales. Thus, because the GW ramp-up is related to the PNS dynamical frequency (Camp & Cornish, 2004), faster PNS contraction will lead to a higher $\dot{f}$ value.

As a note, we acknowledge that empirically measuring $\dot{f}$ from the GW signal simulation outputs would be ideal. However, the frequency components for the $\Omega_0 = 2, 3$ rad s^{-1} simulations have extremely faint GW signals during the accretion phase, which would leave an unreliable fit. Physically, this weaker signal is a product of the *rotational muting* seen in rotating CCSN simulations (Pajkos et al., 2019). Because these simulations are axisymmetric, 3D effects such as the spiral mode of the SASI or low $T/|W|$ instabilities do not arise to re-excite the PNS oscillations (Andresen et al., 2019). In the 3D context, as in nature, these instabilities can arise in rotating cases, creating a detectable GW signal in conjunction with a flatter $\dot{f}$. The use of Equation (3.4) has been shown in previous works (eg., Müller et al., 2013; Pan et al., 2018) to reproduce the peak GW frequency quite well for nonrotating CCSNe. To test its effectiveness for rotating models, we show how it tracks the GW frequency output from our 2D simulations, in the next subsection.

The only model that does not use a semianalytic model, similar to Equation (3.4), to calculate $\dot{f}$ is model s40o1^{3D}. As noted in Pan et al. (2020), 40o1^{3D} displays the low T/W instability during the accretion phase. Accompanying the instability is a bar-mode-like configuration of the rotating PNS (Ott et al., 2005). Compared to the slight oblateness seen in our 2D rotating models, this bar mode deviates from spherical symmetry enough to create a lower fidelity prediction of the peak

GW frequency. Instead, we opt to empirically extract the peak GW frequencies to construct $\dot{f}$ for s40o1^{3D}. While other GW signals have been associated with non-axisymmetric instabilities—the emission of quasiperiodic GWs $\sim$ 100 Hz from the spiral SASI (Kuroda et al., 2014; Andresen et al., 2017) or transient approximate kilohertz signal from the low $T/|W|$ instability (Ott et al., 2005)—we note these signals do not interfere with the empirical calculation of $\dot{f}$ from the dominant oscillation mode produced by s40o1^{3D}. While we acknowledge $\dot{f}$ values between models s40o1 and s40o1^{3D} differ by $\sim$ 10%, we cannot conclude this difference in *non-normalized* ramp-up slope is due to the presence of the low T/W instability because of the difference in respective neutrino treatments (M1 and IDSA) and progenitor structure ((Woosley & Heger, 2007) and Sukhbold et al. (2016b)). For the reader interested in the exact details of the spectrogram for s40o1^{3D}, we direct them to Figure 9 of Pan et al. (2020).

3.4.5 Quantifying Rotational Flattening

While the correlation between $\dot{f}$ and ξ_M is indeed valuable, this relationship has only been shown for nonrotating cases thus far. As all stars rotate to some degree, we now generalize this relationship beyond simple nonrotating cases, granting the final piece needed for our new analysis method: extracting rotational information from the accretion phase signal.

During the accretion phase of a CCSN, the PNS is accreting mass while cooling via neutrino emission. These two factors cause the PNS to contract as the supernova evolves. Observationally, this cooling manifests itself in the ramp-up slope of the GW signal. Intuitively, a PNS with a smaller radius (or higher dynamical frequency) will oscillate at higher frequencies. Thus, as the PNS radius gradually decreases, its frequency of emission should gradually increase. However, if the PNS is rotating, it will receive centrifugal support during that cooling process. Not only is the PNS accreting matter, but angular momentum from the overlying stellar material. This accretion will *spin up* the PNS, allowing it to end with a larger radius, compared to the nonrotating case. With a larger radius (or smaller dynamical frequency), one expects the GW frequency to be lower. If one were to observe the GW evolution in the time-frequency domain, the rotating PNS would

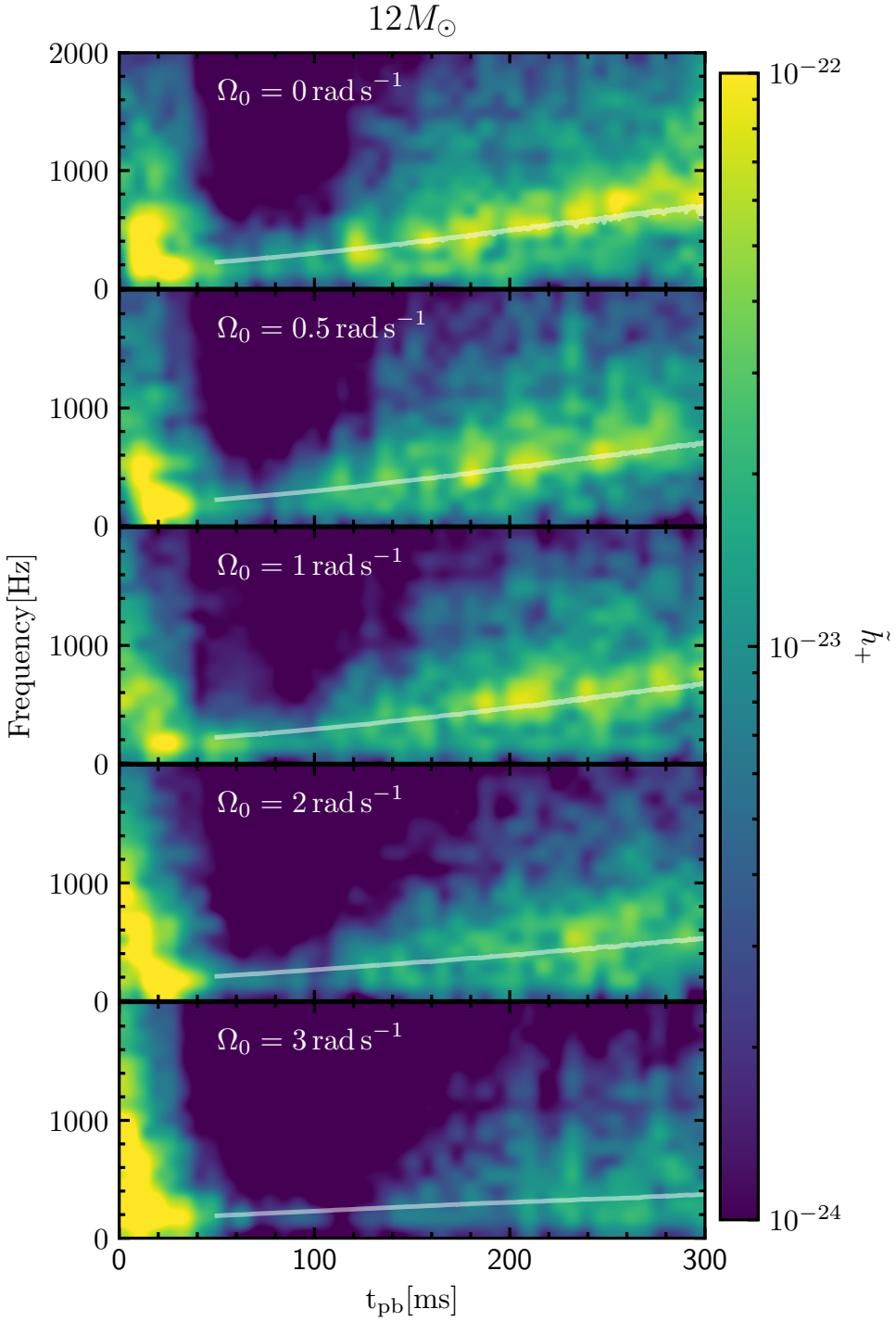

Figure 3.7: Spectrograms for the $12\,M_\odot$ progenitor at different rotational velocities: models s12o[0-3]. Overplotted in gray is the peak GW frequency of the PNS (Equation (3.4)), displaying the rotational flattening of the PNS, as the rotation rate increases. The colors correspond to values of $\tilde{h}_+$, the Fourier transform of the GW strain h_+.

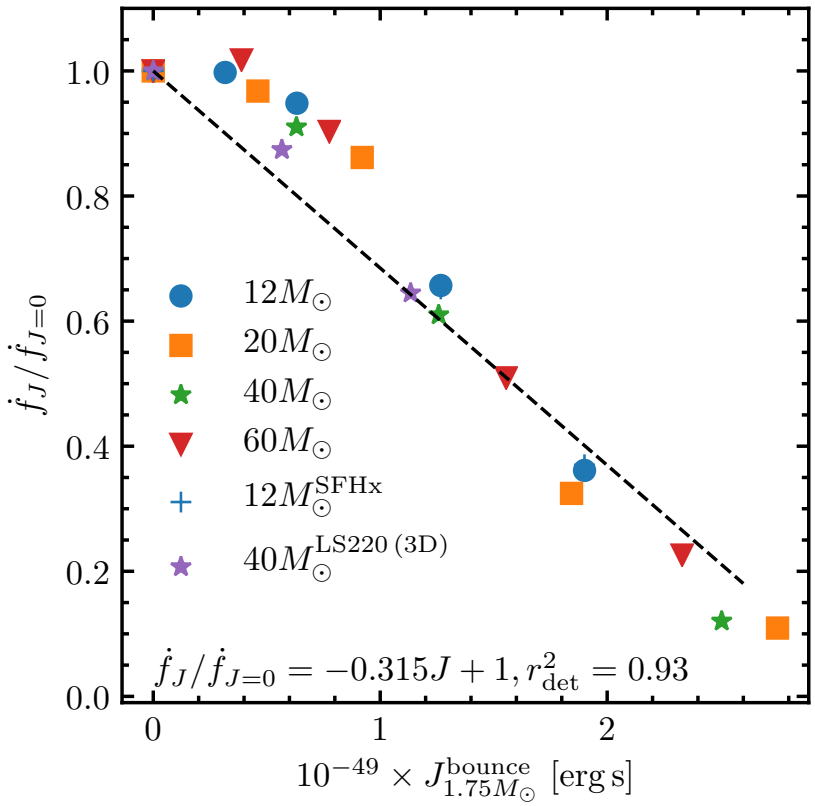

Figure 3.8: Linear correlation between how much the ramp-up slope is flattened vs. $J_{1.75M_\odot}$. We perform three additional simulations for the 12 $M_\odot$ progenitor using the SFHx EOS and see almost no EOS impact on the flattening effect. This fact indicates the pre-accretion angular momentum distribution is more important when quantifying flattening. In total, the models included in this figure are s12o[0-3], s20o[0-3], s40o[0-2], s60o[0-3], s12o[0,2,3]x, and s40o[0-1]^{3D}.

appear to have an $\dot{f}$ that is *flatter* (closer to 0) than the nonrotating case. Now we quantify this *rotational flattening* by examining the ramp-up slopes of different progenitors.

In Figure 3.7, we display spectrograms for the five 12 $M_\odot$ simulations for various rotation rates: models s12o[0-3]. Brighter hues correspond to greater contributions to the GW signal at a given frequency. Overlaid in gray is the $f_{\rm peak}$ produced by Equation (3.4). Indeed, with increasing rotation rate, $f_{\rm peak}$ evolves with a flatter slope. Figure 3.7 shows how tightly $f_{\rm peak}$ tracks the frequency evolution of the emitted GWs.

After calculating $\dot{f}$ for each simulation, we normalize by the respective nonrotating ramp-up slope. Interestingly, we find a tight correlation between how much the slopes are flattened over

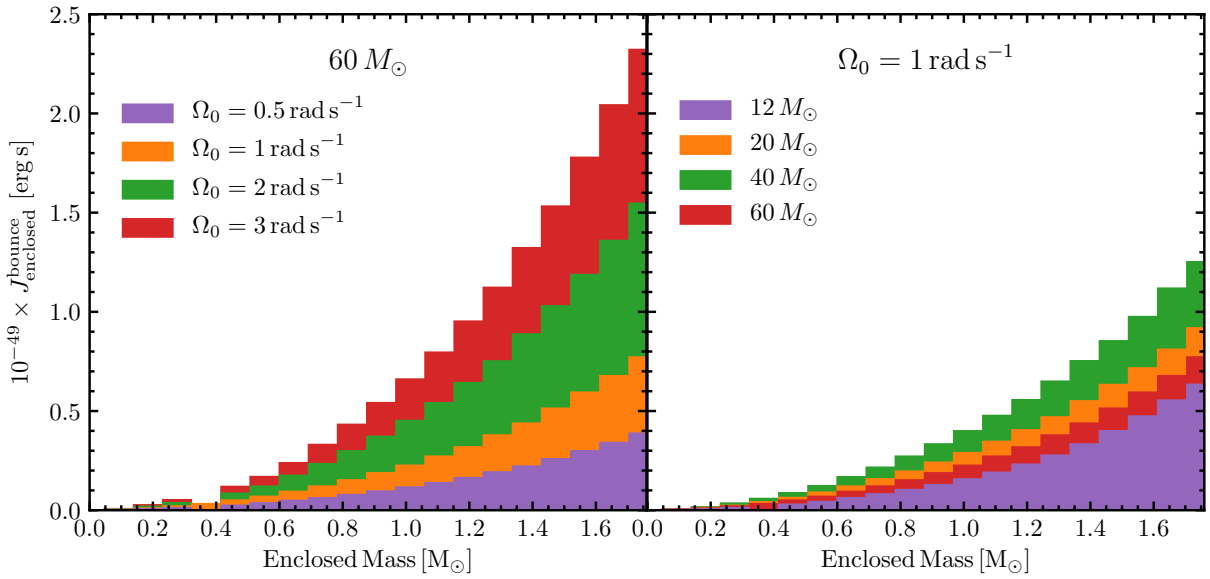

Figure 3.9: (Left) Enclosed angular momentum (J_{enclosed}) binned by mass coordinate (20 total bins) for the 60 $M_\odot$ progenitor at different rotation rates: models s60o0.5, s60o1, s60o2, and s60o3. As rotation rate increases, the J_{enclosed} profile becomes steeper. (Right) J_{enclosed} binned by mass coordinate (20 total bins) for all progenitor masses for Ω_0 = 1 rad s^{-1}: models s12o1, s20o1, s40o1, and s60o1. In this case, the J_{enclosed} profile becomes steeper with increasing compactness. This is expected as the differential rotation parameter A used in Equation (3.1) depends linearly on compactness. Thus, the more compact models begin with larger angular momentum values at collapse. (Both) In both cases, a steeper J_{enclosed} profile provides more angular momentum for the PNS to accrete after bounce—in turn, this provides more centrifugal support and a flatter $\dot{f}_J$.

time and the angular momentum of the inner 1.75 $M_\odot$ at bounce. Figure 3.8 displays this linear fit to the 19 2D SFHo runs. For comparison, we overlay the three 2D SFHx runs and three 3D LS220 runs. Specifically, the models included in this figure are s12o[0-3], s20o[0-3], s40o[0-2], s60o[0-3], s12o[0,2,3]x, and s40o[0-1]^{3D}. For the rapidly rotating 12 $M_\odot$ 2D SFHx runs, we notice very little EOS dependence on the normalized ramp-up slopes, as they nearly overlap with the corresponding SFHo runs. While in general these slopes are driven by the cooling of the PNS—a process heavily dependent on the EOS—we notice differences in non-normalized slopes of only $\sim$ 3% between SFHo and SFHx.

To explain the relationship seen in Figure 3.8 and justify our mass cut of 1.75 $M_\odot$, we appeal to Figure 3.9. Displayed in the left panel of Figure 3.9 is the enclosed angular momentum (J_{enclosed}) for the 60 $M_\odot$ progenitor, binned by a mass coordinate over 20 bins: specifically, models s60o0.5,

s60o1, s60o2, and s60o3. For increasing Ω_0 we note a steeper $J_{\rm enclosed}$ profile. In the right panel, we identically bin our data, but display $J_{\rm enclosed}$ for the four progenitor masses with $\Omega_0 = 1$ rad s^{-1}: specifically, models s12o1, s20o1, s40o1, and s60o1. In this case, the higher the progenitor compactness, the steeper $J_{\rm enclosed}$ profile. This behavior is expected because at collapse, the differential rotation parameter (A in Equation (3.1)) is assigned based on initial compactness (Pajkos et al., 2019). In general, with a larger differential rotation parameter (more solid body) we expect a steeper $J_{\rm enclosed}$ profile. In both panels of Figure 3.9, a significant amount of J is deposited in the outer layers of the rotating supernova at the time of core bounce. As mass is accreted, so too is J; this accretion will centrifugally support the contracting PNS. The effect on the physical observable is a flatter $\dot{f}$. With mass cuts less than 1.75 $M_\odot$, the tight linear relationship seen in Figure 3.8 breaks down because less information about the accreted J would be accounted for. While a slightly higher mass cut could have been chosen, our computational domain only contains $\sim$ 1.85 $M_\odot$ of material, and this slight difference does not produce a noticeable change in Figure 3.8. Moreover, depending on the progenitor, stellar material at that mass cut may not get accreted even hundreds of milliseconds after bounce. Hence, we justify a mass cut of 1.75 $M_\odot$. Of course, for future work, optimizing this mass cut on computational domains that contain more mass could refine this analysis.

One large uncertainty that can affect $\dot{f}$ is the influence of angular momentum transport within stellar interiors (Aerts et al., 2019), so it is important to highlight how it may modify the relationship seen in Figure 3.8. In our current simulation suite, J is advected along with the fluid. However, other influences that are not included in this work (such as magnetic fields) may change how J is displaced throughout the supernova evolution. In the event of stronger J transport, less J would be accreted onto the PNS. As such, the PNS would receive less centrifugal support, allowing it to cool to smaller radii. This effect would result in larger values of $\dot{f}$, even in the rapidly rotating cases. Physically, this would diminish the flattening effect seen in rotating simulations. Systematically, the points at large values of $J^{\rm bounce}_{1.75M_\odot}$ seen in Figure 3.8 would shift upwards.

Coefficient	Value	Standard Deviation	Units
α	-1.17	± 0.11	$10^{-168}(\mathrm{erg\,s})^{-3}$
β	4.74	± 0.27	$10^{-119}(\mathrm{erg\,s})^{-2}$
γ	-0.315	± 0.015	$10^{-49}(\mathrm{erg\,s})^{-1}$
δ	925	± 87	$\mathrm{Hz\,s^{-1}}$
ϵ	1760	± 50	$\mathrm{Hz\,s^{-1}}$

Table 3.2: Coefficients used to constrain progenitor core compactness.

3.4.6 Constraining the Stellar Core Mass Distribution

For clarity, we now outline the established three pieces of information from GWs emitted in a rotating CCSN. We have shown that the amplitude of the bounce signal (Δh) correlates with $J_{1.75M_\odot}$ at bounce. The ramp-up slope ($\dot{f}$) of the GW signal for nonrotating CCSNe relates to $\xi_{1.75}$. And using our new findings, we quantify how much this slope is flattened, depending on $J_{1.75M_\odot}$. We now synthesize these three points to place constraints on the mass distribution of the supernova progenitor. Note in this section, unadorned β refers to a polynomial fitting coefficient, whereas in previous sections, $\beta_{\mathrm{core}}^{\mathrm{bounce}}$ refers to the ratio of rotational kinetic energy to gravitational binding energy ($T/|W|$).

From examining the bounce signal, we have shown the relationship between core bounce and inner angular momentum as

$$\Delta h = \alpha J_{1.75M_\odot}^3 + \beta J_{1.75M_\odot}^2. \tag{3.7}$$

From the accretion phase, we know the angular momentum quantifies how much the GW signal is flattened

$$\dot{f}_J / \dot{f}_{J=0} = \gamma J_{1.75M_\odot} + 1. \tag{3.8}$$

Lastly, we link core structure and nonrotating ramp-up slope

$$\dot{f}_{J=0} = \delta \xi_{1.75} + \epsilon. \tag{3.9}$$

To begin, substitute Eqn. (3.9) into Eqn. (3.8) and solve for $J_{1.75M_\odot}$ to yield

$$J_{1.75M_\odot} = \frac{1}{\gamma}\left(\frac{\dot{f}_J}{\delta \xi_{1.75} + \epsilon} - 1\right). \tag{3.10}$$

Next, substitute Eqn. (3.10) into Eqn. (3.7) resulting in

$$\Delta h = \alpha \mathcal{J}^3 + \beta \mathcal{J}^2, \tag{3.11}$$

where $\mathcal{J}$ is represented by

$$\mathcal{J} = \frac{1}{\gamma}\left(\frac{\dot{f}_J}{\delta \xi_{1.75} + \epsilon} - 1\right)$$

and the coefficients of interest are located in Table 3.2. Equation (3.11) results in a cubic polynomial that has three unknowns: Δh, $\dot{f}_J$, and $\xi_{1.75}$. In the event of a rotating CCSN detection, the two most distinct parts of the signal—Δh and $\dot{f}_J$—can be directly obtained. Thus, $\xi_{1.75}$ can be solved for using a numerical root finder.

It is important to note that Equation (3.8), and the resulting analysis, solves for $\xi_{1.75}$ of a nonrotating progenitor. To apply this solution to a hypothetical rotating CCSN, one needs to assume the core mass distributions are the same between a rotating and nonrotating case.

In principle, this analysis solidifies how the fundamental rotational quantities Δh and $\dot{f}$ relate to $\xi_{1.75}$. In practice, however, we find the numerical inversion of Equation (3.11) poses convergence challenges with numerical root finders in certain regions of parameter space because of its highly nonlinear nature. In the next subsection, we describe how to streamline the analysis and remedy these convergence challenges.

3.4.7 Estimating Stellar Properties Based on Compactness

We begin inspecting the parameter space covered by Δh, $\dot{f}$, and $\xi_{1.75}$—visually represented in Figure 3.10. In an attempt to prevent overfitting, while appropriately modeling the data, we construct a planar fit between these three variables (red plane in Figure 3.10)

$$\xi_{1.75}^{\text{collapse}} = 0.146 \Delta h + 0.794 \dot{f} - 0.134, \tag{3.12}$$

where Δh is scaled by 10^{21} and $\dot{f}$ is in units of (kilohertz per seconds). We treat our 19 2D SFHo models as the *fit data* used to calculate the planar coefficients in Equation (3.12): models s12o[0-3], s12o[0-3], s40o[0-2], and s60o[0-3]. In an attempt to reduce bias from verifying our planar fit, we

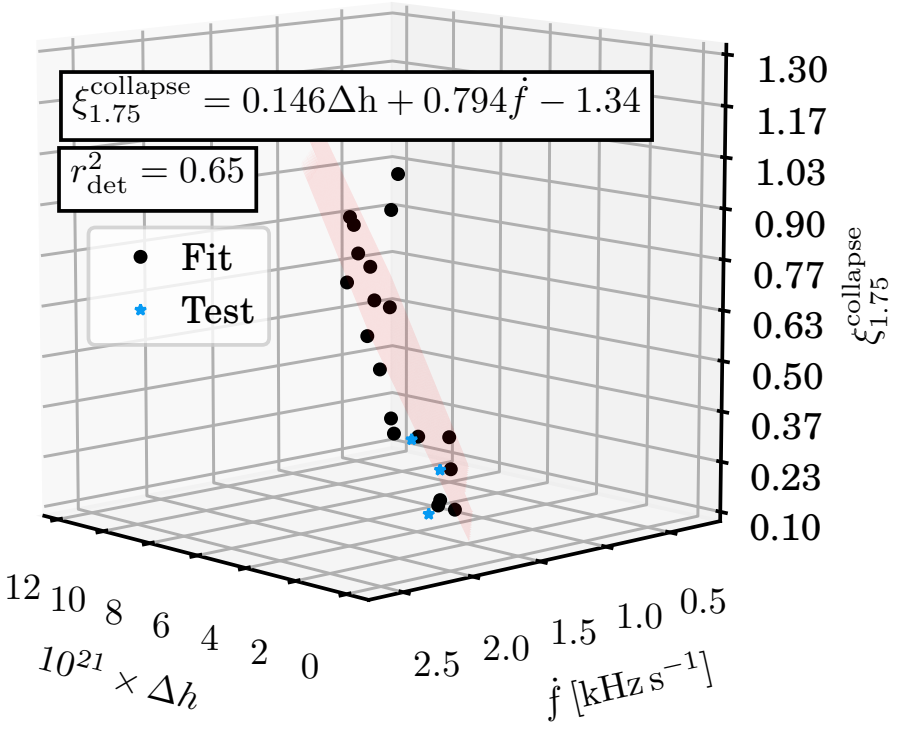

Figure 3.10: Three-dimensional planar fit to the bounce amplitude, ramp-up slope, and core compactness at collapse. Black dots denote data used to construct the planar fit (models s12o[0-3], s12o[0-3], s40o[0-2], and s60o[0-3]) or the fit data. Cyan stars represent the test data, namely, the three 12 $M_\odot$ simulations using the SFHx EOS (models s12o[0,2,3]x) and are not involved in the fitting process, to reduce bias when verifying the planar fit. The standard deviation errors of the fitting coefficients for the bounce, frequency, and vertical shift coefficients are σ_h = ±0.026, σ_f = ±0.150, and σ_s = ±0.35, respectively.

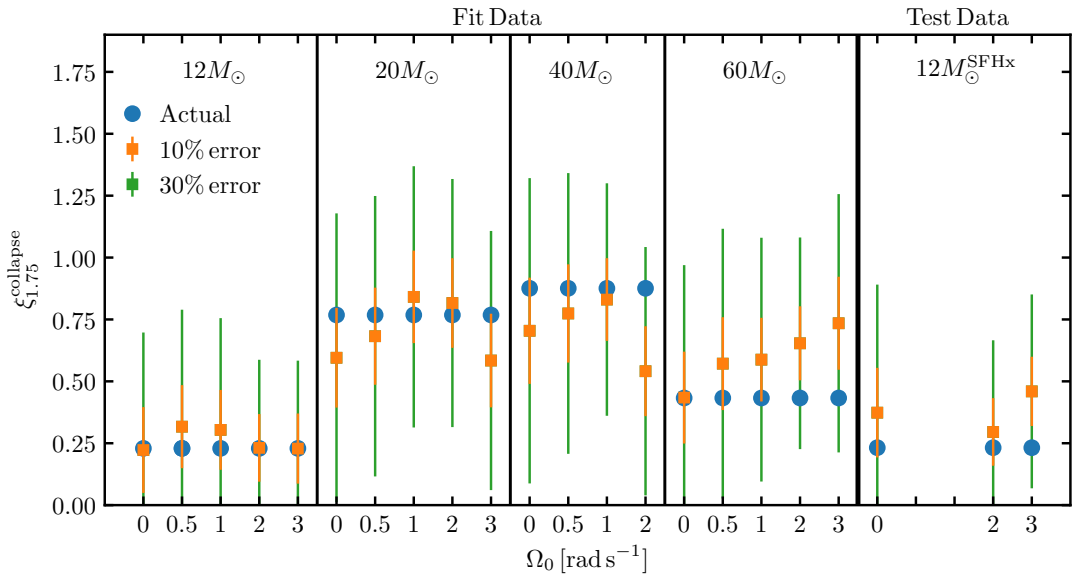

Figure 3.11: Input (actual) $\xi_{1.75}$ for progenitors at collapse compared against the estimated $\xi_{1.75}$ value using the planar fit, with identical Δh and $\dot{f}$ inputs. Orange (green) error bars represent one standard deviation of error assuming 10% (30%) uncertainty in the Δh and $\dot{f}$ measurement. Models included in the fit data are s12o[0-3], s12o[0-3], s40o[0-2], and s60o[0-3]. Models included in the test data are s12o[0,2,3]x.

withhold 3 2D SFHx simulations (models s12o[0,2,3]x) from the fitting process, and reserve them as our *test data* to test the reliability of Equation (3.12) for different EOSs.

Armed with Equation (3.12), we apply the previously used Δh and $\dot{f}$ values to yield estimated $\xi_{1.75}$ values. Figure 3.11 compares actual (blue dots) versus estimated (squares) $\xi_{1.75}$. Included with the estimated values are the error bars assuming a standard deviation of 10% (30%) of both the Δh and $\dot{f}$ measurements. Convolved with the error of each planar coefficient yields error bars displayed in orange (green) that correspond to the standard deviation of the estimated $\xi_{1.75}$. We note while the majority our test data and fit data are captured by the 10% error case, there are still outliers. Returning to Figure 3.10, one can observe the presence of data points that deviate from the planar fit. While a more complex fit could mitigate the error, this raises the risk of overfitting. Ideally, a larger number of simulations, spanning a finer resolution in parameter space would help estimate more accurate and statistically significant values for $\xi_{1.75}$. Acknowledging areas for future improvement, we note the exciting implications this relationship has.

The mass distribution within a supernova progenitor is still highly uncertain and extremely difficult to constrain with EM observations alone. The strength of this work is that it provides a framework to make the critical ξ_M measurement solely using GWs. This new analysis method now allows scientists to leverage various previous studies that have shown that ξ_M has a significant impact on properties of the explosion (O'Connor & Ott, 2011; Sukhbold et al., 2016b). For example, Sukhbold et al. (2016b) use a suite of simulations to connect $\xi_{2.5}$ to two physical observables: explosion energy and ^{56}Ni yield. Thus, as the needed GW signals for this analysis happen less then 0.5 s after core bounce, astronomers potentially can *predict* future explosion properties of the supernova—helping provide valuable input for EM follow-up. Furthermore, after the explosion has succeeded, making EM measurements of the explosion energy and ^{56}Ni mass provide a testable case that can either validate or refine the accuracy of this GW prediction.

3.4.8 Observability of GW Signal

When discussing possible GW signals from rotating CCSNe, it is important to anticipate the likelihood of observation. Current GW detectors are limited to Galactic core-collapse events–an estimated rate of ~ 2 per century (Diehl et al., 2006). Convolved with the estimate that only 1% of massive stars can reach the rapid rotation regime, this estimate drops to a rapidly rotating, Galactic CCSN rate of 2 every 10,000 yr. Nevertheless, due to the poorly understood influence of binarity and magnetic braking, this estimate could be higher (Woosley & Heger, 2006; de Mink et al., 2013). Likewise, the possible GW signals from so-called *failed supernovae* also potentially can act as sources of detectable GWs (Fryer & New, 2003). Another key consideration are the effects of viewing angle. As outlined in Oohara et al. (1997), the relative orientation between the CCSN and observer impacts the amplitude of the GW signal measured. As such, the $\dot{f}$ measurement should be unaffected. By contrast, the measured Δh for this analysis is completely degenerate with detector orientation. In all likelihood, the equator of an arbitrarily oriented CCSN will be off axis with GW detectors. This viewing angle effect would yield a smaller amplitude detected for Δh. Hence, in the conservative case where no orientation information can be gathered, a given Δh would serve as

a lower limit for the $\xi_{1.75}$ estimate.

An alternative to help constrain CCSN orientation is the use of neutrinos. For a rotating CCSN, depending on the degree of differential rotation, the shape of the neutrinosphere can become deformed, namely, oblate (Kotake et al., 2003a). The resulting nonspherical emission of neutrinos in principle contains information about the supernova orientation. More recently, Nagakura et al. (2021) more concretely noted the angular variations in the event rate and—more modestly—in the time-integrated signal. While research into the dependence of neutrino emission based on viewing angle is still ongoing, its continued progress and recent advances stand as a promising sign to one day help constrain CCSN properties purely using multimessenger methods.

In the rotating core-collapse scenario, there are two main sources of detectable GWs that occur at different times. The first is the core-bounce signal, which occurs immediately after core bounce. The second is during the accretion phase of the supernova. As seen in Figure 3.7, these fundamental modes of the PNS can last hundreds of milliseconds and display an increase in frequency as the PNS cools. Likewise, in some cases, rotational instabilities can induce GW production with similar amplitudes to the bounce signal, when viewed along the axis of rotation (Scheidegger et al., 2010a; Kuroda et al., 2014).

In order for a GW observatory to successfully *detect* a GW event, two factors must be considered: detector sensitivity and signal reconstruction (Abbott et al., 2016a). Detector sensitivity limits the frequency range of potential GW signals as well as GW strengths, due to signal-to-noise (S/N) constraints. Signal reconstruction is the act of separating the GW signal from the detector noise and is highly sensitive to S/N constraints as well (McIver, 2015). Thus, even though a given CCSN may emit multiple GW modes at a variety of frequencies, it is likely only the dominant features of the GW signal will be reconstructed.

These observational considerations lie at the heart of this project. Whereas other works are limited to progenitors of a certain compactness or depend on observing multiple oscillatory modes of the PNS, ours depends only on the dominant bounce signal as well as the main ramp-up of the PNS. In extreme cases, although rare, the amplitude of the bounce signal from rotating CCSNe can

be nearly an order of magnitude larger than the GWs from PNS oscillations, as seen in Figure 3.3. This effect can push the detection volume out by a corresponding order of magnitude because the GW amplitude scales as the inverse of the distance to the source.

3.5 Summary and Conclusion

We present a new method to constrain supernova progenitor compactness at collapse by using information from two parts of the GW signal: the core bounce and slope of the early ramp-up. Our findings are summarized as follows.

- We highlight the importance of robust treatments of deleptonization (eg., M1) on collapse, as it impacts the magnitude and directional dependence of the $Y_e(\rho)$ profile of the CCSN core and consequently $\Delta h_{\rm bounce}$, seen in Figure 3.5.

- We build upon the findings of Warren et al. (2020) by corroborating that the slope of the early ramp-up of nonrotating CCSNe correlates with compactness of the inner 1.75 $M_\odot$ in 2D simulations, seen in Figure 3.6.

- We relate the amplitude of the bounce signal to the angular momentum of the inner 1.75 $M_\odot$, seen in Figure 3.4.

- We quantify the dependence of PNS ramp-up slope on the angular momentum of the inner 1.75 $M_\odot$ at bounce, seen in Figure 3.8.

- We combine the two parts of a given rotating CCSN GW signal—bounce and main ramp-up slope—to constrain progenitor core structure by estimating $\xi_{1.75}$, seen in Figure 3.10.

- For a rotating CCSN, these two parts of the GW signal are the most likely to be detected and reconstructed by current GW detectors.

- Because the GW signal used is emitted $\lesssim$ 0.5 s after core bounce, we provide astronomers predictive power for EM emission, leveraging other works making EM correlations with ξ_M.

While we have introduced a new method that uses GWs to constrain supernova properties and potentially predict their behavior, it is important to outline the limitations of this work. The majority of this work was completed using axisymmetric simulations. While previous works have used axisymmetry to predict bounce signals for a variety of rotational configurations (Abdikamalov et al., 2014), 3D simulations remain the gold standard. Later in the supernova, for the GW signal during the accretion phase, certain instabilities may arise—low $T/|W|$ or spiral SASI—that are inherently three dimensional. Nevertheless, including four 3D models does corroborate the relationships between J, $\dot{f}$, and Δh noted in this work. We also do not include magnetic fields. Two instabilities that may arise when including magnetic fields are the $\alpha-\Omega$ dynamo (Mösta et al., 2015) and MRI (Akiyama et al., 2003). While the impact of the $\alpha-\Omega$ dynamo and the MRI on dynamically relevant timescales is uncertain, these instabilities may drive convection in the post-shock region shortly after core bounce (Bonanno et al., 2005; Cerdá-Durán et al., 2007). Our simulations also use the GREP, neglecting full GR. While the GREP could affect $\dot{f}$ by overestimating the peak GW frequency when compared to GR, it has been shown to produce GW amplitudes of similar scale and similar PNS compactness (Müller et al., 2013). In principle, this could affect the correlations presented in this work. Likewise, exploring a wider range of EOSs could help isolate the slight EOS dependence of $\dot{f}$.

This work also provides scientific motivation to continue research into electron capture rates onto heavy nuclei. As noted in Section 3.4.3, we observed differences in Δh at bounce up to 40% for identical rotation profiles with differing electron capture rates. As Δh at bounce is a fundamental parameter in determining $\xi_{1.75}$, more accurate rate measurements will allow astronomers to better constrain progenitor core compactness for a future Galactic CCSN.

We emphasize that this paper takes an empirical approach to finding these correlations. We do not rely on assuming functional forms for quantities such as the moment of inertia at the center of the supernova. This feature is advantageous for future GW observations of rotating CCSNe because it allows us to probe the mass distribution within a progenitor without deciding a priori how the mass may be distributed.

We acknowledge the robustness of these fits can be increased by including more 3D simulations with higher fidelity treatments of gravity and magnetic fields. Nevertheless, the focus of this work is to show that the accretion phase signal indeed contains information about the structure of CCSN progenitors. By quantifying this information and combining it with rotational information encoded in the bounce signal, astronomers take one step closer toward determining the physical conditions that set the stage for the onset of stellar explosions.

We thank the anonymous referee for their constructive feedback. We thank Sheldon Wasik for helping us access the modified electron capture rates and Brandon Barker for assisting with the statistical analysis. M.A.P. was supported by a Michigan State University Distinguished Fellowship. M.L.W. is supported by an NSF Astronomy and Astrophysics Postdoctoral Fellowship under award AST-1801844. S.M.C. is supported by the U.S. Department of Energy, Office of Science, Office of Nuclear Physics, Early Career Research Program under Award Number DE-SC0015904. This material is based upon work supported by the U.S. Department of Energy, Office of Science, Office of Advanced Scientific Computing Research and Office of Nuclear Physics, Scientific Discovery through Advanced Computing (SciDAC) program under Award Number DE- SC0017955. This research was supported by the Exascale Computing Project (17-SC-20-SC), a collaborative effort of two U.S. Department of Energy organizations (Office of Science and the National Nuclear Security Administration) that are responsible for the planning and preparation of a capable exascale ecosystem, including software, applications, hardware, advanced system engineering, and early testbed platforms, in support of the nation's exascale computing imperative. E.O.C. is supported by the Swedish Research Council (Project No. 2018-04575). K.C.P. is supported by the Ministry of Science and Technology of Taiwan through grants MOST 107-2112-M-007-032-MY3. The software used in this work was in part developed by the DOE NNSA-ASC OASCR Flash Center at the University of Chicago.

Software used in this work: FLASH (see footnote 7) (Fryxell et al., 2000, 2010), Matplotlib[8]

[8] https://matplotlib.org/

(Hunter, 2007), NuLib[9] (O'Connor, 2015), NumPy[10] (van der Walt et al., 2011), SciPy[11] (Jones et al., 2001–)

[9] http://www.nulib.org
[10] http://www.numpy.org/
[11] https://www.scipy.org/

CHAPTER 4

TECHNIQUES TO IDENTIFY THE DIRECTIONAL DEPENDENCE OF GRAVITATIONAL WAVE EMISSION FROM ASTROPHYSICAL EVENTS

This section reviews unpublished work conducted by undergraduate research assistant Steven VanCamp: M.A. Pajkos, S. VanCamp, S. Couch, in prep.

4.1 Abstract

We analyze the directional dependence of the gravitational wave (GW) emission from eight 3D neutrino radiation hydrodynamic simulations of core-collapse supernovae. We develop a new analytic technique to characterize the distribution of GW emission over all angles. By applying this new technique throughout the supernova duration, a distribution of preferred directions of GW emission is constructed. Our findings indicate CCSNe do not have a single 'optimal' viewing angle along which the strongest GWs can be detected. For nonrotating cases, this dominant viewing angle drifts isotropically throughout the supernova. For rotating cases, the strongest early time GW signal is observed along the equator. During the accretion phase, comparable—if not stronger—GW amplitudes are generated along the axis of rotation. Moreover, rotating CCSNe have a preferred direction of GW generation that precesses around the axis of rotation for both polarization modes. We do not notice any impact of instabilities such as the standing accretion shock instability or the lepton-number emission self-sustained asymmetry on the direction of emission for GWs, but note a possible influence from the low T/W instability.

4.2 Introduction

The end of massive stellar evolution is marked by a core-collapse supernova (CCSN). These stellar explosions, and in some cases implosions, are dynamic events influenced from a variety of physical processes, from neutrino emission, to hydrodynamic turbulence, to magnetically driven jet structures. Moments after the supernova is launched, the birth of a compact object called the protoneutron star (PNS) occurs, which will ultimately cool to a neutron star or—with sufficient

mass accretion—will collapse to a black hole. The PNS contains the neutron rich remnants of the once-stellar iron core and is characterized by nuclear matter at densities $\sim 2 \times 10^{14}$ g cm^{-3}. As turbulent downflows interact with the PNS surface and convection within the PNS develops, the PNS can oscillate, generating gravitational waves (GWs) (Sotani & Takiwaki, 2016).

These oscillations can exhibit different 'modes' which correspond to unique frequencies of emission, based on the restoring force driving the PNS. Some examples include g-modes driven by gravity, p-modes driven by pressure, r-modes driven by rotation, and w-modes driven by oscillations in spacetime. As each mode has a unique restoring force, encoded in the GW observables are different characteristics, such as the average density of the PNS (g-modes) or degree of rotation (r-modes) (Unno et al., 1989).

Beyond PNS oscillations, other sources of GWs within CCSNe include the 'bounce signal' from a deformed rotating PNS (Dimmelmeier et al., 2008), hydrodynamic turbulence (Pajkos et al., 2019), asymmetric emission of neutrinos (Vartanyan & Burrows, 2020), compact object ejection (Burrows & Hayes, 1996), and GWs from fluid instabilities like the standing accretion shock instability (SASI) (Andresen et al., 2019), or the low T/W instability (Shibagaki et al., 2020). While generating predicted waveforms for CCSNe can be valuable for improving detectability of the next Galactic event, connecting characteristics of the signals to internal source physics is vital. Each of these sources also encodes physical characteristics of the supernova center, a region previously unobservable from electromagnetic (EM) radiation. GWs from fluid instabilities provide information regarding the strength of convection and the timescale on which it occurs (Andresen et al., 2017; Takiwaki et al., 2016; Radice et al., 2019). Neutrino sources provide the degree of asymmetric neutrino production (and to some extent mass accretion) (Vartanyan & Burrows, 2020). The bounce signal is directly related to the rotational content of the PNS just after core bounce (Dimmelmeier et al., 2008). Furthermore, GWs from CCSNe depend on the hot nuclear EOS (Pan et al., 2018).

With various physical insights from CCSN gravitational radiation, considering these signals in the context of observability is important to distinguish between signal features that are interesting

and signal features that are detectable, therefore more valuable. One often considered factor is the GW amplitude, or the GW strain, commonly denoted h. Depending on the specifications of the GW observatory, detectors have certain sensitivities, or a minimum threshold below which GW amplitudes fall below the noise floor. Supernova models often produce time domain waveforms (TDWFs) to observe the predicted GW amplitudes over time for a supernova event.

The frequency content of the signal is equally as valuable. GW detectors have limiting factors that constrain the frequency range of observable signals. For example, for the Laser Interferometer Gravitational-wave Observatory (LIGO), shot noise imparted by the individual laser photons on the test mass limit the upper limit of the frequency range $\sim$ 1 kHz. By contrast, seismic noise establishes the lower limit of the frequency range $\sim$ 1 Hz (Aasi et al., 2013). One common tool for determining the frequency content of the CCSN GW signal includes spectrograms, that display the frequency contributions to the signal as time evolves. Characteristic strain plots are another method that displays the frequency distribution of the signal summed over a given time interval. Characteristic strain plots are often used to compare cumulative GW frequency content to GW detector sensitivity curves (Moore et al., 2015).

Directly measuring the polarization of the GW signal is an ongoing area of research. According to Einstein's theory of general relativity (GR), GWs exhibit two polarization states: plus (h_+) and cross ($h_\times$) modes. These states can serve as a set of bases, a linear combination of which can describe any GW signal; as a parallel with EM radiation, GWs too can be circularly or elliptically polarized. In principle, arrays of GW detectors at different orientations can be used to detect GW polarization, however, current detector sensitivities have difficulty discerning GW polarization from sources such as black hole mergers (Gair et al., 2013). One tool that has emerged to predict polarization from numerical models includes 'pologrames', which describe the relative strength between the h_+ and $h_\times$ modes.

With the first direct detection of GWs only occurring within the last decade, observational considerations of GW predictions from CCSN models remain a growing field. Hayama et al. (2016) connect the circular polarization of GWs with rotation near the center of the supernova. Hayama

et al. (2018) conclude the circular polarization from nonrotating CCSNe can encode information regarding the SASI and PNS g-mode oscillations. Chan & Hayama (2021) quantify the degree of circular polarization through quantities such as Stoke's Parameter, within existing GW detection pipelines, such as Coherent WaveBurst (cWB) (Klimenko et al., 2021). Beyond polarization, Vartanyan & Burrows (2020) investigate the directional dependence of GW emission generated directly from asymmetric neutrino emission. With increased access to computing resource capable of performing fully 3D CCSN simulations, pursuing additional investigations that explore the angular dependence of GW emission from CCSNe has become a timely area of research. These studies provide important implications for the future of GW observations; identifying viewing angles, if present, of dominant GW emission would help inform future population studies of GW sources to the GW background. Likewise, understanding the emergence of a preferred direction of GW emission—if any—during the presence of certain instabilities within CCSNe could refine predictions regarding their likelihood of detection.

To fill the need to address observational considerations, we present a new method to understanding *the directionality* of GW emission from CCSNe, which can be extended to any arbitrary GW source as well. We determine a preferred direction of GW emission during CCSNe particularly for rotating cases. We do not observe any preferred directions with the SASI or LESA instabilities, but possible correlations with the presence of the low T/W instability.

This paper is organized as follows: in Section 4.3 we review the methods used to setup our simulations and perform our analysis. In Section 4.4.1 we review current techniques used to analyze GW signals. Section 4.4.2 introduces a novel visualization method to investigate the directional dependence of the GW emission at a given instance in time. Section 4.4.3 uses this method to track the time evolution of the directionality of GWs. Section 4.5.1 discusses the physical implications generating the directional dependence. Section 4.5.2 discusses future benefits for observability. Finally, in Section 5.7.2 we summarize.

4.3 Methods

4.3.1 Numerical Models

This work examines eight 3D neutrino radiation hydrodynamic simulations of CCSNe. The first set of five models are referred to as the 'mesa' set, which are nonrotating 20 $M_\odot$ progenitors used in O'Connor & Couch (2018a). They make use of the SFHo EOS (Hempel et al., 2012; Steiner et al., 2013a), M1 neutrino transport (O'Connor & Couch, 2018b), and are evolved for ~ 0.5 sec post bounce (pb). Three additional simulations, one nonrotating and two rotating, are analyzed of a 40 $M_\odot$ model from Pan et al. (2021). These use the LS220 EOS (Lattimer & Swesty, 1991), and the isotropic diffusion source approximation (IDSA) for neutrino transport (Liebendörfer et al., 2009). All eight models are completed with the FLASH multiphysics code (Dubey et al., 2009; Fryxell et al., 2010). Likewise they use the Newtonian multipole solver from Couch et al. (2013), supplemented by the general relativistic effective potential (GREP) proposed by Marek et al. (2006).

4.3.2 Gravitational Wave Analysis

As the gravitational treatments used in these models do not formally evolve a spacetime metric, the GW generation must be calculated during a post processing step. We make use of the generic quadrupole formulae presented in Oohara et al. (1997)

$$h_+ = \frac{G}{c^4 D}\left(\ddot{Q}_{\theta\theta} - \ddot{Q}_{\phi\phi}\right), \tag{4.1}$$

and

$$h_\times = \frac{2G}{c^4 D}\ddot{Q}_{\theta\phi}, \tag{4.2}$$

where $\ddot{Q}_{ij}$ represents the second time derivative of the mass quadrupole moment in an orthonormal basis, D is the distance to the source, G is Newton's gravitational constant, and c is the speed of light. For all calculations of h_+ and $h_\times$, we assume a fiducial distance of $D = 10$ kpc. Expanding

the angular Q values in terms of Cartesian components yields

$$Q_{\theta\theta} = \Big(Q_{xx}\cos^2\phi + Q_{yy}\sin^2\phi + Q_{xy}\sin 2\phi\Big)\cos^2\theta + Q_{zz}\sin^2\theta - \Big(Q_{xz}\cos\phi + Q_{yz}\sin\phi\Big)\sin 2\theta, \tag{4.3}$$

$$Q_{\phi\phi} = Q_{xx}\sin^2\phi + Q_{yy}\cos^2\phi - Q_{xy}\sin 2\phi, \tag{4.4}$$

and

$$Q_{\theta\phi} = \Big(Q_{yy} - Q_{xx}\Big)\cos\theta\sin\phi\cos\phi + Q_{xy}\cos\theta\cos 2\phi + Q_{xz}\sin\theta\sin\phi - Q_{yz}\sin\theta\cos\phi. \tag{4.5}$$

In practice, simulation data tracks each of the $\dot{Q}_{ii}$ components through numerical integration (Finn & Evans, 1990), and a finite difference in time is performed to construct $\ddot{Q}_{ii}$. These values are then applied to all altitudinal angles of $0 < \theta \leq \pi$ and azimuthal angles $0 < \phi \leq 2\pi$ to construct the surface plots outlined in Section 4.4.2.

4.4 Visualizing Gravitational Wave Emission

In this section, we begin with existing methods quantifying GW data, and sequentially generalize these techniques to eventually consider GW directionality. All visualizations in this work make use of the nonrotating ($\Omega_0 = 0$ rad s^{-1}), slow rotating ($\Omega_0 = 0.5$ rad s^{-1}), and fast rotating ($\Omega_0 = 1$ rad s^{-1}), 40 $M_\odot$ progenitor; Ω_0 refers to the central angular velocity of the model. Details regarding the full rotation profile can be found within Pan et al. (2018).

4.4.1 Time Domain Waveforms

We begin with TDWF from the 40 $M_\odot$ models at all three rotation rates. Figure 4.1 displays h_+ throughout the simulation duration. The left column corresponds to the expected GW signal for an observer along the line of site of the CCSN equator. The right column corresponds to an observer along the supernova north pole, which represents the axis of rotation for rotating models.

The top row represents the nonrotating model, the central row represents the slow rotating model, and the bottom row represents the fast rotating model. As a note, the scales of the vertical axes differ between rows of different rotation rates. As rotation increases, coherent motion of the fluid generates stronger oscillations of the PNS. Likewise in the fast rotating model, beginning $\sim$ 150 ms pb, the presence of the low T/W instability excites the PNS to generate GW with larger amplitudes as well (Pan et al., 2018).

When comparing signals of a given rotation rate, but differing viewing angle, there are only moderate differences for the nonrotating progenitor. This result is expected because there is no centrifugal support to deform the PNS along a particular plane (eg. a more oblate PNS in the xy plane for an axis of rotation in the z direction). However, as rotation increases, the GW signal detected by observers at different viewing angles becomes more pronounced. For the rotating cases, the GW signal just after bounce, $t_{pb} = 0$ sec, commonly called the bounce signal, has a large GW amplitude when viewed along the equator, but has an amplitude of 0 when viewed along the axis of rotation. This effect is explained through Equation (4.1) and Equation (4.2). When viewed along the equator, the oblate PNS will have a cross section similar to an ellipse. As the infalling material deforms the PNS at the time of bounce, the cross section changes to a more spherical shape, and $\ddot{Q}_{xz}$, $\ddot{Q}_{yz}$, and $\ddot{Q}_{zz}$ will take on a correspondingly larger values—a higher amplitude bounce signal is generated. By contrast, when observed along the axis of rotation, the PNS cross section is circular. As the infalling material does not have an azimuthal dependence, just after bounce, the cross section of the PNS retains its circular shape, the dominant $\ddot{Q}_{xx}$, $\ddot{Q}_{xy}$, and $\ddot{Q}_{yy}$ retain smaller values, thereby preventing an observed GW signal. Hundreds of milliseconds after bounce, the GW amplitude related to the PNS oscillations also displays variations in amplitude, depending on viewing angle.

Examining TDWFs can be valuable in investigations such as this one. However, they are inherently limited to observing one viewing angle at a time. Thus, there is no guarantee that the maximum GW signal must be along the equator or pole. Furthermore, as the mechanism of GW generation can change throughout the supernova evolution, in principle, a viewing angle of

preferred GW emission may evolve through time.

4.4.2 Visualizing GWs in Multiple Dimensions

To address the need to observe GW emission along every viewing angle, we introduce the *strain surface plot*. This figure is inspired from those in Vartanyan & Burrows (2020) that display the GW emission by color and concavity on a 3D surface. In practice it can be difficult to compare color or concavity by eye, so we offer another form of visualization, with examples provided in Figure 4.2.

The surfaces in Figure 4.2 are taken from different points in time for the fast rotating 40 $M_{\odot}$ model. To interpret these plots, consider Figure 4.2a. The distance from the origin to any point on the green surface corresponds to h_+ along that viewing angle. The purple star indicates the direction along which there is a maximum observed h_+. The x and y axes form the plane of the supernova equator, and the z axis is the axis of rotation. Figure 4.2a displays similar h_+ emission when viewed at any angle in line with the equator. By contrast, when viewed along the axis of rotation, the surface does not extend far from the origin, indicating a weak GW amplitude. Physically, this behavior is justified. In this panel, $t_{pb} \sim 1.5$ ms after bounce. As explained in Section 4.4.1 and shown in the top row of TDWFs in Figure 4.1, the bounce signal is detected when observed along the equator due to the geometry of the deformed PNS. Figure 4.2a offers a compact way to conclude this directional dependence without relying on multiple TDWFs.

In Figure 4.2b, we notice a deviation from azimuthal symmetry. At this point, a combination of the ringdown from the bounce and emergence of post bounce convection begins to skew the symmetry of the emission. The direction of maximum h_+ amplitude is nearly aligned with the x axis at this time. Furthermore, moderate GW amplitude can be observed along the z axis, in contrast to before.

Figure 4.2c displays GW amplitudes nearly 250 ms later. The configuration of the h_+ surface preferentially lies along the axis of rotation, with a distinct four lobed structure. There are also non-negligible deformations of the PNS along all three spatial degrees of freedom, likely due to the turbulent nature of the accreting matter. Figure 4.2d shows a similar shape, indicating a similar

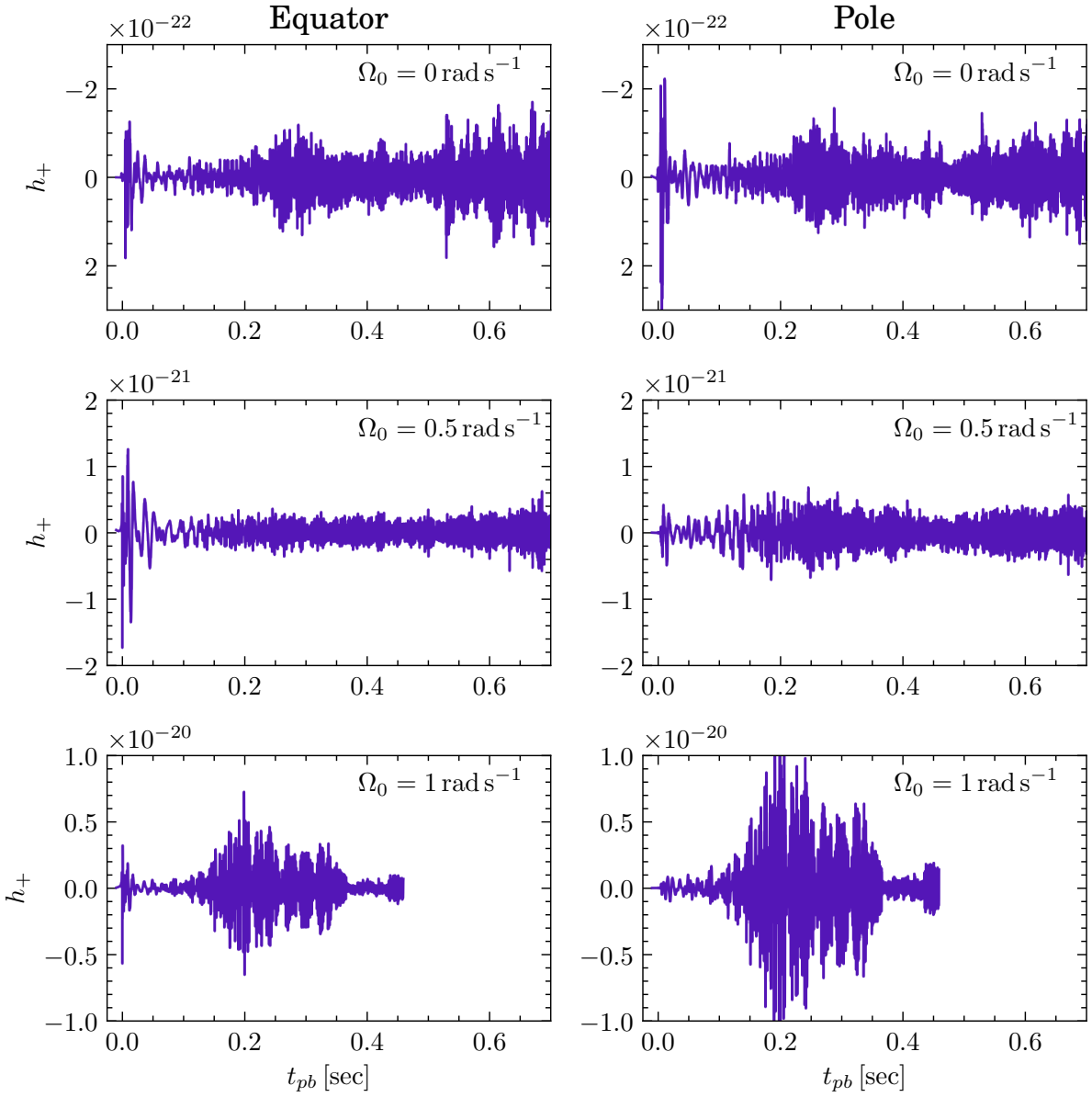

Figure 4.1: Time domain waveforms (plus polarization) for the three 40 $M_\odot$ models in Pan et al. (2018). The left (right) column corresponds to an observed h_+ when viewed along the equator (pole). While TDWFs are useful for analyzing GW emission throughout the supernova simulation, they are inherently limited to GW signals at a single, fixed viewing angle. This motivates the need for additional analysis methods that can identify a dominant viewing angle beyond the equator or pole and determine if this direction evolves in time.

geometry of the PNS deformations. However, because of the smaller h_+ along all viewing angles, this indicates a period of quiescence for the PNS. For scale, the grey sphere provides a reference value of $h_+ = 5 \times 10^{-22}$. Points on green surfaces extending beyond the grey sphere exhibit larger h_+, points within grey the sphere exhibit smaller h_+.

For convenience, we offer methodology to translate from strain surface plots to TDWFs:

1. Construct a strain surface plot at a time of interest t
2. Identify a desired line of site (θ, ϕ). In this example we pick the equator $(\pi/2, 0)$
3. The distance from the origin to the green surface along this line of site represents the detected GW strain $h(\theta, \phi, t)$
4. The values (t, h) correspond to the ordered pair on the TDWF.

As a point of emphasis, these surface plots represent h_+ detected from an observer far from the GW source. Equation (4.1) and Equation (4.2) are applicable only for distant observers. Thus these do not represent the GW amplitudes generated just inside the supernova. To calculate these quantities, a more robust treatment of relativity is needed, with numerical models that track quantities of the spacetime metric.

4.4.3 Finding Preferred Directions

Strain surface plots can be powerful diagnostic tools for analyzing the directionality of GW emission at a specific instance in time. However, CCSNe are dynamic systems whose GW generation evolves over seconds. To track the evolution of the preferred direction emitting gravitational radiation, refer to Figure 4.3. Each point in this 3D scatter plot refers to the direction along which a maximum h_+ would be measured; that is, all of the purple stars in Figure 4.2 are recorded from the entire simulation duration and plotted. Points that have brighter colors occur later in the supernova evolution.

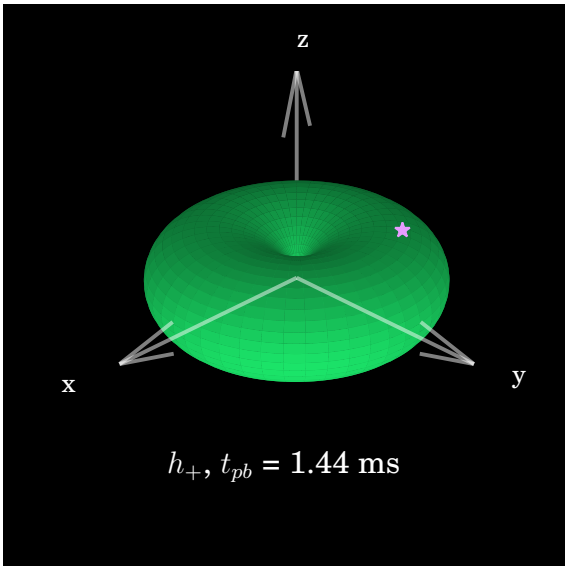

(a) Azimuthal symmetry exhibited by h_+ during the bounce.

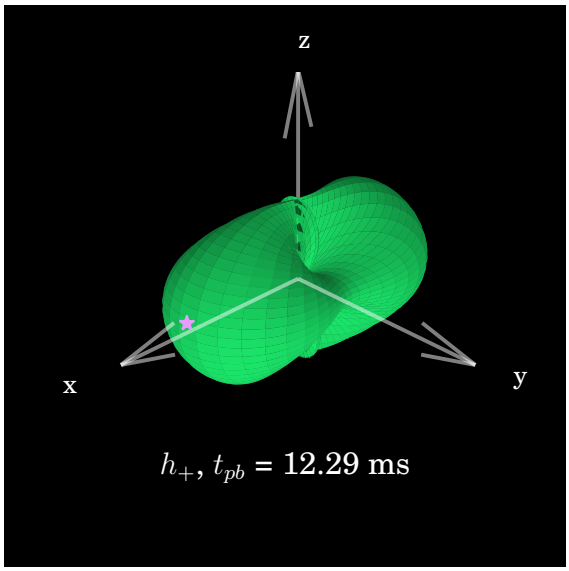

(b) Azimuthal asymmetries arise as the cause of PNS deformations transitions from post bounce ringdown to turbulent post bounce convection.

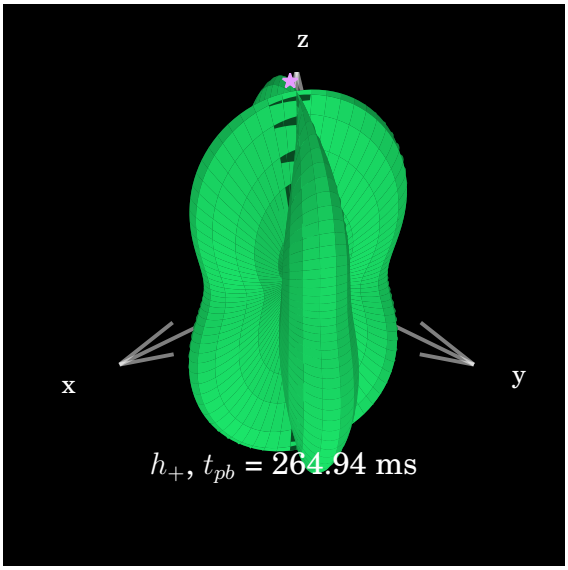

(c) Due to coherent fluid flow around the PNS during the accretion phase, this four lobed surface describes preferential GW emission along the axis of rotation. Note this is orthogonal to the equator, which was the original preferential direction from the bounce.

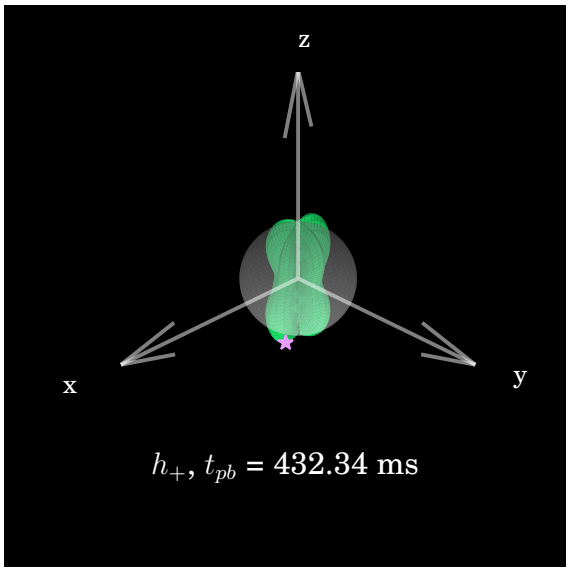

(d) Similar distribution of h_+, however with smaller amplitudes. This behavior is indicative of less pronounced hydrodynamic activity around the PNS compared to Figure 4.2c.

Figure 4.2: Strain surface plots for the fast rotating 40 $M_\odot$ case. The x and y axes form the equator of the supernova; the z axis indicates the axis of rotation. The distance from the origin to a point on the green surface represents the detected h_+ along that direction. Purple stars indicate the direction with the largest GW amplitude. For linear scale, the grey sphere in panel 4.2d represents an $h_+ = 5 \times 10^{-22}$. Points on the green surfaces beyond the sphere indicate larger h_+ values; points on the green surfaces within the sphere indicate smaller h_+ values.

The nonrotating model is represented in Figure 4.3a. As dark points (early times) are close to the center of the h_+ distribution, this indicates a relative period of quiescence for the early time GW emission. As the supernova develops, GW amplitudes become more pronounced, shown through the brighter points (later times) near the outer parts of the distribution. We do not observe any particular structure or morphology from this distribution for the nonrotating 40 $M_\odot$ model for either the plus or cross polarization.

The slowly rotating model is represented in Figure 4.3b. The slow rotating case exhibits noticeable h_+ amplitudes from the early evolution. These points originate from the bounce signal, generating a dark purple distribution along the equator. In the medium brightness, blue points display columnated behavior along the axis of rotation, we attribute to the coherent matter motion circulating around the PNS due to rotation. The final few hundred ms of evolution displays a relatively stochastic preferred GW direction. In total, the entire distribution of preferred GW directions is slightly more prolate than the nonrotating case. Figure 4.3d also displays the slow rotating case, but for the cross polarization of GWs. The later times also exhibit an isotropic distribution of preferred angles for $h_\times$. Interestingly, the early times display coherent paths for preferred directions of $h_\times$. Because of the cyclic nature of the paths traced out by darker points, we attribute this to azimuthal fluid motion around the PNS due to the presence of rotation.

The plus polarization for the fast rotating model is represented in Figure 4.3c. Similar to the slow rotating case, the darkest points display preferred directions along the supernova equator, consistent with the dominant bounce signal. As time evolves, however, the dominant direction for h_+ becomes noticeably columnated along the axis of rotation. This conclusion is important because many GW works that investigate the detectability of GWs from CCSNe assume the 'optimal' source orientation for CCSNe lies along the equator. This is indeed true for detecting the bounce signal. However, as illustrated in Figure 4.3c, the dominant viewing angle changes $\sim 90^\circ$ to the axis of rotation. Furthermore, GW amplitudes along this direction are larger by the nearly a factor of two. *These results draw two main conclusions: (1) GW amplitudes along the axis of rotation can be comparable, if not greater, than GW measurements viewed along the equator for rotating CCSNe.*

(2) There is no single optimal orientation to observe GWs over the entire duration of a CCSN. Similar to the slow rotating case, the dominant viewing angle also traces a coherent path around the axis of rotation. We notice this behavior for both h_+ and $h_\times$. In Figure 4.4, we provide the distribution of preferred viewing angles for $h_\times$. We scale the axes differently than Figure 4.3c to more clearly illustrate the precession of the preferred direction of GW emission around the rotation axis.

As noted in Section 4.3, we also investigate the dominant viewing angle evolution for the 20 $M_\odot$ models from (O'Connor & Couch, 2018a). Similar to the nonrotating case for the 40 $M_\odot$ model, they display an isotropic distribution of dominant viewing angles for both h_+ and $h_\times$. Likewise, we do not notice any coherent paths for preferred GW directions during instabilities like the SASI or Lepton-number Emission Self-sustained Asymmetry (LESA) (Tamborra et al., 2014).

As a caveat, we note these scatter plots record *the magnitude* of h_+ or $h_\times$. The nature of GW strain can elongate or contract objects, corresponding to positive and negative strain. Thus, these visualization do not capture the sign of the GW strain, whereas those in Vartanyan & Burrows (2020) account for the sign. Nevertheless, because Figure 4.3 is used to identify dominant directions (ie. along certain axes), the sign remains unimportant for the scope of this work.

4.5 Discussion and Summary

4.5.1 Relating GW Directionality to Supernova Physics

There are a variety of physical mechanisms responsible for impacting the PNS oscillations that drive GWs. Pan et al. (2021) note several potential factors such as the SASI, the low T/W instability, and possibly the precession of the PNS rotation axis. As the GW directionality for the mesa models with and without SASI were explored, with no clear preferred direction, we do not attribute dominant viewing angles for GW emission to this hydrodynamic instability. In the fast rotating model, Pan et al. (2021) note the possible emergence of the low T/W instability, based on the low frequency of GW emission beginning $\sim$ 150 ms pb. As the fast rotating model exhibits a preferred direction of GW emission along the axis of rotation and coherent paths in the evolution of the

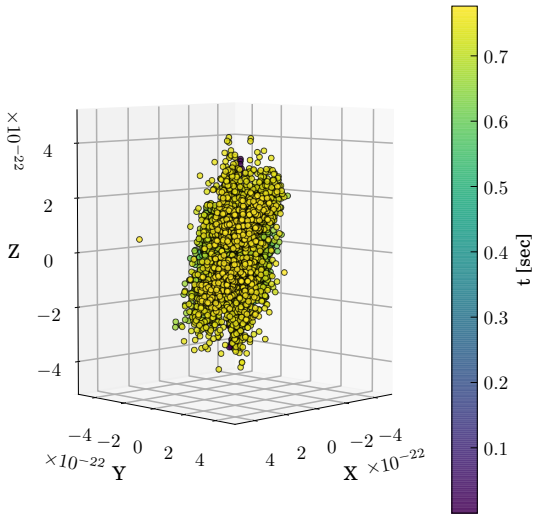

(a) Dominant viewing angles of h_+ for the non-rotating case. The distribution of dominant GW viewing angles remains isotropic for the duration of the supernova evolution.

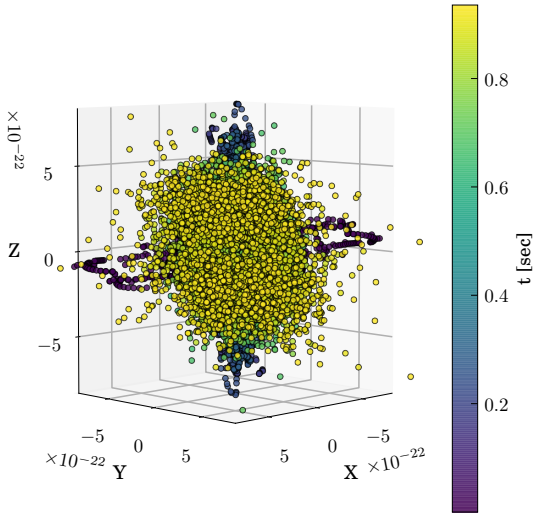

(b) Dominant viewing angles of h_+ for the slow rotating case. The dark (early time) points distributed along the equatorial plane are generated from the bounce signal. The dominant signal direction then aligns with axis of rotation.

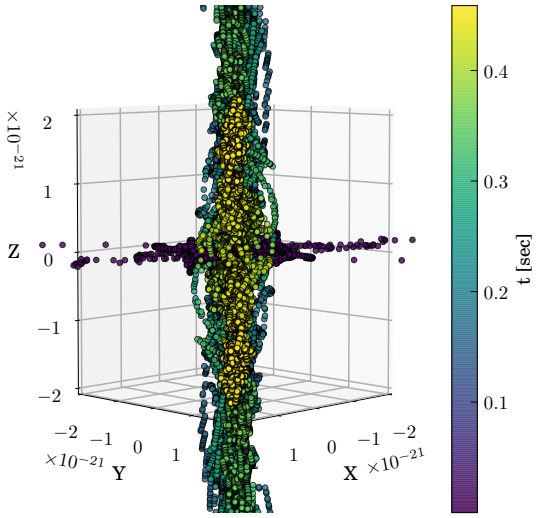

(c) Dominant viewing angles of h_+ for the fast rotating model. The preferred GW direction is noticeably columnated and follows coherent paths that precess around the axis of rotation.

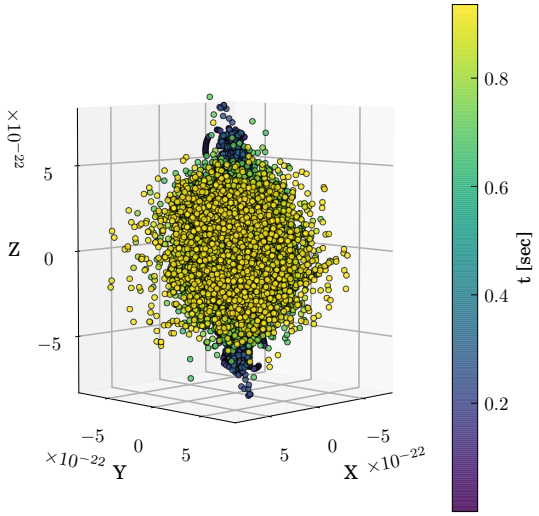

(d) Same slow rotating model as in Figure 4.3b, however for the cross polarization $h_\times$. The dominant viewing angle follows coherent paths for darker points (earlier times), encoding rotational content of the supernova.

Figure 4.3: These distributions represent compiling the direction of maximum GW emission (purple stars from Figure 4.2) throughout the supernova evolution. Brighter points correspond to later times. The xy plane forms the equator of the supernova. The z axis identifies the axis of rotation for rotating cases.

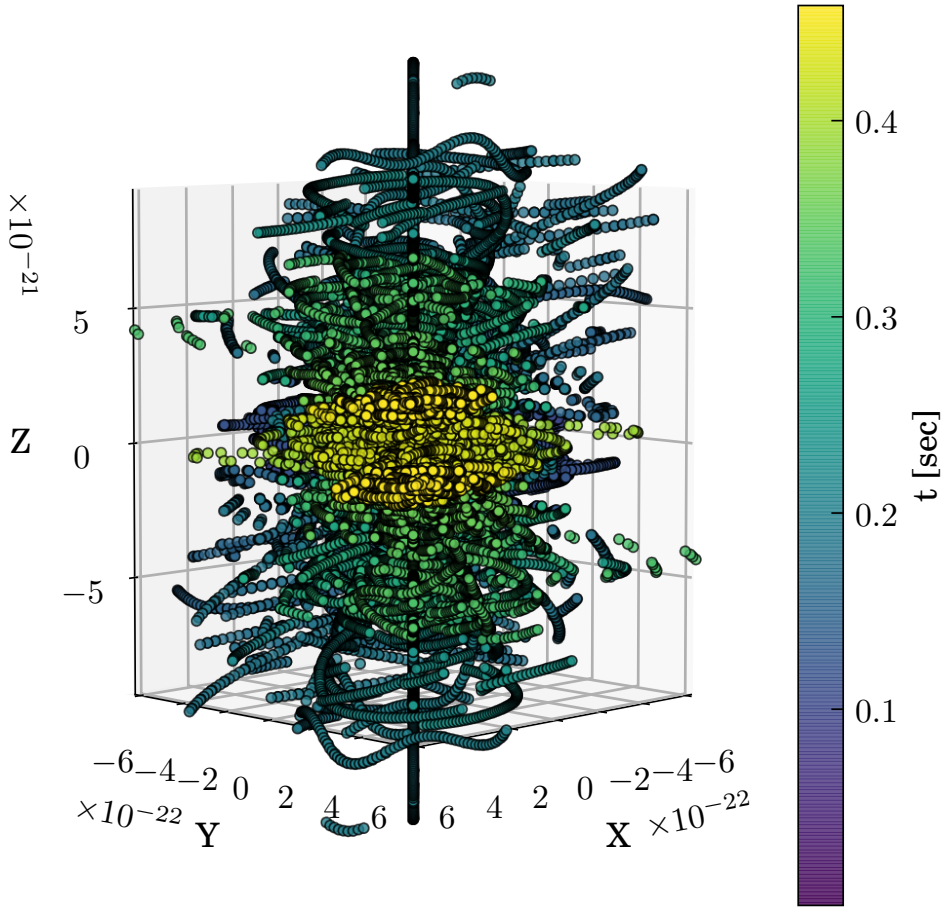

Figure 4.4: Dominant viewing angles of $h_\times$ for the fast rotating model. This image is the same orientation as Figure 4.3c, however we rescale the axes to more clearly display the precession of the preferred viewing angle around the axis of rotation.

preferred direction, it is possible this instability contributes. However, the presence of the low T/W instability is not requisite for these two behaviors as the slow rotating model—which shows no sign of low T/W—also remains slightly columnated and exhibits clear paths in Figure 4.2d.

We acknowledge many of these descriptions of the GW viewing angle evolution are qualitative and rely upon visual inspection of the panels in Figure 4.3. For future work, we aim to provide more quantitative descriptions of the distributions of points in Figure 4.3. One example includes performing a spherical harmonic decomposition of the points to determine exactly when the dominant viewing angle transitions from isotropic to exhibiting a dipole behavior (in the rotating

cases). Furthermore, plotting the evolution of the precession of the PNS rotation axis alongside the GW dominant angles may provide an additional insight as to the nature of GW directionality in CCSNe.

4.5.2 Implications for Observability

These directional dependencies help prepare for the first direct detection of GWs from CCSNe. As detector sensitivities improve and signal search algorithms become more advanced, identifying which components of the signal can be reconstructed is vital. For example, the observability of a GW now not only depends on the physical mechanism generating it, but also the angle it which it is observed. For a rotating supernova, the bounce signal is most visible when viewed along the supernova equator. However, potentially stronger GW amplitudes along the axis of rotation may be missed. By contrast, if viewed along the axis of rotation, the broadband bounce signal will not be detected, but high frequency oscillations from the PNS may have stronger amplitudes. For a randomly oriented supernova, the viewing angle will likely be off-axis, so GW detection algorithms should search for both components of the signal.

Contributions to the GW background are also affected by consequences of directionality. For detectors attempting to quantify the spectrum of the GW background (Christensen, 2019), this work offers motivation to consider CCSN population studies. Theoretical works could construct populations of randomly oriented and distributed CCSNe, with varying rotation rates, to better quantify which components of the signal may be detectable for GWs from a superposition of sources.

4.5.3 Summary

This work has considered a new factor regarding the observability of GWs from CCSNe, particularly the impact of viewing angle. Here we review the findings from our work:

- strain surface plots can characterize the nature of the mechanism generating GWs at a given point in time, Figure 4.2,

- viewing the collective distribution of preferred directions for GW emission shows CCSNe do not have a single 'optimal' viewing angle, Figure 4.3,
- depending on the degree of rotation, rotating CCSNe can exhibit strong GW amplitudes along the axis of rotation, rather than the equator,
- the dominant viewing angle of GW emission in rotating CCSNe can follow coherent paths that precess around the axis of rotation.

We have reviewed a new method towards visualizing, and consequently analyzing, GW emission from arbitrary astrophysical sources. While this study uses CCSNe, in general, any GW source can make use of these visualization methods. As a cautionary note, we emphasize the panels of Figure 4.3 only display the direction along which a maximum GW strain occurs. Indeed, GWs are emitted in other directions, many times orthogonal to this dominant angle. While other metrics exist, such as taking moments of the surfaces from Figure 4.2, the methods outlined here are appropriate for identifying dominant angles that evolve.

To further refine these results for future work, we could quantify the distributions seen in Figure 4.3 using spherical harmonics, to track how distributions in dominant angle transition from isotropic to prolate. Likewise, we aim to quantify correlations between the coherent paths traced out by the dominant viewing angle and the physical PNS rotation or SASI axis (eg. using Spearman's correlation coefficients). Acknowledging these caveats, this study offers another observable factor to consider when generating gravitational waveforms from CCSNe. By considering both theoretical factors like CCSN source physics and observational factors like the impact of viewing angle, the GW community will be better prepared for the first direct detection of GWs from stellar explosions.

M.A.P. was supported by a Michigan State University Distinguished Fellowship. S.M.C. is supported by the U.S. Department of Energy, Office of Science, Office of Nuclear Physics, under award Nos. DE-SC0015904 and DE-SC0017955 and the *Chandra X-ray Observatory* under grant No. TM7-18005X. This research was supported by the Exascale Computing Project (17-SC-20-SC), a collaborative effort of two U.S. Department of Energy organizations (Office of Science and

the National Nuclear Security Administration) that are responsible for the planning and preparation of a capable exascale ecosystem, including software, applications, hardware, advanced system engineering, and early testbed platforms, in support of the nation's exascale computing imperative. The software used in this work was in part developed by the DOE NNSA-ASC OASCR Flash Center at the University of Chicago.

Software used in this work: FLASH (see footnote 7) (Fryxell et al., 2000, 2010), Matplotlib[8] (Hunter, 2007), NuLib[9] (O'Connor, 2015), NumPy[10] (van der Walt et al., 2011), SciPy[11] (Jones et al., 2001–)

[8] https://matplotlib.org/
[9] http://www.nulib.org
[10] http://www.numpy.org/
[11] https://www.scipy.org/

CHAPTER 5

INCORPORATING RELATIVISTIC EFFECTS INTO THE FLASH MULTIPHYSICS CODE

This section builds upon published work: S. Couch, J. Carlson, M.A. Pajkos, Brian W. O'Shea, A. Dubey, T. Klosterman, 2021, *Parallel Computing*, 102830. It also reviews unpublished work: M.A. Pajkos, S. Fromm, S.M. Couch, E.P. O'Connor, P. Mosta, in prep.

5.1 Abstract

We present a new general-relativistic, multidimensional, magnetohydrodynamic solver in the FLASH framework that is compatible with adaptive-mesh-refinement. We outline the details of our numerical implementation of this new solver in the ideal MHD limit, including relativistic terms in the magnetohydrodynamics and a novel treatment of evolving spacetimes in multiple dimensions. A variety of tests are presented to display the robustness of the code compared to analytic solutions and numerical tests performed by other GRMHD codes: relativistic (magnetized) shock tubes, compact star evolution, and collapse of a dust cloud to a black hole. We also present applications of these new physics features to six spherically-symmetric and two axisymmetric neutrino radiation hydrodynamic simulations of core-collapse supernovae (CCSNe). We explore the impact on the overall supernova evolution and the changes to the neutrino emission. Accounting for relativistic hydrodynamics paired with evolving spacetimes creates a more compact protoneutron star, a higher neutrino luminosity, and launches shocks to smaller radii after core bounce.

5.2 Introduction

The field of astrophysics is dominated with spectacular events that contain a wealth of information regarding how the laws of physics behave when pushed beyond limits of what terrestrial laboratories can achieve. While technology used in experiments attempts to approach astrophysical conditions, one useful resource for analyzing energetic, space-based events are numerical models. Core-collapse supernovae (CCSNe) are examples of events that have been extensively examined

using simulations. The value in completing such sophisticated calculations of stellar explosions is multifold. CCSNe are one of the principle drivers of chemical evolution in the universe, provide the main sites for the creation of compact objects like neutron stars or black holes, and create unique signals like ripples in spacetime called gravitational waves (GWs) whose observations make up a growing field within astronomy. These disruptive events at the end of the life of a massive star ($\gtrsim 8M_{\odot}$) rely on high fidelity treatments of gravity, radiation transport, hydrodynamics, and nuclear burning, to name a few. As such, they require the use of high performance computing (HPC) resources to achieve practical runtimes. With many numerical physics implementations involved, one vital element to the success or failure of these stellar explosions is gravity.

A variety of gravitational treatments exist for CCSNe, with varying levels of sophistication. The simplest case is a Newtonian treatment, which involves solving Poisson's equation for gravity, typically approximating the gravitational potential with a series of spherical harmonics (e.g., Couch et al., 2013). An often used treatment that is more sophisticated than the Newtonian case is the GR effective potential (GREP). First introduced by (Rampp & Janka, 2002) and improved by (Marek et al., 2006), the GREP applies empirical factors to a modified gravitational potential in order to reproduce 3D full GR calculations quite well. While computationally efficient, only requiring a solution to two elliptic equations, it does not formally evolve spacetime quantities and has been show to overestimate GW frequencies from the central compact object, when used without relativistic hydrodynamics (Müller et al., 2013).

A more accurate model is the conformal flatness condition (CFC) (Isenberg, 2008). CFC assumes the spatial three metric is a scaled version of the flat spacetime metric. Inherently this approximation assumes the spacetime is spherically-symmetric. Under the CFC, five elliptic equations require solutions. CFC evolves elements of the spacetime, offering a natural integration with relativistic hydrodynamic schemes, by granting access to quantities not available with GREP (e.g., elements of the spatial metric).

Current state of the art treatments of gravity evolve a full set of Einstein's field equations, such as the Baumgarte-Shapiro-Shibata-Nakamura (BSSN) formulation (Baumgarte & Shapiro,

1998; Shibata & Nakamura, 1995). This method involves solving a set of 40 hyperbolic equations. Physically, BSSN and CFC produce similar CCSN behavior soon after bounce, but BSSN more properly captures GW signals later in the supernova evolution (Shibata & Sekiguchi, 2004). An equally robust method is the so called Z4c formulation, which only requires solving ~ 25 hyperbolic equations (Cao & Hilditch, 2012).

Incorporating relativistic effects into the MHD scheme is also a vital element to properly modeling highly energetic astrophysical events. It accounts for magnetic field evolution while incorporating the effects of curved spacetime, time dilation, and captures fluid velocities near the speed of light. Likewise, it more properly captures the strong field effects that tend to slow convective overturn in extreme spacetime environments, compared to Newtonian cases (Müller et al., 2013). Some examples of codes that have incorporated numerical treatments of GRMHD are the `HARM` code (Gammie et al., 2003), `GRHydro` (Mösta et al., 2014) (built from the original `Whisky` code (Baiotti et al., 2010)), `Athena` MHD (Stone et al., 2008), `Echo` (Del Zanna et al., 2007), the GRMHD code from the Tokyo and Kyoto group (Shibata & Sekiguchi, 2005), UIUC GRMHD code (Duez et al., 2005; Etienne et al., 2010), `WhiskyMHD` code (Giacomazzo & Rezzolla, 2007), and the LSU GRMHD code (Anderson et al., 2006).

The software architecture in this work is `FLASH` (Fryxell et al., 2000; Dubey et al., 2009). While `FLASH` contains a suite of multiphysics features, it previously made use of Newtonian hydrodynamics and the GREP to account for gravity. In an effort to provide more physics features to `FLASH` users, create another code with relativistic capabilities to serve as a verification tool for other works, and conduct higher fidelity scientific campaigns, we present new features:

- a cell centered treatment of relativistic MHD,
- a fully general relativistic 1D treatment of evolving spacetimes,
- a multidimensional extension of the evolving spacetime in 2D cylindrical coordinates and 3D Cartesian coordinates,

- and magnetic contributions to the spacetime curvature for the multidimensional relativity scheme.

In this work we also present a series of numerical baseline tests verifying the code behavior, multiple 1D and 2D CCSN simulations incorporating these new physics features, and recent progress in `FLASH` to prepare these features for exascale platforms.

This paper is organized as follows: Section 5.3 outlines the details of our MHD formulation. In Section 5.4 we review the relevant numerical methods employed in the `FLASH` code. Section 5.5 verifies the code with a series of established baseline tests. Section 5.6 presents CCSN behavior with relativistic features. Section 5.7.1 outlines future-focused considerations for integrating these features into exascale-ready codes. Finally, in Section 5.7.2 we summarize.

5.3 Formulation of MHD

We express the spacetime metric in the Arnowitt-Deser-Misner (ADM) form (Arnowitt et al., 2008):

$$ds^2 = g_{\mu\nu}dx^\mu dx^\nu \equiv (-\alpha^2 + \beta_i\beta^i)dt^2 + 2\beta_i dt dx^i + \gamma_{ij}dx^i dx^j \tag{5.1}$$

where α, β_i, γ_{ij}, and $g_{\mu\nu}$ are the lapse function, shift vector, spatial metric, and spacetime metric, respectively. Greek indices denote 4 quantities and Latin indices denote 3 quantities. We use a spacetime signature of $(-,+,+,+)$ and work in units of $c = G = M_\odot = 1$ unless otherwise noted.

Our solver assumes the magnetized fluids have infinite conductivity and do not experience charge separation—the ideal MHD approximation. This treatment implies the electric fields in the rest frame of the fluid $E^\nu = u_\mu F^{\mu\nu} = 0$. In this paper, for cleaner notation, we avoid the use of the permeability and permitivity of free space in cgs-Gaussian units. To this end, we absorb a factor of $1/\sqrt{4\pi}$ into the relativistic Faraday tensor $F^{\mu\nu}$, its dual ${}^*F^{\mu\nu} = \frac{1}{2}\epsilon^{\mu\nu\alpha\beta}F_{\alpha\beta}$, the electric fields, and magnetic fields. Note $\epsilon^{\mu\nu\alpha\beta}$ is the antisymmetric fourth-rank tensor (Jackson, 1998).

These electromagnetic (EM) quantities, namely the magnetic fields, contribute to the evolution of a magnetized fluid. Thus the stress energy tensor can be separated into different contributions.

The purely hydrodynamic terms are,

$$T^{\mu\nu}_{\text{Hydro}} = \rho h u^\mu u^\nu + P g^{\mu\nu} = (\rho + \rho\epsilon + P) u^\mu u^\nu + P g^{\mu\nu}, \tag{5.2}$$

where ρ, ϵ, P, u^ν, and $h = 1 + \epsilon + P/\rho$ are the rest mass density, specific internal energy, pressure, four velocity, and specific enthalpy. The purely EM terms are

$$T^{\mu\nu}_{\text{EM}} = F^{\mu\kappa} F^\nu_\kappa - \frac{1}{4} g^{\mu\nu} F^{\kappa\sigma} F_{\kappa\sigma} = b^2 u^\mu u^\nu - b^\mu b^\nu + \frac{b^2}{2} g^{\mu\nu}, \tag{5.3}$$

where $b^\mu = u^*_\nu F^{\mu\nu}$ is the magnetic four vector; b^2 can be expressed in terms of the magnetic pressure P_m, $b^2 = b^\mu b_\mu = 2P_m$.

Combining the hydrodynamic and EM contributions yields a stress energy tensor of the following form:

$$\begin{aligned} T^{\mu\nu} &= \left(\rho + \rho\epsilon + P + b^2\right) u^\mu u^\nu + \left(P + \frac{b^2}{2}\right) g^{\mu\nu} - b^\mu b^\nu \\ &= \rho h^* u^\mu u^\nu + P^* g^{\mu\nu} - b^\mu b^\nu, \end{aligned} \tag{5.4}$$

where the specific enthalpy and pressure are now modified to contain magnetic contributions: $h^* = 1 + \epsilon + (P + b^2)/\rho$ and $P^* = P + b^2/2$.

The relativistic MHD equations we evolve originate from local GR conservation laws for mass and energy-momentum,

$$\nabla_\mu J^\mu = 0, \quad \nabla_\mu T^{\mu\nu} = 0, \tag{5.5}$$

where ∇_μ is the covariant derivative with respect to the four-metric and the mass current is represented by $J^\mu = \rho u^\mu$. Likewise the following is yielded from Maxwell's equations,

$$\nabla_\nu {}^*F^{\mu\nu} = 0. \tag{5.6}$$

When evolving the hydrodynamics, we follow the scheme outlined in Toro (2009) outlining the relationship between the vector of evolved variables $\mathbf{U}$, vector of fluxes $\mathbf{F}$, and associated source

terms **S**:

$$\frac{\partial \mathbf{U}}{\partial t} + \frac{\partial \mathbf{F}^i}{\partial x^i} = \mathbf{S}. \tag{5.7}$$

The MHD components of $\mathbf{U}$ and $\mathbf{F}^i$ govern the behavior of the magnetized fluid, in an evolution scheme known as the Valencia formulation (Martí et al., 1991; Banyuls et al., 1997; Ibanez et al., 1999; Antón et al., 2006) which inspires the following definitions

$$\mathbf{U} = [D, DY_e, S_j, \tau, \mathcal{B}^k], \tag{5.8}$$

$$\mathbf{F}^i = \alpha \times \begin{bmatrix} D\tilde{v}^i \\ DY_e\tilde{v}^i \\ S_j\tilde{v}^i + \sqrt{\gamma}P^*\delta^i_j - b_j\mathcal{B}^i/W \\ \tau\tilde{v}^i + \sqrt{\gamma}P^*v^i - \alpha b^0\mathcal{B}^i/W \\ \mathcal{B}^k\tilde{v}^i - \mathcal{B}^i\tilde{v}^k \end{bmatrix}, \tag{5.9}$$

$$\mathbf{S} = \alpha\sqrt{\gamma} \times \begin{bmatrix} 0 \\ R^\nu_{Y_e}/\alpha\sqrt{\gamma} \\ T^{\mu\nu}\left(\frac{\partial g_{\nu j}}{\partial x^\mu} - \Gamma^\lambda_{\mu\nu}g_{\lambda j}\right) + Q^{\nu,E}_{S_j}/\alpha + Q^{\nu,M}_{S_j}/\alpha \\ \alpha\left(T^{\mu 0}\frac{\partial \ln\alpha}{\partial x^\mu} - T^{\mu\nu}\Gamma^0_{\mu\nu}\right) + Q^{\nu,E}_\tau/\alpha + Q^{\nu,M}_\tau/\alpha \\ \vec{0} \end{bmatrix}, \tag{5.10}$$

with $\tilde{v}^i = v^i - \beta^i/\alpha$ and $\Gamma^\lambda_{\mu\nu}$ are Christoffel symbols; $R^\nu_{Y_e}$ and Q values are related to neutrino effects and discussed in Section 5.4.4.

The evolved variables D, S_j, τ, and $\mathcal{B}^k$ can is written in terms of the primitive quantities

$$D = \sqrt{\gamma}\rho W, \tag{5.11}$$

$$DY_e = \sqrt{\gamma}\rho W Y_e, \tag{5.12}$$

$$S_j = \sqrt{\gamma}\Big(\rho h^* W^2 v_j - \alpha b^0 b_j\Big), \tag{5.13}$$

$$\tau = \sqrt{\gamma}\Big(\rho h^* W^2 - P^* - (\alpha b^0)^2\Big) - D, \tag{5.14}$$

$$\mathcal{B}^k = \sqrt{\gamma} B^k, \tag{5.15}$$

where γ is the determinant of the spatial metric γ_{ij}, and Y_e is the electron fraction—the ratio of free electrons to baryons. We select v^i to represent the velocity measured by an Eulerian observer at rest in the current spatial three-hypersurface (York, 1983),

$$v^i = \frac{u^i}{W} + \frac{\beta^i}{\alpha}, \tag{5.16}$$

where $W = 1/\sqrt{1 - v^i v_i}$ is the Lorentz factor.

In terms of the primitive quantity representing the components of the magnetic field for an Eulerian observer B^i, the components of the magnetic field in the rest frame of the fluid b^μ can be written

$$b^0 = \frac{W B^k v_k}{\alpha}, \tag{5.17}$$

$$b^i = \frac{B^i}{W} + W(B^k v_k)\left(v^i - \frac{\beta^i}{\alpha}\right), \tag{5.18}$$

$$b^2 = \frac{B^i B_i}{W^2} + (B^i v_i)^2. \tag{5.19}$$

5.3.1 Alternate form of Numeric Source Terms

Equation (5.10) properly describes the expression for the MHD source terms. However, in practice, retaining the Christoffel symbols can be memory intensive and involves time derivatives of the spacetime metric which, in general, do not have a closed form. As an alternate approach, we

generalize the formulation in Rezzolla & Zanotti (2013) (see their Section 7.3.3 for a detailed derivation to go from Equation (5.10) to Equation (5.20)):

$$\mathbf{S} = \sqrt{\gamma} \times \begin{bmatrix} 0 \\ R^{\nu}_{Y_e}/\sqrt{\gamma} \\ \frac{1}{2}\alpha S^{ik}\partial_j \gamma_{ik} + S_i \partial_j \beta^i - E\partial_j \alpha + Q^{\nu,E}_{S_j} + Q^{\nu,M}_{S_j} \\ \alpha S^{ij} K_{ij} - S^j \partial_j \alpha + Q^{\nu,E}_{\tau} + Q^{\nu,M}_{\tau} \\ \vec{0} \end{bmatrix}. \tag{5.20}$$

Here, the stress energy tensor has been decomposed into quantities measured by normal observers through in a 3+1 split of spacetime described by $T^{\mu\nu} = En^\mu n^\nu + S^\mu n^\nu + S^\nu n^\mu + S^{\mu\nu}$. The MHD quantities of interest can be recovered via the following projections:

$$E = T^{\mu\nu} n_\mu n_\nu, \tag{5.21}$$

$$S^\mu = -\gamma^\mu_\alpha n_\beta T^{\alpha\beta}, \tag{5.22}$$

$$S^{\mu\nu} = \gamma^\mu_\alpha \gamma^\nu_\beta T^{\alpha\beta}, \tag{5.23}$$

where n^μ (n_μ) describe a unit normal vector (one-form) to a spatial hypersurface Σ, with components $n^\mu = \frac{1}{\alpha}(1, -\beta^i)$ and $n_\mu = (-\alpha, \vec{0})$. Likewise, $K_{ij} = -\gamma^\mu_i \gamma^\nu_j \nabla_\mu n_\nu$ represents the extrinsic curvature. For a detailed connection of expressing K_{ij} explicitly in terms of the relevant 'remapped' metric quantities in this work, see Appendix A.3. Source terms $R^\nu_{Y_e}$ and $Q^{\nu,(E/M)}$ represent neutrino contributions; they are described in Section 5.4.4 and explicitly derived in Appendix A.5.

5.4 Numerical Methods

Having described the GRMHD formulation, we now briefly review existing relevant physics capabilities and detail new physics features in `FLASH`. The test cases in Section 5.5 are completed

with similar setups to previous works (O'Connor & Ott, 2010; Mösta et al., 2014) by using a uniformly spaced grid. The resolution requirements vary by each test problem and are specified in each subsection.

The CCSN results were completed using PARAMESH (v.4-dev) adaptive mesh refinement (AMR) library (MacNeice et al., 2000). The 1D models are performed over a domain of 10^4 km and use 10 levels of refinement, for a finest grid resolution in the supernova core of ~ 0.08 km. The 2D models are performed on a domain 10^4 km in each direction and use 9 levels of refinement, for a finest grid resolution ~ 0.65 km.

We select 12-, 40-, and 60 $M_\odot$ progenitors for the CCSN models (Sukhbold et al., 2016b). These progenitors are intentionally chosen because they span a wide range of compactness values. As a reminder, compactness was first introduced by O'Connor & Ott (2011) and quantifies how much mass is within a given radius of the progenitor

$$\xi_M = \left.\frac{M/M_\odot}{R(M_{\rm bary} = M)/1000\,{\rm km}}\right|_{\rm collapse}, \tag{5.24}$$

for a baryonic mass M and radial coordinate for the enclosed mass $R(M)$. The corresponding $\xi_{2.5}$ values for the 12-, 40-, and 60 $M_\odot$ progenitors are 0.074, 0.53, and 0.17, respectively (Pajkos et al., 2019).

5.4.1 The Method of Lines Update

When coupling different physics treatments, ensuring the simultaneous update of primitive variables is important for problems that evolve on relatively short timescales. For the relativistic test cases and supernova system results presented here, a method of lines (MoL) update is appropriate (Hyman, 1979). MoL progresses through different physics subunits and stores relevant evolved variables and right hand sides (RHS). As a simple example, for a purely hydrodynamic problem, refer to Equation (5.7). The evolved variables correspond to $\mathbf{U}$ and the RHSs correspond to $-\partial \mathbf{F}^i/\partial x^i + \mathbf{S}$, scaled by a timestep dt. The RHSs are then added to the evolved variables, and recovery of the

primitive variables ("con2prim") is performed. When all physics treatments are integrated into an MoL scheme, all primitive variables are updated at equivalent time steps.

By contrast, an operator split type method may use a mix of variables from a previous stage and the current stage to calculate a new value. For example, after a hydrodynamic update, an evolved variable D at the $n+1$ state and a metric element γ_{11} at state n may be used to recover a primitive ρ at the $n+1$ state. For models that have rapidly evolving spacetimes and fluid configurations (e.g., during BH formation) this inconsistency between variable stages can introduce numerical instabilities.

The MoL subunit in `FLASH` provides Butcher tableaus to select different integration schemes for multiphysics updates. Examples of time integration schemes vary from a simple forward Euler approach to a 4th order Runge–Kutta scheme to generalized-structure additive Runge–Kutta (IMEX-MRI-GARK) methods (Chinomona & Reynolds, 2020). All test problems in this work and CCSN simulations use an explicit, strong stability preserving (SSP), second order Runge–Kutta (RK2) time integration scheme (Gottlieb et al., 2001).

5.4.2 Magnetohydrodynamic Update

This work makes use of the `Spark` MHD solver. It has finite-volume and finite-difference capabilities, though for these simulations we use the finite volume approach. For finite-volume simulations, `Spark` is flux conservative; this implies for simulations with AMR, where blocks of different resolutions meet, a standard flux differencing scheme is applied to ensure flux conservation across fine-coarse boundaries (Berger & Colella, 1989). For further details of `Spark`, we refer the reader to Couch et al. (2020a). While the Newtonian MHD version of `Spark` allows for different Riemann solvers, the relativistic simulations conducted here make use of the Harten-Lax-van Leer-Einfeldt (HLLE) approximate Riemann solver (Harten et al., 1983; Einfeldt, 1988), due to the relatively straightforward extension to the GR case of calculating the wavespeeds for the Riemann fan (Gammie et al., 2003).

5.4.3 Gravitational Treatment

We introduce a novel multidimensional gravitational treatment inspired by the GR1D code (O'Connor & Ott, 2011). The metric that is evolved corresponds to

$$ds^2 = g_{\mu\nu}dx^\mu dx^\nu = -\alpha^2 dt^2 + X^2 dr^2 + r^2 d\Omega^2 \tag{5.25}$$

where α and X can be expressed in terms of the metric potential Φ and enclosed gravitational mass $m(r,t)$,

$$\alpha = \exp(\Phi), \;\; X = \left(1 - \frac{2m(r,t)}{r}\right)^{-1/2}. \tag{5.26}$$

Evolving our spacetime in spherical symmetry corresponds to radial gauge and polar slicing (RGPS) coordinates. To calculate the gravitational mass, the Hamiltonian in RGPS is

$$m(r,t) = 4\pi \int_0^r r'^2(\rho h^* W^2 - P^* + \tau_m^\nu)dr', \tag{5.27}$$

where τ_m^ν represents the neutrino contributions to the gravitational mass and is related to the neutrino pressure P_ν by $\tau_m^\nu = (4W^2 - 1)P_\nu$ (O'Connor & Ott, 2010). To calculate the metric potential Φ, apply the momentum constraints and polar slicing condition

$$\Phi(r,t) = \int_0^r X^2 \left[\frac{m(r',t)}{r'^2} + 4\pi r'(\rho h^* W^2 v^2 + P^* + \tau_\Phi^\nu)\right]dr' + \Phi_0, \tag{5.28}$$

where τ_Φ^ν is the neutrino contribution to the metric potential and given by $\tau_\Phi^\nu = (4W^2v^2 + 1)P_\nu$. Φ_0 is found by assuming vacuum at the edge of the computational domain and matching the solution to the Schwarzschild metric,

$$\Phi(R_*,t) = \ln[\alpha(R_*,t)] = \frac{1}{2}\ln\left[1 - \frac{2m(R_*,t)}{R_*}\right]. \tag{5.29}$$

We emphasize these definitions for $m(r,t)$ and $\Phi(r,t)$ differ slightly from the expressions found in O'Connor & Ott (2011), by including additional magnetic field contributions to the metric terms. We now move to outlining how this previously 1D scheme is extended to multiple dimensions.

5.4.3.1 Averaging and Remapping

As the spacetime in our gravitational scheme is updated along a 1D ray, averaging and remapping procedures are required to translate to a multidimensional domain. After the vector of evolved variables $\mathbf{U}$ is known at the $n+1$ time state, the multidimensional matter profile is averaged to a 1D profile. Specifically, the user defines the resolution of a 1D spacetime vector by dividing the maximum spherical radius from the origin to the corner of the grid by a user-selected number of zones, either uniformly- or logarithmically-spaced. An equally weighted average is then performed of the quantities $(D + \tau + \sqrt{\gamma}\tau_{\nu}^{m})$ and $(\rho h^{*} W^{2} v^{2} + P^{*} + \tau_{\Phi}^{\nu})$, as they are pivotal in constructing Equation (5.30) and Equation (5.28). These quantities are chosen purposefully as they aid in the evolution of the spacetime-related quantities.

The code then uses a modified form of Equation (5.27), what we will call the *evolved form*. Using Equation (5.11) and Equation (5.14), we note

$$m(r,t) = 4\pi \int_{0}^{r} r'^{2} (D + \tau + \sqrt{\gamma}\tau_{m}^{\nu}) / \sqrt{\gamma} dr'. \tag{5.30}$$

Pay special attention to the factor of $\sqrt{\gamma}$ in the denominator. In this formulation of GRMHD the evolved variables D and τ are densitized by a factor related to the determinant of the spatial metric, in contrast to the formulation in `GR1D`. They first must be undensitized before integrating outwards. However, note $\sqrt{\gamma}$ depends on X, which depends on m. Thus the mass in Equation (5.30) depends implicitly upon itself.

After the averaging procedure, Equation (5.30) and Equation (5.28) are integrated radially outward, updating 1D vector of $m(r,t)$ and $\Phi(r,t)$ values to the $n+1$ time state. From these two variables, the remaining metric-related quantities (e.g., γ_{ij} and α) can be calculated. The details of the implicit mass integration are outlined in Appendix A.4.

With a 1D vector of X and Φ values, the code then undergoes the remapping procedure: when the 1D updated spacetime results are remapped onto the multidimensional grid. A brief description of the remapping procedure involves transforming the coordinates of a differential

path length ds^2 (see Equation (5.1)) from RGPS coordinates to a coordinate system of choice: cylindrical or Cartesian. Based on the coefficients of the terms $dx^i dx^j$, γ_{ij} can be identified for a multidimensional, spherically-symmetric spacetime. Likewise, the metric derivatives can be calculated as well. At this point, α, γ_{ij}, and the metric derivatives are known at the $n+1$ time step. The needed spacetime terms are then available for the hydrodynamic update at the next timestep. For an in depth derivation of the metric remapping procedure with relevant metric derivatives, see Appendix A.1 and Appendix A.2.

The strength of this procedure is its inexpensive computational cost. While other spacetime evolution approximations that also assume spherically-symmetric spacetimes (e.g., CFC) require solving five elliptic equations, this scheme only requires solving two . Likewise, compared to fully robust schemes such as the BSSN formulation that require 40 hyperbolic equations, this scheme is less computationally intensive. Of course, the averaging procedure on the evolved variables to update the spacetime does not guarantee explicit conservation; nevertheless, we find good agreement with numerical test problems and CCSN results.

We acknowledge the original version of `GR1D` was not formulated with the evolution of magnetic fields due to the assumed spherical symmetry. In many contexts, multiple dimensions are needed to capture the proper evolution of B fields. As `FLASH` is capable of 3D simulations, to capture the multidimensional magnetic field effects on the metric potential and gravitational mass, we account for b^2 contributions through the h^* and P^* quantities in Equation (5.27) and Equation (5.28).

Recall, the dot product of two vectors u^μ and u^ν is related to the metric by $\vec{u} \cdot \vec{u} = g_{\mu\nu} u^\mu u^\nu$. Thus multidimensional contributions to the spacetime can still be captured through the dot products of the velocity (via W) and magnetic field (via b^2) with the spatial metric, even if the spacetime evolution occurs only in one dimension.

5.4.4 Radiation Transport

During the collapse phase, a parameterized deleptonization scheme (Liebendörfer, 2005) is employed, which approximates the electron fraction (Y_e) at a given zone by its density value. While

not exactly correct, it provides an accelerated method to evolve simulations through collapse.

After core bounce—when the central density exceeds 2×10^{14} g cm^{-3} and the central entropy reaches 3 k_B/baryon—the code makes use of a leakage scheme to account for the loss of leptons streaming from the PNS core (O'Connor & Ott, 2010). The interaction of the radiation to the momentum, energy, and electron fraction is accounted via the source terms outlined in Equation (5.10): $R^{\nu}_{Y_e}$, $Q^{\nu,E}_{S_j}$, $Q^{\nu,M}_{S_j}$, $Q^{\nu,E}_{\tau}$, and $Q^{\nu,M}_{\tau}$. $R^{\nu}_{Y_e}$ is a source/sink that accounts for changes in Y_e due to energy deposition of neutrinos into matter. $Q^{\nu,E}_{S_j}$ and $Q^{\nu,E}_{\tau}$ account for momentum and energy changes of the fluid stemming from neutrino heating. $Q^{\nu,M}_{S_j}$ and $Q^{\nu,M}_{\tau}$ account for the impact of the radiation field on the momentum of the fluid-neutrino system. These latter two quantities depend on the neutrino pressure gradient $\partial P_{\nu}/\partial r$. The neutrino source terms are explicitly derived in Appendix A.5.

When calculating the necessary metric terms in the evolution of the spacetime, namely X and Φ, there is dependence on the spatial coordinate, hydrodynamic evolved variables, and the radiation transport primitives (e.g., τ^{ν}_{m}). In the version of `FLASH` used to complete these simulations (version 4), after the update step, the hydrodynamic evolved variables are known at the $n+1$ timestep, yet the value of τ^{ν}_{m} is only known at timestep n, or $\tau^{\nu\,n}_{m}$. This technique is similar to that used in other work (e.g., `GR1D`) and allows for performant explorations of CCSN behavior. While the neutrino contributions to the spacetime may be lagged by a timestep, the aforementioned neutrino source terms for the MHD scheme (e.g., $R^{\nu}_{Y_e}$ and $Q^{\nu,E}_{S_j}$) are properly synchronized. We reserve including $\tau^{\nu\,n+1}_{m}$ in the spacetime update for future work.

5.4.5 Ordering the Multiphysics Update

While the MoL scheme ensures each multiphysics subunit is updated simultaneously, the respective calls within `FLASH` are still called sequentially. For clarity, we offer the ordering of the calls to each physics subunit. After the MoL update is executed—RHSs added to the evolved variables—the evolved variables are at the $n+1$ time step. The primitive variables must now be recovered.

The first step is recovering the spatial metric. According to Equation (5.30), the $m(r,t)$ can be

expressed as a function of the evolved variables. Then the averaging and remapping procedure is followed as outlined in Section 5.4.3.1. Once $m(r,t)$ is calculated, γ_{ij} can be recovered using the transformations outlined in Appendix A.1 and Appendix A.2.

With an updated spatial metric, we follow the `con2prim` procedure(s) outlined in Section 5.4.6. This process yields the primitive MHD variables. With the spatial metric and primitive MHD quantities we use Equation (5.28) to recover the lapse dependent terms.

Lastly, the radiation transport terms are updated to the $n+1$ time step. This sequence concludes the recovery process needed for Input/Output (IO) and guard cell filling. The next multiphysics update begins and the process is repeated.

Below offers a succinct review of the different steps of an MoL update and the inputs used:

1. Calculate RHSs for vector of evolved variables
2. Update evolved variables
3. Spacetime: calculate γ_{ij}^{n+1} using $\mathbf{U}^{n+1}$ and $\tau_m^{\nu\, n}$
4. MHD: con2prim using γ_{ij}^{n+1} and $\mathbf{U}^{n+1}$
5. Spacetime: calculate α^{n+1} using ρ^{n+1}, ϵ^{n+1}, v_i^{n+1}, b_i^{n+1}, γ_{ij}^{n+1}, and $\tau_\Phi^{\nu\, n}$
6. Radiation Transport: calculate P_ν^{n+1} and $R_{Y_e}^{\nu\ \ n+1}$
7. Repeat

5.4.6 Conservative to Primitive Transformation

In our finite volume (FV) scheme, evolved (sometimes called conservative) variables can be analytically calculated in terms of the primitives variables and spatial metric through use of Equations (5.11-5.15)—these steps represent the primitive to conservative (prim2con) transformation. However, once the RHSs are applied during the update step, the con2prim transformation must be done numerically. We use the formulation introduced in Neilsen et al. (2014) and Palenzuela et al.

(2015) because of its robustness (Siegel et al., 2018). For convenience we outline the details of this 1D root finder that uses Brent's method (Brent, 1971) and a 3D Newton-Raphson (NR) rootfinder (Cerdá-Durán et al., 2008).

5.4.6.1 1D Brent Rootfinder

For clarity, variables with a hat (e.g., $\hat{h}$) are updated each iteration step. This method solves

$$f(x) = x - \hat{h}\hat{W} = x - \left(1 + \hat{\epsilon} + \frac{P(\hat{\rho}, \hat{\epsilon}, Y_e)}{\hat{\rho}}\right)\hat{W} \tag{5.31}$$

for the unknown $x \equiv hW$. We introduce the shortcut variables

$$q \equiv \tau/D \tag{5.32}$$

$$r \equiv S^2/D \tag{5.33}$$

$$s \equiv B^2/D \tag{5.34}$$

$$t \equiv B_i S^i/D^{3/2} \tag{5.35}$$

which bound x according to

$$1 + q - s < x < 2 + 2q - s. \tag{5.36}$$

We now review the steps taken to perform a single iteration step.

1. Using the definition of S_i (Equation (5.13)) and the previous shortcut variables, the Lorentz factor can be written as
$$\hat{W}^{-2} = 1 - \frac{x^2 r + (2x + s)t^2}{x^2(x + s)^2} \tag{5.37}$$
2. Using Equation (5.11) solve for the density at the given iteration: $\hat{\rho} = D/\hat{W}$.

3. Apply the definition of specific internal energy $\epsilon = h - 1 - P/\rho$ and the previous shortcut variables for

$$\hat{\epsilon} = -1 + \frac{x}{\hat{W}}(1 - \hat{W}^2) + \hat{W}\left[1 + q - s + \frac{1}{2}\left(\frac{t^2}{x^2} + \frac{s}{\hat{W}^2}\right)\right] \tag{5.38}$$

4. If temperature is needed, an EOS call can be used to invert $\hat{\epsilon}$ and find the pressure $P(\hat{\rho}, \hat{\epsilon}, Y_e)$.

Once x is found within a user-defined tolerance, ρ can be found using Equation (5.11) and Equation (5.37); ϵ can be found using Equation (5.38). The velocity components can be found with the following equation

$$v^i = \frac{\gamma^{ij} S_j}{z + B^2} + \frac{B^j S_j B^i}{z(z + B^2)} \tag{5.39}$$

where $z = x\rho W$.

5.4.6.2 3D Newton-Raphson Rootfinder

The `con2prim` solver attempts the 3D NR method described here first, as it has demonstrated accuracy and fast convergence for given roots (Siegel et al., 2018). This method finds the roots for temperature T, W, and z through solving a system of three equations:

$$\left(\tau + D - z - B^2 + \frac{(B^i S_i)^2}{2z^2} + P\right)W^2 - \frac{B^2}{2} = 0, \tag{5.40}$$

$$\left((z + B^2)^2 - S^2 - \frac{2z + B^2}{z^2}(B^i S_i)^2\right)W^2 - (z + B^2)^2 = 0, \tag{5.41}$$

$$\frac{z - DW - PW}{DW} - \epsilon(\rho, T, Y_e) = 0. \tag{5.42}$$

During the iterations, P and $\epsilon(\rho, T, Y_e)$ are obtained through calls to the EOS. With solutions for T, W, and z, ρ is obtained through Equation (5.11), v^i from Equation (5.39), and ϵ from an EOS call. As this NR scheme is not guaranteed to converge, if 200 iterations (user-defined) have occurred without a converged root, the `con2prim` solver falls back on the 1D Brent method described in Section 5.4.6.1 which is guaranteed to converge for bounded roots.

IC #1	IC #2
$(\rho_L, \rho_R) = (10, 1)$	$(\rho_L, \rho_R) = (1, 1)$
$(P_L, P_R) = (13.33, 0)$	$(P_L, P_R) = (10^3, 10^{-2})$
$(v_L, v_R) = (0, 0)$	$(v_L, v_R) = (0, 0)$

Table 5.1: Sets of initial conditions (IC) for pure hydrodynamic shock tube test, as first shown in (Martí & Müller, 2003). The subscripts left (L) and right (R) describe the dimensionless primitive variables on each side of an interface at $x = 0.5$, for a domain $x = [0, 1]$.

5.4.7 Maintaining Divergence Free Magnetic Field

To enforce $\nabla \cdot \vec{B} = 0$, we use a method of generalized Lagrangian multipliers (GLM), also called divergence cleaning (Dedner et al., 2002; Mignone et al., 2010). Rather than requiring additional memory to store face-centered data like the alternate constrained transport method (Mignone et al., 2019), divergence cleaning only requires cell centered data and advects away nonzero divergence terms at the speed of light. We test the behavior of this method for a series of flat spacetime MHD tests in Section 5.5.2. In practice, for a curved spacetime, the scalar field ψ which advects away nonzero $\nabla \cdot \vec{B}$ terms depends upon γ_{ij}. While this dependence will be weak for flatter spacetime, it becomes more important as it becomes more extreme (e.g., before BH formation). Thus, we refrain from conducting MHD tests in curved spacetimes. For future work, we will implement more robust treatments such as those suggested in Mösta et al. (2014) or (Porth et al., 2017).

5.5 Tests

To verify the behavior of our code, and stress the multiphysics evolution in different ways, we perform a suite of tests for four scenarios: a purely hydrodynamic relativistic shock tube, a magnetized relativistic shock tube, a highly energetic compact star, and the collapse of a uniform dust cloud into a black hole. While up to fourth order time integration is possible with the current MoL implementation in FLASH, all tests are completed with a 2nd order Runge–Kutta (RK) time integrator and the HLLE approximate Riemann solver.

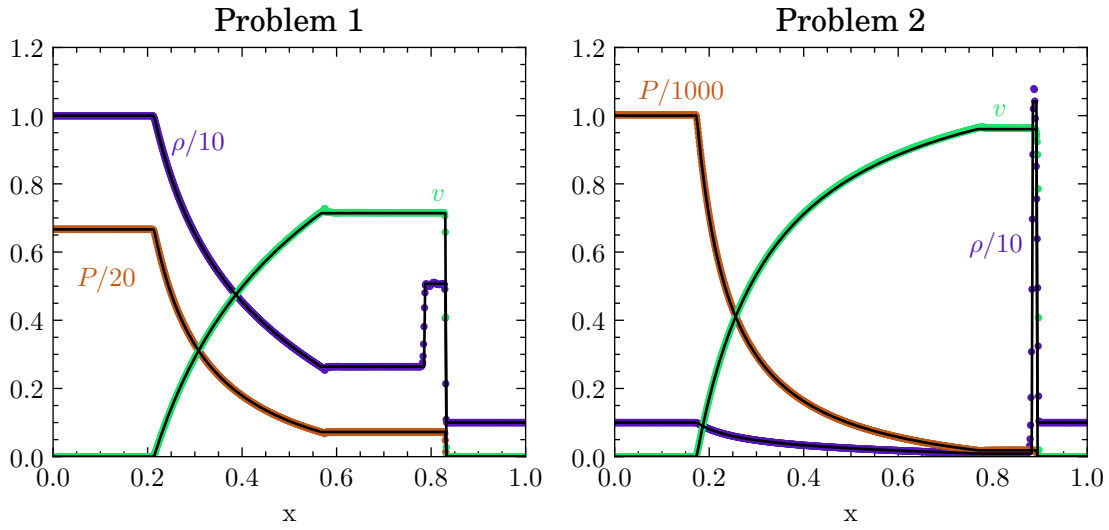

Figure 5.1: Relativistic, pure hydrodynamic shock tube results, originally proposed by (Martí & Müller, 2003). Colored points represent FLASH output for the density, pressure, and velocity; black lines are exact solutions at a simulation time of $t = 0.4$. Initial conditions for each problem can be found in Table 5.1.

5.5.1 Relativistic Shock tube.

The relativistic shock tube explores two different sets of initial conditions, as proposed by Martí & Müller (2003); the specific initial conditions are outlined in Table 5.1. By design, this problem is constructed to stress the code with the formation of shocks at high energies and velocities that approach the speed of light. These 1D tests assume a Minkowski spacetime with an EOS of the form $P = (\Gamma - 1)\rho\epsilon$, with $\Gamma = 5/3$. These tests use 1000 equally spaced grid zones over a dimensionless domain running from $x = [0, 1]$ and WENO5 reconstruction (Shu, 2009). They are performed with a Courant-Fredericks-Levi (CFL) factor of 0.5. In Figure 5.1 we notice good agreement between the analytic solution (black line) and FLASH output (colored points) at a time of $t = 0.4$.

5.5.2 Magnetized Shock Tube

Name	(ρ_L, ρ_R)	(ϵ_L, ϵ_R)	v_L	B^t_L	v_R	B^t_R	B^n	Γ	T_{end}
B1	(1, 0.125)	(1, 0.8)	0	(1.0, 0)	0	(-1.0, 0)	0.5	2	0.4
B2	(1, 1)	(45, 1.5)	0	(6.0, 6.0)	0	(0.7, 0.7)	5.0	5/3	0.4
B3	(1, 1)	(1500, 0.15)	0	(7.0, 7.0)	0	(0.7, 0.7)	10.0	5/3	0.4
B4	(1, 1)	(0.15, 0.15)	(0.999, 0, 0)	(7.0, 7.0)	(-0.999, 0, 0)	(-7.0, -7.0)	10.0	5/3	0.4
B5	(1.08, 1)	(1.425, 1.5)	(0.4, 0.3, 0.2)	(0.3, 0.3)	(-0.45, -0.2, 0.2)	(-0.7, 0.5)	2.0	5/3	0.55

Table 5.2: Initial conditions for relativistic MHD shock tubes. The subscripts left (L) and right (R) describe the dimensionless primitive variables on each side of an interface. $v = (v^x, v^y, v^z)$ indicates the x, y, and z velocity components are indicated by the ordered triplet. $B^t = (B^y, B^z)$ indicates the ordered pair represents the transverse y and z components of the magnetic field. $B^n = B^x$ indicates the normal component of the magnetic field is in the x direction.

The magnetized shock tube is a reliable test to ensure the code is properly exhibiting MHD wave behavior, in the presence of high pressures and relativistic fluid velocities. This setup once again sets left and right states for the various primitive variables inspired from Balsara (2001) and is a generalization of the Brio-Wu shock tube setup (Brio & Wu, 1988), with similar nomenclature for each test problem (e.g., B1 for 'Balsara 1') (Mösta et al., 2014). The specific initial conditions are outlined in Table 5.2. Each test uses a gamma law EOS, $P = (\Gamma - 1)\rho\epsilon$, with 1000 equally spaced grid points on a domain $x = [0, 1]$ and a CFL condition of 0.8. The five simulations use TVD reconstruction.

In Figure 5.2 observe `FLASH` output (colored points) matching the analytic result (black line) for the first set of initial conditions in the Balsara suite of tests. The small spike at x $\sim$ 0.5 for density and pressure is the formation of a slow moving compound wave, originally noted with the introduction of these test problems (Brio & Wu, 1988). For space considerations, we display the remaining four baseline results in Appendix A.6. For all five tests, we notice good agreement between `FLASH` output and the analytic results, provided by Giacomazzo & Rezzolla (2006).

5.5.3 TOV Star

To test how our relativistic hydrodynamics scheme couples to an evolving spacetime, we study the oscillations of a TOV star maintaining hydrostatic equilibrium. Our initial 1D profile is obtained by solving the Tolman-Oppenheimer-Volkhoff equations (Tolman, 1939). During the hydrodynamic and spacetime evolution, a polytropic EOS $P = K\rho^{\Gamma}$ with polytropic constant $K = 100\,(\sim 1.455 \times 10^5$ [cgs]), adiabatic index $\Gamma = 2$, and central density $\rho_c = 4.929 \times 10^{14}$g cm^{-3} is used. To determine ϵ we make use of a gamma-law EOS $P = (\Gamma - 1)\rho\epsilon$. These 3D models use WENO5 reconstruction to reduce the numerical dissipative effects that would be introduced with TVD reconstruction.

As the spacetime and fluid evolve, the TOV star attempts to achieve hydrostatic equilibrium. Between numerical diffusion causing the star to collapse and overshooting upon expansion causing the central density to lower, the star will experience oscillations about an equilibrium point. Figure

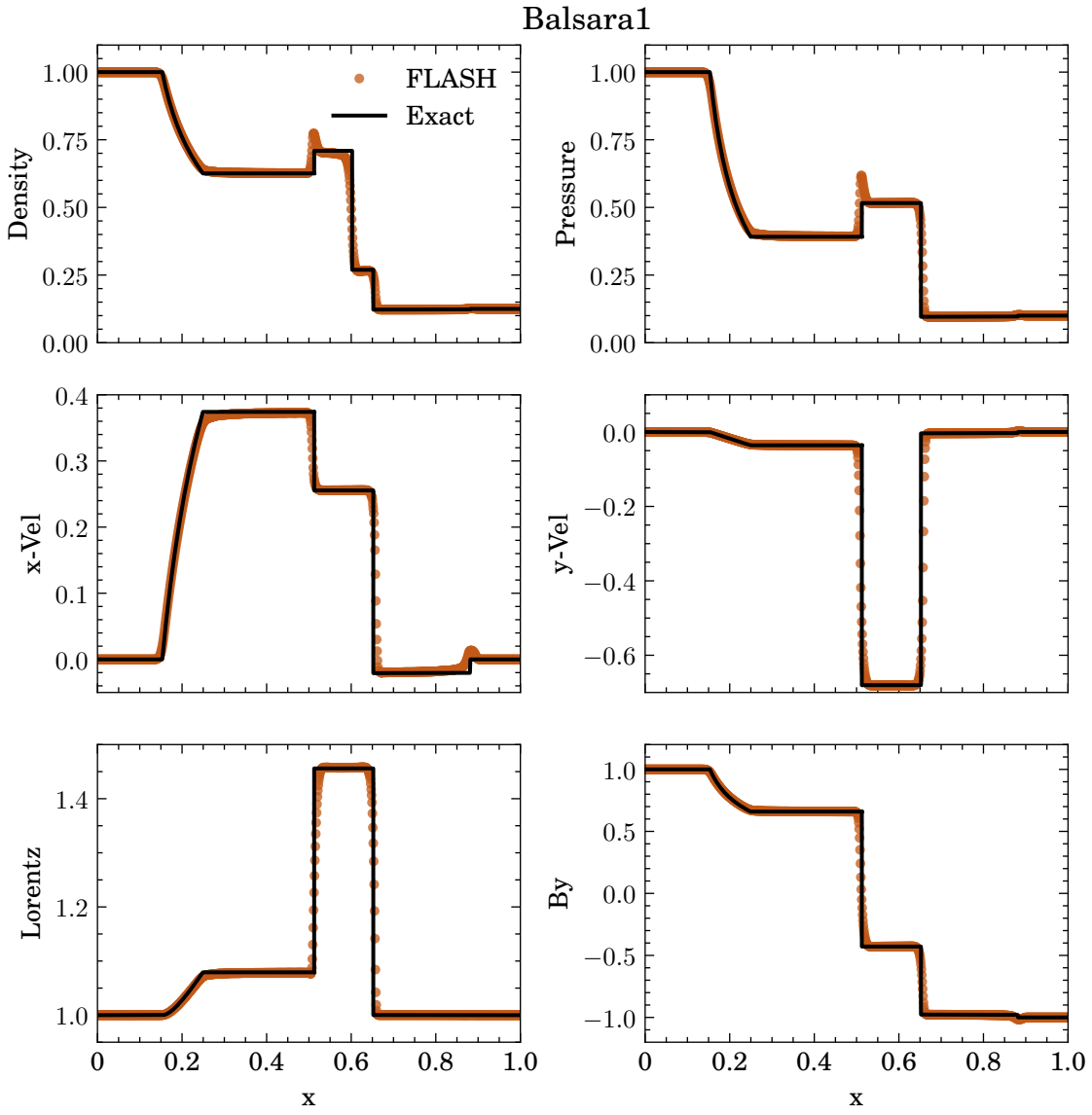

Figure 5.2: Primitive variables density, pressure, x-velocity, y-velocity, Lorentz factor, and y component of the magnetic field (By) at $t = 0.4$ for the Balsara1 test problem. The slight spike seen x $\sim$ 0.5 is a slow moving compound wave originally seen in (Brio & Wu, 1988).

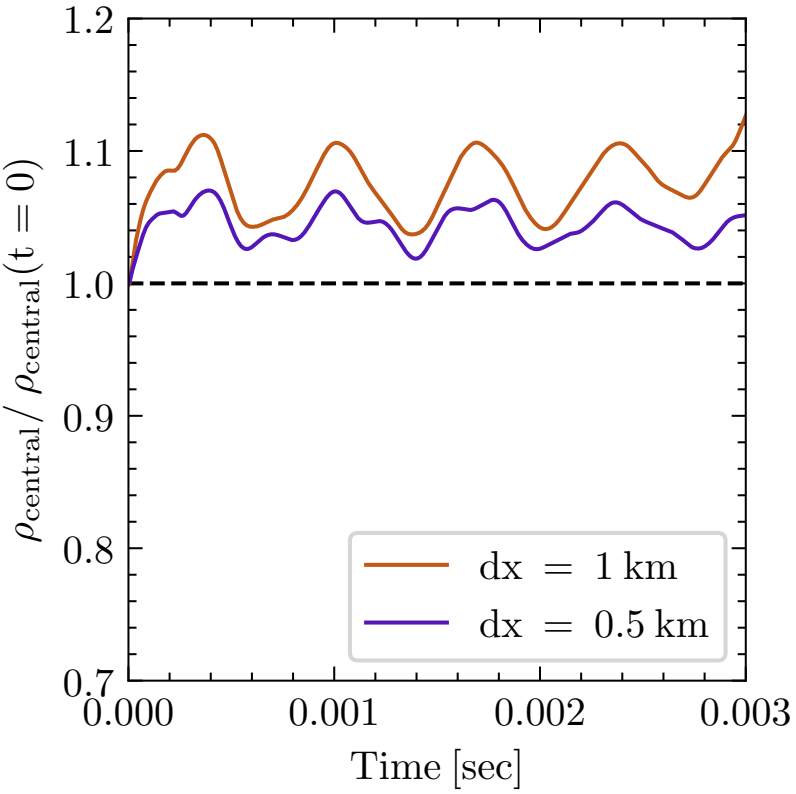

Figure 5.3: TOV star normalized central density over 3 ms evolution for two different resolutions. This test is conducted in 3D, using Cartesian coordinates. We see smaller amplitude oscillations, for increasing resolution as expected. The black dashed line indicates the original central density at $t = 0$.

5.3 displays the central density oscillations for a 3D test case in Cartesian coordinates. The initial matter profile is centered at the origin and extends 20 km in each direction on a uniform grid. The low resolution case 40 grid zones along each axis for a resolution of 1 km. The high resolution case has 80 grid zones along each axis, yielding 0.5 km resolution. For the high resolution case, we notice smaller oscillations and convergence toward the original central density.

For comparison, we offer Figure 5.4, which displays the normalized central density evolution in the top panel for three different resolutions: $r0 \sim 1.5$ km, $r1 \sim 0.74$ km, and $r2 = 0.37$ km (Mösta et al., 2014). Both test cases use the same EOS. However the TOV star in Figure 5.4 has a central density $\sim$ 1.5 times larger at $\rho_c = 7.91 \times 10^{14}$g cm^{-3}. The setup also contains a magnetic field that evolves along with the fluid and spacetime. These contributions can change the behavior of

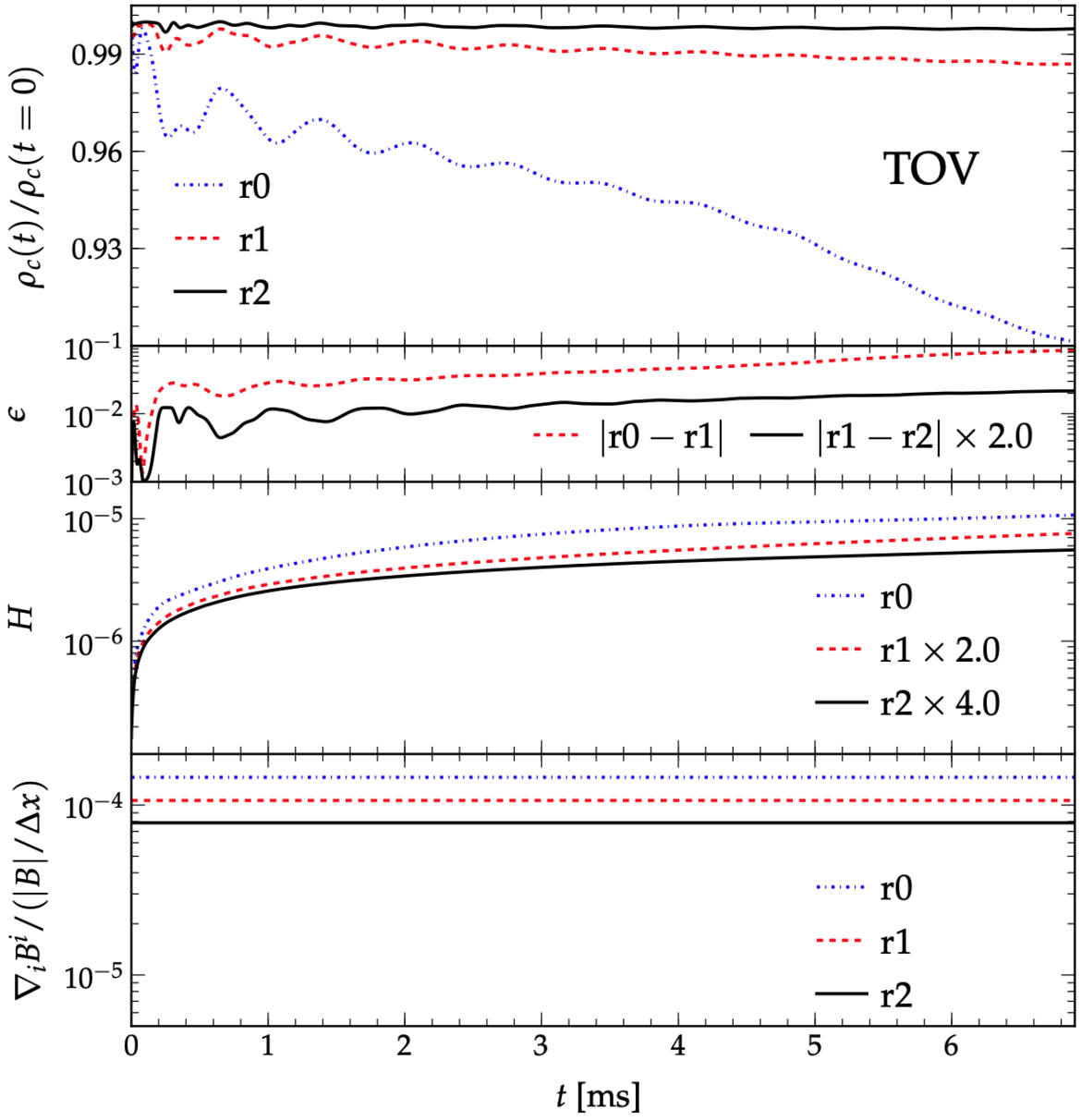

Figure 5.4: Three dimensional TOV star over 6 ms of evolution for three different resolutions, taken from Mösta et al. (2014). From top to bottom, panels represent normalized central density, difference in normalized central density between two resolutions, L_2 norm of the Hamiltonian constraint, and normalized divergence of the magnetic field. Relevant to this work is the top panel, which can be compared to Figure 5.3. The three resolutions correspond to $r0 \sim 1.5$ km, $r1 \sim 0.74$ km, and $r2 = 0.37$ km.

the star by having a higher central pressure, due to the higher central density along with magnetic contributions. These effects can provide additional support, causing it to initially expand, thereby lowering the initial central density. A more identical setup with the matter profile and magnetic field would be ideal and is reserved for future work.

5.5.4 Oppenheimer-Snyder Collapse

To test the coupled evolution of the spacetime and hydrodynamics in an extreme spacetime environment, we model the collapse of an initially constant density sphere with no pressure ($P = 0$): Oppenheimer-Synder collapse (OSC) (Oppenheimer & Volkoff, 1939). We use an identical setup used in the `GR1D` code (O'Connor & Ott, 2011); for completeness, we include the simulation details. The dust cloud has an initial mass of $M = 1$ and $R = 10\,(\sim 14.8$ km). We use a polytropic EOS $P = K\rho^{\Gamma}$, where we select $K = 10^{-20}$ [cgs] and adiabatic index $\Gamma = 5/3$. The atmosphere outside the dust is set to a value of $\rho = 1$ g cm^{-3}. The simulation is initialized on a 1D uniform grid of 9000 data points and uses TVD reconstruction.

To verify the behavior of the spacetime evolution in extreme regimes, refer to Figure 5.5. Color points refer to the `FLASH` outputs and black lines are the analytic profiles at various times: $t = 0.15$, 0.17, 0.20, 0.21, & 0.30 ms. The top panel displays the density profile, normalized by the initial central density $\rho_0 = 1.475 \times 10^{14}$ g cm^{-3}. The bottom panel displays the α profile. The lapse function approaches an expected value of 0 as the edge of the dust cloud approaches its Schwarzschild radius of $r = 2\,(\sim 3.0$ km). As seen in O'Connor & Ott (2010), we notice an expected spike in the central density near $r = 0$; this artifact is attributed to factors in the source terms that depend on $1/r$ which diverge near the coordinate origin.

5.6 Supernova Simulations

Having stressed the code through a variety of baseline tests, we examine the impact of the new relativistic features in the more sophisticated CCSN multiphysics system: coupled evolving spacetimes, GR hydrodynamics, and radiation transport. All models make use of the SFHo EOS (Steiner et al., 2013a) and WENO5 reconstruction.

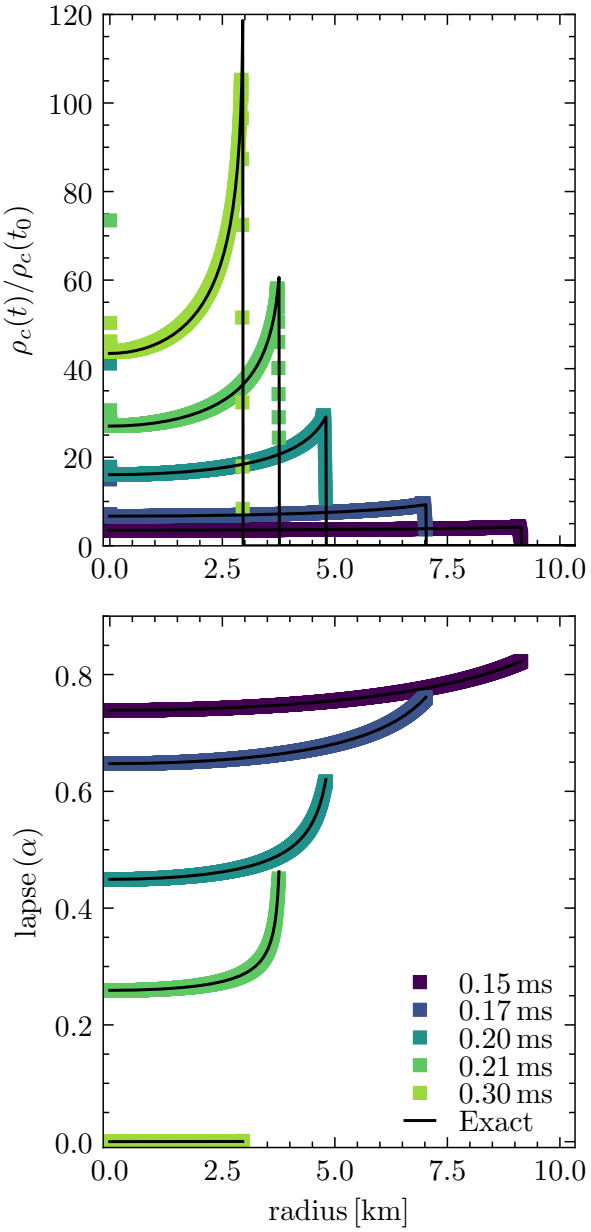

Figure 5.5: One dimensional evolution of the OSCollapse test, in which a dust cloud collapses into a black hole. Brighter colors correspond to later times, with the last time indicating black hole formation. (Top) Normalized central density radial profile. (Bottom) Lapse function radial profile.

5.6.1 1D CCSN Models

We begin with a suite of six 1D simulations evolved ~ 0.5 sec after bounce. We select a 12-, 40-, and 60 $M_\odot$ progenitors for their varying ξ values. To isolate the impact of the evolving spacetime and GRMHD scheme, we do not employ multidimensional effects of turbulence, such as the Simulating Turbulence in Reduced-dimensionality (STIR) framework (Couch et al., 2020b), which still only has Newtonian treatments of turbulence, or the relativistic analogue from Boccioli et al. (2021).

Figure 5.6 displays the results of this 1D CCSN simulation suite. Progenitor masses are indicated by colors of different brightness. Different physics treatments are indicated by line pattern: solid dark lines use an evolving spacetime with GR hydrodynamics and dotted lines use GREP with Newtonian hydrodynamics. The left column displays properties of hydrodynamic evolution—shock radius and PNS quantities—and the right column displays properties of the neutrino emission—luminosity, energy, and neutrinosphere radius for ν_e−.

5.6.1.1 Shock Radius Behavior

The top left panel of Figure 5.6 displays the shock radius evolution for all six models. Within the ~ 0.5 ms pb window, these models do not explode. These models are inherently 1D, preventing them from depositing sufficient turbulent kinetic energy behind the shock that is more easily accomplished in 3D. As turbulence behind the shock is one of the principle drivers towards a successful explosion (Couch & Ott, 2015; Burrows & Vartanyan, 2021), this behavior is expected.

We note that shock radii for the GR case are marginally smaller compared to the GREP case. We expect the GR method to produce more gravitationally bound systems, compared to GREP. Furthermore, this behavior is noted in other work that compares shock evolution between GR hydrodynamics and less sophisticated hydrodynamic treatments (Kuroda et al., 2012).

5.6.1.2 PNS Characteristics

The properties of the PNS offers valuable insight regarding the birth of compact remnants from CCSNe. The lower left panel of Figure 5.6 displays the radius of the PNS. In our work, we define

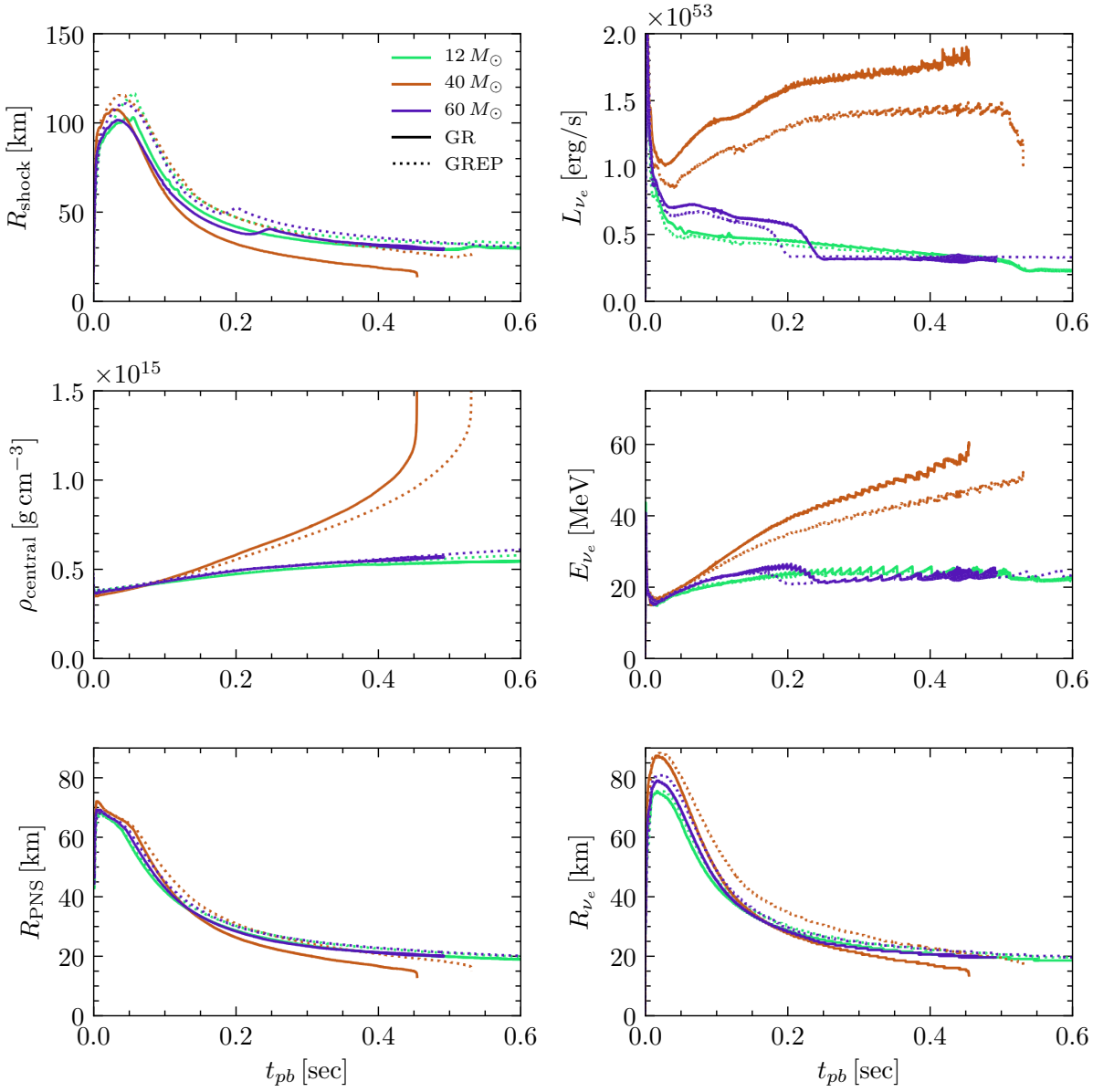

Figure 5.6: Results from six 1D CCSN models. Colors represent different progenitors and line styles represent different physics treatments; solid lines use evolving spacetime with GR hydrodynamics, and dotted lines use GREP with Newtonian hydrodynamics. (Top left) Shock radius evolution. GR cases show marginally smaller smaller shock radii compared to GREP. (Central left) Central density evolution. Less compact progenitors show similar central density evolution. The 40 $M_\odot$ case with GR reaches BH formation $\sim$ 75 ms earlier than GREP. (Lower left) PNS radius evolution. (Upper right) Electron type neutrino luminosity. (Central right) Electron type neutrino energy. We notice harder ν_e- spectra for GR, compared to GREP, with the more compact progenitors exhibiting more of a difference. (Lower right) Neutrinosphere for ν_e-.

the 'surface' of the PNS as the density contour of 10^{11} g cm^{-3}. For the less compact 12 $M_\odot$ and 60 $M_\odot$ cases, the PNS evolution is nearly identical. However, the 40 $M_\odot$ case displays differences in $R_{\rm PNS} \sim 5$ km beginning 100 ms pb. This difference is attributed to the fact that the 40 $M_\odot$ is more compact. Thus, the differences between the approximate GREP and GR case, that properly accounts for contributions to the spacetime, will become more pronounced.

5.6.1.3 Central Density Evolution and Black Hole Formation

The central left panel displays the central density evolution. The lower compactness 12 $M_\odot$ and 60 $M_\odot$ display similar central density evolution throughout the simulation duration. Similar to the previous case, the lower ξ progenitors will have less contributions to the spacetime curvature, lending to similar evolution between the GREP and GR cases.

The high-ξ 40 $M_\odot$ case collapses to BH within 600 ms after bounce for both cases. This formation is indicated by the asymptotic increase in $\rho_{\rm central}$. We note BH formation roughly 75 ms earlier in the GR case, compared to GREP. The ability of the relativistic hydrodynamics to capture strong field effects allows the collapse to BH to occur on smaller timescales. O'Connor & Couch (2018b) compare BH formation time between the GREP and GR case (with `GR1D`) and note BH formation to occur $\sim$ 20 ms later with GREP, compared to GR. As this reference case uses a different 40 $M_\odot$ progenitor (Woosley & Heger, 2007), we attribute a delay in BH formation that is also 10s of ms promising behavior for the implemented GR case in `FLASH`.

5.6.1.4 Neutrino Signal

As mentioned in the previous subsection, a more compact PNS is a result of the inclusion of relativistic effects. Another observable modified will thus be the neutrinos. Forming at a smaller radius, the temperature at the neutrinosphere will, on average, be higher. This higher temperature will, in turn, shift the emitted neutrinos to higher energies—a harder neutrino spectrum. However, the more gravitationally bound core will cause greater redshift of the neutrinos as they stream to the outer parts of the supernova gravitational potential well. These competing effects offer a

quintessential example of the nonlinear nature of the CCSN system. Nevertheless, in practice, the net result is a higher neutrino luminosity and the production of neutrinos with higher energies (Kuroda et al., 2012).

The lower right panel of Figure 5.6 displays the neutrinosphere radii for ν_e- to be smaller for the GR cases, as compared to GREP. The central right panel shows similar neutrino energies for electron type neutrinos E_{ν_e-} for the low compactness progenitors. The energy difference for the $40\,M_\odot$ case shows a larger difference between the GREP and GR case, which is a direct consequence of the difference in R_{ν_e-}. All cases capture the gradual increase in E_{ν_e-}, which is indicative of the contracting PNS due to ν losses. As R_{ν_e-} decreases, it recedes to regions of higher temperature. The upper right panel shows an associated larger neutrino luminosity for ν_e- for GR, compared to GREP. These findings emphasize the importance of incorporating relativistic effects into multiphysics simulations because of the noticeable impact on predictions of multimessenger observables.

5.6.1.5 Code Performance

Our 1D models show sustained evolution by evolving ~ 0.5 sec after core bounce. As such, we choose to analyze the performance metrics of the 600 ms evolution of the $12\,M_\odot$ case. The GR case required 500 core hours for completion, whereas the GREP case required only 20 core hours. The 25× increase in computational cost can be explained by two factors: the number of calls to evolve gravity and the more computationally intensive GRMHD procedure.

The physics routine that updates gravity is called six times as much for the GR case, compared to the GREP case. Below details the calling procedures for each physics treatment. For the GREP case, the call to update gravity within `FLASH` is made once per time step. For the GR case, the MoL approach evolves the MHD scheme alongside the spacetime. As noted in Section 5.4.5, the spacetime evolution must be called twice, once to calculate γ_{ij} and once to evolve α. Thus, spacetime is called twice per MHD evolution. As these simulations use an RK2 integration method, which uses two stages per time step, spacetime evolution occurs four times in the MoL

procedure. For any physics updates that happen outside the MoL procedure, such as parameterized deleptonization, γ_{ij} and α must be updated once again. In review, for the GR case, the call to update gravity is made six times per time step.

The GRMHD procedure also incurs more computational expense than the Newtonian case used alongside the GREP. For example, the time step restriction—which depends on the sound speed c_s—is calculated using two different expressions. The GREP case relies on a simple relation

$$c_s^2 = \frac{\Gamma_c P}{\rho}, \tag{5.43}$$

where Γ_c is an adiabatic index. By contrast, the relativistic analogue given in Rezzolla & Zanotti (2013) is

$$c_s^2 = \frac{c^2}{h}\left[\left(\frac{\partial P}{\partial \rho}\right)_\epsilon + \frac{P}{\rho^2}\left(\frac{\partial P}{\partial \epsilon}\right)_\rho\right], \tag{5.44}$$

where $(\partial P/\partial \rho)_\epsilon$ is the derivative of pressure with respect to density at constant specific internal energy. $(\partial P/\partial \epsilon)_\rho$ is the derivative of pressure with respect to specific internal energy at constant density. In practice, just after bounce, for a time step dt, we notice $dt_{\rm GR} = 0.25 dt_{\rm GREP}$. In addition to the time step restriction, the `con2prim` procedure requires multiple calls to the EOS, as outlined in Section 5.4.6. For tabulated EOSs, this iterative interpolation procedure can be costly, compared to simple analytic relations used in Newtonian hydrodynamics. Between the time step restriction and EOS calls, we attribute the remaining factor of 4 discrepancy between the GR and GREP run time.

Improving the performance of the spacetime evolution and GRMHD scheme would be a valuable revision to the work presented here. Likewise, the motivation for this work is not to outperform GREP, but remain competitive with CFC. Such a comparison is not currently viable within the FLASH framework and would require a cross collaborative project with a code such as `CoCoNut` (Cerdá-Durán et al., 2013).

5.6.2 2D CCSN Models

We also perform two, nonrotating axisymmetric simulations of the $12\,M_{\odot}$ progenitor to test the code in higher dimensions. Figure 5.7 displays the early time behavior of the same quantities described in the previous section, and focuses on the first $\sim$ 30 ms pb. We acknowledge prolonged evolution would allow clearer differences between GREP and GR to manifest, thus we limit our discussion of the 2D models to qualitative descriptions and save quantitative relations for future work with more suites of longer simulations. As these models are conducted in 2D, we note the GREP case does not include any additional, Newtonian multipole corrections to the gravitational potential.

5.6.2.1 Shock Radius Behavior

Figure 5.7 shows similar shock behavior to the corresponding 1D case; the less bound GREP system launches a larger shock just after core bounce. However, as these models are 2D, they capture another degree of freedom exhibited by the turbulence behind the shock. In general, the inclusion of relativistic hydrodynamics will increase the timescale on which convection occurs (Müller et al., 2013). To understand this difference, we appeal to the expression for the Brunt-Vaisala frequency $\omega_{\rm BV}$ for the Newtonian case given by Aerts et al. (2010)

$$\omega_{\rm BV}^2 = \frac{1}{\rho}\frac{\partial \Phi_N}{\partial r}\left(\frac{1}{c_s^2}\frac{\partial P}{\partial r} - \frac{\partial \rho}{\partial r}\right), \tag{5.45}$$

where Φ_N is the Newtonian gravitational potenital and c_s is the sound speed. The relativistic expression is given by Müller et al. (2013)

$$\omega_{\rm BV}^2 = \frac{\alpha}{\rho h \phi^4}\frac{\partial \alpha c^2}{\partial r}\left(\frac{1}{c_s^2}\frac{\partial P}{\partial r} - \frac{\partial \rho(1+\epsilon/c^2)}{\partial r}\right), \tag{5.46}$$

where ϕ is known as the conformal factor. This term originates from the CFC scheme. Physically it quantifies the deformation of spacetime through γ_{ij}. For the purposes of this work, ϕ^2 is similar to X from Equation (5.26). The physicality of $\omega_{\rm BV}$ represents the frequency with which a blob of material oscillates in an ambient medium. The larger $\omega_{\rm BV}$, the shorter the oscillation timescale.

One key difference between the Newtonian and GR description lies the first term. Between Equation (5.45) and Equation (5.46) there is a difference by a factor of $\alpha/h\phi^4$ which is $\sim \alpha/hX^2$ in this work. Thus, the strong field effects of time dilation $\alpha \leq 1$ and $X \geq 1$ create a smaller $\omega_{\rm BV}$, or the fluid will evolve on longer timescales. To show these effects, we produce slices of the CCSN Y_e profiles 30 ms after bounce, during the prompt convection phase of the CCSN. The panels in Figure 5.8 illustrate turbulence, through the mixing of material with differing Y_e. As displayed in the left panel of Figure 5.8, the GR case has not experienced enough time to create the finer turbulent structure seen in the GREP case (right panel). As such, more turbulent kinetic energy is deposited behind the shock and results in a larger $R_{\rm shock}$ for the GREP case.

5.6.2.2 PNS Characteristics

Both the $\rho_{\rm central}$ and $R_{\rm PNS}$ display similar behavior between the GR and GREP cases. This is behavior is expected because the low ξ of the progenitor does not exhibit pronounced differences compared to a high ξ case, as explained in the 1D results. Also, the early simulation time prevents differences arising from multidimensional accretion onto the PNS to influence the evolution. While longer simulation times would be ideal, the similarity of the PNS characteristics of the 12 $M_\odot$ model serves as an initial verification of the 2D extension of the evolving spacetime, because of similar behavior in the 1D case for 12 $M_\odot$.

5.6.2.3 Neutrino Signal

The neutrino properties remain extremely similar between the GR and GREP cases. The neutrinosphere for ν_e- and therefore E_{ν_e-} are nearly exact. L_{ν_e-} remains only marginally higher for GR, compared to GREP, as in the 1D case. For longer simulation times, a topic of investigation will be examining how multidimensional downflows onto the PNS are modified by relativistic hydrodynamics and therefore affect L_{ν_e-}.

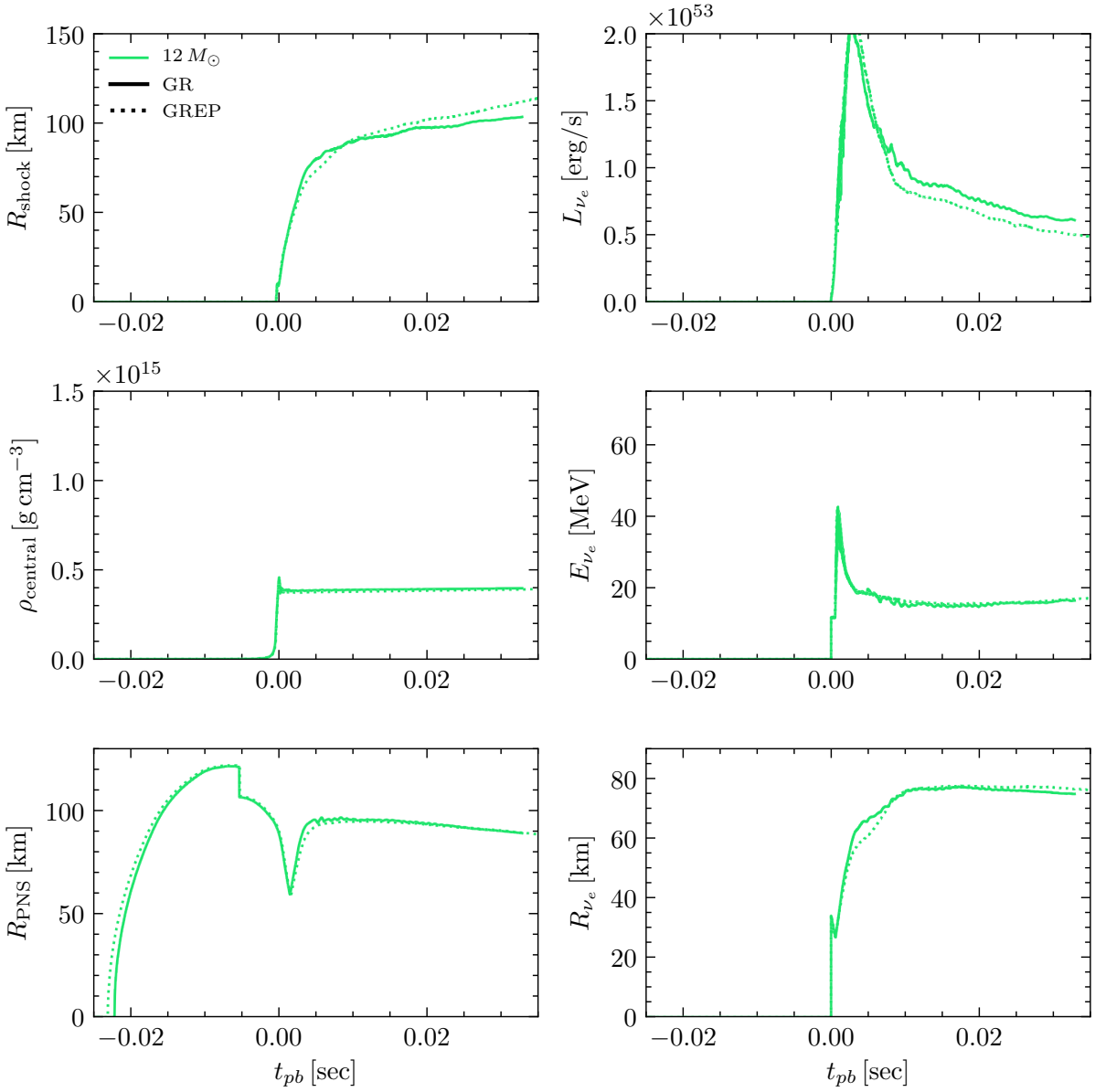

Figure 5.7: Equivalent panel labels as outlined in Figure 5.6, except applied to axisymmetric 12 $M_\odot$ models, emphasizing the first 30 ms of post bounce evolution. We notice similar characteristics between all quantities. There is a slightly larger shock radius for the GREP case, compared to the GR case. Likewise, there is a slightly smaller ν_e- luminosity for the GREP case, compared to the GR case.

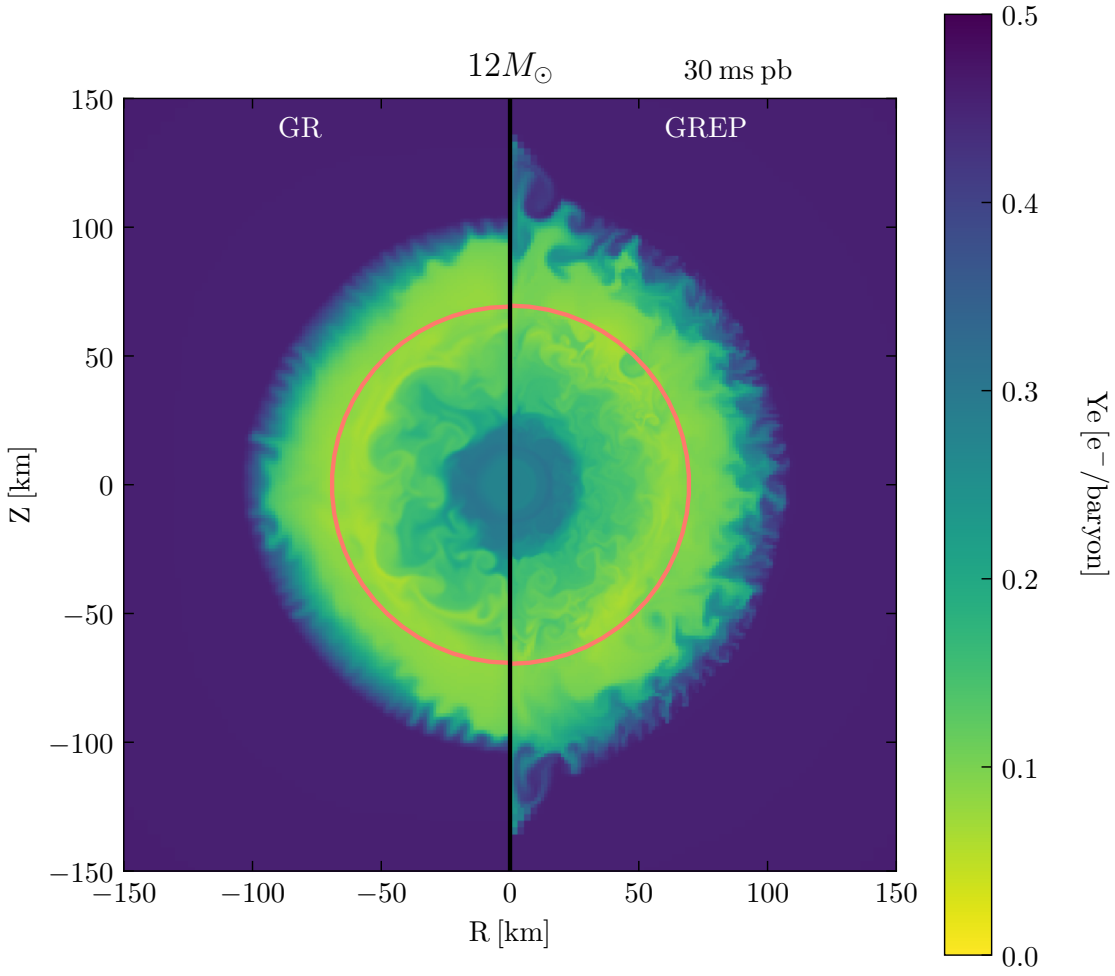

Figure 5.8: Central electron fraction (Y_e) profile at 30 ms post bounce. Left panel represent CCSN models with evolving spacetime and GR hydrodynamics, the model in the right panel uses GREP and Newtonian hydrodynamics, without any higher Newtonian multipole corrections. The orange arc represents the surface of the PNS. For the GR case we notice larger convective plumes developing and less mixing of low Y_e material at the shock interface.

5.7 Discussion and Summary

5.7.1 Looking Towards the Exascale

With the advent of exascale machines, the modern HPC ecosystem is requiring software development to adapt to machines with different hardware architectures and maximally utilize the number of processing units (e.g., CPUs and GPUS) available. This idea of performance portability is one of the cornerstones for the ongoing Exascale Computing Project (ECP)[1]. The goal of the ECP is to lead a national effort for advances in software design to address computationally intensive problems, only tractable on leadership class platforms achieving 10^{18} floating point operations per second (FLOPs). Of particular relevance to this work is the *ExaStar* project [2], whose computational aim is to develop multiphysics software compatible with AMR; the scientific goal is to better understand the origin of heavy element production from astrophysical explosions such as CCSNe.

To address this need, the future version of `FLASH`, named `Flash-X`[3] is currently public. `Flash-X` has been designed with performance portability in mind, by allowing input from the physics unit developers, those who maintain the code, and the hardware which the code is run on. Some examples include generating code that adapts to a given hardware-specific platform (Rudi et al., 2021) or modify data movement based on the memory layout of a computing resource (O'Neal et al., 2021).

To promote the use of the various physics implementations proposed here, we have integrated the MoL framework and memory layout into `Flash-X`. The integration of the GRMHD scheme is currently being ported over to `Flash-X` from `FLASH`. As a part of the larger *ExaStar* goal, this GRMHD scheme will be integrated with other multiphysics features. One implementation includes a dynamically evolving spacetime, following the 'Z4c' formulation of GR (Cao & Hilditch, 2012), to account for matter geometries that significantly deviate from spherical symmetry. Other physics features that will be coupled include accounting for neutrino transport such as `Thornado` (Laiu

[1] https://www.exascaleproject.org/
[2] https://www.exascaleproject.org/research-project/exastar/
[3] https://flash-x.org/

et al., 2020), a Monte-Carlo based approach, and a general relativistic M1 approach. Coupling these features together using the proposed MoL scheme will allow flexibility for users to select different physics features, provide numerical methods advanced enough to exercise the performance capabilities of exascale machines, and leverage adaptable code that can make use of many computing hardware layouts.

5.7.2 Summary

We have reviewed our new relativistic solver that is compatible with adaptive mesh refinement. The new elements integrated into `FLASH` are as follows:

- a GRMHD scheme accounting for magnetized fluid with high velocities and large energies,
- a fully general relativistic evolving spacetime in 1D,
- a novel multidimensional extension of the evolving spacetime,
- the inclusion of magnetic contributions to the spacetime curvature.

We offer a variety of baseline tests that verify the code behavior in the following scenarios:

- hydrodynamic shock tube evolution with relativistic velocities, see Figure 5.1,
- magnetized fluid with high Lorentz factors, see Figure 5.2 or Appendix A.6,
- highly energetic and dense material found in compact stars, see Figure 5.3,
- rapidly evolving spacetimes tracking BH formation, see Figure 5.5.

We also perform a suite of 1D and 2D CCSN simulations, comparing two sets of physics treatments: relativistic hydrodynamics with evolving spacetime (GR-case) and Newtonian hydrodynamics with the GREP (GREP-case). For both the 1D and 2D cases, we notice general trends that the GR-case generates PNSs more gravitationally bound than the GREP case. As these systems are more gravitationally bound, they launch weaker shocks. The neutrino quantities are also affected.

As the neutrinospheres form at smaller radii, CCSNe with the GR-case emit more energetic ν_e- and produce higher ν_e- luminosities, compared to the GREP-case.

Lastly, we highlight the performance portability of `Flash-X` and our recent integration of the MoL numerical tools. There is ongoing development to incorporate these GRMHD features into its framework in order to couple more general treatments of spacetime evolution and neutrino transport. Ultimately, these features will make use of exascale computing platforms to perform simulations of complex astrophysical systems such as CCNSe.

While these updates have allowed `FLASH` to become a more versatile tool, there is still work to be done. We plan to move beyond a Newtonian treatment of divergence cleaning, to account for the coupling between $\nabla \cdot \vec{B}$ and curved spacetimes (Porth et al., 2017). After this implementation, more multidimensional MHD tests in extreme spacetimes should be conducted, such as tracking magnetized CCSNe to BH formation. Likewise, more extensive multidimensional testing should be completed to quantify the impact of this evolving spacetime paired with relativistic hydrodynamics, as it compares to other treatments of gravity.

Acknowledging these caveats, the future of CCSN science into the exascale era remains optimistic. Anticipating future hardware architectures not only provides numerical tools that can utilize next generation machines, but provides an avenue to promote the longevity of decoding the physics that drives these stellar explosions.

M.A.P. was supported by a Michigan State University Distinguished Fellowship. S.M.C. is supported by the U.S. Department of Energy, Office of Science, Office of Nuclear Physics, under award Nos. DE-SC0015904 and DE-SC0017955 and the *Chandra X-ray Observatory* under grant No. TM7-18005X. This research was supported by the Exascale Computing Project (17-SC-20-SC), a collaborative effort of two U.S. Department of Energy organizations (Office of Science and the National Nuclear Security Administration) that are responsible for the planning and preparation of a capable exascale ecosystem, including software, applications, hardware, advanced system engineering, and early testbed platforms, in support of the nation's exascale computing imperative. The software used in this work was in part developed by the DOE NNSA-ASC OASCR Flash

Center at the University of Chicago.

Software used in this work: FLASH (see footnote 7), (Fryxell et al., 2000, 2010), Matplotlib[8] (Hunter, 2007), NuLib[9] (O'Connor, 2015), NumPy[10] (van der Walt et al., 2011), SciPy[11] (Jones et al., 2001–), Flash-X[12,13]

[8] https://matplotlib.org/
[9] http://www.nulib.org
[10] http://www.numpy.org/
[11] https://www.scipy.org/
[12] https://flash-x.org/
[13] https://github.com/Flash-X/Flash-X

CHAPTER 6

SUMMARY

6.1 Summary

This work presented new connections between GW signal features and CCSN source physics. Likewise, it introduced novel numerical solvers in the `FLASH` code that account for relativistic effects in multiphysics simulations. Chapter 2 incorporated 15 axisymmetric CCSN models with varying degrees of rotation. The early time GW bounce signals verify the behavior of the code to capture stellar collapse when dominated by rotational dynamics. During the accretion phase, we note the stabilizing effect of rotation on convection, per the Solberg-Hoiland stability criterion. This effect dampens the PNS oscillations, which is responsible for the 'rotational muting' of GWs in axisymmetry. Likewise, we note the tendency of rotation to centrifugally support the PNS as it accretes matter and contracts. This effect shifts the peak GW frequencies to lower values, due to the larger dynamical frequency of the compact object. Because the slope of the peak GW frequency $\dot{f}$ approaches zero with increasing rotation, we describe this effect as 'rotational flattening'. We also find the stabilizing effect of rotation slows the timescale on which convective overturn occurs within the shocked material. This effect consequently lowers the frequencies of the GWs directly emitted from the turbulent matter.

Chapter 3 analyzes 34 new axisymmetric and four previous 3D CCSN models quantifying the degree to which rotation modifies GW signals in CCSNe. We show the importance of robust neutrino transport during collapse, displaying differences in GW bounce signal amplitudes by $\sim$ 40% between simplified and advanced treatments. We show the bounce signal amplitude and angular momentum content near the supernova center can be approximated by a third order polynomial. For the first time using multidimensional models, we show a direct relationship between the compactness of the progenitor and the rate at which the peak GW frequency increases. This effect leverages multimessenger signals to show the importance of mass accretion on the rate

at which the PNS contracts. Building on the previous chapter, we quantify the impact of rotation on the rotational flattening of $\dot{f}$. We note an equation of state–independent, linear relationship between the degree which $\dot{f}$ decreases and the angular momentum content of the inner $1.75\,M_{\odot}$ of material. This observation shows the angular momentum content of the accreted material has a distinct impact on the PNS evolution. We introduce a novel method that combines two of the most detectable components of a single GW event to determine of the compactness of the progenitor. Furthermore, we outline a heuristic to use this method to predict explosion properties hours–days before shock breakout.

Chapter 4 reviews work with my undergraduate research assistant, Steven VanCamp. We address observational considerations by investigating the poorly explored impact of viewing angle on GW emission from CCSNe. We introduce a novel visualization method to characterize the distribution of GW emission over all angles, at a given moment in time. Applying this method throughout the supernova duration yields a distribution that identifies dominant directions of GW emission, depending on the physical mechanism generating gravitational radiation. We conclude there is no single dominant viewing angle over the entire CCSN, rather a preferred direction of GW emission that evolves in time. For nonrotating cases, this angle drifts over all viewing angles. For rotating cases, the preferred direction of GW emission lies along the supernova equator and then aligns with the axis of rotation. Furthermore, for rotating CCSNe this preferred direction seems to precess around the axis of rotation. The only instability we observe that potentially influences these preferred directions is the hydrodynamic instability related to matter rotation, the low T/W instability. Accounting for these directional effects could help extract CCSN GWs from the GW background and potentially inform GW detection pipelines which features of the CCSN GW signal are most likely to be reconstructed.

Chapter 5 outlines the new numerical solvers implemented in `FLASH`. We update a previously Newtonian magnetohydrodynamic (MHD) solver, `Spark`, to properly accounts for magnetized fluids moving near the speed of light and in extreme spacetimes—general relativistic magnetohydrodynamics (GRMHD). We verify the GRMHD scheme using a series of baseline shocktube tests

for purely hydrodynamic and magnetized fluid with moderate Lorentz factors. We implement a separate physics subunit, inspired by the GR1D code, that allows for dynamically evolving spacetime in 1D, and verify its behavior by tracking the collapse of a dust cloud to black hole formation. We introduce a novel method that extends this evolving spacetime to multiple dimensions, in either cylindrical or Cartesian coordinates. Testing this multidimensional evolving spacetime coupled to the GRMHD scheme, we track the stable evolution of a compact, or so called 'TOV', star in 3D. We also allow for contributions of magnetic fields to the spacetime curvature, a feature that can be particularly important for future simulations of magnetic, jet-driven supernovae. In addition, we perform six 1D and two 2D CCSN simulations examining the influence of these relativistic effects (GR case). In comparison to the Newtonian hydrodynamics and approximate relativistic potential (GREP case), we notice the GR case produces a generally more gravitationally bound system. The GR case launches shock fronts to smaller radii, creates smaller PNSs, and develops neutrino emission of ν_e^- with higher energies. We also introduce the newly implemented method of lines numerical method for performing multiphysics updates in the next generation Flash-X code, and review the future outlook for incorporating these new physics solvers into the Flash-X framework, to allow for astrophysical simulations on next generation supercomputers.

APPENDICES

APPENDIX A

DERIVATIONS FOR RELATIVISTIC ADDITIONS TO FLASH

In the below sections we explicitly derive the remapping procedure from radial gauge, polar slicing (RGPS) in spherical coordinates to 3D cylindrical and Cartesian coordinates. This step is used to remap the evolved spacetime metric to multidimensional coordinates. The spherical coordinates used are for a distance from the origin r, altitudinal angle from the z axis θ, and azimuthal angle from the x axis ϕ. These terms are useful for calculating the extrinsic curvature K_{ij} which depend on the metric elements and derivatives.

A.1 Transforming the Metric in RGPS: from Spherical to Cylindrical Coordinates

We begin with the line element from RGPS in spherical coordinates:

$$ds^2 = -\alpha^2 dt^2 + X^2 dr^2 + r^2 d\theta^2 + r^2 \sin^2\theta d\phi^2 \tag{A.1}$$

In order to remap to cylindrical coordinates, observe how the spherical differential line elements relate to the cylindrical ones,

$$dr = \sin\theta d\rho + \cos\theta dz, \quad r d\theta = \cos\theta d\rho - \sin\theta dz, \quad r\sin\theta d\phi = \rho d\phi. \tag{A.2}$$

Substitute the respective line elements from Equation (A.2) into Equation (A.1) and expand to yield

$$ds^2 = -\alpha^2 dt^2 + (X^2\sin^2\theta + \cos^2\theta)d\rho^2 + \sin 2\theta(X^2 - 1)d\rho dz + (X^2\cos^2\theta + \sin^2\theta)dz^2 + \rho^2 d\phi^2. \tag{A.3}$$

Assuming the metric is known in the ADM form (Arnowitt et al., 2008), the metric (with vanishing shift) will appear as

$$ds^2 = g_{\mu\nu}dx^\mu dx^\nu \equiv -\alpha dt^2 + \gamma_{ij}dx^i dx^j \tag{A.4}$$

for cylindrical coordinates of the form (ρ, z, ϕ).

Explicitly, the remapped spacetime metric can then be described as

$$g^{\text{cyl}}_{\mu\nu} = \begin{pmatrix} -\alpha^2 & 0 & 0 & 0 \\ 0 & (X^2 \sin^2\theta + \cos^2\theta) & (\sin 2\theta (X^2 - 1)) & 0 \\ 0 & (\sin 2\theta (X^2 - 1)) & (X^2 \cos^2\theta + \sin^2\theta) & 0 \\ 0 & 0 & 0 & \rho^2 \end{pmatrix}. \tag{A.5}$$

When evolving the equations of GRMHD, the required source terms depend on spatial and temporal derivatives of the spacetime metric. In Table A.1 we list the analytic forms of the derivatives for convenience.

From the differential line elements in Equation (A.2) the following coordinate derivatives become useful when applied to Table A.1 for the spherical radial coordinate

$$\partial_\rho r = \sin\theta, \quad \partial_z r = \cos\theta, \quad \partial_\phi r = 0,$$

for the altitudinal coordinate

$$\partial_\rho \theta = \frac{\cos\theta}{r}, \quad \partial_z \theta = -\frac{\sin\theta}{r}, \quad \partial_\phi \theta = 0,$$

for the azimuthal coordinate

$$\partial_\rho \phi = 0, \quad \partial_z \phi = 0, \quad \partial_\phi \phi = 1.$$

and for the cylindrical radial coordinate

$$\partial_\rho \rho = 1, \quad \partial_z \rho = 0, \quad \partial_\phi \rho = 0. \tag{A.6}$$

Metric term	Derivative	Expression (Cylindrical)
$\ln(\alpha)$	t	$\partial_t \ln(\alpha) = \partial_t \Phi$
$\ln(\alpha)$	$i = \rho, z, \phi$	$\partial_i \ln(\alpha) = \partial_i \Phi$
g_{00}	t	$\partial_t g_{00} = -2\alpha^2 \partial_t \Phi$
g_{00}	$i = \rho, z, \phi$	$\partial_i g_{00} = -2\alpha^2 \partial_i r \partial_r \Phi$
g_{11}	t	$\partial_t g_{11} = 2X\partial_t X \sin^2\theta$
g_{11}	$i = \rho, z, \phi$	$\partial_i g_{11} = 2X\partial_i r \partial_r X \sin^2\theta + (X^2 - 1)\sin 2\theta \partial_i \theta$
g_{12}	t	$\partial_t g_{12} = 2X\partial_t X \sin 2\theta$
g_{12}	$i = \rho, z, \phi$	$\partial_i g_{12} = 2(X^2 - 1)\cos 2\theta \partial_i \theta + 2X \sin 2\theta \partial_i r \partial_r X$
g_{22}	t	$\partial_t g_{22} = 2X\partial_t X \cos^2\theta$
g_{22}	$i = \rho, z, \phi$	$\partial_i g_{22} = 2X\partial_i r \partial_r X \cos^2\theta - (X^2 - 1)\sin 2\theta \partial_i \theta$
g_{33}	t	$\partial_t g_{33} = 0$
g_{33}	$i = \rho, z, \phi$	$\partial_i g_{33} = 2\rho \partial_i \rho$

Table A.1: Nonzero spatial and temporal derivatives of the spacetime metric for cylindrical coordinates. In practice, the following quantities are saved from the 1D spacetime evolution step: $\partial\Phi_r$, $\partial_t X$, and $\partial_r X$. The remaining quantities can be calculated analytically from the derivatives in Equation (A.6): $\partial_i r$, $\partial_i \theta$, $\partial_i \phi$, and $\partial_i \rho$.

A.2 Transforming the Metric in RGPS: from Spherical to Cartesian Coordinates

Begin with the line element from RGPS in spherical coordinates:

$$ds^2 = -\alpha^2 dt^2 + X^2 dr^2 + r^2 d\theta^2 + r^2 \sin^2\theta d\phi^2. \tag{A.7}$$

In order to remap to Cartesian coordinates, observe how the spherical differential line elements relate to the Cartesian ones,

$$dr = \sin\theta\cos\phi dx + \sin\theta\sin\phi dy + \cos\theta dz,$$

$$r d\theta = \cos\theta\cos\phi dx + \cos\theta\sin\phi dy - \sin\theta dz,$$

$$r\sin\theta d\phi = -\sin\phi dx + \cos\phi dy. \tag{A.8}$$

Assuming the metric is known in the ADM form (Arnowitt et al., 2008), the metric (with vanishing shift) will appear as

$$ds^2 = g_{\mu\nu}dx^\mu dx^\nu \equiv -\alpha dt^2 + \gamma_{ij}dx^i dx^j, \tag{A.9}$$

for Cartesian coordinates of the form (x, y, z).

Explicitly, the remapped spacetime metric can then be described as

$$g^{\text{cart}}_{\mu\nu} = \begin{pmatrix} -\alpha^2 & 0 & 0 & 0 \\ 0 & \sin^2\phi + \cos^2\phi(X^2\sin^2\theta + \cos^2\theta) & \sin 2\phi(-1 + X^2\sin^2\theta + \cos^2\theta) & \cos\phi\sin 2\theta(X^2-1) \\ 0 & “” & \cos^2\phi + \sin^2\phi(X^2\sin^2\theta + \cos^2\theta) & \sin\phi\sin 2\theta(X^2-1) \\ 0 & “” & “” & X^2\cos^2\theta + \sin^2\theta \end{pmatrix} \tag{A.10}$$

where “" corresponds to the symmetric matrix element across the diagonal.

When evolving the equations of GRMHD, the source terms needed depend on spatial and temporal derivatives of the spacetime metric. In Table A.2 we list the analytic forms of the derivatives for convenience.

From the differential line elements in Equation (A.2) the following coordinate derivatives become useful when applied to Table A.2 for the spherical radial coordinate

$$\partial_x r = \sin\theta\cos\phi, \quad \partial_y r = \sin\theta\sin\phi, \quad \partial_z r = \cos\theta,$$

for the altitudinal coordinate

$$\partial_x \theta = \cos\theta\cos\phi/r, \quad \partial_y \theta = \cos\theta\sin\phi/r, \quad \partial_z \theta = -\sin\theta/r,$$

and for the azimuthal coordinate

$$\partial_x \phi = \frac{-\sin\phi}{r\sin\theta}, \quad \partial_y \phi = \frac{\cos\phi}{r\sin\theta}, \quad \partial_z \phi = 0. \tag{A.11}$$

Metric term	Derivative	Expression (Cartesian)
$\ln(\alpha)$	t	$\partial_t \ln(\alpha) = \partial_t \Phi$
$\ln(\alpha)$	$i = x, y, z$	$\partial_i \ln(\alpha) = \partial_i r \partial_r \Phi$
g_{00}	t	$\partial_t g_{00} = -2\alpha^2 \partial_t \Phi$
g_{00}	$i = x, y, z$	$\partial_i g_{00} = -2\alpha^2 \partial_i r \partial_r \Phi$
g_{11}	t	$\partial_t g_{11} = 2X\partial_t X \sin^2\theta \cos^2\phi$
g_{11}	$i = x, y, z$	$\partial_i g_{11} = \sin 2\phi \partial_i \phi (1 - X^2 \sin^2\theta) + \sin 2\theta \partial_i \theta \cos^2\phi (X^2 - 1)$ $+ 2X\partial_i r \partial_r X \sin^2\theta \cos^2\phi - \sin 2\phi \partial_i \phi \cos^2\theta$
g_{12}	t	$\partial_t g_{12} = 2X\partial_t X \sin^2\theta \sin 2\phi$
g_{12}	$i = x, y, z$	$\partial_i g_{12} = 2\cos 2\phi \partial_i \phi (X^2 \sin^2\theta + \cos^2\theta - 1) + \sin 2\theta \partial_i \theta \sin 2\phi (X^2 - 1)$ $+ 2X\partial_i r \partial_r X \sin^2\theta \sin 2\phi$
g_{22}	t	$\partial_t g_{22} = 2X\partial_t X \sin^2\theta \sin^2\phi$
g_{22}	$i = x, y, z$	$\partial_i g_{22} = \sin 2\phi \partial_i \phi (X^2 \sin^2\theta + \cos^2\theta - 1) + \sin 2\theta \partial_i \theta \sin^2\phi (X^2 - 1)$ $+ 2X\partial_i r \partial_r X \sin^2\phi \sin^2\theta$
g_{13}	t	$\partial_t g_{13} = 2X\partial_t X \sin 2\theta \cos\phi$
g_{13}	$i = x, y, z$	$\partial_i g_{13} = 2\cos 2\theta \partial_i \theta \cos\phi (X^2 - 1) - \sin 2\theta \sin\phi \partial_i \phi (X^2 - 1)$ $+ 2X\partial_i r \partial_r X \sin 2\theta \cos\phi$
g_{23}	t	$\partial_t g_{23} = 2X\partial_t X \sin 2\theta \sin\phi$
g_{23}	$i = x, y, z$	$\partial_i g_{23} = \sin 2\theta \cos\phi \partial_i \phi (X^2 - 1) + 2\cos 2\theta \partial_i \theta \sin\phi (X^2 - 1)$ $+ 2X\partial_i r \partial_r X \sin 2\theta \sin\phi$
g_{33}	t	$\partial_t g_{33} = 2X\partial_t X \cos^2\theta$
g_{33}	$i = x, y, z$	$\partial_i g_{33} = \sin 2\theta \partial_i \theta (1 - X^2) + 2X\partial_i r \partial_r X \cos^2\theta$

Table A.2: Nonzero spatial and temporal derivatives of the spacetime metric for Cartesian coordinates. In practice, the following quantities are saved from the 1D spacetime evolution step: $\partial \Phi_r$, $\partial_t X$, and $\partial_r X$. The remaining quantities can be calculated analytically from the derivatives in Equation (A.11): $\partial_i r$, $\partial_i \theta$, and $\partial_i \phi$.

A.3 Expressing the Extrinsic Curvature

A crucial quantity for GRMHD evolution is the extrinsic curvature K_{ij}, as it influences the energy source term (see Equation (5.20)). As the previous appendices have shown how to calculate arbitrary metric elements—and their derivatives—in terms of spacetime quantities of interest, we show how to express K_{ij} as well.

Begin with the definition of K_{ij}

$$K_{ij} = -\gamma_i^\alpha \gamma_j^\beta \nabla_\alpha n_\beta. \tag{A.12}$$

Expanding $\nabla_\alpha n_\beta$ yields

$$K_{ij} = -\gamma_i^\alpha \gamma_j^\beta (\partial_\alpha n_\beta - n_\epsilon \Gamma^\epsilon_{\alpha\beta}). \tag{A.13}$$

Retaining nonzero terms from $n_\epsilon \Gamma^\epsilon_{\alpha\beta}$ and expressing the mixed component spatial metric in terms of the delta function and normals $\gamma_i^\alpha = \delta_i^\alpha + n^\alpha n_i$ yields,

$$K_{ij} = -\delta_i^\alpha \delta_j^\beta (\partial_\alpha n_\beta - n_0 \Gamma^0_{\alpha\beta}) = (\partial_i n_j - n_0 \Gamma^0_{ij}) = \alpha \Gamma^0_{ij}. \tag{A.14}$$

Observe the definition the Christoffel symbol,

$$\Gamma^\nu_{\alpha\mu} = \frac{1}{2} g^{\nu\beta} (g_{\mu\beta,\alpha} + g_{\alpha\beta,\mu} - g_{\alpha\mu,\beta}), \tag{A.15}$$

leading to

$$\Gamma^0_{ij} = \frac{1}{2} g^{0\beta} (g_{j\beta,i} + g_{i\beta,j} - g_{ij,\beta}). \tag{A.16}$$

Because the shift vector is zero in RGPS coordinates, all $g_{i0} = g^{i0} = 0$ simplifying Equation (A.14),

$$K_{ij} = \frac{-\alpha}{2} g^{00} g_{ij,0} = \frac{1}{2\alpha} g_{ij,0}. \tag{A.17}$$

This result provides a simple form for K_{ij} in terms of the time derivative of the g_{ij} elements of the metric, which are provided in the previous tables. In particular, it depends on the spatial metric term X, the position on the grid (ie. θ and ϕ), and the time derivative of the spatial metric term $\partial_t X$. As outlined in O'Connor & Ott (2011), $\partial_t X$ can be analytically expressed

$$\partial_t X = -4\pi r \alpha X^3 \rho h W^2 v^r, \tag{A.18}$$

where we define v^r as the magnitude of the radial component of the velocity measured by an observer in the laboratory frame. Thus, this formulation of evolving spacetimes avoids any finite differencing of the metric elements.

A.4 Mass Integration

This Appendix outlines the mass integration procedure as the 1D vector of spacetime values are calculated. As in `GRHydro`, but with $\beta^i = 0$ from RGPS coordinates, the vector of evolved variables $\mathbf{U}$ has components

$$D = \sqrt{\gamma}\rho W, \tag{A.19}$$

$$S = \sqrt{\gamma}(\rho h^* W^2 v_j - \alpha b^0 b_j), \tag{A.20}$$

$$\tau = \sqrt{\gamma}\Big(\rho h^* W^2 - P^* - (\alpha b^0)^2\Big) - D, \tag{A.21}$$

where $\sqrt{\gamma}$, ρ, h, P, W, and v are the determinant of the spatial metric, density, specific enthalpy, pressure, Lorentz factor, and velocity as observed in an at rest laboratory frame. For a simulation with arbitrary dimension these *densitized* evolved variables are averaged down to 1D profiles, so as to follow the assumption that the spacetime is spherically symmetric.

In 1D, the hydrodynamic update follows,

$$\frac{\partial \mathbf{U}}{\partial t} + \frac{1}{r^2}\frac{\partial r^2 \mathbf{F}^i}{\partial r} = \mathbf{S}, \tag{A.22}$$

for a vector of fluxes $\mathbf{F}^i$ and source terms $\mathbf{S}$. For the 1D problem, after factoring out r^2 terms as in `GR1D`, $\sqrt{\gamma} = X$, where $X = 1/\sqrt{1 - 2m(r)/r}$. Note X depends on the enclosed gravitational mass and can be rewritten in terms of Equation (5.11) and Equation (5.14),

$$m(r) = \int \left(\rho h^* W^2 - P^* + \frac{\sqrt{\gamma}}{\sqrt{\gamma}}\tau_m^\nu\right) dV = \int 4\pi r^2 (\tau + D + \tau_m'^\nu)/X dr, \tag{A.23}$$

where we denote $\tau_m'^\nu = \sqrt{\gamma}\tau_m^\nu$.

Making use of the definition of X yields an implicit integral equation for mass for $m(m,r)$ and resulting differential equation for $dm/dr|_j^m$

$$m(m,r) = 4\pi \int dr\, r^2(\tau + D + \tau_m'^{\nu})\sqrt{1-2m(r)/r}\,,\ \left.\frac{dm}{dr}\right|_i^m = 4\pi r^2(\tau + D + \tau_m'^{\nu})\sqrt{1-2m(r)/r}. \tag{A.24}$$

After each hydrodynamic update, the values of $(\tau + D)$ are known at the i^{th} cell center and n+1 stage, or $(\tau + D)_i^{\mathrm{n+1}}$. The neutrino quantity $\tau_m'^{\nu}$ is used from the previous timestep, but will be fully synchronized in a future code release. As the integration continues along the 1D domain, an updated $m(r)_i^{\mathrm{n+1}}$ can be calculated using 4th order RK integration

$$m(m,r)_i^{\mathrm{n+1}} = m(m,r)_{i-1}^{\mathrm{n+1}} + m_{i-1}^{\mathrm{RK4}} + m_{i-1/2}^{\mathrm{RK4}}. \tag{A.25}$$

The three terms on the RHS correspond to the enclosed mass at the $i-1$st cell center, the mass in the right half of the $i-1$st cell, and the mass in the left half of the ith cell, respectively. A general m_j^{RK4} is calculated as

$$m_j^{\mathrm{RK4}} = \frac{1}{6}(k_1 + 2k_2 + 2k_3 + k_4), \tag{A.26}$$

with corresponding k values

$$k_1 = \frac{dr}{2}\left.\frac{dm}{dr}\right|_j^{m_j},\ k_2 = \frac{dr}{2}\left.\frac{dm}{dr}\right|_{j+1/4}^{m_j+0.5k_1},\ k_3 = \frac{dr}{2}\left.\frac{dm}{dr}\right|_{j+1/4}^{m_j+0.5k_2},\ k_4 = \frac{dr}{2}\left.\frac{dm}{dr}\right|_{j+1/2}^{m_j+k_3}. \tag{A.27}$$

Note for a given $dm/dr|_j$ (where $i-1/2 < j < i+1/2$), $(\tau + D + \tau_m'^{\nu})$ is assumed to be constant across the entire cell.

With $m(r)_i^{\mathrm{n+1}}$, $X_i^{\mathrm{n+1}}$ is obtained. For multidimensional cases, the remapping procedure outlined in Appendix A.1 or Appendix A.2 is then used to construct $\gamma_{ij}^{\mathrm{n+1}}$. The updated evolved variables can then be undensitized with $\sqrt{\gamma}^{\mathrm{n+1}}$ for the con2prim transformation, or

$$\hat{D} = D/\sqrt{\gamma}^{\mathrm{n+1}},\ \hat{S_j} = S_j/\sqrt{\gamma}^{\mathrm{n+1}},\ \hat{\tau} = \tau/\sqrt{\gamma}^{\mathrm{n+1}}. \tag{A.28}$$

A.5 Deriving Neutrino Quantities

A.5.1 Electron Fraction Neutrino Source Term

Begin with the conservation law for Y_e

$$\nabla_\mu(\rho Y_e u^\mu) = R^0_{Y_e}, \tag{A.29}$$

which depends on a source term output from the neutrino leakage scheme $R^0_{Y_e}$. Expanding the definition of the covariant derivative ∇_μ for a coordinate frame $u^\mu = W(1/\alpha, v^i)$ gives

$$\partial_t\left(\sqrt{-g}\frac{\rho W Y_e}{\alpha}\right) + \partial_r(\sqrt{-g}\rho W Y_e v^i) = \sqrt{-g}R^0_{Y_e}, \tag{A.30}$$

where g is the determinant of the spacetime metric. Applying the identity $\sqrt{-g} = \alpha\sqrt{\gamma}$ and simplifying yields the evolution equation for Y_e in multiple dimensions

$$\partial_t(DY_e) + \partial_r(\alpha D Y_e v^i) = \alpha\sqrt{\gamma}R^0_{Y_e} = R^\nu_{Y_e}. \tag{A.31}$$

A.5.2 Momentum and Energy Neutrino Source Terms

To determine the neutrino contributions to the energy and momentum source terms, begin with the 4 vector

$$\vec{q} = (Q^0_E, Q^0_{M_x}, Q^0_{M_y}, Q^0_{M_z}). \tag{A.32}$$

From O'Connor & Ott (2010), recall Q^0_E is the total heating change due to neutrinos and $Q^0_M = -\partial P_\nu/\partial r$ is approximated by the gradient of the neutrino pressure. Here the subscripted $Q^0_{M_i}$ represent partial derivatives along the ith direction, explicitly,

$$Q^0_{M_x} = -\frac{\partial r}{\partial x}\frac{\partial P_\nu}{\partial r} = -\sin\theta\cos\phi\frac{\partial P_\nu}{\partial r}, \tag{A.33}$$

$$Q^0_{My} = -\frac{\partial r}{\partial y}\frac{\partial P_\nu}{\partial r} = -\cos\theta\frac{\partial P_\nu}{\partial r}, \tag{A.34}$$

$$Q^0_{Mz} = -\frac{\partial r}{\partial z}\frac{\partial P_\nu}{\partial r} = -\sin\theta\sin\phi\frac{\partial P_\nu}{\partial r}. \tag{A.35}$$

In the fluid rest frame (FRF), the four velocity can be described as $u^\mu_{(\mathrm{FRF})} = (1,0,0,0)$. We select a radial vector (orthonormal to u^μ) described as $n^\mu_{(\mathrm{FRF})} = (0, \sin\theta\cos\phi, \cos\theta, \sin\theta\sin\phi)$. In frame independent notation, this yields $\vec{q} = Q^0_E\vec{u} + Q^0_M\vec{n}$. To transform to the coordinate frame (CF) the relevant orthonormal vectors become

$$\vec{u} = W(1/\alpha, v_x, v_y, v_z), \tag{A.36}$$

and

$$\vec{n} = \frac{W}{\sqrt{v^2}}(\frac{v^2}{\alpha}, v_x, v_y, v_z), \tag{A.37}$$

where $v^2 = \gamma_{ij}v^iv^j$.

Expressing $\vec{q}$ in the coordinate frame becomes

$$\vec{q} = \begin{bmatrix} \frac{W}{\alpha}(Q^0_E + Q^0_M\sqrt{v^2}) \\ Wv_x(Q^0_E + Q^0_M/\sqrt{v^2}) \\ Wv_y(Q^0_E + Q^0_M/\sqrt{v^2}) \\ Wv_z(Q^0_E + Q^0_M/\sqrt{v^2}) \end{bmatrix}. \tag{A.38}$$

The evolution equations then become

$$\nabla_\mu T^{\mu\nu} = q^\nu + \vec{S}_{\mathrm{MHD}}, \tag{A.39}$$

$$(\sqrt{-g}T^{\mu i})_{,\mu} = \sqrt{-g}q^i + \vec{S}'_{\mathrm{MHD}} = \alpha\sqrt{\gamma}q^i + \vec{S}'_{\mathrm{MHD}}, \tag{A.40}$$

where we group MHD relevant source terms in $\vec{S}'_{\rm MHD}$. This expression yields the final source terms in Equation (5.20):

$$\mathbf{S} = \sqrt{\gamma} \times \begin{bmatrix} 0 \\ R^{\nu}_{Y_e}/\sqrt{\gamma} \\ \frac{1}{2}\alpha S^{ik}\partial_j \gamma_{ik} + S_i \partial_j \beta^i - E\partial_j \alpha + Q^{\nu,E}_{S_j} + Q^{\nu,M}_{S_j} \\ \alpha S^{ij} K_{ij} - S^j \partial_j \alpha + Q^{\nu,E}_{\tau} + Q^{\nu,M}_{\tau} \\ \vec{0} \end{bmatrix}. \tag{A.41}$$

where the neutrino terms are explicitly,

$$Q^{\nu,E}_{S_j} = \alpha W v_j Q^0_E, \quad Q^{\nu,M}_{S_j} = \alpha W v_j Q^0_M/\sqrt{v^2}, \tag{A.42}$$

for the momentum and

$$Q^{\nu,E}_{\tau} = W Q^0_E, \quad Q^{\nu,M}_{\tau} = W Q^0_M \sqrt{v^2}, \tag{A.43}$$

for the energy.

A.5.3 Neutrino Luminosities

Begin with the expression of the momentum of a neutrino in the FRF

$$\vec{p} = (E^{\rm FRF}, E^{\rm FRF}_x, E^{\rm FRF}_y, E^{\rm FRF}_z), \tag{A.44}$$

where $E^{\rm FRF}$ is the total energy of the neutrino measured in the FRF and $E^{\rm FRF}_i$ is the neutrino momentum along a given direction.

$$E^{\rm FRF}_x = -\frac{\partial r}{\partial x} E^{\rm FRF} = -\sin\theta\cos\phi E^{\rm FRF}, \tag{A.45}$$

$$E^{\rm FRF}_y = -\frac{\partial r}{\partial y} E^{\rm FRF} = -\cos\theta E^{\rm FRF}, \tag{A.46}$$

$$E_z^{\mathrm{FRF}} = -\frac{\partial r}{\partial z} E^{\mathrm{FRF}} = -\sin\theta \sin\phi E^{\mathrm{FRF}}. \tag{A.47}$$

Similar to the previous Appendix, the four velocity in FRF is $u^{\mu}_{(\mathrm{FRF})} = (1, 0, 0, 0)$. Once again, we select a radial vector described as $n^{\mu}_{(\mathrm{FRF})} = (0, \sin\theta\cos\phi, \cos\theta, \sin\theta\sin\phi)$, thus describing the neutrino momentum as $\vec{p} = E^{\mathrm{FRF}}\vec{u} + E^{\mathrm{FRF}}\vec{n}$. In the coordinate frame

$$\vec{u} = W(1/\alpha, v_x, v_y, v_z), \tag{A.48}$$

and

$$\vec{n} = \frac{W}{\sqrt{v^2}}(\frac{v^2}{\alpha}, v_x, v_y, v_z). \tag{A.49}$$

Consider an observer at rest in the CF described by $\vec{U} = (1, 0, 0, 0)$; the energy of the neutrino measured by that observer is

$$E_{\mathrm{CF}} = -g_{\mu\nu} p^{\mu} U^{\nu}. \tag{A.50}$$

Simplifying this expression provides a simple translation between FRF and CF:

$$E_{\mathrm{CF}} = -g_{00} E^{\mathrm{FRF}}(u^0 + n^0) = \alpha W(1 + \sqrt{v^2}) E^{\mathrm{FRF}}. \tag{A.51}$$

This quantity is useful for calculating the luminosity of the neutrino production, which requires integrating the energy output of the neutrinos over the computational domain which is expressed as

$$L_{\nu_i}^{\mathrm{CF}} = 4\pi \int_0^r \left[\frac{\alpha(r')}{\alpha(r)}\right] [Q_{\mathrm{eff},\nu_i}(r') - Q_{\nu_i}^{\mathrm{heat}}(r')][\alpha(r')W(r')(1 + \sqrt{v(r')^2})]\sqrt{\gamma} r'^2 dr', \tag{A.52}$$

where the first term in brackets [] accounts for gravitational redshift, the second term expresses the heating rates of the neutrinos, and the third term involves the transformation from FRF calculations to the CF.

A.6 Magnetized Shock Tube Profiles

Below are the remaining four numeric baseline tests for magnetized shock tubes mentioned in Section 5.5.2, with initial conditions specified in Table 5.2.

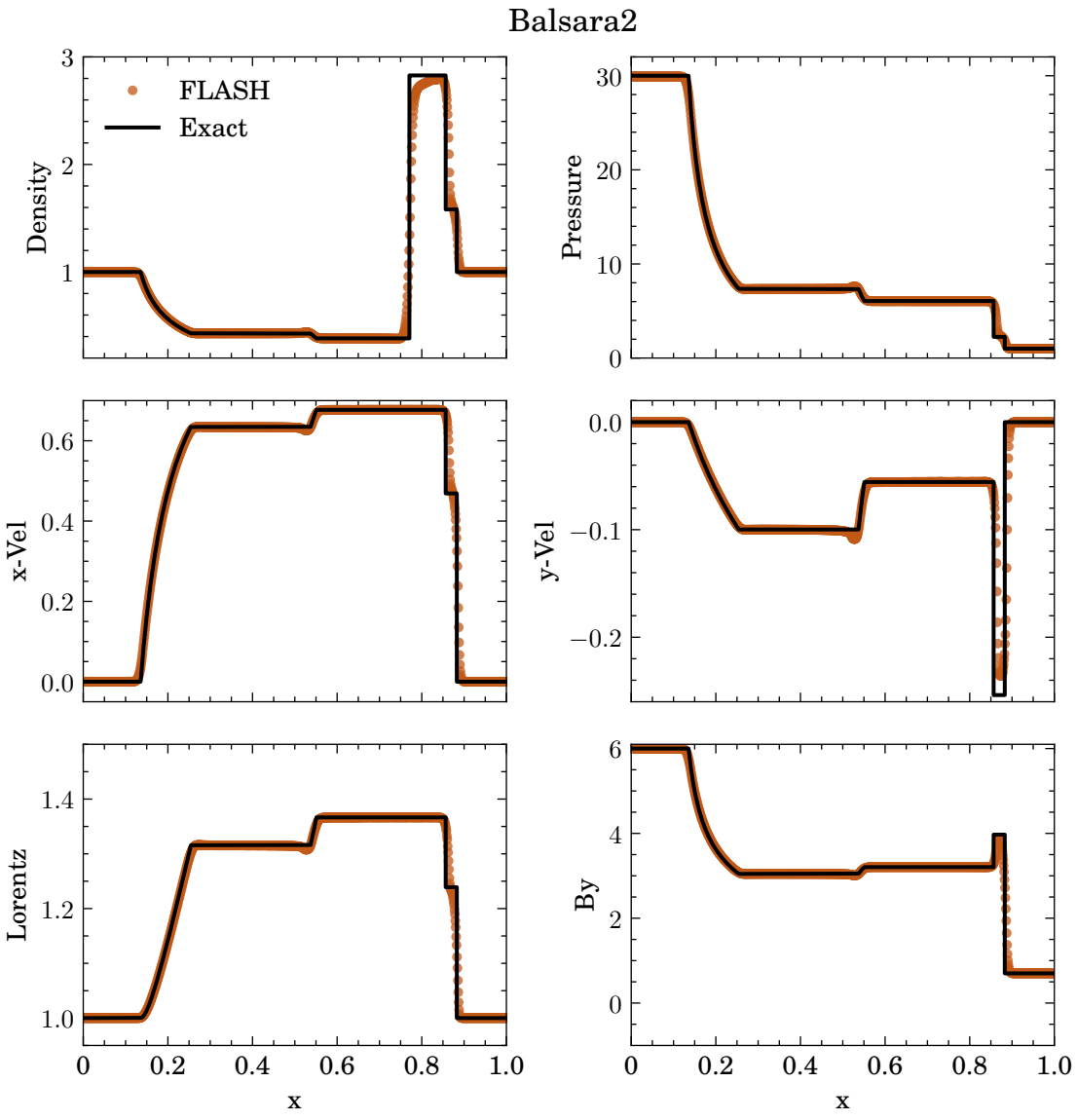

Figure A.1: Primitive variables density, pressure, x-velocity, y-velocity, Lorentz factor, and y component of the magnetic field (By) at $t = 0.4$ for the Balsara2 test problem.

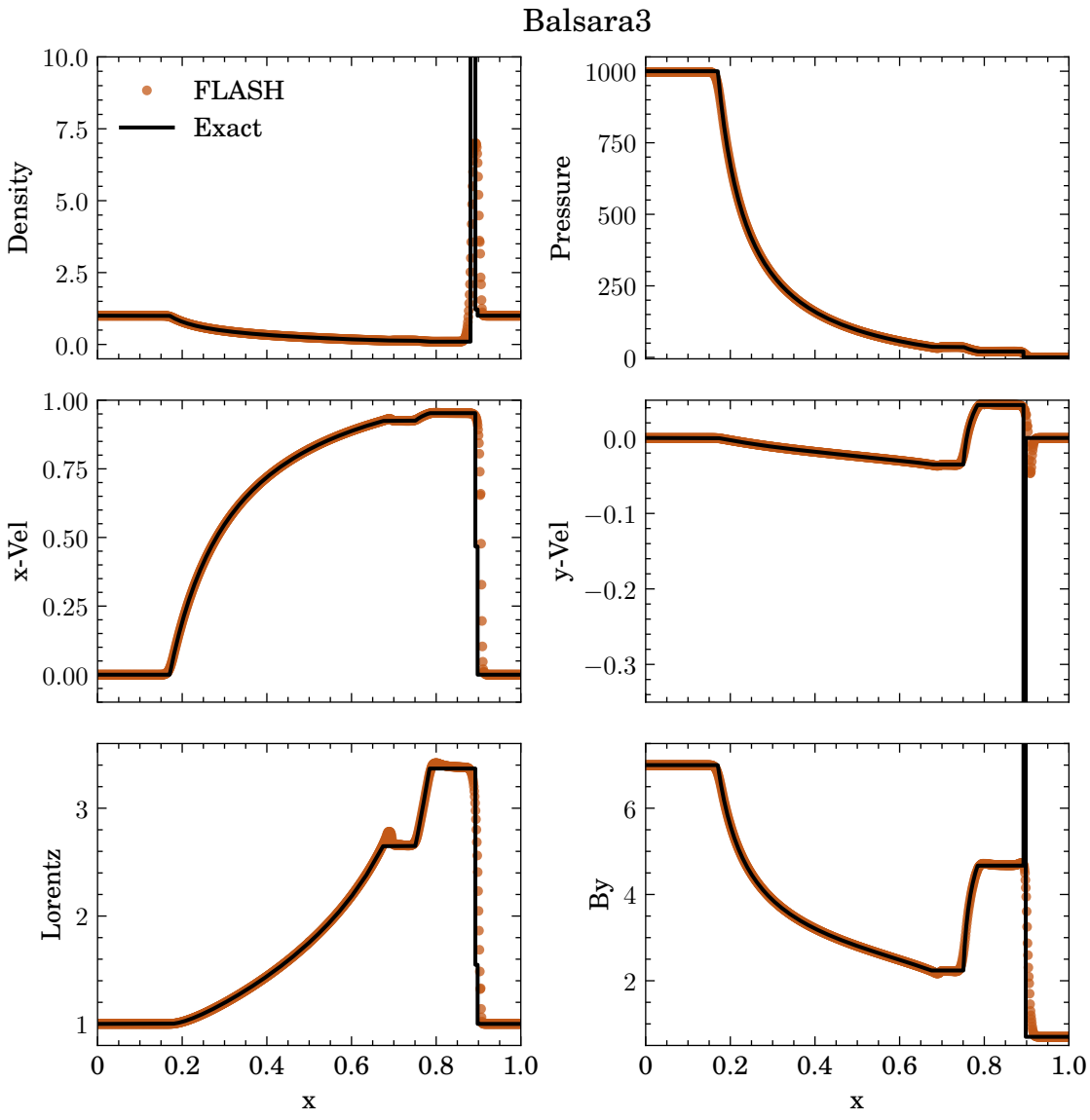

Figure A.2: Primitive variables density, pressure, x-velocity, y-velocity, Lorentz factor, and y component of the magnetic field (By) at $t = 0.4$ for the Balsara3 test problem.

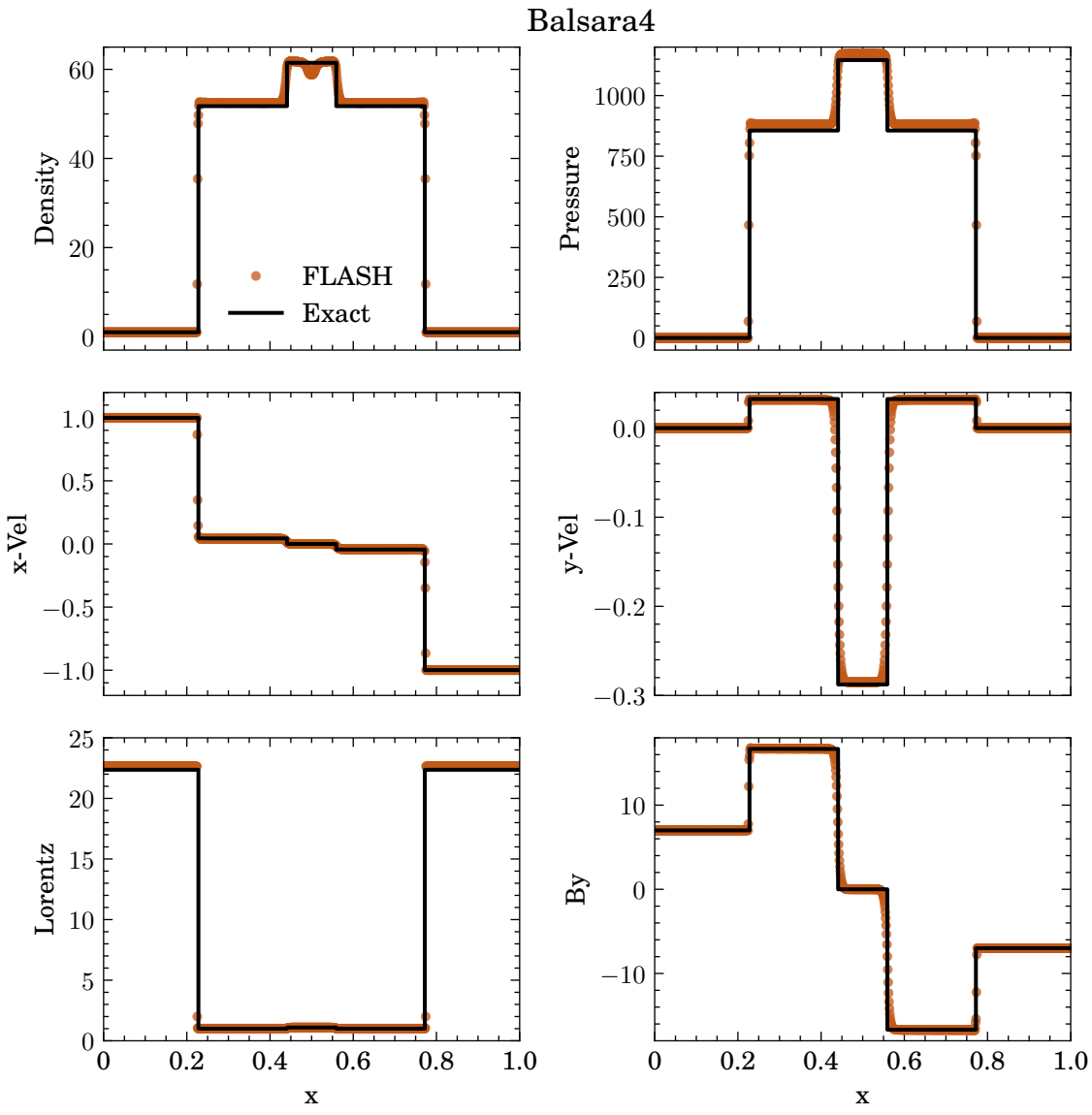

Figure A.3: Primitive variables density, pressure, x-velocity, y-velocity, Lorentz factor, and y component of the magnetic field (By) at $t = 0.4$ for the Balsara4 test problem.

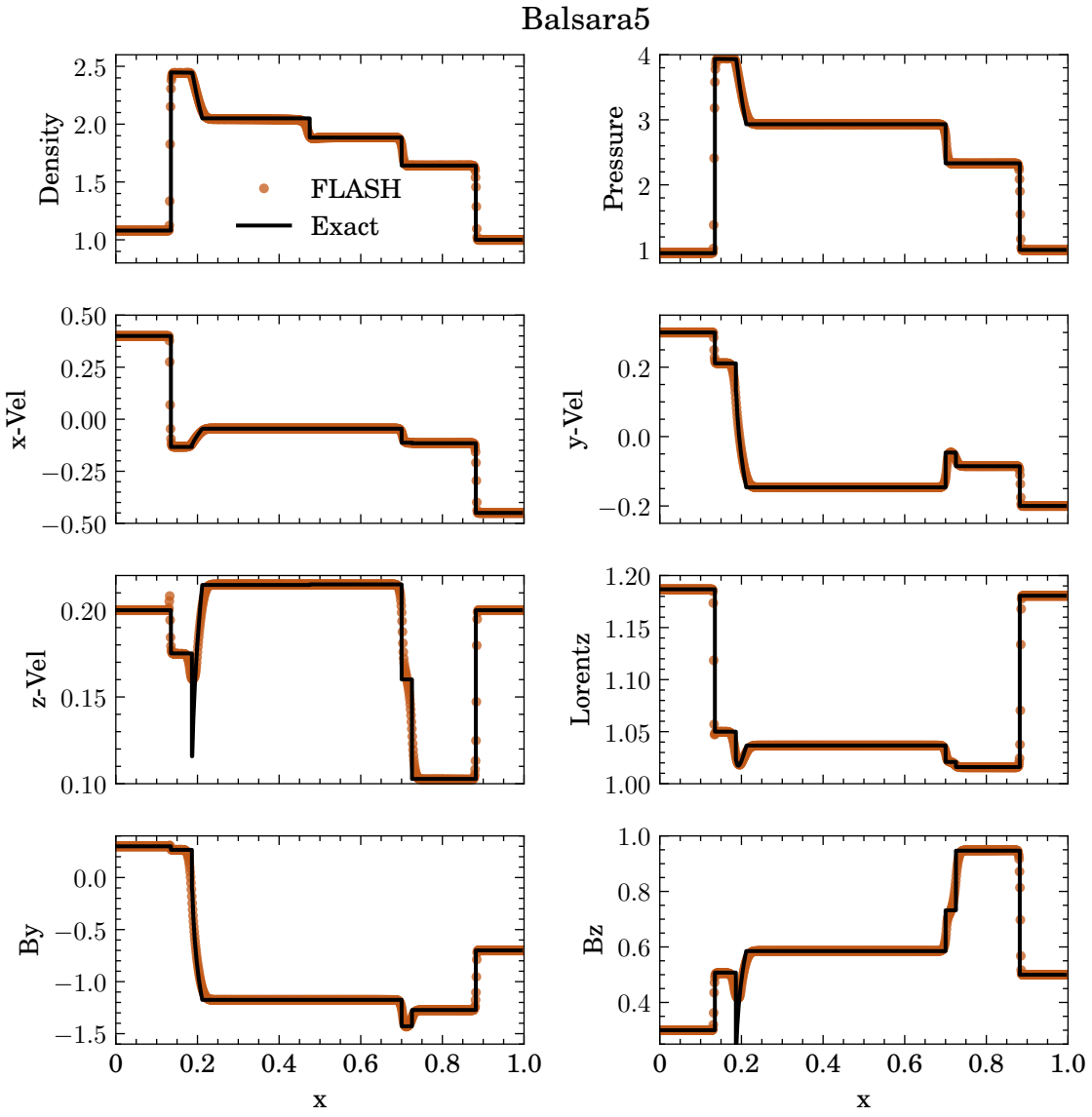

Figure A.4: Primitive variables density, pressure, x-velocity, y-velocity, z-velocity, Lorentz factor, y component of the magnetic field, and z component of the magnetic field (Bz) at $t = 0.55$ for the Balsara5 test problem.

BIBLIOGRAPHY

BIBLIOGRAPHY

Aasi, J., Abadie, J., Abbott, B. P., et al. 2013, Nature Photonics, 7, 613

Abbott, B. P., Abbott, R., Abbott, T. D., et al. 2016a, , 94, 102001

—. 2016b, Physical Review Letters, 116, 241103

—. 2016c, Physical Review Letters, 116, 061102

—. 2017, Physical Review Letters, 119, 161101

—. 2018, Living Reviews in Relativity, 21, 3

Abbott, R., Abbott, T. D., Abraham, S., et al. 2020, The Astrophysical Journal Letters, 902, L21

—. 2021, The Astrophysical Journal Letters, 915, L5

Abdikamalov, E., Gossan, S., DeMaio, A. M., & Ott, C. D. 2014, , 90, 044001

Abdikamalov, E. B., Ott, C. D., Rezzolla, L., et al. 2010, , 81, 044012

Abe, K., Adrich, P., Aihara, H., et al. 2021, The Astrophysical Journal, 916, 15

Abi, B., Acciarri, R., Acero, M. A., et al. 2021, European Physical Journal C, 81, 423

Acernese, F., Agathos, M., Agatsuma, K., et al. 2015, Classical and Quantum Gravity, 32, 024001

Aerts, C., Christensen-Dalsgaard, J., & Kurtz, D. W. 2010, Asteroseismology

Aerts, C., Mathis, S., & Rogers, T. M. 2019, Annual Reviews of Astronomy and Astrophysics, 57, 35

Akiyama, S., Wheeler, J. C., Meier, D. L., & Lichtenstadt, I. 2003, The Astrophysical Journal, 584, 954

Amaro-Seoane, P., Audley, H., Babak, S., et al. 2017, arXiv e-prints, arXiv:1702.00786

An, F., An, G., An, Q., et al. 2016, Journal of Physics G Nuclear Physics, 43, 030401

Anderson, M., Hirschmann, E. W., Liebling, S. L., & Neilsen, D. 2006, Classical and Quantum Gravity, 23, 6503

Anderson, S., Anderson, W., Blackburn, K., et al. 2004, LIGOT010095-00-Z, Tech. rep.

Andersson, N. 1998, The Astrophysical Journal, 502, 708

Andersson, N., & Kokkotas, K. D. 1996, Physical Review Letters, 77, 4134

Andresen, H., Müller, B., Müller, E., & Janka, H. T. 2017, Monthly Notices of the Royal Astronomical Society, 468, 2032

Andresen, H., Müller, E., Janka, H. T., et al. 2019, Monthly Notices of the Royal Astronomical Society, 486, 2238

Antón, L., Zanotti, O., Miralles, J. A., et al. 2006, The Astrophysical Journal, 637, 296

Antoniadis, J., Freire, P. C. C., Wex, N., et al. 2013, Science, 340, 448

Arcones, A., & Montes, F. 2011, The Astrophysical Journal, 731, 5

Arnett, W. D., Bahcall, J. N., Kirshner, R. P., & Woosley, S. E. 1989, Annual Reviews of Astronomy and Astrophysics, 27, 629

Arnowitt, R., Deser, S., & Misner, C. W. 2008, General Relativity and Gravitation, 40, 1997

Baiotti, L., Giacomazzo, B., Hawke, I., & et al. 2010, WhiskyMHD: Numerical Code for General Relativistic Magnetohydrodynamics, ascl:1010.084

Balsara, D. 2001, The Astrophysical Journal Supplement, 132, 83

Banyuls, F., Font, J. A., Ibáñez, J. M., Martí, J. M., & Miralles, J. A. 1997, The Astrophysical Journal, 476, 221

Barker, B. L., Harris, C. E., Warren, M. L., O'Connor, E. P., & Couch, S. M. 2021, arXiv e-prints, arXiv:2102.01118

Baron, E., & Cooperstein, J. 1990, The Astrophysical Journal, 353, 597

Barsotti, L., Fritschel, P., Evans, M., & Gras, S. 2018, LIGO Document T1800044-v5, Tech. rep.

Baumgarte, T. W., & Shapiro, S. L. 1998, , 59, 024007

—. 1999, , 59, 024007

Baumgarte, T. W., & Shapiro, S. L. 2021, Numerical Relativity: Starting from Scratch (Cambridge University Press), doi:10.1017/9781108933445

Bellm, E. C., Kulkarni, S. R., Graham, M. J., et al. 2019, Publications of the Astronomical Society of the Pacific, 131, 018002

Berger, M. J., & Colella, P. 1989, Journal of Computational Physics, 82, 64

Bethe, H. A., & Wilson, J. R. 1985, The Astrophysical Journal, 295, 14

Bionta, R. M., Blewitt, G., Bratton, C. B., et al. 1987, Physical Review Letters, 58, 1494

Bisnovatyi-Kogan, G. S. 1970, , 47, 813

Blanchet, L., Damour, T., & Schaefer, G. 1990, Monthly Notices of the Royal Astronomical Society, 242, 289

Blondin, J. M., & Mezzacappa, A. 2006, The Astrophysical Journal, 642, 401

Blondin, J. M., Mezzacappa, A., & DeMarino, C. 2003, The Astrophysical Journal, 584, 971

Blondin, J. M., & Shaw, S. 2007, The Astrophysical Journal, 656, 366

Boccioli, L., Mathews, G. J., & O'Connor, E. P. 2021, The Astrophysical Journal, 912, 29

Bonanno, A., Urpin, V., & Belvedere, G. 2005, Astronomy & Astrophysics, 440, 199

Brent, R. P. 1971, The Computer Journal, 14, 422

Brio, M., & Wu, C. C. 1988, Journal of Computational Physics, 75, 400

Brown, T. M., Baliber, N., Bianco, F. B., et al. 2013, Publications of the Astronomical Society of the Pacific, 125, 1031

Bruenn, S. W. 1985, The Astrophysical Journal Supplement Series, 58, 771

—. 1989, The Astrophysical Journal, 340, 955

Bruenn, S. W., Lentz, E. J., Hix, W. R., et al. 2016, The Astrophysical Journal, 818, 123

Bruenn, S. W., Blondin, J. M., Hix, W. R., et al. 2020, The Astrophysical Journal Supplement, 248, 11

Burbidge, E. M., Burbidge, G. R., Fowler, W. A., & Hoyle, F. 1957, Rev. Mod. Phys., 29, 547

Burrows, A., Dessart, L., Livne, E., Ott, C. D., & Murphy, J. 2007, The Astrophysical Journal, 664, 416

Burrows, A., Dolence, J. C., & Murphy, J. W. 2012, The Astrophysical Journal, 759, 5

Burrows, A., & Fryxell, B. A. 1992, Science, 258, 430

Burrows, A., & Hayes, J. 1996, Physical Review Letters, 76, 352

Burrows, A., Radice, D., & Vartanyan, D. 2019, Monthly Notices of the Royal Astronomical Society, 485, 3153

Burrows, A., & Vartanyan, D. 2021, Nature, 589, 29

Camp, J. B., & Cornish, N. J. 2004, Annual Review of Nuclear and Particle Science, 54, 525

Cao, Z., & Hilditch, D. 2012, , 85, 124032

Cardall, C. Y., Endeve, E., & Mezzacappa, A. 2013, , 87, 103004

Cerdá-Durán, P., DeBrye, N., Aloy, M. A., Font, J. A., & Obergaulinger, M. 2013, The Astrophysical Journal, 779, L18

Cerdá-Durán, P., Font, J. A., Antón, L., & Müller, E. 2008, Astronomy & Astrophysics, 492, 937

Cerdá-Durán, P., Font, J. A., & Dimmelmeier, H. 2007, Astronomy & Astrophysics, 474, 169

Cerdá-Durán, P., Gabler, M., Müller, E., et al. 2013, 940

Chan, M. L., & Hayama, K. 2021, Phys. Rev. D, 103, 103024

Chinomona, R., & Reynolds, D. R. 2020, arXiv e-prints, arXiv:2007.09776

Christensen, N. 2019, Reports on Progress in Physics, 82, 016903

Colgate, S. A., & White, R. H. 1966, The Astrophysical Journal, 143, 626

Cordero-Carrión, I., Cerdá-Durán, P., Dimmelmeier, H., et al. 2009, , 79, 024017

Couch, S. M., Carlson, J., Pajkos, M., et al. 2021, Parallel Computing, 108, 102830

Couch, S. M., Graziani, C., & Flocke, N. 2013, The Astrophysical Journal, 778, 181

Couch, S. M., & O'Connor, E. P. 2014, The Astrophysical Journal, 785, 123

Couch, S. M., & Ott, C. D. 2015, The Astrophysical Journal, 799, 5

Couch, S. M., Warren, M. L., & O'Connor, E. P. 2020a, The Astrophysical Journal, 890, 127

—. 2020b, The Astrophysical Journal, 890, 127

da Silva Schneider, A., O'Connor, E., Granqvist, E., Betranhandy, A., & Couch, S. M. 2020, The Astrophysical Journal, 894, 4

de Mink, S. E., Langer, N., Izzard, R. G., Sana, H., & de Koter, A. 2013, The Astrophysical Journal, 764, 166

Dedner, A., Kemm, F., KrÃ¶ner, D., et al. 2002, Journal of Computational Physics, 175, 645

Del Zanna, L., Zanotti, O., Bucciantini, N., & Londrillo, P. 2007, Astronomy & Astrophysics, 473, 11

Deppe, N., Throwe, W., Kidder, L. E., et al. 2022, `SpECTRE v2022.03.07`, 10.5281/zenodo.6335350, doi:10.5281/zenodo.6335350

Diehl, R., Halloin, H., Kretschmer, K., et al. 2006, Nature, 439, 45

Dimmelmeier, H., Font, J. A., & Müller, E. 2002, Astronomy & Astrophysics, 393, 523

Dimmelmeier, H., Ott, C. D., Marek, A., & Janka, H. T. 2008, , 78, 064056

Dolence, J. C., Burrows, A., Murphy, J. W., & Nordhaus, J. 2013, The Astrophysical Journal, 765, 110

Dubey, A., Reid, L. B., Weide, K., et al. 2009, ArXiv e-prints, arXiv:0903.4875

Duez, M. D., Liu, Y. T., Shapiro, S. L., & Stephens, B. C. 2005, , 72, 024028

Edwards, M. C., Meyer, R., & Christensen, N. 2014, Inverse Problems, 30, 114008

Einfeldt, B. 1988, SIAM Journal on Numerical Analysis, 25, 294

Ellis, J., Lewicki, M., & No, J. M. 2019, , 2019, 003

Endal, A. S., & Sofia, S. 1978, The Astrophysical Journal, 220, 279

Eriguchi, Y., & Mueller, E. 1985, Astronomy & Astrophysics, 146, 260

Etienne, Z. B., Liu, Y. T., & Shapiro, S. L. 2010, , 82, 084031

Fernández, R. 2010, The Astrophysical Journal, 725, 1563

Finn, L. S., & Evans, C. R. 1990, The Astrophysical Journal, 351, 588

Foglizzo, T., Galletti, P., Scheck, L., & Janka, H. T. 2007, The Astrophysical Journal, 654, 1006

Fryer, C. L., & Heger, A. 2000, The Astrophysical Journal, 541, 1033

Fryer, C. L., & New, K. C. B. 2003, Living Reviews in Relativity, 6, 2

Fryer, C. L., & Warren, M. S. 2004, The Astrophysical Journal, 601, 391

Fryxell, B., Olson, K., Ricker, P., et al. 2000, The Astrophysical Journal Supplement Series, 131, 273

—. 2010, FLASH: Adaptive Mesh Hydrodynamics Code for Modeling Astrophysical Thermonuclear Flashes, ascl:1010.082

Gade, A., & Sherrill, B. M. 2016, , 91, 053003

Gair, J. R., Vallisneri, M., Larson, S. L., & Baker, J. G. 2013, Living Reviews in Relativity, 16, 7

Gammie, C. F., McKinney, J. C., & Tóth, G. 2003, The Astrophysical Journal, 589, 444

Gautschy, A., & Saio, H. 1995, Annual Reviews of Astronomy and Astrophysics, 33, 75

Giacomazzo, B., & Rezzolla, L. 2006, Journal of Fluid Mechanics, 562, 223

—. 2007, Classical and Quantum Gravity, 24, S235

Gill, K., Wang, W., Valdez, O., et al. 2018, arXiv e-prints, arXiv:1802.07255

Gossan, S. E., Sutton, P., Stuver, A., et al. 2016, , 93, 042002

Gottlieb, S., Shu, C.-W., & Tadmor, E. 2001, SIAM Review, 43, 89

Greiner, J., Peimbert, M., Esteban, C., et al. 2003, GRB Coordinates Network, 2020, 1

Greiner, J., Mazzali, P. A., Kann, D. A., et al. 2015, Nature, 523, 189

Gutiérrez, C. P., Anderson, J. P., Hamuy, M., et al. 2017, The Astrophysical Journal, 850, 89

Halevi, G., & Mosta, P. 2018, Monthly Notices of the Royal Astronomical Society, 477, 2366

Harten, A., Lax, P. D., & Leer, B. v. 1983, SIAM Review, 25, 35

Hayama, K., Kuroda, T., Kotake, K., & Takiwaki, T. 2018, Monthly Notices of the Royal Astronomical Society: Letters, 477, L96

Hayama, K., Kuroda, T., Nakamura, K., & Yamada, S. 2016, Phys. Rev. Lett., 116, 151102

Heger, A., Langer, N., & Woosley, S. E. 2000, The Astrophysical Journal, 528, 368

Heger, A., Woosley, S. E., & Spruit, H. C. 2005, The Astrophysical Journal, 626, 350

Hempel, M., Fischer, T., Schaffner-Bielich, J., & Liebendörfer, M. 2012, The Astrophysical Journal, 748, 70

Herant, M., Benz, W., & Colgate, S. 1992, The Astrophysical Journal, 395, 642

Hirata, K., Kajita, T., Koshiba, M., et al. 1987, Phys. Rev. Lett., 58, 1490

Hix, W. R., & Thielemann, F.-K. 1996, The Astrophysical Journal, 460, 869

Hix, W. R., & Thielemann, F. K. 1999, Journal of Computational and Applied Mathematics, 109, 321

Ho, W. C. G. 2018, Philosophical Transactions of the Royal Society of London A: Mathematical, Physical and Engineering Sciences, 376, doi:10.1098/rsta.2017.0285

Horowitz, C. J., Caballero, O. L., Lin, Z., O'Connor, E., & Schwenk, A. 2017, , 95, 025801

Hughes, A. J., & Grawoig, D. E. 1971, Statistics, a Foundation for Analysis (Addison-Wesley Pub. Co Reading, Mass), xvi, 525 p. :

Hunter, J. D. 2007, Computing in Science and Engineering, 9, 90

Hyman, J. M. 1979, in Advances in Computer Methods for Partial Differential Equations - III, 313–321

Ibanez, J. M., Aloy, M. A., Font, J. A., et al. 1999, arXiv e-prints, astro

Isenberg, J. A. 2008, International Journal of Modern Physics D, 17, 265

Ivezić, Ž., Kahn, S. M., Tyson, J. A., et al. 2019, The Astrophysical Journal, 873, 111

Iwakami, W., Kotake, K., Ohnishi, N., Yamada, S., & Sawada, K. 2009, The Astrophysical Journal, 700, 232

Jackson, J. D. 1998, Classical Electrodynamics, 3rd Edition

Janka, H.-T., Melson, T., & Summa, A. 2016, Annual Review of Nuclear and Particle Science, 66, 341

Jones, E., Oliphant, T., Peterson, P., et al. 2001–, SciPy: Open source scientific tools for Python

Kagra Collaboration, Akutsu, T., Ando, M., et al. 2019, Nature Astronomy, 3, 35

Kasen, D., Metzger, B., Barnes, J., Quataert, E., & Ramirez-Ruiz, E. 2017, Nature, 551, 80

Kawamura, S., Ando, M., Seto, N., et al. 2021, Progress of Theoretical and Experimental Physics, 2021, 05A105

Klimenko, S., Vedovato, G., Necula, V., et al. 2021, cWB pipeline library: 6.4.0, doi:10.5281/zenodo.4419902

Kochanek, C. S., Beacom, J. F., Kistler, M. D., et al. 2008, The Astrophysical Journal, 684, 1336

Kochanek, C. S., Shappee, B. J., Stanek, K. Z., et al. 2017, Publications of the Astronomical Society of the Pacific, 129, 104502

Kokkotas, K. D., & Schutz, B. F. 1992, Monthly Notices of the Royal Astronomical Society, 255, 119

Kokkotas, K. D., & Stergioulas, N. 1999, Astronomy & Astrophysics, 341, 110

Komori, K., Michimura, Y., & Somiya, K. 2017, Parameters for the latest estimated sensitivity of KAGRA, Tech. rep.

Köpke, L., & IceCube Collaboration. 2011, in Journal of Physics Conference Series, Vol. 309, Journal of Physics Conference Series, 012029

Kotake, K. 2013, Comptes Rendus Physique, 14, 318, gravitational waves / Ondes gravitationnelles

Kotake, K., Iwakami, W., Ohnishi, N., & Yamada, S. 2009, The Astrophysical Journal Letters, 697, L133

Kotake, K., Sumiyoshi, K., Yamada, S., et al. 2012, Progress of Theoretical and Experimental Physics, 2012, 01A301

Kotake, K., Yamada, S., & Sato, K. 2003a, The Astrophysical Journal, 595, 304

—. 2003b, , 68, 044023

Kuroda, T., Kotake, K., & Takiwaki, T. 2012, The Astrophysical Journal, 755, 11

Kuroda, T., Kotake, K., Takiwaki, T., & Thielemann, F.-K. 2018, Monthly Notices of the Royal Astronomical Society, 477, L80

Kuroda, T., Takiwaki, T., & Kotake, K. 2014, , 89, 044011

—. 2016, The Astrophysical Journal Supplement, 222, 20

Laiu, M. P., Harris, J. A., Chu, R., & Endeve, E. 2020, Journal of Physics: Conference Series, 1623, 012013

Langanke, K., & Martinez-Pinedo, G. 2001, Atomic Data and Nuclear Data Tables, 79, 1

Langanke, K., & Martínez-Pinedo, G. 2003, Reviews of Modern Physics, 75, 819

Lattimer, J. M., & Prakash, M. 2000, , 333, 121

—. 2001, The Astrophysical Journal, 550, 426

Lattimer, J. M., & Swesty, D. F. 1991, , 535, 331

LeBlanc, J. M., & Wilson, J. R. 1970, The Astrophysical Journal, 161, 541

Liebendörfer, M. 2005, The Astrophysical Journal, 633, 1042

Liebendörfer, M., Whitehouse, S. C., & Fischer, T. 2009, The Astrophysical Journal, 698, 1174

LIGO Scientific Collaboration, Aasi, J., Abbott, B. P., et al. 2015, Classical and Quantum Gravity, 32, 074001

Lindquist, R. W. 1966, Annals of Physics, 37, 487

Lippuner, J., & Roberts, L. F. 2017, The Astrophysical Journal Supplement, 233, 18

Mabanta, Q. A., & Murphy, J. W. 2018, The Astrophysical Journal, 856, 22

MacNeice, P., Olson, K. M., Mobarry, C., de Fainchtein, R., & Packer, C. 2000, Computer Physics Communications, 126, 330

Marek, A., Dimmelmeier, H., Janka, H. T., Müller, E., & Buras, R. 2006, Astronomy & Astrophysics, 445, 273

Marek, A., & Janka, H. T. 2009, The Astrophysical Journal, 694, 664

Marek, A., Janka, H. T., & Müller, E. 2009, Astronomy & Astrophysics, 496, 475

Martí, J. M., Ibáñez, J. M., & Miralles, J. A. 1991, Phys. Rev. D, 43, 3794

Martí, J. M., & Müller, E. 2003, Living Reviews in Relativity, 6, 7

Martynov, D. V., Hall, E. D., Abbott, B. P., et al. 2016, , 93, 112004

Matheson, T. 2004, in Cosmic explosions in three dimensions, ed. P. Höflich, P. Kumar, & J. C. Wheeler, 351

Mazurek, T. J. 1982, The Astrophysical Journal, 259, L13

McIver, J. 2015, PhD thesis, U Mass Amherst

Mezzacappa, A., Marronetti, P., Landfield, R. E., et al. 2020, , 102, 023027

Mignone, A., Mattia, G., Bodo, G., & Del Zanna, L. 2019, Monthly Notices of the Royal Astronomical Society, 486, 4252

Mignone, A., Tzeferacos, P., & Bodo, G. 2010, Journal of Computational Physics, 229, 5896

Minerbo, G. N. 1978, , 20, 541

Minkowski, R. 1941, Publications of the Astronomical Society of the Pacific, 53, 224

Mirizzi, A., Tamborra, I., Janka, H. T., et al. 2016, Nuovo Cimento Rivista Serie, 39, 1

Moenchmeyer, R., Schaefer, G., Mueller, E., & Kates, R. E. 1991, Astronomy & Astrophysics, 246, 417

Moore, C. J., Cole, R. H., & Berry, C. P. L. 2014, Classical and Quantum Gravity, 32, 015014

Moore, C. J., Cole, R. H., & Berry, C. P. L. 2015, Classical and Quantum Gravity, 32, 015014

Morozova, V., Radice, D., Burrows, A., & Vartanyan, D. 2018, The Astrophysical Journal, 861, 10

Mösta, P., Ott, C. D., Radice, D., et al. 2015, Nature, 528, 376

Mösta, P., Roberts, L. F., Halevi, G., et al. 2018, The Astrophysical Journal, 864, 171

Mösta, P., Mundim, B. C., Faber, J. A., et al. 2014, Classical and Quantum Gravity, 31, 015005

Mueller, E. 1982, Astronomy & Astrophysics, 114, 53

Mueller, E., & Janka, H. T. 1997, Astronomy & Astrophysics, 317, 140

Mukhopadhyay, M., Cardona, C., & Lunardini, C. 2021, arXiv e-prints, arXiv:2105.05862

Müller, B. 2017, arXiv e-prints, arXiv:1703.04633

Müller, B., & Janka, H.-T. 2014, The Astrophysical Journal, 788, 82

Müller, B., Janka, H.-T., & Dimmelmeier, H. 2010, The Astrophysical Journal Supplement, 189, 104

Müller, B., Janka, H.-T., & Marek, A. 2012, The Astrophysical Journal, 756, 84

—. 2013, The Astrophysical Journal, 766, 43

Müller, B., Melson, T., Heger, A., & Janka, H.-T. 2017, Monthly Notices of the Royal Astronomical Society, 472, 491

Müller, E., Rampp, M., Buras, R., Janka, H. T., & Shoemaker, D. H. 2004, The Astrophysical Journal, 603, 221

Murphy, J. W., Dolence, J. C., & Burrows, A. 2013, The Astrophysical Journal, 771, 52

Murphy, J. W., Ott, C. D., & Burrows, A. 2009, The Astrophysical Journal, 707, 1173

Müller, B. 2019, Annual Review of Nuclear and Particle Science, 69, 253

Nagakura, H., Burrows, A., Vartanyan, D., & Radice, D. 2021, Monthly Notices of the Royal Astronomical Society, 500, 696

Nagakura, H., Iwakami, W., Furusawa, S., et al. 2018, The Astrophysical Journal, 854, 136

Neilsen, D., Liebling, S. L., Anderson, M., et al. 2014, , 89, 104029

Obergaulinger, M., & Aloy, M. Á. 2017, Monthly Notices of the Royal Astronomical Society, 469, L43

Obergaulinger, M., Just, O., & Aloy, M. A. 2018, Journal of Physics G Nuclear Physics, 45, 084001

O'Connor, E. 2015, The Astrophysical Journal Supplement Series, 219, 24

O'Connor, E., Horowitz, C. J., Lin, Z., & Couch, S. 2017, Proceedings of the International Astronomical Union, 12, 107–112

O'Connor, E., & Ott, C. D. 2010, Classical and Quantum Gravity, 27, 114103

—. 2011, The Astrophysical Journal, 730, 70

O'Connor, E. P., & Couch, S. M. 2018a, The Astrophysical Journal, 865, 81

—. 2018b, The Astrophysical Journal, 854, 63

Ohnishi, N., Kotake, K., & Yamada, S. 2006, The Astrophysical Journal, 641, 1018

Olausen, S. A., & Kaspi, V. M. 2014, The Astrophysical Journal Supplement, 212, 6

O'Neal, J., Wahib, M., Dubey, A., Weide, K., & Klosterman, T. 2021, doi:10.2172/1810307, doi:10.2172/1810307

Oohara, K.-i., Nakamura, T., & Shibata, M. 1997, Progress of Theoretical Physics Supplement, 128, 183

Oppenheimer, J. R., & Volkoff, G. M. 1939, Physical Review, 55, 374

Ott, C. D. 2009, Classical and Quantum Gravity, 26, 204015

Ott, C. D., Dimmelmeier, H., Marek, A., et al. 2007, Classical and Quantum Gravity, 24, S139

Ott, C. D., Ou, S., Tohline, J. E., & Burrows, A. 2005, The Astrophysical Journal Letters, 625, L119

Ott, C. D., Reisswig, C., Schnetter, E., et al. 2011, Physical Review Letters, 106, 161103

Ott, C. D., Abdikamalov, E., O'Connor, E., et al. 2012, , 86, 024026

Pajkos, M. A., Couch, S. M., Pan, K.-C., & O'Connor, E. P. 2019, The Astrophysical Journal, 878, 13

Pajkos, M. A., Warren, M. L., Couch, S. M., O'Connor, E. P., & Pan, K.-C. 2021, The Astrophysical Journal, 914, 80

Palenzuela, C., Liebling, S. L., Neilsen, D., et al. 2015, , 92, 044045

Pan, K.-C., Liebendörfer, M., Couch, S., & Thielemann, F.-K. 2020, arXiv e-prints, arXiv:2010.02453

Pan, K.-C., Liebendörfer, M., Couch, S. M., & Thielemann, F.-K. 2018, The Astrophysical Journal, 857, 13

Pan, K.-C., Liebendörfer, M., Hempel, M., & Thielemann, F.-K. 2016, The Astrophysical Journal, 817, 72

Pan, K.-C., Liebendörfer, M., Couch, S. M., & Thielemann, F.-K. 2021, The Astrophysical Journal, 914, 140

Paxton, B., Bildsten, L., Dotter, A., et al. 2010, The Astrophysical Journal Supplement Series, 192, 3

Pons, J. A., Ibáñez, J. M., & Miralles, J. A. 2000, Monthly Notices of the Royal Astronomical Society, 317, 550

Porth, O., Olivares, H., Mizuno, Y., et al. 2017, Computational Astrophysics and Cosmology, 4, 1

Radice, D., Morozova, V., Burrows, A., Vartanyan, D., & Nagakura, H. 2019, The Astrophysical Journal Letters, 876, L9

Radice, D., Rezzolla, L., & Galeazzi, F. 2014, Classical and Quantum Gravity, 31, 075012

Rampp, M., & Janka, H. T. 2002, Astronomy & Astrophysics, 396, 361

Rezzolla, L., & Zanotti, O. 2013, Relativistic Hydrodynamics

Richers, S., Ott, C. D., Abdikamalov, E., O'Connor, E., & Sullivan, C. 2017, , 95, 063019

Rudi, J., O'Neal, J., Wahib, M., & Dubey, A. 2021, doi:10.2172/1778932, doi: 10.2172/1778932

Saijo, M. 2004, The Astrophysical Journal, 615, 866

Scheck, L., Janka, H. T., Foglizzo, T., & Kifonidis, K. 2008, Astronomy & Astrophysics, 477, 931

Scheidegger, S., Käppeli, R., Whitehouse, S. C., Fischer, T., & Liebendörfer, M. 2010a, Astronomy & Astrophysics, 514, A51

Scheidegger, S., Whitehouse, S. C., Käppeli, R., & Liebendörfer, M. 2010b, Classical and Quantum Gravity, 27, 114101

Schneider, A. S., Roberts, L. F., Ott, C. D., & O'Connor, E. 2019, Phys. Rev. C, 100, 055802

Shibagaki, S., Kuroda, T., Kotake, K., & Takiwaki, T. 2020, Monthly Notices of the Royal Astronomical Society, 493, L138

—. 2021, Monthly Notices of the Royal Astronomical Society, 502, 3066

Shibata, M., Kiuchi, K., Sekiguchi, Y., & Suwa, Y. 2011, Progress of Theoretical Physics, 125, 1255

Shibata, M., & Nakamura, T. 1995, , 52, 5428

Shibata, M., & Sekiguchi, Y.-I. 2004, , 69, 084024

—. 2005, , 72, 044014

Shu, C.-W. 2009, SIAM Review, 51, 82

Siegel, D. M., Mösta, P., Desai, D., & Wu, S. 2018, The Astrophysical Journal, 859, 71

Skinner, M. A., Dolence, J. C., Burrows, A., Radice, D., & Vartanyan, D. 2019, The Astrophysical Journal Supplement, 241, 7

Smith, N. 2014, Annual Review of Astronomy and Astrophysics, 52, 487

Sotani, H., Kuroda, T., Takiwaki, T., & Kotake, K. 2017, , 96, 063005

Sotani, H., & Sumiyoshi, K. 2019, , 100, 083008

Sotani, H., & Takiwaki, T. 2016, , 94, 044043

—. 2020a, Monthly Notices of the Royal Astronomical Society, 498, 3503

—. 2020b, , 102, 023028

Spruit, H. C. 2002, Astronomy & Astrophysics, 381, 923

Steiner, A. W., Hempel, M., & Fischer, T. 2013a, The Astrophysical Journal, 774, 17

Steiner, A. W., Lattimer, J. M., & Brown, E. F. 2010, The Astrophysical Journal, 722, 33

—. 2013b, The Astrophysical Journal Letters, 765, L5

Stone, J. M., Gardiner, T. A., Teuben, P., Hawley, J. F., & Simon, J. B. 2008, The Astrophysical Journal Supplement, 178, 137

Strolger, L.-G., & Riess, A. G. 2006, The Astronomical Journal, 131, 1629

Sukhbold, T., Ertl, T., Woosley, S. E., Brown, J. M., & Janka, H. T. 2016a, The Astrophysical Journal, 821, 38

—. 2016b, The Astrophysical Journal, 821, 38

Sullivan, C., O'Connor, E., Zegers, R. G. T., Grubb, T., & Austin, S. M. 2016, The Astrophysical Journal, 816, 44

Summa, A., Hanke, F., Janka, H.-T., et al. 2016, The Astrophysical Journal, 825, 6

Summa, A., Janka, H.-T., Melson, T., & Marek, A. 2018, The Astrophysical Journal, 852, 28

Takiwaki, T., Kotake, K., & Foglizzo, T. 2021, Monthly Notices of the Royal Astronomical Society, 508, 966

Takiwaki, T., Kotake, K., & Suwa, Y. 2012, The Astrophysical Journal, 749, 98

—. 2016, Monthly Notices of the Royal Astronomical Society, 461, L112

Tamborra, I., Hanke, F., Janka, H.-T., et al. 2014, The Astrophysical Journal, 792, 96

Timmes, F. X., & Swesty, F. D. 2000, The Astrophysical Journal Supplement, 126, 501

Titus, R., Sullivan, C., Zegers, R. G. T., Brown, B., & Gao, B. 2018, JPhG, 45, 014004

Todd-Rutel, B. G., & Piekarewicz, J. 2005, Physical Review Letters, 95, 122501

Tolman, R. C. 1939, Physical Review, 55, 364

Toro, E. 2009, Riemann Solvers and Numerical Methods for Fluid Dynamics: A Practical Introduction (Springer Berlin Heidelberg)

Toro, E. F., Spruce, M., & Speares, W. 1994, Shock Waves, 4, 25

Torres-Forné, A., Cerdá-Durán, P., Obergaulinger, M., Müller, B., & Font, J. A. 2019a, Physical Review Letters, 123, 051102

Torres-Forné, A., Cerdá-Durán, P., Passamonti, A., & Font, J. A. 2018, Monthly Notices of the Royal Astronomical Society, 474, 5272

Torres-Forné, A., Cerdá-Durán, P., Passamonti, A., Obergaulinger, M., & Font, J. A. 2019b, Monthly Notices of the Royal Astronomical Society, 482, 3967

Unno, W., Osaki, Y., Ando, H., & Shibahashi, H. 1989, Nonradial Oscillation of Stars (2nd ed.; Tokyo: University of Tokyo Press)

Utrobin, V. P., Wongwathanarat, A., Janka, H. T., & Müller, E. 2017, The Astrophysical Journal, 846, 37

van der Walt, S., Colbert, S. C., & Varoquaux, G. 2011, Computing in Science and Engineering, 13, 22

Vartanyan, D., & Burrows, A. 2020, The Astrophysical Journal, 901, 108

Vartanyan, D., Burrows, A., & Radice, D. 2019, Monthly Notices of the Royal Astronomical Society, 489, 2227

Vartanyan, D., Burrows, A., Radice, D., Skinner, M. A., & Dolence, J. 2018, Monthly Notices of the Royal Astronomical Society, 477, 3091

Warren, M. L., Couch, S. M., O'Connor, E. P., & Morozova, V. 2020, The Astrophysical Journal, 898, 139

Weaver, T. A., Zimmerman, G. B., & Woosley, S. E. 1978, The Astrophysical Journal, 225, 1021

Wheeler, J. A. 1966, Annual Reviews of Astronomy and Astrophysics, 4, 393

Winteler, C., Käppeli, R., Perego, A., et al. 2012, The Astrophysical Journal Letters, 750, L22

Woosley, S. E., & Bloom, J. S. 2006, Annual Reviews of Astronomy and Astrophysics, 44, 507

Woosley, S. E., & Heger, A. 2006, The Astrophysical Journal, 637, 914

—. 2007, , 442, 269

Woosley, S. E., Heger, A., & Weaver, T. A. 2002, Reviews of Modern Physics, 74, 1015

Yamada, S., & Sato, K. 1995, The Astrophysical Journal, 450, 245

York, J. W., J. 1983, The initial value problem and dynamics., Vol. 124, 175–201

Zha, S., O'Connor, E. P., Chu, M.-c., Lin, L.-M., & Couch, S. M. 2020, Physical Review Letters, 125, 051102

Zwerger, T., & Mueller, E. 1997, Astronomy & Astrophysics, 320, 209